Dynamics of mantle plumes: Linking scales and coupling physics

Kumulative Dissertation
zur Erlangung des akademischen Grades
"doctor rerum naturalium"
(Dr. rer. nat.)
in der Wissenschaftsdisziplin Geophysik

eingereicht an der
Mathematisch-Naturwissenschaftlichen Fakultät
der Universität Potsdam

von
Juliane Dannberg

Potsdam, 17. Mai 2016

Mentor:	Prof. Dr. Stephan V. Sobolev
Erstbetreuer:	Prof. Dr. Michael Weber
Zweitbetreuer:	Prof. Dr. Volker John
Gutachter:	Prof. Thorsten Becker
	Dr. Maxim Ballmer

Published online at the
Institutional Repository of the University of Potsdam:
URN urn:nbn:de:kobv:517-opus4-91024
http://nbn-resolving.de/urn:nbn:de:kobv:517-opus4-91024

Abstract

Mantle plumes are a link between different scales in the Earth's mantle: They are an important part of large-scale mantle convection, transporting material and heat from the core-mantle boundary to the surface, but also affect processes on a smaller scale, such as melt generation and transport and surface magmatism. When they reach the base of the lithosphere, they cause massive magmatism associated with the generation of large igneous provinces, and they can be related to mass extinction events (Wignall, 2001) and continental breakup (White and McKenzie, 1989).

Thus, mantle plumes have been the subject of many previous numerical modelling studies (e.g. Farnetani and Richards, 1995; d'Acremont et al., 2003; Lin and van Keken, 2005; Sobolev et al., 2011; Ballmer et al., 2013). However, complex mechanisms, such as the development and implications of chemical heterogeneities in plumes, their interaction with mid-ocean ridges and global mantle flow, and melt ascent from the source region to the surface are still not very well understood; and disagreements between observations and the predictions of classical plume models have led to a challenge of the plume concept in general (Czamanske et al., 1998; Anderson, 2000; Foulger, 2011). Hence, there is a need for more sophisticated models that can explain the underlying physics, assess which properties and processes are important, explain how they cause the observations visible at the Earth's surface and provide a link between the different scales.

In this work, integrated plume models are developed that investigate the effect of dense recycled oceanic crust on the development of mantle plumes, plume–ridge interaction under the influence of global mantle flow and melting and melt migration in form of two-phase flow.

The presented analysis of these models leads to a new, updated picture of mantle plumes: Models considering a realistic depth-dependent density of recycled oceanic crust and peridotitic mantle material show that plumes with excess temperatures of up to 300 K can transport up to 15% of recycled oceanic crust through the whole mantle. However, due to the high density of recycled crust, plumes can only advance to the base of the lithosphere directly if they have high excess temperatures, high plume volumes and the lowermost mantle is subadiabatic, or plumes rise from the top or edges of thermo-chemical piles. They might only cause minor surface uplift, and instead of the classical head–tail structure, these low-buoyancy plumes are predicted to be broad features in the lower mantle with much less pronounced plume heads. They can form a variety of shapes and regimes, including primary plumes directly advancing to the base of the lithosphere, stagnating plumes, secondary plumes rising from the core–mantle boundary or a pool of eclogitic material in the upper mantle and failing plumes. In the upper mantle, plumes are tilted and deflected by global mantle flow, and the shape, size and stability of the melting region is influenced by the distance from nearby plate boundaries, the speed of the overlying plate and the movement of the plume tail arriving from the lower mantle. Furthermore, the structure of the lithosphere controls where hot material is accumulated and melt is generated. In addition to melting in the plume tail at the plume arrival position, hot plume material flows upwards towards opening rifts, towards mid-ocean ridges and towards other regions of thinner lithosphere, where it produces additional melt due to decompression. This leads to the generation of either broad ridges of thickened magmatic crust or the separation into multiple thinner lines of sea mount chains at the surface. Once melt is generated within the plume, it influences its dynamics, lowering the viscosity and density, and while it rises the melt volume is increased up to 20% due to decompression. Melt has the tendency to accumulate at the top of the plume head, forming diapirs and initiating small-scale convection when the plume reaches the base of

the lithosphere. Together with the introduced unstable, high-density material produced by freezing of melt, this provides an efficient mechanism to thin the lithosphere above plume heads.

In summary, this thesis shows that mantle plumes are more complex than previously considered, and linking the scales and coupling the physics of different processes occurring in mantle plumes can provide insights into how mantle plumes are influenced by chemical heterogeneities, interact with the lithosphere and global mantle flow, and are affected by melting and melt migration. Including these complexities in geodynamic models shows that plumes can also have broad plume tails, might produce only negligible surface uplift, can generate one or several volcanic island chains in interaction with a mid–ocean ridge, and can magmatically thin the lithosphere.

Zusammenfassung

Mantelplumes verbinden Prozesse auf verschiedenen Skalen im Erdmantel: Sie sind ein wichtiger Teil der globalen Mantelkonvektion, sie transportieren Material und Wärmeenergie von der Kern-Mantel-Grenze zur Erdoberfläche, aber beeinflussen auch kleinskaligere Prozesse wie Schmelzbildung und -transport und die damit verbundenen magmatischen Ereignisse. Wenn Plumes die Unterseite der Lithosphäre erreichen, entstehen große Mengen partiell geschmolzenen Gesteins, was zu großräumigen Vulkaneruptionen sowie der Entstehung von Plateaubasaltprovinzen führt, und auch mit Massenaussterbeereignissen und dem Auseinanderbrechen von Kontinenten in Zusammenhang stehen kann.

Aufgrund dieser erdgeschichtlichen Bedeutung wurde bereits eine große Anzahl an Studien über Plumes durchgeführt (z.B. Farnetani und Richards, 1995; d'Acremont u. a., 2003; Lin und van Keken, 2005; Sobolev u. a., 2011; Ballmer u. a., 2013). Trotzdem ist unser Verständnis komplexerer Vorgänge und Interaktionen in Plumes noch nicht vollständig: Beispiele sind die Entwicklung von chemisch heterogenen Plumes, der Einfluss dieses chemisch andersartigen Materials auf die Aufstiegsdynamik, die Wechselwirkung zwischen Plumes und mittelozeanischen Rücken sowie den globalen Konvektionsströmungen und das Aufsteigen von Schmelze von ihrer Entstehungsregion bis hin zur Erdoberfläche. Unterschiede zwischen Beobachtungen und den Aussagen klassischer Modelle werden als Argumente gegen das Plumekonzept insgesamt angeführt (Czamanske u. a., 1998; Anderson, 2000; Foulger, 2011). Daher gibt es weiterhin einen Bedarf für ausgereiftere Modelle, welche die Skalen verschiedener Prozesse verbinden, den Einfluss dieser Prozesse sowie der Material- und Strömungseigenschaften berücksichtigen und quantifizieren, ihre Auswirkungen an der Erdoberfläche erklären und diese mit Beobachtungen vergleichen.

Im Rahmen dieser Arbeit wurden Plume-Modelle erstellt, welche den Einfluss dichter, recycelter ozeanischer Kruste auf die Entwicklung van Mantelplumes, die Interaktion von Plumes und mittelozeanischen Rücken und den Einfluss globaler Mantelkonvektion sowie Aufschmelzung und Schmelzaufstieg in Form von Zweiphasenströmung ("two-phase flow") untersuchen.

Die vorgestellte Analyse dieser Modelle ergibt ein neues, aktualisiertes Konzept von Mantelplumes: Wenn ein realistischer Dichteunterschied zwischen recycelter ozeanischer Kruste und peridotitischem Mantel angenommen wird, kann ein Plume bis zu 15% recyceltes Material durch den gesamten Mantel transportieren. Durch die hohe Dichte der recycelten Kruste können Plumes aber nur bis zur Lithosphäre aufsteigen, wenn ihre Temperatur und ihr Volumen hoch genug sind, und wenn die Temperatur im unteren Mantel subadiabatisch ist oder die Plumes von aufgewölbten thermo-chemischen "Piles" aufsteigen. Es ist durchaus möglich, dass diese Plumes nur eine geringe Hebung der Oberfläche verursachen, und anstatt der klassischen pilzförmigen Kopf-Tail-Struktur bilden sie breite Strukturen im unteren Mantel mit weitaus weniger ausgeprägtem Plumekopf. Dafür können sie in verschiedenen Formen und Regimes auftreten: Primäre Plumes, welche direkt von der Kern-Mantel-Grenze zur Lithosphäre aufsteigen, stagnierende Plumes, sekundäre Plumes von der Kernmantelgrenze oder einer Ansammlung eklogitischen Materials im oberen Mantel und scheiternde Plumes, die die Lithosphäre nicht erreichen. Im oberen Mantel werden Plumes durch globale Konvektion abgelenkt und geneigt, und die Form, Größe und Stabilität der Schmelzregion wird durch den Abstand zu nahen Plattengrenzen, der Geschwindigkeit der sich darüber bewegenden Platte und der Bewegung des aus dem unteren Mantel ankommenden Plume-Tails bestimmt. Weiterhin beeinflusst auch die Struktur der Lithosphäre wo sich warmes Material sammeln kann und Schmelze entsteht. Zusätzlich zur Aufschmelzung beim Erreichen der Untergrenze der Lithosphäre strömt heißes Plumematerial auch lateral und weiter nach oben zu sich öffnenden Rifts, zu mit-

telozeanischen Rücken sowie zu anderen Regionen dünnerer Lithosphäre, wo durch die Druckentlastung weitere Schmelze generiert wird. Diese führt an der Erdoberfläche zur Entwicklung von entweder breiten Rücken verdickter magmatischer Kruste oder der Aufteilung in mehrere ozeanischen Inselketten. Sobald Schmelze generiert wurde, beeinflusst diese auch die Dynamik des Plumes, indem sie Viskosität und Dichte verringert. Während des Plumeaufstiegs kann sich das Schmelzvolumen dabei durch die Dekompression um bis zu 20% vergrößern. Schmelze hat die Tendenz sich an der Oberseite des Plumes anzusammeln, wo sie Diapire formt und kleinräumige Konvektion auslöst, wenn der Plume die Lithosphäre erreicht. Zusammen mit dem dichten, instabilen Material, das entsteht, wenn die Schmelze wieder erstarrt, bildet dies einen effektiven Mechanismus zur Erosion der Lithosphäre durch Plume-Heads.

Zusammenfassend zeigt die vorliegende Arbeit, dass Mantelplumes komplexer sind als bisher angenommen, und dass die Verbindung von Skalen und die Kombination verschiedener in Mantelplumes auftretender physikalischer Prozesse Erkenntnisse liefern kann, wie Mantelplumes durch chemische Heterogenität beeinflusst werden, wie sie mit mittelozeanischen Rücken und globaler Mantelkonvektion interagieren und wie sie durch Aufschmelzung und Schmelzmigraiton beeinflusst werden. Die Einbindung dieser Prozesse in geodynamische Modelle zeigt, dass Plumes breite Tails haben können, potentiell nur geringe Oberflächenhebung verursachen, in Interaktion mit einem mittelozeanischen Rücken eine oder mehrere vulkanische Inselketten erzeugen können und magmatisch die Lithosphäre erodieren können.

Contents

Chapter 1

Introduction

1.1 Importance of Mantle Plumes

Geodynamic processes cover a wide range of scales – both spatially and temporally. While the mantle spans thousands of kilometres and the characteristic time scale of mantle convection is on the order of hundreds of millions of years, melt migrates through lithosphere and crust on a time scale of thousands of years, and volcanic eruptions can occur within a few hours or minutes. Mantle plumes are one link between those scales: They are a part of large-scale mantle convection, transporting material and heat from the core-mantle boundary to the surface, but also affect processes on a smaller scale, such as melt generation and transport and surface magmatism.

As the Earth is cooling over time – transporting heat from the center to the outside – the Earth's core is hotter than the mantle and there is a temperature gradient across the core–mantle boundary, allowing hot material to accumulate and finally buoyantly ascend towards the surface as mantle plumes. When the head of such a mantle plume approaches the base of the lithosphere, its temperature exceeds the solidus and causes the generation of a large amount of melt. This melt migrates upwards through the lithosphere and crust, resulting in massive eruptions – in many cases of several million cubic kilometres of flood basalts – in only a few million years (Richards et al., 1989; Campbell and Griffiths, 1990) and the formation of a large igneous province (LIP). Throughout the Earth's history, these LIPs are temporally associated with mass extinction events such as the end-Permian extinction with an extinction rate of more than 50% (Wignall, 2001; White and Saunders, 2005; Sobolev et al., 2011). Moreover, they are often accompanied by a significant thinning of the lithosphere, sometimes ending in continental breakup (White and McKenzie, 1989). After the initial plume-head stage, a stable plume conduit remains in the mantle for up to hundreds of millions of years and typically generates a hotspot track, an age-progressive volcanic chain caused by melting in the stationary plume tail as it is overridden by a moving plate.

Due to this significant impact on surface processes, many observations are available that constrain the properties of mantle plumes. As the Earth's mantle still remains inaccessible to direct observation methods, geodynamic modelling has become a valuable tool to investigate the dynamics of mantle plumes. However, complex mechanisms, such as the development and implications of chemical heterogeneities in plumes, their interaction with mid-ocean ridges and global mantle flow, and melt ascent from the source region to the surface are still not very well understood; and disagreements between observations and the predictions of classical plume models have led to a challenge of the plume concept in general (Czamanske et al., 1998; Anderson, 2000; Foulger, 2011). Hence, there is still a

need for more sophisticated models that can explain the underlying physics, assess which properties and processes are important, provide a link between the different scales and explain how they cause the observations visible at the Earth's surface.

This chapter will summarize the classical mantle plume theory, available observations and previous modelling studies, deducing a number of important open questions that aim at improving our understanding of the processes occurring within the Earth.

1.2 Plume Hypothesis

Tuzo Wilson (1963a, 1963b) was probably the first to recognize a link between large igneous provinces, age-progressive volcanic island chains and stable upwellings in the Earth's mantle. He proposed that melting takes place above regions where convection patterns result in stable upward flow, or when a fast-moving surface layer moves over a more slowly moving source of melt in the mantle. He concluded that through this process, an active volcano remains fixed above the rising vertical currents and a line of progressively older, extinct volcanoes develops in the direction of surface motion, leading to a correlation between the age of the oceanic islands and their distance from the source region. However, Wilson related hotspot volcanism to the large-scale convection pattern, and he proposed an origin of the melting source material in a depth of only 200 km, within the relatively immobile centres of convection cells. Jason Morgan (1971) later revised this hypothesis, suggesting hot plumes rising from the deep mantle and spreading radially below the rigid plates as mechanism to generate hotspot volcanism. His theory is based on the observation that ocean island basalts have a different, "primordial" composition (in contrast to the more depleted signature of mid-ocean ridge basalts from the asthenosphere), which indicates their origin from different, potentially chemically isolated reservoirs. In addition, stable upward flow of hot material also explains the high dynamic topography and gravitational potential above hotspots. Morgan (1981) furthermore recognized flood basalts and oceanic plateaus as the initial stages of plume volcanism, possibly linked to continental breakup and followed by weaker magmatic activity producing the hotspot tracks.

This theory, together with a growing number of observations, gave rise to a multitude of theoretical, laboratory and numerical modelling studies to better understand mantle plumes. Whitehead and Luther (1975) were the first to execute laboratory experiments that aimed at improving our understanding of the shape and dynamics of mantle plumes (Condie, 2001). They studied the development of instabilities in a low-density thin bottom layer overlain by a layer of thick and denser material in dependence of the viscosity contrast between these layers; and they found that if the viscosity was lower in the upwelling material, it tended to form spherical pockets fed by thin conduits. The observation is explained by the fact that the force required for the material ascent is mainly determined by the higher viscosity of the ambient fluid, so that instabilities in the bottom layer grow in diameter until the velocity of buoyant ascent is greater than their growth rate. In contrast, for a higher viscous upwelling the forces needed to deform the rising fluid are the limiting factor so that thin, finger-like structures a favoured. These results led to the idea of the separation of mantle plumes into a bulbous head and a narrow tail. Olson and Singer (1985) extended this theory, recognizing that due to their reduced viscosity plume conduits can act as ascent channels for new material from a boundary layer. Yuen and Peltier (1980) applied these insights to the Earth's mantle in a theoretical study and came to the conclusion that temperature-induced viscosity reduction leads to instabilities of the D"-layer in the lowermost mantle and rapidly rising mantle plumes. Later, Griffiths (1986) and Griffiths and Campbell (1990) pointed out the differences between the ascent

of a chemically and a thermally buoyant plume: Considering both isolated "thermals" and plumes continuously fed by a boundary layer, they used artificial polybutene oils and glucose syrup, respectively, to investigate the effect of the temperature-dependence of viscosity (and density) on the dynamics of thermal plumes. Their theoretical and laboratory experiments showed that in contrast to chemically buoyant upwellings, which form circular heads, thermal plumes heat and entrain the surrounding material, resulting in a flattening of the plume head to a torus and giving the impression of a mushroom-shaped plume (Figure 1.1a).

The application of these results to continental flood basalts and hotspot tracks (Morgan, 1981; Olson and Singer, 1985; Richards et al., 1989; Campbell and Griffiths, 1990) supported the hypothesis of mantle plumes as the cause of intraplate volcanism and provided an explanation for the different manifestations of magmatism in form of a flood basalt initiation related to the plume head and the subsequent long-term oceanic island chain stage associated with the plume conduit.

As more computer power became available, increasingly also numerical models of mantle plumes were developed (Richter, 1978). For these models, the resolution is always limited by the available computing power, and in the beginning they were restricted to two dimensions. Thus, many early models focused on convection in general (e.g. Torrance and Turcotte, 1971; Richter, 1973; McKenzie et al., 1974; Parmentier et al., 1976; Christensen, 1984a) instead of the more localized mantle plumes. That said, numerical models have the advantage that more complex physical processes can be included, which are expected to play a crucial role for convection in general and mantle plumes in particular. Examples are non-linear rheology (Parmentier et al., 1976; Christensen, 1984a), internal heating (McKenzie et al., 1974), phase transitions (Richter, 1973), or melting (Farnetani and Richards, 1994); and forces in the model can be evaluated to improve the understanding of the dynamics.

A number of studies followed that investigated starting mantle plumes: Olson et al. (1988) compared experimental and numerical models of plume formation from a hot, low-viscosity boundary layer to validate their results. They concluded that numerical models successfully reproduce experiments, with only a temporal discrepancy – due to the reduction to two dimensions in the computation. Extending their numerical models to mantle parameters, they also found that a weakening mechanism is needed in order for plumes to be able to thin the lithosphere. Farnetani and Richards (1994) and Farnetani and Richards (1995) were some of the first to investigate the surface expressions of mantle plumes in numerical models (Figure 1.1b). The authors predicted a surface uplift of several kilometres above rising plume heads and plume excess temperatures of approximately 300 K to reach the estimated melt volumes of large igneous provinces. They showed that despite the entrainment of ambient mantle material into the rising plume, the melting region still mainly samples plume source material, supporting the idea that plume-generated melts primarily originate from enriched material carried from a reservoir at the core–mantle boundary to the surface. In addition, they recognized that a viscosity decrease, such as it is expected to occur from the lower to the upper mantle, induces a narrowing of the plume due to its increased upward velocity. This theory was revised by van Keken (1997), who reinforced the statement that melting in the plume head primarily samples material originating from the initial boundary layer, but also demonstrated that a stronger and more realistic temperature-dependence of viscosity drastically increases entrainment, that the plume tail also contains a large fraction of ambient mantle material, and that consideration of stress-dependent rheology significantly changes the plume shape and increases mixing (Figure 1.1c,d).

Together with the laboratory models of Griffiths and Campbell (1990), these results

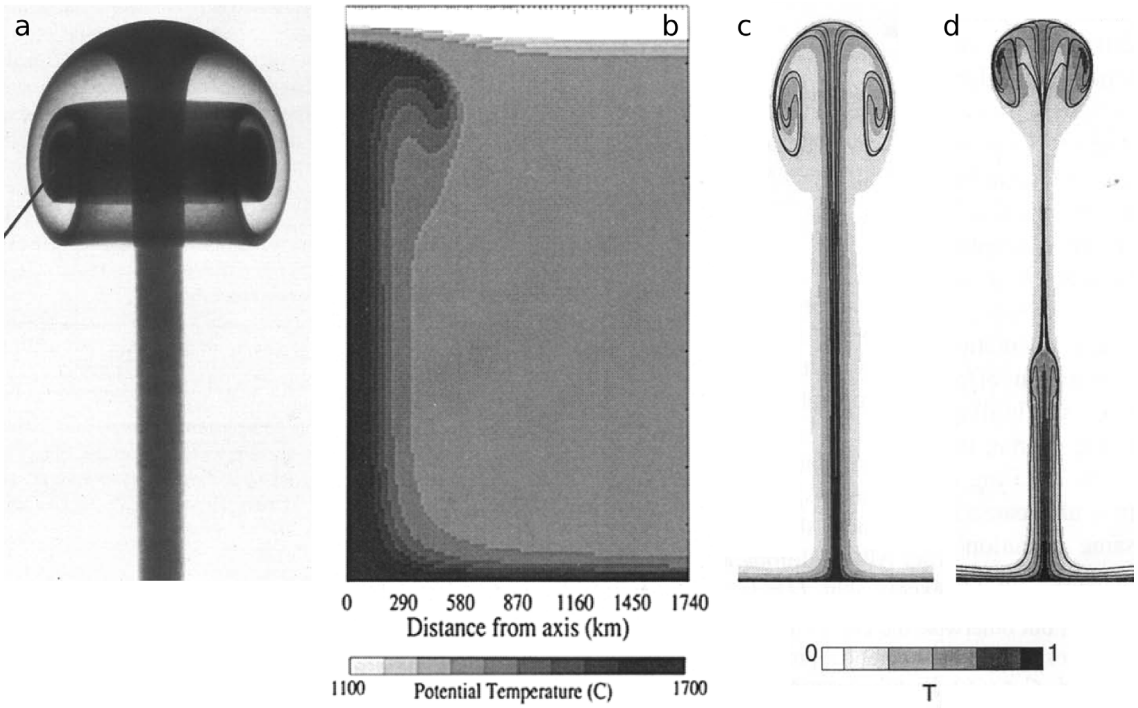

Figure 1.1: The classical plume model. (a) Laboratory model of Griffiths and Campbell (1990), (b) numerical model of Farnetani and Richards (1995), and numerical models of van Keken (1997) without (c) and with (d) stress-dependent rheology.

shaped what would become the classical mantle plume model (Figure 1.1). For a more comprehensive review, the interested reader is referred to Jellinek and Manga (2004) and Ribe et al. (2007).

As more observational data became available in the last years, more detailed studies about individual aspects of mantle plumes and their relation to these observations were conducted. The following sections will give an overview about the most important observations (Section 1.3), and summarize recent relevant modelling studies (Section 1.4).

1.3 Observations

1.3.1 Large Igneous Provinces and Ocean Island Basalts

The plume model (see Section 1.2) suggests massive melting associated with the formation of a large igneous province when the head of a hot mantle plume reaches the base of the lithosphere, and subsequently the development of a volcanic chain as the plate moves over the relatively stable plume tail (e.g. Richards et al., 1989). Hence, the characterization of LIPs and ocean island basalts can give us criteria to test the plume hypothesis and constrain the properties of mantle plumes in general as well as individual plumes.

Coffin and Eldholm (1994) defined large igneous provinces as "massive crustal emplacements of predominantly mafic (Mg and Fe rich) extrusive and intrusive rock which originate via processes other than 'normal' seafloor spreading." This means that LIPs are anomalous magmatic events, generated by different processes than the "normal" plate boundary volcanism and not associated with plate tectonics. Typical features include (Bryan and Ernst, 2008):

- Their large areal extension ($> 0.1 \times 10^6\,\mathrm{km}^2$, in most cases $> 1 \times 10^6\,\mathrm{km}^2$) and volume ($> 0.1 \times 10^6\,\mathrm{km}^3$), implying a typical thickness of extrusive rocks of more than 1 km,
- The emplacement of this large amount of magma over a geologically short and finite period and in a focused area with a pulsed character of the igneous events (with >75% of the total magma volume being emplaced in less than 1 – 5 Ma), implying high melt production rates,
- Their independence from plate boundaries, often in an intraplate tectonic setting and with a distinct petrological, geochemical and isotopic signature (see Section 1.3.4).

Morover, in many cases LIP volcanism precedes or is accompanied by rifting and continental breakup (e.g. Richards et al., 1989; White and McKenzie, 1989; Coffin and Eldholm, 1994; Ernst et al., 2005), generating volcanic rifted margins characterized by seaward-dipping reflectors and high-velocity lower crustal bodies presumably originating from underplating material (Ernst et al., 2005). However, it is still debated if mantle plumes can cause or assist continental breakup, or if they only passively erupt into the rift.

The timing of LIPs has also been correlated with mass extinction events throughout the Earth's history (Courtillot and Renne, 2003; White and Saunders, 2005). It has been proposed (Wignall, 2001; Sobolev et al., 2011) that released gases associated with the magmatism such as CO_2, SO_2 and HCl could change the global temperature and influence the climate if injected into the stratosphere, leading to an environmental catastrophe. Nevertheless, it is still debated if mantle plumes are really the main cause of extinction events, and other mechanisms have been suggested, most notably meteorite impacts, which also show a temporal correlation with mass extinctions (Ernst et al., 2005; White and Saunders, 2005).

Hotspots, the surface expression of plume tails, are characterized by the following features (Condie, 2001):

- An active (or recently active) volcano at the present location of the hotspot, and an age-progressive chain of extinct volcanoes leading away from it in the direction of the absolute plate motion, in some cases connecting the active volcano to a large igneous province,
- A topographic swell of 500 – 1000 m and a typical width of 1000 – 2000 km and an associated gravity/geoid high,
- An anomalous mass flux of 300 – 6300 kg/s (Steinberger, 2000),
- A high heat flux, determined by their bouyancy flux and their excess temperature (see Section 1.3.2),
- A different chemical composition of the melts compared to MORB (see Section 1.3.4),
- Low seismic velocities, sometimes visible down to the lower mantle (see Section 1.3.5).

All of these observations provide excellent criteria to constrain plume properties in numerical models.

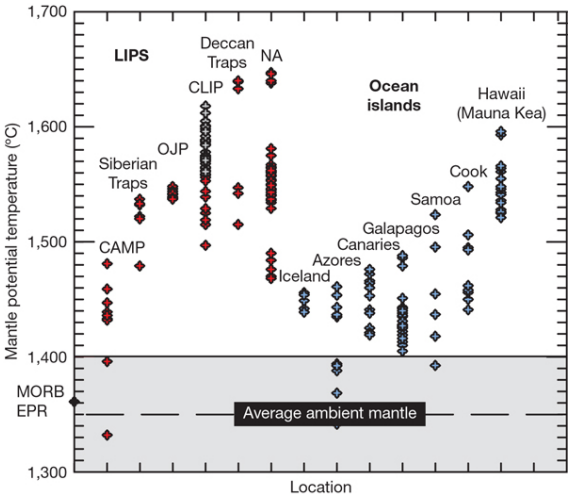

Figure 1.2: Potential temperatures of large igneous provinces and ocean island basalts in comparison to the ambient mantle temperature. From Herzberg and Gazel (2009).

1.3.2 Plume Temperatures

Both the composition of ocean island basalts and flood basalts, in particular their MgO and FeO contents, and the effects of hotspots on nearby mid-ocean ridges allow estimates about the temperatures of mantle plume heads and tails. Schilling (1991) investigated plume-influenced mid-ocean ridges, and used the extent of the plume-induced geochemical anomaly and the excess elevation at the ridge caused by the positive plume buoyancy to constrain plume temperatures. Combining the two methods, he obtains excess temperatures of 160 – 280 K. Using the MgO content of lavas from different LIPs and ocean island basalts, Herzberg and Gazel (2009) estimate their potential temperatures and compare it to that of mid-ocean ridge basalts. They infer generally higher melt fractions and higher excess temperatures of up to 300 K for large igneous provinces compared to the younger ocean island basalts (up to 250 K, Figure 1.2), which is explained by the origin of LIPs from the hotter plume head as opposed to the more effectively cooled plume tail for OIBs. In a different study, Putirka (2008) also use petrological models to calculate potential temperatures of several hotspots, and find values of 175 –195 K for most of them. Moreover, they see a correlation between excess temperatures and plume buoyancy fluxes, indicating a thermal origin of buoyancy (and thus, hotspot swells).

However, if plumes originate from the core-mantle boundary, their excess temperatures should relate to the temperature difference across the thermal boundary layer at the base of the mantle. Estimates for the CMB temperature range from 3300 – 4400 K (Boehler, 2000; Hernlund et al., 2005; Lay et al., 2008), implying a temperature jump of 500 – 1800 K (Lay et al., 2008). As the plume excess temperature close to the surface seems to be much smaller, there has to be some mechanism that reduces the plume temperatures during their ascent. Plumes rise adiabatically, and on a higher temperature adiabat than the ambient mantle, explaining a part of the decrease in excess temperature. However, presumably neither adiabatic cooling nor thermal diffusion/entrainment of ambient material (Farnetani, 1997) can account for such a high temperature drop, and thus other explanations have been proposed: Farnetani (1997) has suggested that a chemically dense bottom boundary layer could effectively reduce the plume excess temperature as it prevents the lowermost part of the layer from rising with the plume. Another theory was brought forward by Bunge (2005), who has argued that radiogenic heat production in

the mantle leads to a subadiabatic mantle temperature profile, while plumes still rise adiabatically, thus explaining a decrease in excess temperature from the CMB to the surface.

Whichever explanation (or combination of processes) is the reason, numerical models of mantle plumes should satisfy both constraints for the bottom boundary layer temperature and the surface plume excess temperature, and these estimates can serve as a criterion to assess how realistic a given model is.

1.3.3 Domal Uplift

If large igneous provinces are the surface expression of mantle plume heads, they should be characterized by a significant domal uplift of the surface before magma emplacement due to the presence of the hot, buoyant upwelling material. Thus, the magnitude and extent of uplift should allow estimates about the plume temperature and size/shape, respectively, if a purely thermal origin is assumed (Ernst et al., 2005). This idea was already invoked by Griffiths and Campbell (1991) for laboratory and theoretical plume models, implying a maximum uplift of 500 – 1000 m, and for numerical models by Farnetani and Richards (1994), who predicted a surface uplift on the order of 2 – 4 km.

Geologic observations can help to test this hypothesis and estimate surface uplift before the onset of LIP magmatism (Campbell, 2007): For older flood basalts, erosion surfaces at the base of the basaltic layers can provide evidence for premagmatic uplift, both for terrestrial and shallow marine sediments that are lifted above sea level. In addition, radiating patterns of river drainage may indicate uplift (Ernst et al., 2005). Even for sediments remaining below sea level, a facies change might be present. In addition, for younger flood basalts uplift might even be preserved in form of high topography compared to the surrounding area.

Indeed, premagmatic surface uplift is observed for a number of large igneous provinces, such as the Emeishan Traps (260 Ma), Siberian Traps (251 Ma), Deccan Traps (65 Ma), North Atlantic (Phase 1, 61 Ma and Phase 2, 55 Ma), Yellowstone (16 Ma to recent) and several others (Saunders et al., 2007; Campbell, 2007, and references therein). For the Emeishan LIP, He et al. (2003) estimate an uplift of more than 1000 m. Another prominent example are the Ethiopian flood basalts in East Africa, elevated on a plateau approximately 2000 m high (Campbell, 2007). However, there are also studies that question the occurrence of significant uplift before the onset of magmatism, especially for the Siberian Traps, where subsidence seems to accompany the emplacement of basalts (Czamanske et al., 1998), and the Ontong Java Plateau, which never formed a large subaerial plateau and thus can not have been uplifted as much as predicted by thermal plume models (Roberge et al., 2005), leading to a challenge of a plume origin for these LIPs. But also for other flood basalts it is argued that there is a more complex pattern of subsidence and minor localised uplift (Emeishan Traps, Sun et al., 2010) or a much smaller uplift (on the order of 400 m for the East Greenland flood basalt province, Peate et al., 2003) instead of broad, kilometre-scale surface uplift.

This discrepancy between model predictions and observations calls for an update of the classical plume model, which can also reconcile the absence of significant uplift with a mantle plume origin.

1.3.4 Geochemistry of Mantle Plumes

Most geochemical heterogeneities are generated by melting events: Usually, the mantle only melts partially, and this generally leads to different compositions of melt and solid,

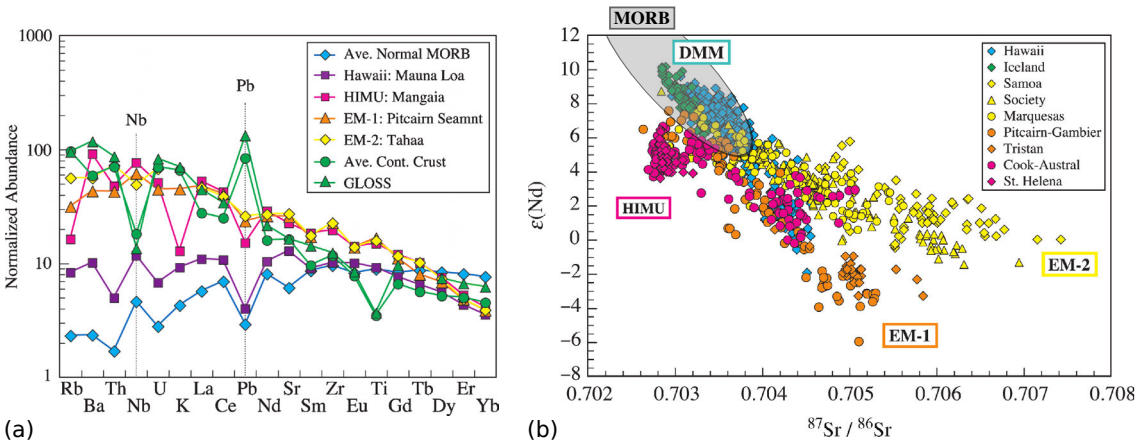

Figure 1.3: Typical geochemical characteristics of ocean island basalts. (a) Primitive-mantle normalized trace element abundance diagrams (spidergrams) for different oceanic island basalts, average MORB, average continental crust and average subducting sediment (GLOSS), from Hofmann (2003). Elements are arranged in order of increasing compatibility from left to right. (b) $^{143}Nd/^{144}Nd$ ($\epsilon(Nd)$) versus $^{87}Sr/^{86}Sr$ for OIB (excluding island arcs). The islands or island groups selected are chosen to represent extreme isotopic compositions in isotope diagrams. The gray field for MORB is plotted for comparison. Modified from Hofmann (2003).

depending on the partition coefficients of the involved elements. Some elements can be accommodated very well in the crystal lattice of the minerals: These are the compatible elements that preferentially stay in the solid residuum. But other elements do not fit into the mineral structure very well – usually because of either ionic size or charge – and hence will have a higher concentration in the melt than in the solid: These are the incompatible elements. The distribution of these elements in mantle rocks allows us to draw conclusions about melt fractions (the larger the melt fraction, the more compatible elements will also be present in the melt), their origin (because the composition of the melt still reflects the composition of the source rock) and sometimes even which processes were involved in creating a certain geochemical heterogeneity (because different elements are compatible/incompatible in different processes). The following section will only give a short overview about this complex topic, and for a more thorough review the reader is referred to Hofmann (2003), White (2010), and Farnetani and Hofmann (2011).

The discovery that ocean island basalts are chemically different from MORBs was already made a very long time ago (e.g. Schilling, 1973; Hart et al., 1973) and was part of the original plume concept (Morgan, 1971). As these differences do not only appear in the major element composition, indicating higher potential temperatures than for the passively upwelling ridge basalts (see Section 1.3.2), but also in trace elements (Schilling, 1973) and isotope ratios (Hart et al., 1973), they imply a different mantle source and depth of origin, consistent with the model of melting in a hot mantle plume.

Hofmann and White (1982) were the first to suggest a theory that fits many of these observations: that this distinct source composition originates from ancient oceanic crust subducted into the mantle all the way to the core-mantle boundary, where it segregates from the oceanic lithosphere and is stored at the base of the mantle until it is hot enough to be entrained in an ascending mantle plume. Since then, many geochemical data have been presented that support this idea (Sobolev et al., 2005; Sobolev et al., 2007; Sobolev et al., 2011; Hofmann, 2003; Farnetani and Hofmann, 2011).

Two distinct characteristics speak for this theory.

First, there are essential differences between the trace element distribution in rocks

thought to be generated by mantle plumes and the ones created at mid-ocean ridges, as highlighted in Figure 1.3a: MORBs show a low abundance of incompatible elements, and the abundance of trace elements increases with their compatibility (towards the right of the diagram). This reflects their source reservoir, the depleted upper mantle. Many ocean island basalts show an opposite trend: They are enriched in incompatible elements, and the abundance of trace elements decreases with their compatibility, indicating an enriched source of these magmas. It also suggests that this heterogeneity was created in the upper mantle: with some exceptions, the relative abundance of elements is correlated/anti-correlated with their compatibility with respect to upper mantle minerals, which would not be expected if these trends originated from melting in the lower mantle (White, 2010, and references therein). The second important point are the anomalies in these trends: in this case niobium and lead. All of the basalts show a peak in niobium, and a relatively low value for lead, whereas rocks from continental crust and sediments follow opposite trends, which are also commonly observed in the subduction-related arc magmas (Hofmann, 2003). This is attributed to the fact that during subduction, fluids transfer a large percentage of lead to the mantle wedge and the related melts generated there, while niobium (and tantalum) are retained in the slab (Hofmann, 2003). Thus, these opposite trends in OIBs and crustal rocks are thought to indicate that the OIB source rock must have undergone subduction, whereby the elements that now reside in the continental crust were removed (Condie, 2001).

Second, differences in isotope ratios are indicators for a different origin. Most elements have several stable naturally occurring isotopes. Of interest for monitoring geological processes are the ones with a stable, radiogenic isotope whose parent isotope has a half life on geological time scales, and another stable isotope, which is not radiogenic. In principle, if the concentration of parent and daughter isotope is not influenced by other processes, the amount of the radiogenic daughter isotope should increase over time as predicted by the law of decay. However, processes like melting and freezing do change the concentration of the parent isotope as determined by their partition coefficients: The compatibility of an element defines how much of it will partition into the melt or stay in the residuum. This will change the amount of the radiogenic daughter isotope that is generated over time, and hence, measuring the ratio of the radiogenic and the non-radiogenic daughter isotope allows conclusions about fractionation events in the past.

Two parent/daughter pairs that are commonly used for investigating geological processes are $^{147}Sm/^{143}Nd$ and $^{87}Rb/^{87}Sr$. Sm is more compatible than Nd, and ^{147}Sm decays to^{143}Nd, while ^{144}Nd is stable, but not radiogenic, so that a high $^{143}Nd/^{144}Nd$ ratio indicates a past fractionation event where the rock became depleted in incompatible elements. For the Rb-Sr system, it is exactly opposite: Sr is more compatible than Rb, and ^{87}Rb decays to ^{87}Sr, so that a high $^{87}Sr/^{86}Sr$ ratio indicates enrichment in the past. As the isotope ratios are not modified by new melting events, their measurement allows insights into the enrichment/depletion of the melt source without requiring a consideration of how the composition was modified by the melting process itself.

Figure 1.3b shows that although the fields overlap, in comparison to MORBs, OIBs have on average less radiogenic ^{143}Nd and more radiogenic ^{87}Sr. This indicates a more enriched source of OIBs than the asthenosphere, the source of MORBs. In addition, the isotope diagram shows that the OIB isotope compositions can be divided into several distinct components or trends (EMI, EMII, HIMU) starting from a common component (PREMA, “Prevalent Mantle”, Zindler and Hart, 1986). This led to the idea that they may represent different reservoirs or mantle components, which are mixed with DMM (Depleted MORB Mantle) – the source of MORB – in mantle plumes.

Several theories exist for the origin of these reservoirs: lower continental crust (White,

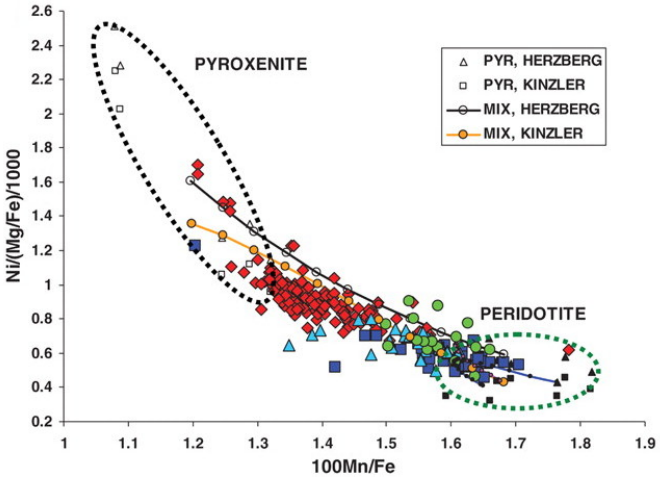

Figure 1.4: Average compositions of the most highly magnesian olivine phenocrysts in samples from MORBs (blue squares) and intra-plate magmas emplaced over thin lithosphere (light blue triangles), emplaced over thick lithosphere (red diamonds) and komatiites (green circles), and equilibrium olivines from peridotite- and pyroxenite-derived melts. Elements and their ratios are shown in ppm. MIX Herzberg and MIX Kinzler correspond to equilibrium olivine compositions calculated for the mixture of pyroxenite-derived and peridotite-derived melt. Natural olivine data are consistent with mixing trends of melts derived from pyroxenite (black ellipse) and peridotite (green ellipse). From Sobolev et al. (2007).

2010), delaminated subcontinental lithosphere or subducted ancient pelagic sediment (Tackley, 2007) for EMI, upper continental crust or subducted, metasomatized oceanic mantle lithosphere (White, 2010), oceanic crust with a small amount of sediment, melt-impregnated oceanic lithosphere, or sediment contamination of plume-derived magmas as they pass through the crust (Hofmann, 2003; Tackley, 2007) for EMII, recycled oceanic crust or magmatically enriched oceanic lithosphere (Hofmann, 2003) for HIMU, with PREMA as material from the lower mantle that is present as a mixing component in all deep-mantle plumes (Hofmann, 2003). Despite the fact that the exact origin and location of the reservoirs is still debated, all ideas have in common that material is subducted and recycled in mantle plumes (White, 2010).

While incompatible trace elements and isotope ratios can provide insights about the origin of melts, it is not possible to use them to constrain the fraction of recycled crust present in mantle plumes (Sobolev et al., 2007). However, it has been shown that a combination of major element compositions and compatible trace elements in parental melts such as nickel and manganese can be used for this purpose (Sobolev et al., 2007). This method assumes that the reaction between high-Si eclogite-derived melt (such as expected when melting recycled oceanic crust) and peridotite produces an olivine-free lithology enriched in pyroxene. In contrast to peridotite-derived melts, in this stable pyroxenite lithology, pyroxene (instead of olivine) controls the principal composition of melts, leading to a higher Ni content and lower Mn/Fe ratios of melts (Figure 1.4). These compositions can be used to compute the amount of the pyroxenite-derived component in the parental melt of a basalt, and based on these calculations, to estimate the amount of recycled oceanic crust in the melt source. Employing this method, Sobolev et al. (2007) predicted an involvement of 2 to 20% of recycled crust in mantle melting. While an estimate of the average amount of recycled oceanic crust in the melt source yields only 4% for MORBs, intra-plate plume-related melts show much higher values of 11 to 16% on average and a maximum of 28%.

But whichever the origin and amount of this chemically distinct material, two important points have to be taken into account when modelling mantle plumes: First, models have to be consistent with the existing geochemical data to be relevant for processes occurring in the Earth. Second, a change in chemical composition also entails a change in material properties such as the density (and hence, the plume buoyancy) and the solidus/liquidus curves, which have an impact on the plume dynamics. Most of the proposed plume compositions imply a higher iron content, a higher density and lower melting temperatures compared to the surrounding mantle.

1.3.5 Seismic Evidence for Mantle Plumes

While geochemical data can shed light on the origin and development of plumes, only seismic investigations are capable of capturing the present thermal state of the mantle. Hence, the identification of anomalies relating to the high temperatures in plume tails – associated with low seismic velocities – in seismic models may provide strong evidence for the existence and deep origin of plumes.

Many regional and global studies have reliably revealed anomalies of low seismic velocities below ocean islands thought to originate from a mantle plume (Montelli et al., 2004; Wolfe et al., 2009; Rickers et al., 2013). However, for a long time the plume theory and the concept of plumes rising from the core-mantle boundary was challenged (e.g. Anderson, 2005) because plume tails could not be imaged consistently and clearly below the transition zone and continuously down to the core-mantle boundary. This is related not only to the limited resolution and coverage of tomographic models around hotspots, but also the difficulty of detecting narrow channels of low seismic velocities, which can be hidden by wave-front healing (French and Romanowicz, 2015). One of the first seismic studies indicating a deeper origin of mantle plumes was Montelli et al. (2004), who found at least six well-resolved plumes reaching down into the lower mantle. Other investigations suggesting whole-mantle plumes followed (Zhao, 2004; Suetsugu et al., 2009). Later, Boschi et al. (2008) confirmed a significant statistical correlation between low S-velocity anomalies and regions where mantle plumes are expected from convection models. A convincing evidence comes from a recent study by French and Romanowicz (2015), who used advanced numerical techniques and included several different wave types in their model to achieve a better illumination also of the lower mantle. They show large, vertically continuous columns of low seismic velocities below major hotspots, reaching down to the core–mantle boundary (Figure 1.5), emphasizing that they must be broad features. While the anomalies are relatively vertical in the lower mantle, they seem to become thinner and more meandering above a depth of 1000 km.

In addition, global tomographic models have revealed two large, antipodal regions of low seismic velocities at the core-mantle boundary, one below the Pacific and one below Africa (Lay and Garnero, 2011, and references therein); and it has been shown that – projected to the Eath's surface – these so-called LLSVPs are correlated with present positions of hotspots and the reconstructed eruption sites of LIPs (Torsvik et al., 2006; Burke et al., 2008). This was interpreted as evidence that these LLSVPs or more specifically, their edges, are "Plume Generation Zones" (Burke et al., 2008), where plumes start to rise. The correlation with the position of LIPs also suggests that they must be stable for hundreds of millions of years (Torsvik et al., 2006). This idea is consistent with seismic observations of sharp gradients in S-velocity at their edges and an anti-correlation between S and bulk-sound velocity anomalies in their interior, indicating compositional heterogeneity (Lay and Garnero, 2011): A different chemical composition involving a higher density could prevent these piles from ascending. The theory of plumes rising from their edges is also

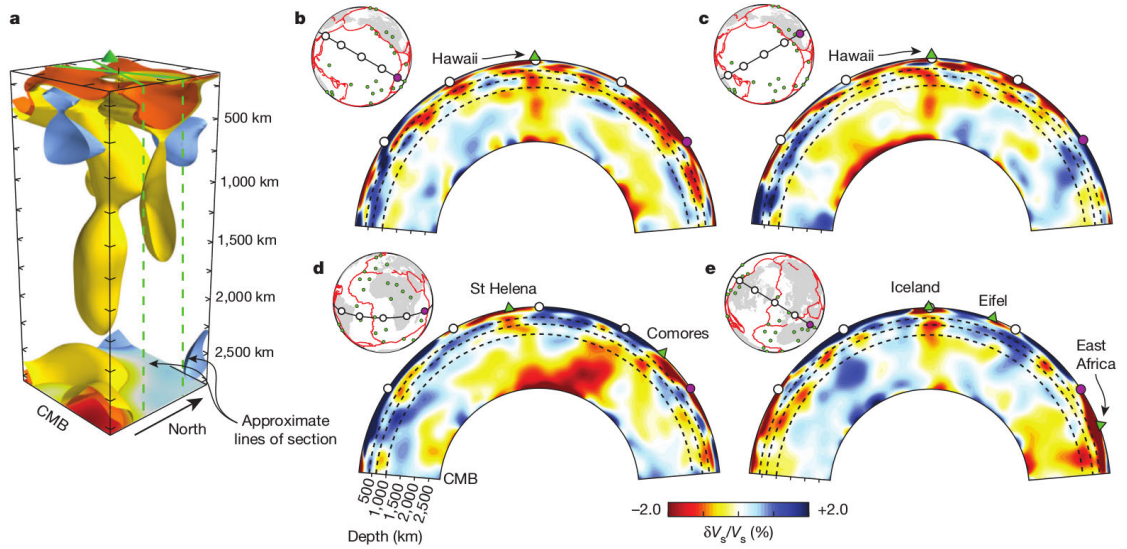

Figure 1.5: Seismic tomographic images of mantle plumes, from French and Romanowicz (2015). (a) Three-dimensional rendering of the Hawaiian plume. (b-e) Two-dimensional vertical cross-sections, positions are indicated in the inset maps.

supported by recent tomographic models (French and Romanowicz, 2015) that show a direct connection in form of quasi-vertical low-velocity columns between hotspots at the surface and these domes of low shear velocity (Figure 1.5).

1.4 Numerical Modelling of Mantle Plumes

Since the establishment of the classical plume concept (Section 1.2), new observations have led to a refinement and extension of this theory. Some of the observations can help to determine initial conditions, boundary conditions or the material properties of plume models, such as density, rheology, etc., while others can serve as criteria to assess how well models can reproduce the processes in the Earth, and to discard certain models that do not agree with these observations. Nevertheless, incorporating all available observations into a single model would lead to an immense model complexity and would also be extremely numerically challenging, as different processes occur on different scales. Instead, different investigations have focused on different aspects of mantle plumes.

Studies have been made that focus on the entrainment of a dense layer (Christensen, 1984b; Farnetani, 1997; Tackley et al., 1998; Zhong and Hager, 2003; Lin and van Keken, 2006a; Lin and van Keken, 2006b), the evolution of geochemical signatures and chemical zonation inside a plume (Farnetani et al., 2002; Samuel and Farnetani, 2003; Farnetani and Hofmann, 2010; Li et al., 2014), the formation of plumes from the top or the edges of thermo-chemical piles at the core–mantle boundary (Steinberger and Torsvik, 2012; Bower et al., 2013; Li et al., 2014), the influence of mantle rheology (Christensen, 1984a; Farnetani and Richards, 1995; Moore et al., 1999; Zhong et al., 2000; Lin and van Keken, 2006a; Lin and van Keken, 2006b) and phase transitions (Davies, 1995; Farnetani and Samuel, 2005; Leng and Zhong, 2010; Bossmann and van Keken, 2013), the surface expressions in comparison to regional geologic observations (d'Acremont et al., 2003; Leng and Zhong, 2010; Sobolev et al., 2011), plume–lithosphere interaction (d'Acremont et al., 2003; Sobolev et al., 2011; Ballmer et al., 2013; Burov and Gerya, 2014), influence on continental break-up (Burov and Gerya, 2014; Koptev et al., 2015), interaction with mov-

ing plates (Ribe and Christensen, 1994; Moore et al., 1998; Farnetani and Samuel, 2005; Ballmer et al., 2013; Agrusta et al., 2015), cause of environmental catastrophes (Wignall, 2001; Sobolev et al., 2011) and many other topics. It is outside of the scope of this work to summarize all previous insights on these topics, and for a review the reader is referred to Ribe et al. (2007) and Farnetani and Hofmann (2011).

The following sections will focus on relevant studies for the subject of this thesis: The effects of entrained recycled oceanic crust on plume dynamics, the interaction with a mid-ocean ridge and global mantle flow, and melting and melt migration on the dynamics of mantle plumes.

1.4.1 Thermochemical Plumes

As it became clear from geochemical data that plumes originate from a region of chemical heterogeneity and also carry a component of material that is chemically distinct from the ambient mantle up to the Earth's surface (e.g. Hofmann and White, 1982), this heterogeneity was also included in numerical models. Since the proposed plume composition involves a high density, thermo-chemical plumes have a lower buoyancy than purely thermal plumes, which leads to a difference in ascent dynamics and development of different dynamical regimes. One of the first to study the initiation of thermo-chemical plumes was Christensen (1984b). Farnetani (1997) showed that plumes originating from a thermo-chemical boundary layer have decreased, more realistic excess temperatures than purely thermal plumes and Tackley et al. (1998) studied the entrainment in plumes and the stability of a dense bottom boundary layer in three dimensions.

Later, Lin and van Keken (2005), Lin and van Keken (2006a), and Lin and van Keken (2006b) conducted a systematic study of the formation of plumes from a dense layer composed of recycled oceanic crust, investigating entrainment of material, influence on plume morphology and dynamical regimes in dependence of a number of parameters, such as the density contrast, temperature dependence of viscosity and thickness of the dense layer. They find that for the most realistic, strongly temperature-dependent viscosity cases the dynamics is mainly determined by the chemical density contrast in comparison to the density change due to high plume temperatures: For a chemical buoyancy much lower than the thermal buoyancy the chemical layer is entrained almost completely; for a chemical buoyancy much higher than the thermal buoyancy, no plume develops or almost no material is entrained and a low-temperature plume rises from the top of the chemical layer; and for intermediate cases a complex plume morphology and episodic pulses of rising material are observed. In addition, they observe a strong influence of the chemically dense material on the flow field within the plume head, the timing of the plume ascent, and the formation of secondary instabilities. The complexity of thermo-chemical plume dynamics was further highlighted by Farnetani and Samuel (2005), who employed high-resolution 3D numerical models to investigate the influence of phase transitions and the interaction with a moving plate on plume morphology. These computations predict a variety of plume shapes and sizes with strong asymmetry. Plumes may have a head–tail structure, but can also be thin filaments without a plume head when spouts rise from a plume ponding at the upper–lower mantle boundary. A variety of plume shapes and a transient nature, including strongly irregular, failing, oscillating and stagnating plumes were also predicted by Kumagai et al. (2008) and Samuel and Bercovici (2006).

A number of models also concentrate on the development of thermo-chemical plumes in the upper mantle, and their interaction with the lithosphere. At the example of the Siberian LIP, Sobolev et al. (2011) showed that a plume containing 15% recycled oceanic crust in form of dense eclogite agrees with the observations much better than a purely

thermal plume. Due to the high eclogite density, its lower solidus temperature and greater melt productivity, the plume generates a significantly lower pre-magmatic surface uplift, extremely thins the lithosphere, causes substantially more melting, and has a much higher potential to lead to an environmental catastrophe. Ballmer et al. (2013) model the mantle plume below Hawaii, and discover that an eclogite-bearing plume tends to form a pool at 300 – 400 km depth, which explains seismic observations of this region. Due to the specific density profile of eclogite, the plume is almost neutrally buoyant in this depth range, and rising material from this "pool" in interaction with a moving plate can account for the asymmetry and time-dependent behaviour of the hotspot.

1.4.2 Plume–Ridge Interaction

Both plumes and mid-ocean ridges are important sites of melting in the Earth's mantle. However, these melting processes should not only be studied as isolated systems: Many present-day hotspots such as Tristan da Cunha, Galapagos, Reunion, Kerguelen or Iceland lie in the vicinity of mid-ocean ridges, or were close to ridges during their history, some plumes even coinciding with rifting and continental breakup. Already in the 80s (Schilling, 1985) it was recognised that ridge segments close to hotspots show anomalies in their geochemical signature as well as an elevated morphology and crustal thickness, suggesting an interaction between plumes and nearby ridges with flow deflected from the hotspot to the ridge. These observations raise the question how and under which conditions plume material can flow towards the ridge, and what shape this flow will assume (Ito et al., 2003).

In general, the physical process relevant in these investigations is the competition between the shear forces of the plate, dragging the plume away from the ridge, and the plume buoyancy, promoting an upwards movement and flow towards the ridge, where the lithosphere becomes thinner (Ribe et al., 2007). This interaction is complicated by the fact that the spreading plates also cool the plume, diminishing the buoyant forces.

Previous modelling studies investigated ridge-centered plumes, including temporally variable buoyancy flux, and "off-axis" plumes, and they made use of theoretical, numerical and laboratory models. The theoretical analysis of plume–ridge interaction (Ribe et al., 1995; Ribe, 1996), facilitating lubrication theory, already reveals general scaling laws: The lateral extent of plume material along the ridge axis W increases with the plume volume flux Q and decreases with the half-spreading rate U ($W \propto \sqrt{Q/U}$); and the vertical thickness of the plume head S increases with the plume volume flux Q and decreases with the plume spreadability $\sigma = \Delta\rho g/(48\eta_p)$, which depends on the plume buoyancy $\Delta\rho g$ and viscosity η_p ($S \propto \sqrt[4]{Q/\sigma}$). Additional weaker dependencies on the plume buoyancy and the viscosity contrast between plume and ambient mantle material are predicted.

Numerical (Ribe et al., 1995; Ribe, 1996; Ito et al., 1996; Albers and Christensen, 2001) and laboratory (Feighner and Richards, 1995) models generally confirm and quantify these characteristic length scales and refine this analysis. Albers and Christensen (2001) find that channel flow along the ridge only occurs for slow-spreading ridges (1 cm/yr) and low plume viscosity (10^{17} Pa s), while the plume forms a thin "pancake" that is advected away from the ridge for moderately or fast spreading ridges, or higher plume viscosities. This behaviour can be explained by relating the thickness variations of the lithosphere, which are stronger for slower spreading plates, to the vertical thickness of the plume material, which is decreased by lower plume viscosities. The resulting ratio Π_c, the channeling number, is a measure for the strength of channelised flow, as both thinner plume heads and steeper slopes of the base of the lithosphere favour flow towards the ridge and focusing of plume material along the ridge axis opposed to lateral spreading

of the plume. However, (Ito et al., 1999) have pointed out that considering the effect of dehydration due to melting and melt extraction can increase plume viscosities by 2 – 3 orders of magnitude. This does not only influence the distribution of plume material, but also prevents plume buoyancy from significantly contributing to the upwelling rates and hence decreases the melt production.

For off-axis plumes, models (Ribe, 1996; Ito et al., 1997) predict that the primary controlling factor for the interaction is the self-spreading of the plume (in contrast to the slope of lithospheric thickness or thermal erosion of the lithosphere), and a distance between plume and ridge can be defined where plume flow towards the ridge and plate-driven flow away from the ridge are balanced. This point marks the maximum distance up to that plume material can still reach the ridge, and it scales with plume buoyancy flux and spreading rate ($\propto \sqrt{Q/U}$) and a function of both the buoyancy number $\Pi_b = Q\sigma/U^2$ (reflecting the strength of plume gravitational flow vs. plate-driven flow) and the channeling number $\Pi_c = \kappa\sqrt{\sigma U^3}$ at the distance $W_0 = \sqrt{Q/U}$ from the ridge (κ is the thermal diffusivity). For migrating ridges, the interaction between plume and ridge is expected to be stronger for ridges receding from the plume (Ito et al., 1997; Ribe and Delattre, 1998). The absolute plate motion of the trailing plate (receding side of the ridge) – and thus the motion relative to the plume – is smaller, leading to a stronger effect of the plume-induced flow. For a comprehensive review the reader is referred to Ito et al. (2003) and Ribe et al. (2007).

In addition to these general investigations of plume–ridge interaction, regional studies have been performed for several hotspots influenced by a nearby ridge.

Ruedas et al. (2004) find generally good agreement between their models and the observed crustal thickness variations in Iceland for upper-mantle plume excess temperatures of 150–200 K, and in addition note an influence of the fraction of melt retained in the plume on their results. Proposing an alternative mechanism for the Galapagos plume–ridge interaction, Braun and Sohn (2003) suggest that melt migrating though a melt-rich layer along the base of the lithosphere (instead of solid mantle flow) can account for plume signatures visible at mid-ocean ridges. At the example of Kerguelen, Mittelstaedt and Ito (2005) demonstrate how the influence of a plume can cause a fan-shaped pattern of the least tensile stresses starting from the hotspot and ending at the ridge, along which magma could erupt and form the observed lineaments of volcanic islands with this orientation. Mittelstaedt et al. (2011) investigated how plumes can promote ridge-propagation – jumps of nearby ridge segments towards the hotspot – by dynamic focussing of melt penetrating and thinning the lithosphere, and find that high magmatic heating rates, slower spreading plates, younger plate ages and higher plume volume fluxes favour this process. The asymmetry of the generated oceanic crust close to Iceland was focus of a study by Howell et al. (2014), who model the history of the plume–ridge system from the continental breakup to present-day and find that the asymmetric plume influence can be explained by both the asymmetric geometry of the ridge segments relative to the plume and the NE–SW thickness variations of the lithosphere.

However, the results can not always be generalized, and there are still several ridge-influenced hotspots such as Réunion and Tristan da Cunha that have not been studied in terms of numerical modelling to reveal which physical processes can explain the observations. Moreover, all these models consider the plume–ridge system as isolated and not in the context of the large-scale mantle flow field.

1.4.3 Melting and Melt Migration in Mantle Plumes

High-degree melting in the upper mantle generally takes place when one or more of the following conditions are fulfilled (Schmeling, 2000):

1. The local temperatures are higher than the average geotherm and thus exceed the solidus,
2. mantle material can rise almost adiabatically to lower pressures than present below the average lithosphere (decompression melting, such as at mid-ocean ridges),
3. the composition or volatile fraction is different from the average mantle, lowering the solidus temperature (such as for arc magmas generated due to the release of water from subducted slabs).

In mantle plumes, any of these three mechanisms could play a role (Condie, 2001): They are expected to have $100-300\,\mathrm{K}$ higher temperatures than the ambient mantle (Section 1.3.2), they have the potential to thin the lithosphere and hence ascend to regions of lower pressures (Sobolev et al., 2011), and they might contain recycled oceanic crust that is more fertile than the mantle peridotite (Section 1.3.4). This leads to inferred melt fractions of up to 40% for large igneous provinces, with most LIPs ranging between 25% and 30%, and up to 30% for oceanic island basalts (Herzberg and Gazel, 2009).

Once melt is generated, it also influences the dynamics of upwellings: It is a different phase that can separate from the solid and migrate with a different velocity, it reduces the viscosity of the host rock, and it provides additional buoyancy forces both for the melt phase and for the host rock (Schmeling, 2000). Melt buoyancy varies with depth, being positive at the surface due to a strong density contrast of $400-600\,\mathrm{kg/m^3}$ between melt and solid, but decreases with depth due to the higher melt compressibilities and can eventually become negative. In addition, melting and freezing leads to the creation of chemical heterogeneities, with generally higher densities for frozen melts and lower densities for the residuum (Schmeling, 2000). This effect can accelerate upwellings that have been partially molten, but also trigger instabilities at the base of the lithosphere, where melt freezes, thus providing a mechanism for lithospheric thinning (Sobolev et al., 2011).

These dynamical effects lead to a number of different forms of melt migration: On the one hand, melt may segregate from the solid (pervasive melt percolation). This can happen in the form of solitary waves resulting from dilation of the matrix at the leading flank and compaction at the trailing flank of the wave (Barcilon and Richter, 1986; Barcilon and Lovera, 1989; Scott and Stevenson, 1986; Wiggins and Spiegelman, 1995; Simpson and Spiegelman, 2011). In addition, channeling instabilities can localize melt transport (e.g. Weatherley and Katz, 2012). On the other hand, melt ascent can occur in form of diapirs, where melt and solid rise together due to convection driven by the positive melt buoyancy. Which mechanism prevails depends on the ratio of shear and bulk viscosity, with low shear viscosity favouring diapirism, and low bulk viscosities favouring compaction/melt segregation (Scott, 1988).

Models of melt migration (Schmeling, 2000) indicate that in a rising plume buoyancy effects dominate the motion of melt, leading to an ascent in form of diapirs with small segregation velocities pointing vertically upwards. As the melt ascends with comparable velocities to those of the solid mantle, it is also advected horizontally as the plume head spreads below the lithosphere.

Once partially molten material reaches this cold, highly viscous top thermal boundary layer, the dominant rheology changes from ductile flow to brittle failure (Keller et al.,

2013). Further ascent by viscous creep mechanisms becomes ineffective, and in models with purely viscous rheology, melt stagnates below this impermeable barrier. This transition to elasto-plastically fracturing modes of melt ascent is explored by Keller et al. (2013), who find that in dependence of shear viscosity and tensile rock strength in addition to viscous diapirism also viscoplastic decompaction channeling and elasto-plastic dyking can occur.

1.5 Open Questions

The presented examples show that a lot of research has been done covering the individual aspects of mantle plumes, regarding them as isolated features, or as part of one specific process. However, although mantle convection models generally feature plumes, much less efforts have been devoted to studying plumes as part of the larger system of the Earth's mantle while still retaining the resolution to gain insights on plume dynamics; and on linking the time and length-scales of different processes important for the evolution of plumes. Hence, it is worthwhile to compose these individual parts to a larger picture comprising the whole lifetime and evolution of mantle plumes, starting from their formation at the core–mantle boundary, covering their ascent and the interaction with global mantle flow and plate tectonics, up to their impingement on and interaction with the lithosphere, where melting, the migration of melt and its feedback on solid mantle flow become important.

In this framework, the study will focus on the following questions:

If many mantle plumes contain a component of compositionally distinct material (Section 1.3.4) that reduces their buoyancy (Section 1.4.1), the question remains if and under which conditions these low-buoyancy plumes can ascend from the core-mantle boundary to the base of the lithosphere. Barriers for the plume ascent may be related to the mantle thermal and compositional structure and the associated density variations and mineral phase transitions. Identifying these barriers has the potential to constrain the properties of plumes that are able to overcome them and to predict the resulting plume morphology. Moreover, if we have to update the classical plume models (Section 1.1) to include more complexities (Section 1.4), it is important to see if the thermal and chemical properties of the plume predicted by these models agree with observations (Section 1.3), and how these properties influence the impact of plumes on the Earth's surface and in particular in which scenarios they will still cause massive magmatism.

Beyond that, it should be investigated if there are external influences that play a role for the development, morphology, melt generation and surface expression of mantle plumes, especially the detailed distribution of melt and the thickness of generated magmatic crust. Examples are not only the global flow field of the mantle, but also the structure of the lithosphere the plume impinges on and the plume arrival position at the surface in relation to a given geologic setting. In particular for plume–ridge interaction (Section 1.4.2), one of the key open questions is related to the pattern and distribution of plume flow (Ito et al., 2003), having the potential to crucially influence melt production. Extending this point, not only how much and where melt is generated has to be considered, but also how melt migration changes the distribution and volume of produced melts, and which factors are important in this process. A comparison to all available observations can then illuminate if the numerical models are accurate enough to reproduce the main features of the evolution of a mantle plume as indicated by observations.

Finally, as many models include either the larger-scale plume ascent or only the small-scale migration of melt, the question arises if there is also a feedback of melting in a

plume head on the plume dynamics or the pattern of convection in general. Answering these questions also implies finding and applying strategies to overcome the challenges of incorporating both magma and mantle dynamics in one framework across scales.

1.6 Overview of the Manuscripts

This thesis is structured into three main chapters:

1.6.1 Manuscript I: Low-buoyancy thermochemical plumes resolve controversy of classical mantle plume concept

Chapter 2 covers the ascent dynamics of mantle plumes from the core–mantle boundary to the base of the lithosphere and the role their chemical composition plays for both the style of ascent and their surface manifestations. It demonstrates that plumes containing a fraction of recycled oceanic crust have a much lower buoyancy, but reproduce many observations much better than classical plumes models. Moreover, it identifies barriers for the plumes ascent, categorizes the possible ascent mechanisms of plumes and illustrates which regime is expected to develop under which conditions.

Contributions

Both authors jointly developed the structure and objectives of the study, designed the models, interpreted modelling results and wrote the paper; J.D. set up and performed the computations, implemented necessary changes in the code base, and created the figures and diagrams, including the model analysis required for this purpose.

1.6.2 Manuscript II: Major influence of plume–ridge interaction, lithosphere thickness variations and global mantle flow on hotspot volcanism – the example of Tristan

Chapter 3 focusses on the melt generation in mantle plumes, in particular in interaction with a mid-ocean ridge and the global mantle flow field, at the example of the Tristan Plume in the South Atlantic. It investigates the melt distribution and generated magmatic crustal thickness, the physical processes that lead to this distribution, and how comparison to the observations from the South Atlantic region can be used to constrain the plume properties. In particular, it demonstrates that the global flow field and plate motion – in interaction with the ridge and together with a realistic lithosphere structure of the model – are able to influence the material and heat transport in the plume in such a way that either a thin, a broad and thick or two distinct hotspot tracks are generated, such as it is observed for the Tristan Plume.

Contributions

J.D., R.G. and B.S. jointly developed the structure and objectives of the study, designed the models, interpreted modelling results and created the figures and diagrams, including the model analysis required for this purpose. J.D. and R.G. wrote the main part of the paper, comprising the model results, discussion, conclusion and part of the model setup; B.S. and T.T. contributed the section about the geological setting and B.S. the section about the global flow model. R.G. set up and performed the computations. J.D., R.G. and E.B. implemented several features in the code that were necessary for the computations,

including the melting model and the advection of compositional fields (J.D.) and the interface to the plate reconstruction and global model used as boundary conditions (R.G. and E.B.). T.T. provided the plate reconstruction and B.S. contributed the global mantle convection model and the hotspot motion model used as constraints.

1.6.3 Manuscript III: 3D Compressible Melt Transport with Mesh Adaptivity

Chapter 4 proposes a new formulation of two-phase flow, including the compressibilities of the individual phases, describes how to implement coupled magma/mantle dynamics in a geodynamic modelling code and applies it to the generation and transport of melt in mantle plumes. It addresses the numerical challenges related to coupling melt migration and mantle flow and linking the different scales of these processes, and shows that they can be overcome by the use of adaptive mesh refinement and massive parallelization of the code. The application cases illustrate melting and melt segregation in a rising plume head, including the influence on rheology, reveal controlling factors on the accumulated melt volume and demonstrate that melt migration has the potential to affect both small- and large-scale convection patterns.

Contributions

Both authors jointly developed the structure and objectives of the study, developed the new formulation of the two-phase flow equations, designed the models and analysed and interpreted modelling results. J.D. wrote the main part of the paper, T.H. contributed the sections about the weak formulation, discretization and adaptive convergence test. With the help of T.H., J.D. implemented the necessary changes in the code and set up and performed the computations.

Bibliography

Agrusta, R. et al. (2015). "How partial melting affects small-scale convection in a plume-fed sublithospheric layer beneath fast-moving plates". *Geochemistry, Geophysics, Geosystems*.

Albers, M. and U. R. Christensen (2001). "Channeling of plume flow beneath mid-ocean ridges". *Earth and Planetary Science Letters* 187 (1): 207–220.

Anderson, D. L. (2000). "The thermal state of the upper mantle; no role for mantle plumes". *Geophysical Research Letters* 27 (22): 3623–3626.

Anderson, D. L. (2005). "Scoring hotspots: The plume and plate paradigms". *Geological Society of America Special Papers* 388: 31–54.

Ballmer, M. D. et al. (2013). "Double layering of a thermochemical plume in the upper mantle beneath Hawaii". *Earth and Planetary Science Letters* 376: 155–164.

Barcilon, V. and O. M. Lovera (1989). "Solitary waves in magma dynamics". *Journal of Fluid mechanics* 204: 121–133.

Barcilon, V. and F. M. Richter (1986). "Nonlinear waves in compacting media". *Journal of Fluid mechanics* 164: 429–448.

Boehler, R (2000). "High-pressure experiments and the phase diagram of lower mantle and core materials". *Reviews of Geophysics* 38 (2): 221–245.

Boschi, L, T. W. Becker, and B. Steinberger (2008). "On the statistical significance of correlations between synthetic mantle plumes and tomographic models". *Physics of the Earth and Planetary Interiors* 167 (3): 230–238.

Bossmann, A. B. and P. E. van Keken (2013). "Dynamics of plumes in a compressible mantle with phase changes: Implications for phase boundary topography". *Physics of the Earth and Planetary Interiors* 224: 21–31.

Bower, D. J., M. Gurnis, and M. Seton (2013). "Lower mantle structure from paleogeographically constrained dynamic Earth models". *Geochemistry, Geophysics, Geosystems* 14 (1): 44–63.

Braun, M. G. and R. A. Sohn (2003). "Melt migration in plume–ridge systems". *Earth and Planetary Science Letters* 213 (3): 417–430.

Bryan, S. E. and R. E. Ernst (2008). "Revised definition of large igneous provinces (LIPs)". *Earth-Science Reviews* 86 (1): 175–202.

Bunge, H.-P. (2005). "Low plume excess temperature and high core heat flux inferred from non-adiabatic geotherms in internally heated mantle circulation models". *Physics of the Earth and Planetary Interiors* 153 (1): 3–10.

Burke, K. et al. (2008). "Plume generation zones at the margins of large low shear velocity provinces on the core–mantle boundary". *Earth and Planetary Science Letters* 265 (1): 49–60.

Burov, E. and T. Gerya (2014). "Asymmetric three-dimensional topography over mantle plumes". *Nature* 513 (7516): 85–89.

Campbell, I. H. (2007). "Testing the plume theory". *Chemical Geology* 241 (3): 153–176.

Campbell, I. H. and R. W. Griffiths (1990). "Implications of mantle plume structure for the evolution of flood basalts". *Earth and Planetary Science Letters* 99 (1): 79–93.

Christensen, U (1984a). "Convection with pressure-and temperature-dependent non-Newtonian rheology". *Geophysical Journal International* 77 (2): 343–384.

Christensen, U (1984b). "Instability of a hot boundary layer and initiation of thermo-chemical plumes". *Annales Geophysicae*. Volume 2: 311–319.

Coffin, M. and O Eldholm (1994). "Large igneous provinces: crustal structure, dimensions, and external consequences". *Reviews of Geophysics* 32 (1): 1–36.

Condie, K. C. (2001). *Mantle plumes and their record in Earth history*. Cambridge University Press.

Courtillot, V. E. and P. R. Renne (2003). "On the ages of flood basalt events". *Comptes Rendus Geoscience* 335 (1): 113–140.

Czamanske, G. K. et al. (1998). "Demise of the Siberian plume: paleogeographic and paleotectonic reconstruction from the prevolcanic and volcanic record, north-central Siberia". *International Geology Review* 40 (2): 95–115.

Davies, G. F. (1995). "Penetration of plates and plumes through the mantle transition zone". *Earth and Planetary Science Letters* 133 (3): 507–516.

d'Acremont, E., S. Leroy, and E. B. Burov (2003). "Numerical modelling of a mantle plume: the plume head–lithosphere interaction in the formation of an oceanic large igneous province". *Earth and Planetary Science Letters* 206 (3): 379–396.

Ernst, R. E., K. L. Buchan, and I. H. Campbell (2005). "Frontiers in large igneous province research". *Lithos* 79 (3): 271–297.

Farnetani, C. (1997). "Excess temperature of mantle plumes: The role of chemical stratification across D"". *Geophysical Research Letters* 24 (13): 1583–1586.

Farnetani, C. and H Samuel (2005). "Beyond the thermal plume paradigm". *Geophysical Research Letters* 32 (7).

Farnetani, C. G. and A. W. Hofmann (2010). "Dynamics and internal structure of the Hawaiian plume". *Earth and Planetary Science Letters* 295 (1): 231–240.

Farnetani, C. G. and A. W. Hofmann (2011). "Mantle plumes". *Encyclopedia of Solid Earth Geophysics*. Springer: 857–869.

Farnetani, C. G. and M. A. Richards (1994). "Numerical investigations of the mantle plume initiation model for flood basalt events". *Journal of Geophysical Research* 99: 13–813.

Farnetani, C. G., B. Legras, and P. J. Tackley (2002). "Mixing and deformations in mantle plumes". *Earth and Planetary Science Letters* 196 (1): 1–15.

Farnetani, D. G. and M. A. Richards (1995). "Thermal entrainment and melting in mantle plumes". *Earth and Planetary Science Letters* 136 (3): 251–267.

Feighner, M. A. and M. A. Richards (1995). "The fluid dynamics of plume-ridge and plume-plate interactions: An experimental investigation". *Earth and Planetary Science Letters* 129 (1): 171–182.

Foulger, G. R. (2011). *Plates vs Plumes: a geological controversy*. John Wiley & Sons.

French, S. W. and B. Romanowicz (2015). "Broad plumes rooted at the base of the Earth's mantle beneath major hotspots". *Nature* 525 (7567): 95–99.

Griffiths, R. W. and I. H. Campbell (1990). "Stirring and structure in mantle starting plumes". *Earth and Planetary Science Letters* 99 (1): 66–78.

Griffiths, R. (1986). "Thermals in extremely viscous fluids, including the effects of temperature-dependent viscosity". *Journal of Fluid Mechanics* 166: 115–138.

Griffiths, R. and I. Campbell (1991). "Interaction of mantle plume heads with the Earth's surface and onset of small-scale convection". *Journal of Geophysical Research: Solid Earth (1978–2012)* 96 (B11): 18295–18310.

Hart, S., J.-G. Schilling, and J. Powell (1973). "Basalts from Iceland and along the Reykjanes Ridge: Sr isotope geochemistry". *Nature* 246 (155): 104–107.

He, B. et al. (2003). "Sedimentary evidence for a rapid, kilometer-scale crustal doming prior to the eruption of the Emeishan flood basalts". *Earth and Planetary Science Letters* 213 (3): 391–405.

Hernlund, J. W., C. Thomas, and P. J. Tackley (2005). "A doubling of the post-perovskite phase boundary and structure of the Earth's lowermost mantle". *Nature* 434 (7035): 882–886.

Herzberg, C. and E. Gazel (2009). "Petrological evidence for secular cooling in mantle plumes". *Nature* 458 (7238): 619–622.

Hofmann, A. W. and W. M. White (1982). "Mantle plumes from ancient oceanic crust". *Earth and Planetary Science Letters* 57 (2): 421–436.

Hofmann, A. (2003). "Sampling mantle heterogeneity through oceanic basalts: isotopes and trace elements". *Treatise on geochemistry* 2: 61–101.

Howell, S. M. et al. (2014). "The origin of the asymmetry in the Iceland hotspot along the Mid-Atlantic Ridge from continental breakup to present-day". *Earth and Planetary Science Letters* 392: 143–153.

Ito, G, J. Lin, and D Graham (2003). "Observational and theoretical studies of the dynamics of mantle plume–mid-ocean ridge interaction". *Reviews of Geophysics* 41 (4).

Ito, G., J. Lin, and C. W. Gable (1996). "Dynamics of mantle flow and melting at a ridge-centered hotspot: Iceland and the Mid-Atlantic Ridge". *Earth and Planetary Science Letters* 144 (1): 53–74.

Ito, G., J. Lin, and C. W. Gable (1997). "Interaction of mantle plumes and migrating mid-ocean ridges: Implications for the Galápagos plume-ridge system". *Journal of Geophysical Research: Solid Earth (1978–2012)* 102 (B7): 15403–15417.

Ito, G. et al. (1999). "Mantle flow, melting, and dehydration of the Iceland mantle plume". *Earth and Planetary Science Letters* 165 (1): 81–96.

Jellinek, A. M. and M. Manga (2004). "Links between long-lived hot spots, mantle plumes, D", and plate tectonics". *Reviews of Geophysics* 42 (3).

Keller, T., D. A. May, and B. J. P. Kaus (2013). "Numerical modelling of magma dynamics coupled to tectonic deformation of lithosphere and crust". *Geophysical Journal International* 195 (3): 1406–1442.

Koptev, A et al. (2015). "Dual continental rift systems generated by plume-lithosphere interaction". *Nature Geoscience* 8 (5): 388–392.

Kumagai, I. et al. (2008). "Mantle plumes: thin, fat, successful, or failing? Constraints to explain hot spot volcanism through time and space". *Geophysical Research Letters* 35 (16).

Lay, T. and E. J. Garnero (2011). "Deep mantle seismic modeling and imaging". *Annual Review of Earth and Planetary Sciences* 39: 91–123.

Lay, T., J. Hernlund, and B. A. Buffett (2008). "Core–mantle boundary heat flow". *Nature Geoscience* 1 (1): 25–32.

Leng, W. and S. Zhong (2010). "Surface subsidence caused by mantle plumes and volcanic loading in large igneous provinces". *Earth and Planetary Science Letters* 291 (1): 207–214.

Li, M., A. K. McNamara, and E. J. Garnero (2014). "Chemical complexity of hotspots caused by cycling oceanic crust through mantle reservoirs". *Nature Geoscience* 7 (5): 366–370.

Lin, S.-C. and P. E. van Keken (2005). "Multiple volcanic episodes of flood basalts caused by thermochemical mantle plumes". *Nature* 436 (7048): 250–252.

Lin, S.-C. and P. E. van Keken (2006a). "Dynamics of thermochemical plumes: 1. Plume formation and entrainment of a dense layer". *Geochemistry, Geophysics, Geosystems* 7 (2).

Lin, S.-C. and P. E. van Keken (2006b). "Dynamics of thermochemical plumes: 2. Complexity of plume structures and its implications for mapping mantle plumes". *Geochemistry, Geophysics, Geosystems* 7 (3).

McKenzie, D. P., J. M. Roberts, and N. O. Weiss (1974). "Convection in the Earth's mantle: towards a numerical simulation". *Journal of Fluid Mechanics* 62 (03): 465–538.

Mittelstaedt, E. and G. Ito (2005). "Plume-ridge interaction, lithospheric stresses, and the origin of near-ridge volcanic lineaments". *Geochemistry, Geophysics, Geosystems* 6 (6).

Mittelstaedt, E., G. Ito, and J. van Hunen (2011). "Repeat ridge jumps associated with plume-ridge interaction, melt transport, and ridge migration". *Journal of Geophysical Research: Solid Earth (1978–2012)* 116 (B1).

Montelli, R. et al. (2004). "Finite-frequency tomography reveals a variety of plumes in the mantle". *Science* 303 (5656): 338–343.

Moore, W. B., G. Schubert, and P. Tackley (1998). "Three-dimensional simulations of plume-lithosphere interaction at the Hawaiian swell". *Science* 279: 1008–1011.

Moore, W. B., G. Schubert, and P. J. Tackley (1999). "The role of rheology in lithospheric thinning by mantle plumes". *Geophysical Research Letters* 26 (8): 1073–1076.

Morgan, W. J. (1981). "13. Hotspot tracks and the opening of the Atlantic and Indian Oceans". *The Sea, ideas and observations on progress in the study of the seas* 7: 443–487.

Morgan, W. (1971). "Convection Plumes in the Lower Mantle". *Nature* 230: 42–43.

Olson, P. and H. Singer (1985). "Creeping plumes". *Journal of Fluid Mechanics* 158: 511–531.

Olson, P. et al. (1988). "Plume formation and lithosphere erosion: a comparison of laboratory and numerical experiments". *Journal of Geophysical Research: Solid Earth (1978–2012)* 93 (B12): 15065–15084.

Parmentier, E., D. Turcotte, and T. K.E. (1976). "Studies of Finite Amplitude Non-Newtonian Thermal Convection With Application to Convection in the Earth's Mantle". *Journal of Geophysical Research* 81 (11): 1839–1846.

Peate, I., M. Larsen, and C. Lesher (2003). "The transition from sedimentation to flood volcanism in the Kangerlussuaq Basin, East Greenland: basaltic pyroclastic volcanism during initial Palaeogene continental break-up". *Journal of the Geological Society* 160 (5): 759–772.

Putirka, K. (2008). "Excess temperatures at ocean islands: Implications for mantle layering and convection". *Geology* 36 (4): 283–286.

Ribe, N., A. Davaille, and U. Christensen (2007). "Fluid dynamics of mantle plumes". *Mantle plumes*. Springer: 1–48.

Ribe, N. (1996). "The dynamics of plume-ridge interaction: 2. Off-ridge plumes". *Journal of Geophysical Research: Solid Earth (1978–2012)* 101 (B7): 16195–16204.

Ribe, N. and U. Christensen (1994). "Three-dimensional modeling of plume-lithosphere interaction". *Journal of Geophysical Research: Solid Earth (1978–2012)* 99 (B1): 669–682.

Ribe, N. and W. Delattre (1998). "The dynamics of plume—ridge interaction—III. The effects of ridge migration". *Geophysical Journal International* 133 (3): 511–518.

Ribe, N., U. Christensen, and J Theissing (1995). "The dynamics of plume-ridge interaction, 1: Ridge-centered plumes". *Earth and Planetary Science Letters* 134 (1): 155–168.

Richards, M. A., R. A. Duncan, and V. E. Courtillot (1989). "Flood basalts and hot-spot tracks: plume heads and tails". *Science* 246 (4926): 103–107.

Richter, F. M. (1973). "Finite amplitude convection through a phase boundary". *Geophysical Journal International* 35 (1-3): 265–276.

Richter, F. M. (1978). "Mantle convection models". *Annual Review of Earth and Planetary Sciences* 6: 9.

Rickers, F., A. Fichtner, and J. Trampert (2013). "The Iceland–Jan Mayen plume system and its impact on mantle dynamics in the North Atlantic region: Evidence from full-waveform inversion". *Earth and Planetary Science Letters* 367: 39–51.

Roberge, J. et al. (2005). "Anomalous uplift and subsidence of the Ontong Java Plateau inferred from CO2 contents of submarine basaltic glasses". *Geology* 33 (6): 501–504.

Ruedas, T. et al. (2004). "Temperature and melting of a ridge-centred plume with application to Iceland. Part I: Dynamics and crust production". *Geophysical Journal International* 158 (2): 729–743.

Samuel, H. and D. Bercovici (2006). "Oscillating and stagnating plumes in the Earth's lower mantle". *Earth and Planetary Science Letters* 248 (1): 90–105.

Samuel, H. and C. G. Farnetani (2003). "Thermochemical convection and helium concentrations in mantle plumes". *Earth and Planetary Science Letters* 207 (1): 39–56.

Saunders, A. et al. (2007). "Regional uplift associated with continental large igneous provinces: the roles of mantle plumes and the lithosphere". *Chemical Geology* 241 (3): 282–318.

Schilling, J.-G. (1973). "Iceland mantle plume: geochemical study of Reykjanes Ridge". *Nature* 242: 565–571.

Schilling, J.-G. (1985). "Upper mantle heterogeneities and dynamics". *Nature* 314: 62–67.

Schilling, J.-G. (1991). "Fluxes and excess temperatures of mantle plumes inferred from their interaction with migrating mid-ocean ridges". *Nature* 352: 397–403.

Schmeling, H. (2000). "Partial melting and melt segregation in a convecting mantle". *Physics and Chemistry of Partially Molten Rocks*. Springer: 141–178.

Scott, D. R. (1988). "The competition between percolation and circulation in a deformable porous medium". *Journal of Geophysical Research: Solid Earth (1978–2012)* 93 (B6): 6451–6462.

Scott, D. R. and D. J. Stevenson (1986). "Magma ascent by porous flow". *Journal of Geophysical Research B* 91 (B9): 9283–9296.

Simpson, G. and M. Spiegelman (2011). "Solitary wave benchmarks in magma dynamics". *Journal of Scientific Computing* 49 (3): 268–290.

Sobolev, A. V. et al. (2005). "An olivine-free mantle source of Hawaiian shield basalts". *Nature* 434 (7033): 590–597.

Sobolev, A. V. et al. (2007). "The amount of recycled crust in sources of mantle-derived melts". *Science* 316 (5823): 412–417.

Sobolev, S. V. et al. (2011). "Linking mantle plumes, large igneous provinces and environmental catastrophes". *Nature* 477 (7364): 312–316.

Steinberger, B. (2000). "Plumes in a convecting mantle – Models and observations for individual hotspots". *Journal of Geophysical Research* 105 (B5): 11–127.

Steinberger, B. and T. H. Torsvik (2012). "A geodynamic model of plumes from the margins of Large Low Shear Velocity Provinces". *Geochemistry, Geophysics, Geosystems* 13 (1).

Suetsugu, D et al. (2009). "South Pacific mantle plumes imaged by seismic observation on islands and seafloor". *Geochemistry, Geophysics, Geosystems* 10 (11).

Sun, Y. et al. (2010). "Dating the onset and nature of the Middle Permian Emeishan large igneous province eruptions in SW China using conodont biostratigraphy and its bearing on mantle plume uplift models". *Lithos* 119 (1): 20–33.

Tackley, P. J. (2007). "7. Mantle dynamics". *Treatise on geophysics*. Edited by D. Bercovici and G. Schubert. New York: Elsevier.

Tackley, P. J. et al. (1998). "Three-dimensional simulations of mantle convection with a thermo-chemical basal boundary layer: D". *The Core-Mantle Boundary Region, Geodyn. Ser* 28: 231–253.

Torrance, K. and D. Turcotte (1971). "Thermal convection with large viscosity variations". *Journal of Fluid Mechanics* 47 (01): 113–125.

Torsvik, T. H. et al. (2006). "Large igneous provinces generated from the margins of the large low-velocity provinces in the deep mantle". *Geophysical Journal International* 167 (3): 1447–1460.

van Keken, P. (1997). "Evolution of starting mantle plumes: a comparison between numerical and laboratory models". *Earth and Planetary Science Letters* 148 (1): 1–11.

Weatherley, S. M. and R. F. Katz (2012). "Melting and channelized magmatic flow in chemically heterogeneous, upwelling mantle". *Geochemistry, Geophysics, Geosystems* 13 (5): Q0AC18.

White, R. and D. McKenzie (1989). "Magmatism at rift zones: the generation of volcanic continental margins and flood basalts". *Journal of Geophysical Research: Solid Earth (1978–2012)* 94 (B6): 7685–7729.

White, R. V. and A. D. Saunders (2005). "Volcanism, impact and mass extinctions: incredible or credible coincidences?" *Lithos* 79 (3): 299–316.

White, W. M. (2010). "Oceanic island basalts and mantle plumes: the geochemical perspective". *Annual Review of Earth and Planetary Sciences* 38: 133–160.

Whitehead, J. A. and D. S. Luther (1975). "Dynamics of laboratory diapir and plume models". *Journal of Geophysical Research* 80 (5): 705–717.

Wiggins, C. and M. Spiegelman (1995). "Magma migration and magmatic solitary waves in 3-D". *Geophysical Research Letters* 22 (10): 1289–1292.

Wignall, P. (2001). "Large igneous provinces and mass extinctions". *Earth-Science Reviews* 53 (1): 1–33.

Wilson, J. T. (1963a). "A possible origin of the Hawaiian Islands". *Canadian Journal of Physics* 41 (6): 863–870.

Wilson, J. T. (1963b). "Evidence from Islands on the Spreading of Ocean Floors". *Nature* 197: 536–538.

Wolfe, C. J. et al. (2009). "Mantle shear-wave velocity structure beneath the Hawaiian hot spot". *science* 326 (5958): 1388–1390.

Yuen, D. and W. Peltier (1980). "Mantle plumes and the thermal stability of the D"layer". *Geophysical Research Letters* 7 (9): 625–628.

Zhao, D. (2004). "Global tomographic images of mantle plumes and subducting slabs: insight into deep Earth dynamics". *Physics of the Earth and Planetary Interiors* 146 (1): 3–34.

Zhong, S. and B. H. Hager (2003). "Entrainment of a dense layer by thermal plumes". *Geophysical Journal International* 154 (3): 666–676.

Zhong, S. et al. (2000). "Role of temperature-dependent viscosity and surface plates in spherical shell models of mantle convection". *Journal of Geophysical Research: Solid Earth (1978–2012)* 105 (B5): 11063–11082.

Zindler, A. and S. Hart (1986). "Chemical geodynamics". *Annual review of earth and planetary sciences* 14: 493–571.

Chapter 2

Low-buoyancy thermochemical plumes resolve controversy of classical mantle plume concept

A version of this chapter is published as Dannberg, J. and Sobolev, S.V., (2015) Low-buoyancy thermochemical plumes resolve controversy of classical mantle plume concept. Nature Communications 6, Article number: 6960 | doi:10.1038/ncomms7960.

Abstract

The Earth's biggest magmatic events are believed to originate from massive melting when hot mantle plumes rising from the lowermost mantle reach the base of the lithosphere. Classical models predict large plume heads that cause kilometre-scale surface uplift, and narrow (100 km radius) plume tails that remain in the mantle after the plume head spreads below the lithosphere. However, in many cases, such uplifts and narrow plume tails are not observed. Here using numerical models, we show that the issue can be resolved if major mantle plumes contain up to 15–20% of recycled oceanic crust in a form of dense eclogite, which drastically decreases their buoyancy and makes it depth dependent. We demonstrate that, despite their low buoyancy, large enough thermochemical plumes can rise through the whole mantle causing only negligible surface uplift. Their tails are bulky (>200 km radius) and remain in the upper mantle for 100 millions of years.

2.1 Introduction

Classical starting mantle plume models predict large plume heads that cause kilometre-scale surface uplift, followed by the eruption of a large igneous province (LIP) (Richards et al., 1989; White and McKenzie, 1989), and narrow (100-km radius) plume tails that remain in the mantle after the plume head spreads below the lithosphere (Richards et al., 1989; Campbell and Griffiths, 1990; Farnetani and Richards, 1994). Models of thermal plumes considering major phase transformations in the mantle transition zone and a heterogeneous viscosity structure in the upper mantle (see 2.4 Methods) do not change these predictions radically (Supplementary Fig. 2.6). However, there is growing evidence that neither kilometre-scale uplifts nor narrow tails characterize starting plumes (Sun et al., 2010; Peate et al., 2003; Hales et al., 2005; Czamanske et al., 1998; Wolfe et al., 2009; Montelli et al., 2004). We propose that the reason is not that the entire mantle plume concept is wrong (Czamanske et al., 1998; Anderson, 2000; Foulger, 2011), but that in its present form, it underestimates the effect of the strong chemical heterogeneity of the mantle.

More than 30 years ago, based on isotopic and trace-element geochemical data, it was suggested that a part of the oceanic crust that subducts to the core-mantle boundary (CMB) is then entrained in mantle plumes and transported back to the surface (Hofmann and White, 1982); later this idea was confirmed by numerical models (Christensen and Hofmann, 1994; Tackley, 2007). New geochemical data on olivine compositions of ocean island basalts and LIP magmas (Sobolev et al., 2005; Sobolev et al., 2007; Sobolev et al., 2011) indicate that the fraction of recycled oceanic crust in their sources may be higher than 10%. At sublithospheric depths, basaltic oceanic crust is transformed to eclogite, which has a higher density than average mantle peridotite through most of the Earth's mantle (Aoki and Takahashi, 2004; Litasov and Ohtani, 2005; Hirose et al., 2005). Therefore, the entrainment of a considerable amount of eclogitic material significantly increases the plume density to produce what we will call low-buoyancy plumes (LBPs). More specifically, we only include plumes in this definition whose buoyancy in the upper mantle is reduced at least by half compared with a purely thermal plume. One example is the Siberian plume–its eclogite fraction of 10–20%, together with an excess temperature of ~250 K, made it almost neutrally buoyant, which explains the absence of pronounced premagmatic uplift during the emplacement of the Siberian LIP (Sobolev et al., 2011). Given that a large number of plumes may contain a high content of recycled crust (Sobolev et al., 2007), calculations solely based on excess temperature may strongly overestimate the plume buoyancy.

Geodynamic models that feature thermochemical plumes showed a large diversity of plume behaviours (Lin and van Keken, 2006a; Lin and van Keken, 2006b; Farnetani and Samuel, 2005; Kumagai et al., 2008; Samuel and Bercovici, 2006). These previous studies identified that the competition between thermally and chemically induced density variations, and their depth dependence, play a key role in plume dynamics. However, to advance our current understanding of plumes occurring in the Earth's mantle, these models need to incorporate additional insights from observational and experimental data. This will give us the opportunity to answer the crucial, but still open questions how LBPs can rise through the Earth's entire mantle (if at all) and which conditions favour their ascent. Here we address these questions using numerical thermomechanical modelling. The novelty of this study is that the material properties of the plume and the ambient mantle in our model are more Earth-like than what has previously been published. These properties, such as plume composition, excess temperature in the upper mantle, density and thermal expansivity, were constrained using geochemical and petrological observations

and experimental data. Parameters that are less well constrained by the surface observations, such as the plume initial temperature, its volume and the mantle temperature profile, were systematically varied to investigate their influence on the plume morphology and its surface manifestations.

We find that the conditions for an LBP to ascend through the entire mantle and to cause only a negligible surface uplift on reaching the lithosphere include high plume volume together with moderate lower-mantle subadiabaticity or plume formation several hundred kilometres above the CMB. This, together with a sufficiently high temperature, allows LBPs to directly advance to the base of the lithosphere, while plumes with slightly lower buoyancy pond in a depth of 300–400 km and form pools or a second layer of hot material. We also show that the bulky tails of large and hot LBPs are stable for several tens of millions of years and that their shapes fit seismic tomography data much better than the narrow tails of thermal plumes.

2.2 Results

2.2.1 Effects of realistic buoyancy on plume rise and surface uplift

Our models assume an axisymmetric geometry (Leng and Zhong, 2010) and consider mantle compressibility, strongly temperature- and depth-dependent viscosity and major phase transformations in the mantle transition zone. Experimental data (Aoki and Takahashi, 2004; Litasov and Ohtani, 2005; Hirose et al., 2005) provides the depth-dependent density difference between peridotite and eclogite (Fig. 2.1a). Starting plumes are considered to consist of peridotite and a prescribed amount of eclogite; the mantle is modelled as purely peridotitic. More details of the modelling technique are presented in the Methods Section 2.4 and Supplementary Fig. 2.7. Two regions of greatest density contrast between peridotite and eclogite may act as barriers to the ascent of an eclogite-rich plume: the deep lower mantle and the upper mantle between 300 and 400 km depth (Fig. 2.2a, Supplementary Fig. 2.8). The upper mantle barrier is caused by phase transformations of pyroxenes to garnet structures and the transformation of coesite to stishovite. This leads to an increase in eclogite density, which is not compensated by density increase in peridotite until a depth of 410 km, where olivine transforms to spinel. To cross these barriers, an eclogite-rich plume needs a high excess temperature. More precisely, in an adiabatic mantle and for an initial eclogite content of 15%, a minimum excess temperature of 550 K in the lower mantle is required (see time snapshots of such a plume evolution in Fig. 2.1b–e). Plumes with the same eclogite content and lower excess temperatures do not reach the uppermost mantle and are ponded either in the deep lower mantle or in the mantle transition zone. Owing to adiabatic cooling and loss of heat to surroundings, the maximum excess temperature in the part of the plume that spreads below the lithosphere (Fig. 2.1d,e) is reduced to 370 K. This part has an average eclogite content of about 14%, and the lithosphere above the plume is uplifted by about 400 m. While the predicted surface uplift for this thermochemical plume is smaller than for a thermal plume, it still remains significant, and the excess temperature of 370 K seems to be unusually high (Herzberg and Gazel, 2009).

2.2.2 Effect of mantle subadiabaticity and plume volume

To allow a cooler thermochemical plume to cross the deep mantle buoyancy barrier requires a subadiabatic temperature (a few 100 K colder than adiabatic temperature) in the deep lower mantle, as suggested by mantle convection models (Bunge, 2005). A plume with

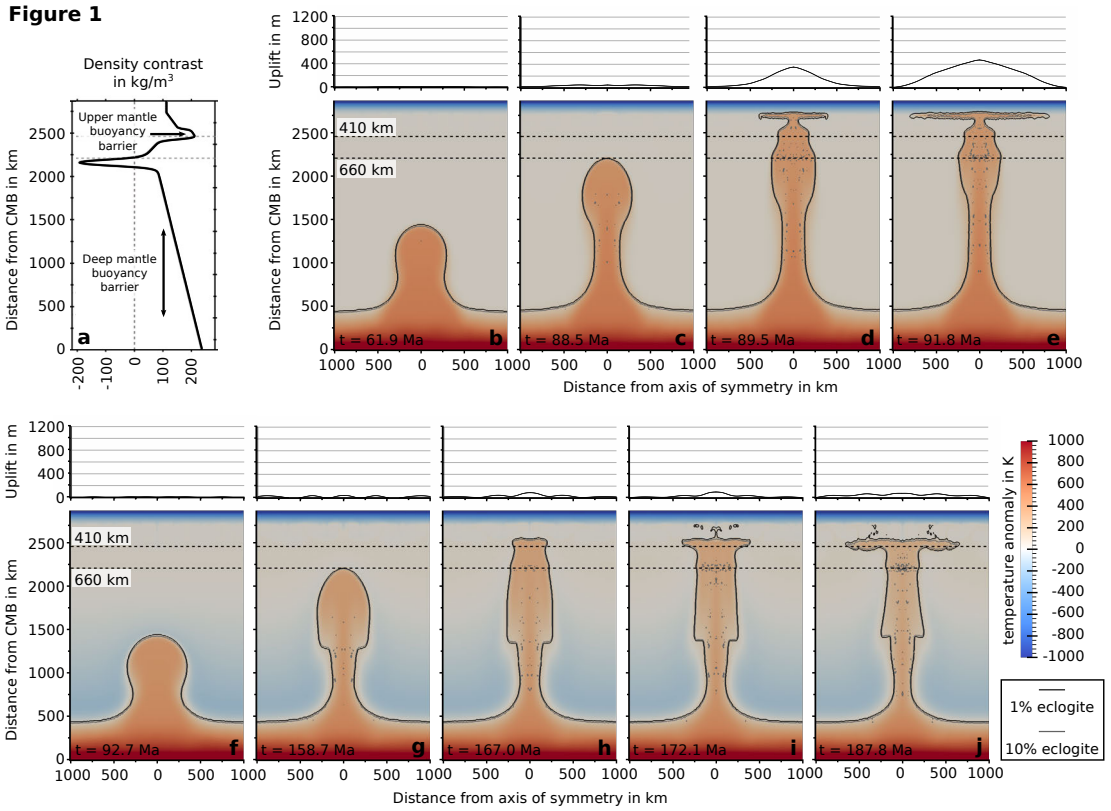

Figure 2.1: Potential barriers for the plume ascent.
(a) Difference between the densities of eclogite and peridotite as function of depth, based on experimental data (Aoki and Takahashi, 2004; Litasov and Ohtani, 2005; Hirose et al., 2005).
(b–e) Evolution of a "primary" thermochemical plume in an adiabatic mantle with an initial excess temperature of 550 K and a "small" initial volume of 1.22×10^8 km^3. Colours give the temperature anomaly (deviation from adiabatic temperature of the ambient mantle) and solid lines denote the composition. The related surface uplift is shown above each model section. Because of the high excess temperature, the plume buoyancy is high enough to overcome the lower mantle buoyancy barrier **(b,c)** and the plume reaches the upper mantle, spreads below the lithosphere **(d,e)** and causes a premagmatic surface uplift of 400 m. However, the maximum excess temperature of more than 350 K seems to be higher than what is typically observed (Herzberg and Gazel, 2009).
(f–j) Evolution of a "failing" thermochemical plume in a subadiabatic mantle with an initial excess temperature of 450 K and a "small" initial volume of 1.22×10^8 km^3, colour scale as in (b–e). Because of the subadiabatic mantle temperature, the plume buoyancy is high enough to overcome the lower mantle buoyancy barrier **(f,g)** and the plume reaches the upper mantle **(h)**. However, due to its low-buoyancy flux, the plume cannot cross the upper mantle buoyancy barrier **(i)** and is ponding in a depth of 300–400 km **(j)**.

Figure 2

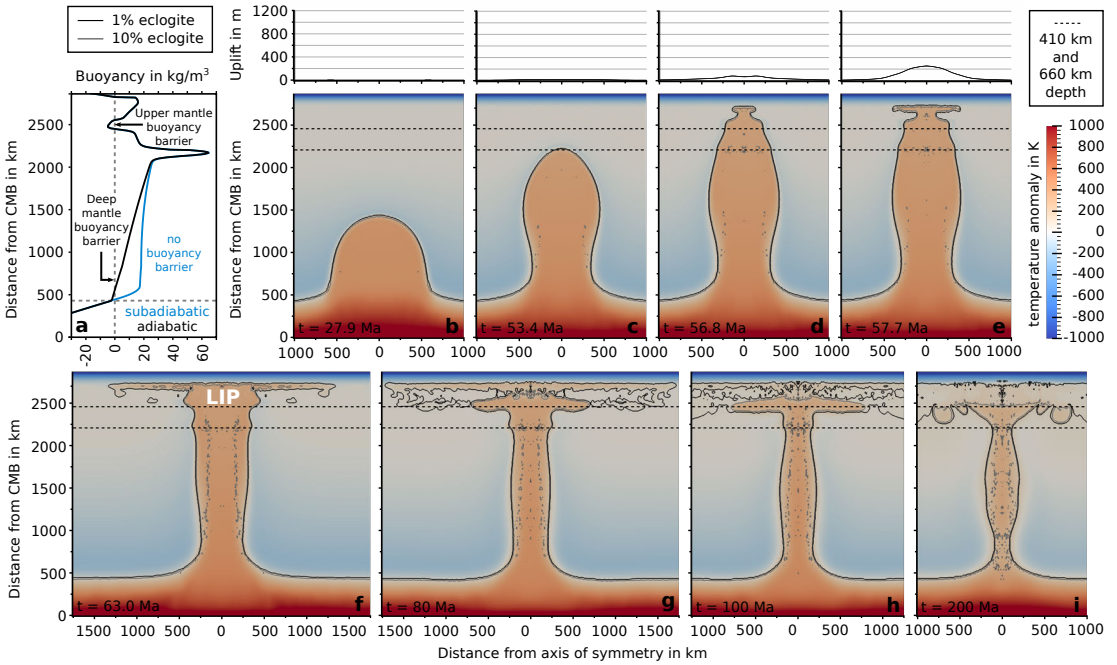

Figure 2.2: Ascent dynamics of an LBP.
(a) Buoyancy as a function of depth for a thermochemical plume containing 15% of eclogite with an initial excess temperature of 450 K in an adiabatic (black line) and subadiabatic (blue line) mantle. The vertical dashed line marks zero buoyancy and the horizontal dashed line marks the top of the thermochemical boundary layer in the lowermost mantle.
(b–i) Evolution of a thermochemical plume in a subadiabatic mantle with an initial excess temperature of 450 K and an initial volume of 3.71×10^8 km^3, that is, best fit model for the Siberian LIP. Colours give the temperature anomaly (deviation from the adiabatic mantle temperature) and solid lines denote the composition. The lines almost merge at the margin of the plume indicating a high compositional gradient. The related surface uplift is shown above each model section.

the same temperature has a higher temperature contrast to its surroundings and therefore higher thermal buoyancy in the subadiabatic lower mantle than in the adiabatic or in a hotter than adiabatic (that is, super-adiabatic) mantle and as a result is able to carry a larger amount of eclogite. However, large intervals of subadiabatic temperatures are likely present only in the deep lower mantle (Bunge, 2005) and therefore cannot help plumes to cross the upper mantle buoyancy barrier. A relatively small LBP initiated in the subadiabatic lower mantle may successfully reach the upper mantle buoyancy barrier, but then is ponded in the mantle transition zone (Fig. 2.1f–j). The way to overcome this obstacle is to increase the plume volume. A sufficiently large LBP starting in the subadiabatic lower mantle crosses both barriers and spreads below the lithosphere (Fig. 2.2). Two factors are responsible for this effect: first, the larger plume rises faster and cools less and therefore approaches the barrier with higher thermal buoyancy. Second, the larger plume volume allows deeper parts of the plume, where eclogite has a lower density than peridotite (for example, just below the 660 km discontinuity, Fig. 2.2a), to compensate the negative buoyancy of the barrier. In this way, the upper mantle buoyancy barrier works like a low-pass filter in seismology, allowing only large LBPs (like long-wavelength seismic waves) to pass through.

2.2.3 Types of low-buoyancy thermochemical plumes

A series of models with different plume temperatures and volumes, and adiabatic and subadiabatic mantle temperatures, shows that plumes reaching the base of the lithosphere can be categorized into three different types (Fig. 2.3). (1) Primary plumes that rise directly from the CMB (Fig. 2.4c, solid diamonds in Fig. 2.3). (2) Secondary plumes from the deep lower mantle (open diamonds in Fig. 2.3) and (3) secondary plumes from the upper mantle (Fig. 2.4b, half open diamonds in Fig. 2.3). Primary plumes have high average excess temperatures in the upper mantle of more than 200 K (Fig. 2.3a) and in this respect are similar to the classical plume models and plume regimes described in previous modelling studies (Lin and van Keken, 2006a; Kumagai et al., 2008). They can transport a large fraction of eclogite from 12% up to 17% (Fig. 2.3b), and are supplied with new material through the plume conduit for several million years. Although they cross the upper-mantle buoyancy barrier, a portion remains in a "pool" at 300–400 km depth (Fig. 2.2f,g). A similar structure has been observed in seismic tomography models of the mantle beneath the Hawaiian islands (Wolfe et al., 2009) and also has been proposed in a recent modelling study (Ballmer et al., 2013). The volumes of primary plume heads approaching the base of the lithosphere can exceed 10^8 km^3 (Fig. 2.3d).

Smaller initial temperatures lead to negative buoyancy of LBPs, which causes them to pond either in the deep lower mantle, if temperatures in the lower mantle are adiabatic or super-adiabatic, or below the buoyancy barrier in the upper mantle, if the lower mantle is subadiabatic. In both cases, these ponding plumes heat the mantle above and can generate secondary plumes. The deep- rooted secondary plumes rise from the top of the thermochemical boundary layer at the CMB and are similar to what is predicted in a previous modelling study (Lin and van Keken, 2006a). They contain only a small amount of eclogite, and have relatively low excess temperatures (<150 K) and small volumes. Secondary plumes rooted in the upper mantle form above the thermochemical plumes ponding in a depth of 300–400 km (Fig. 2.4a,b). These secondary plumes show various excess temperatures and eclogite contents of 4–12.5% (Fig. 2.3a,b) depending on the initial plume temperature, composition and volume and on the time the material ponds in this pool. However, all secondary plumes are short-living features; in all our models, due to the low volume and mixing in the asthenosphere the plume excess temperature decreases by about 10% and the fraction of eclogite by 25% in only five million years.

Another property that distinguishes the different plume regimes is the associated plume buoyancy flux: the buoyancy fluxes of primary plumes show a characteristic evolution pattern with a peak in the beginning, associated with the generation of a LIP when the plume head reaches the lithosphere, and a more stable lower level flux resembling the ongoing hotspot activity caused by the plume tail (Fig. 2.5). As the heads of secondary plumes do not reach the base of the lithosphere and do not generate LIPs, their buoyancy flux only reflects the lower activity associated with a hotspot (Fig. 2.5). Note that the buoyancy fluxes associated with the plume tails of LPBs are within the range of estimates for present-day hot spots (Steinberger, 2000) (grey field in Fig. 2.5).

2.2.4 Conditions for LBPs to reach the lithosphere

Although all these different plume regimes might occur in the terrestrial mantle, only the primary plumes have sufficient temperatures and volumes to generate LIPs. To reach realistic excess temperatures between 200 and 300 K (Herzberg and Gazel, 2009) in the upper mantle, the plume excess temperature in the deep lower mantle needs to be in a range of 400–550 K. Plumes starting in a subadiabatic mantle can ascend at lower initial

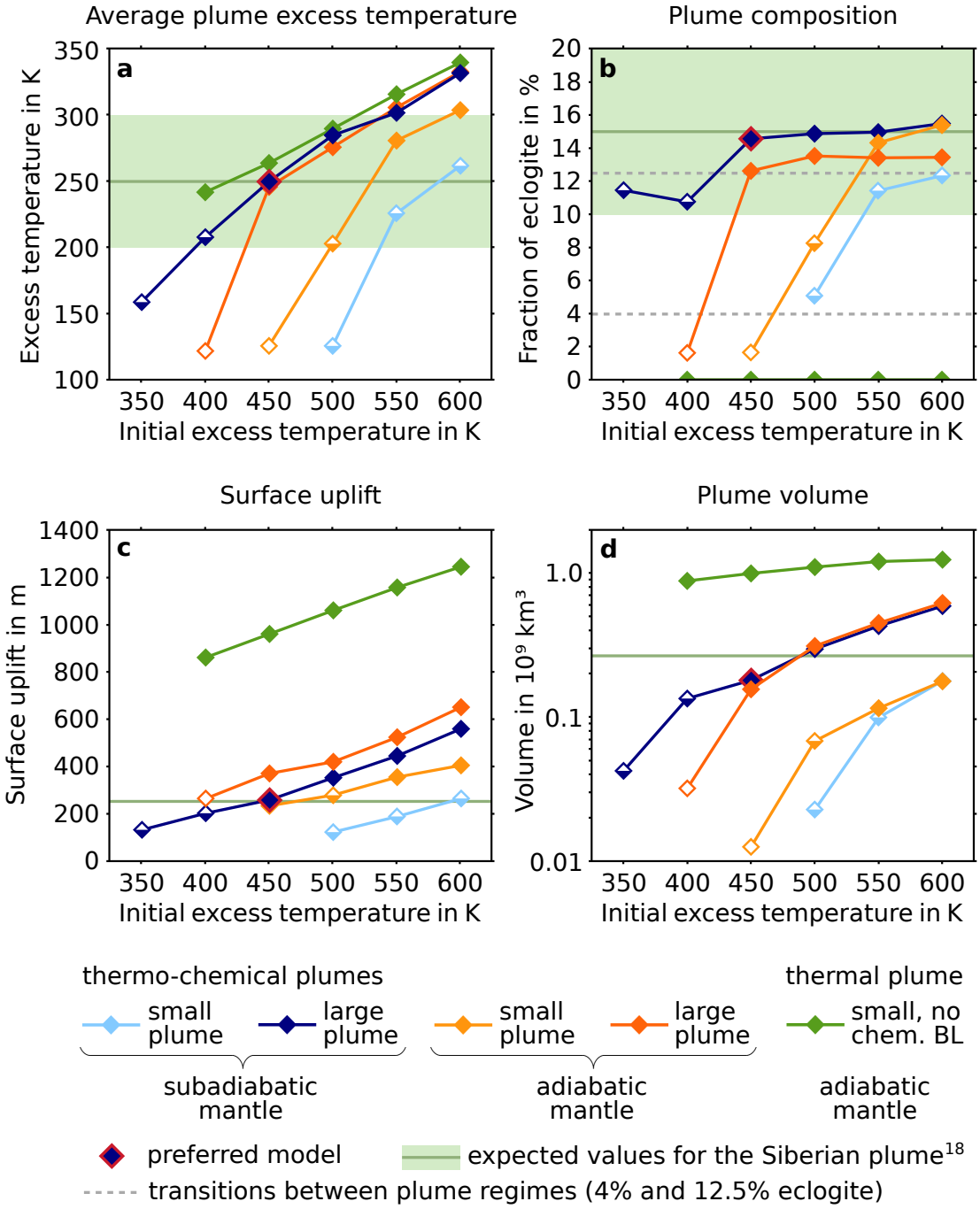

Figure 2.3: Conditions for the ascent of a LBP. Shown are the plume temperature **(a)**, composition **(b)**, premagmatic surface uplift **(c)** and volume **(d)** versus plume initial excess temperature for different plume initial sizes and mantle temperature profiles, leading to different dynamic regimes. Colours give the model configuration; symbols give the plume dynamic regime: primary plume (full diamonds), secondary plume from the upper mantle (half-full diamonds), secondary plume from the deep lower mantle (hollow diamonds) and failing plume (no symbol). "Small" plumes have an initial volume of 1.22×10^8 and "large" plumes 3.71×10^8. Plume excess temperature, volume and composition after arrival at the lithosphere were calculated by averaging over the area with excess temperatures higher than 100 K in a depth <300 km. Average plume excess temperature, average eclogite fraction and maximum surface uplift are presented at 1 Myr and plume volume at 5 Myr after the plumes reach the base of the lithosphere.

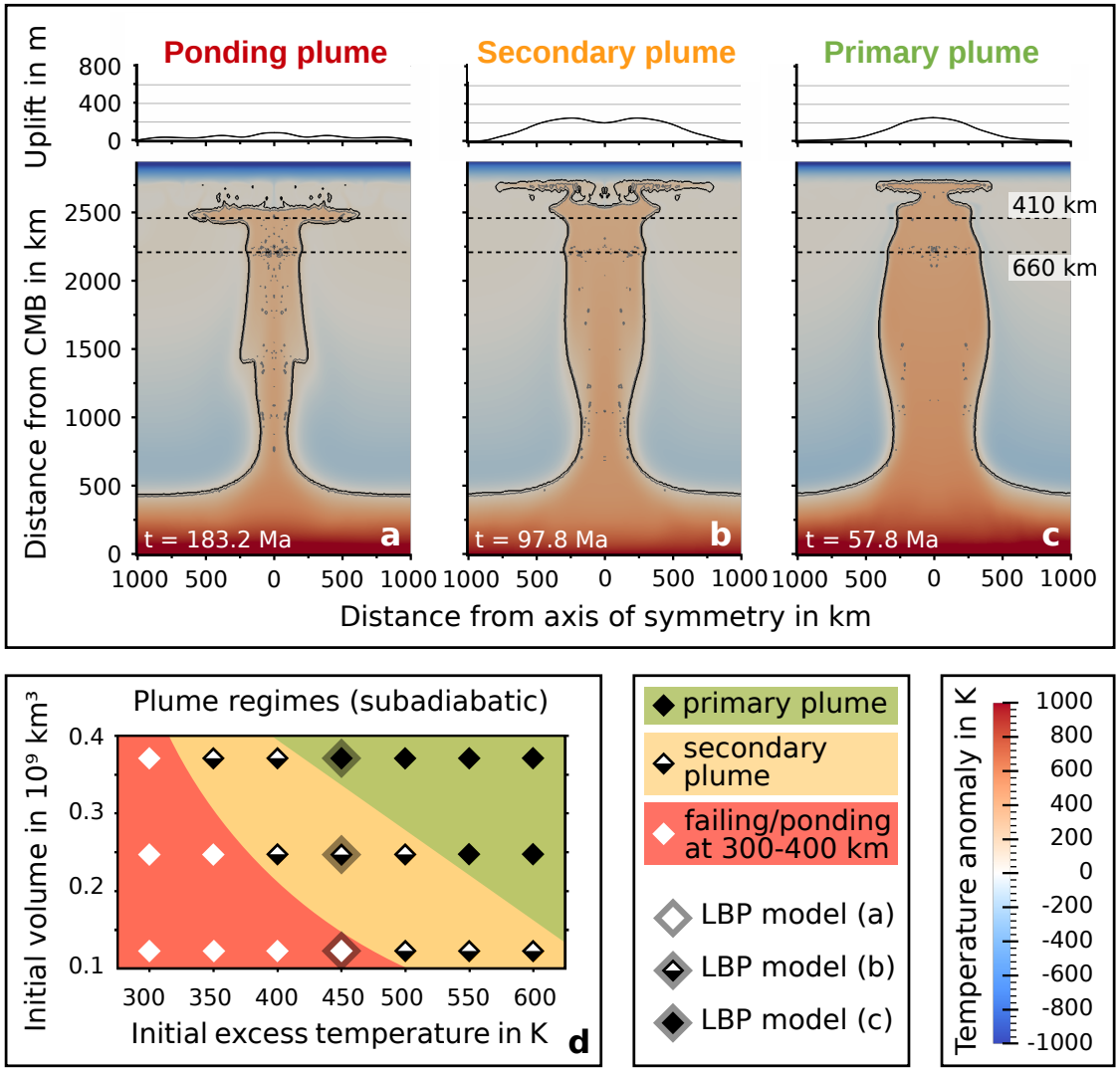

Figure 2.4: Influence of the plume volume on the plume regime for the thermochemical plumes rising in a subadiabatic mantle. Colour scale for the time snapshots as in Fig. 2.1. **(a)** Time snapshot of a "small" plume (initial volume of 1.22×10^8). The plume takes almost 200 Myr to reach the upper mantle and is not able to cross the upper-mantle buoyancy barrier. **(b)** Time snapshot of an "intermediate" plume (initial volume of 2.47×10^8). The plume cannot cross the upper-mantle buoyancy barrier as a whole, only secondary plumes rise from there. **(c)** Time snapshot of a "large" plume (initial volume of 3.71×10^8. The buoyancy flux is sufficiently large for the plume to directly advance to the base of the lithosphere (primary plume). **(d)** Plume regime in dependence of initial plume temperature and volume. Symbols and their colours are described in the figure inset.

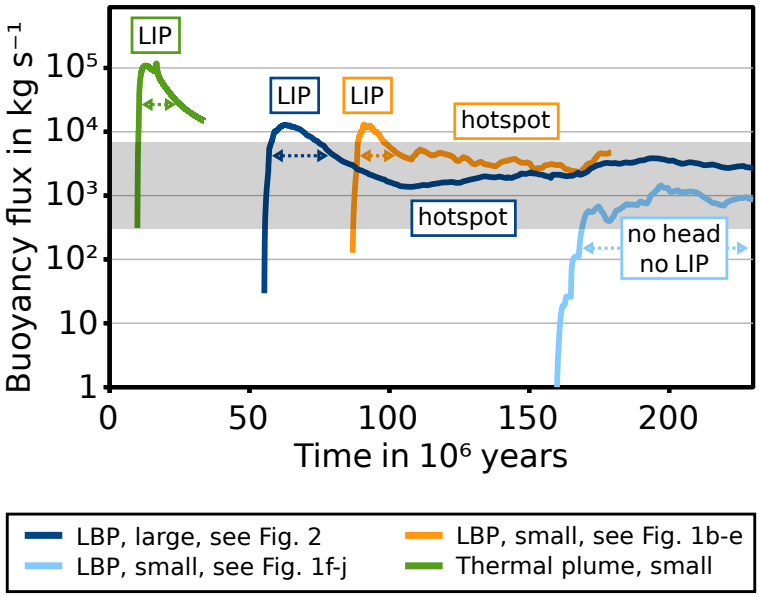

Figure 2.5: Buoyancy flux evolution of thermochemical plumes. Shown is the buoyancy flux within the plume (taken as the region with an excess temperature higher than 25 K) at a depth of 200 km. Model parameters and colouring as in Fig. 2.3. The three primary plumes shown (dark blue, yellow and green line) show a peak in their buoyancy flux associated with massive melting and the generation of a LIP when the plume head reaches the base of the lithosphere. They exceed the values observed for present-day hotspots (Steinberger, 2000) denoted by the grey field, with the thermal plume (green line) reaching a significantly higher buoyancy flux than the thermochemical plumes. Subsequently, the buoyancy flux decreases to a stable level supported by the plume tail with fluctuations caused by smaller scale upwellings, representing long-time hotspot activity. The small "failing" thermochemical plume (light blue line) shows a much lower buoyancy flux without a pronounced peak, resulting from no plume head reaching the base of the lithosphere. The buoyancy fluxes of the tails of the presented thermochemical plumes are all within the estimates for present-day hot spots (Steinberger, 2000).

temperatures than plumes rising from an adiabatic lower mantle and they can carry a higher fraction of eclogite (more than 14%, Fig. 2.3b) to the base of the lithosphere. The combination of high eclogite content and low-temperature results in reduced buoyancy and a smaller surface uplift (Fig. 2.3c). The best fit to the parameters of the Siberian plume (Sobolev et al., 2011), shown by horizontal solid lines in Fig. 2.3, is achieved by the model of a large plume with an initial excess temperature of 450 K, carrying 15% of eclogite and rising in a subadiabatic lower mantle. When this plume arrives at the lithosphere after an ascent time of 58 Myr (Fig. 2.4c), which is several times longer than for a purely thermal plume, it has an average excess temperature of about 250 K and still contains 15% of eclogite. As a result, it generates a surface uplift of only 260 m, which is less than a quarter of the uplift above a purely thermal plume with the same excess temperature. The plume head volume at the base of the lithosphere amounts to 180 million km^3 and hence is sufficient for causing massive volcanism (Sobolev et al., 2011). Note that a LBP with a smaller volume under otherwise identical conditions cannot cross the buoyancy barrier at 300–400 km (Fig. 2.4d) and is stuck below it completely (Fig. 2.4a) or partially (Fig. 2.4b).

2.3 Discussion

Therefore, our modelling shows that a LBP with parameters similar to the Siberian plume can indeed rise through the entire mantle, if its volume is sufficiently large and the lower mantle is subadiabatic. A possible alternative mechanism for overcoming the lower-mantle buoyancy barrier, worth further investigations, is the plume ascent from the upper boundary of thermochemical piles, which have been proposed to be present in the lowermost mantle with parts extending up to more than 1,000 km above the CMB (Burke et al., 2008). This would allow plumes to rise from a shallower depth, where their buoyancy is positive, especially at the edges of the piles, where the surrounding mantle temperature is expected to be adiabatic.

Considering a depth-dependent plume buoyancy constrained by mineral physics and geochemical data also reveals different barriers for the ascent of LBPs compared with what was reported in previous studies (Farnetani and Samuel, 2005; Samuel and Bercovici, 2006): Because of the negative chemical density contrast in 660–750 km depth (Fig. 2.1a), eclogite-bearing plumes cross the spinel-perovskite phase transition despite its negative Clapeyron slope. In addition, the employed experimental data on eclogite density (Hirose et al., 2005) indicate a buoyancy minimum close to the CMB and not in the upper part of the lower mantle, excluding stagnating plumes predicted in the lower mantle (Samuel and Bercovici, 2006).

We also note that the shapes of LBPs are different from those inferred for classical thermal plumes in the lower mantle. The plume heads are much less pronounced, even at the stage when LIPs are generated (compare Fig. 2.2f and Supplementary Fig. 2.6). LBPs also have columnar "tails" with a diameter of more than 500 km, which remain stable in the mantle for tens or hundreds of millions of years after the plume arrives at the base of the lithosphere (Fig. 2.2), in agreement with previous modelling results (Lin and van Keken, 2006a; Lin and van Keken, 2006b). Hence, it should be much easier to resolve these structures with seismic methods than classical narrow plume tails (Boschi et al., 2008). Indeed, seismic tomographic observations (Montelli et al., 2004) suggest that many major plumes are broad features that can be well imaged in many models, with comparable confidence as slabs (Boschi et al., 2008). This implies that many major plumes in fact are thermochemical rather than purely thermal, and are described better by LBP models than by classical models. This conclusion is in accordance with the growing geochemical evidence that mantle sources of both ocean island basalts and LIPs have heterogeneous compositions (Sobolev et al., 2007).

If many major mantle plumes are LBPs, the entire plume concept will need to be reconsidered. While an LBP requires more than 50 Myr for its ascent, a purely thermal plume reaches the lithosphere in less than 20 Myr, the consequence being that the plume buoyancy fluxes of LBPs are radically different, in particular during the LIP stage, where the buoyancy flux of thermal plumes is one order of magnitude higher (Fig. 2.5). Moreover, after the rise of a LBP to the lithosphere and the generation of the associated LIP, in contrast to the classical plume theory, large-scale thermal heterogeneities remain in the mantle for a long time and may act as ascent channels for new hot mantle material tens or even hundred million years later. This stable root of the LBP supports the longevity of the hot-spot stage of the plume evolution and involves a buoyancy flux well within the range of estimates for present-day hot spots (Fig. 2.5).

In summary, the consideration of thermochemical plumes with high content of eclogite constrained by geochemical data together with a realistic depth-dependent density contrast between eclogite and peridotite as well as lower mantle subadiabaticity successfully reproduces the probable characteristics of the sources of LIPs and resolves the controversy

of the classical mantle plume concept concerning high premagmatic uplifts and mantle plume shapes.

2.4 Methods

2.4.1 Model set-up

The two-dimensional axisymmetric version of the Citcom we use here (Leng and Zhong, 2010) employs the anelastic liquid approximation and treats the mantle as compressible (Leng and Zhong, 2008). The model domain comprises the whole mantle in vertical direction and extends over a distance of 2,870 km horizontally. We compute models with both adiabatic and subadiabatic geotherms (Supplementary Fig. 2.7a). Here we do not aim to study the very complex processes of the formation of a thermochemical bottom boundary layer and the entrainment of a dense phase into the mantle plume (Lin and van Keken, 2006a; Lin and van Keken, 2006b; Zhong and Hager, 2003; Solomatov et al., 1993; van Keken et al., 2002; McNamara and Zhong, 2004; Jellinek and Manga, 2004; Lin and van Keken, 2005; Tan and Gurnis, 2007; Deschamps et al., 2011; Li et al., 2014). Instead, we take a simplified approach assuming that such a layer already exists and contains a prescribed amount of the eclogitic material (Supplementary Fig. 2.7b). To start the plume ascent, we also assume that there is an initial temperature perturbation at the central axis that previously entrained a certain fraction of eclogite. The plume initial temperature and volume were varied by changing the excess temperature (relative to the adiabatic temperature) of this perturbation between 300 and 600 K and its volume between 1.22×108 and 3.71×108 km^3. The amount of eclogite within the thermally perturbed region (initial plume) was assumed to be 15%, as estimated for the Siberian plume (Sobolev et al., 2011). Different phase transitions are incorporated for the two chemical components resulting in a depth-dependent density contrast between peridotite and eclogite, which is based on recent experimental data (Aoki and Takahashi, 2004; Litasov and Ohtani, 2005; Hirose et al., 2005) and also includes the effect of composition-dependent compressibility in the lower mantle (Supplementary Fig. 2.7c,d). We use a temperature- and depth-dependent viscosity modified from a previous modelling study (Leng and Zhong, 2010) (Supplementary Fig. 2.7e) and additionally test the effect of increasing the activation energy by a factor of 3. The depth-dependent thermal expansivity is based on mineral physics data (Steinberger and Calderwood, 2006) (Supplementary Fig. 2.7f). Together with the depth-dependent compositional density contrast and the plume temperature changes due to adiabatic cooling, this results in a typical buoyancy profile for a rising plume (Supplementary Fig. 2.8a) constrained by geochemical observations and experimental data, which is one of the novel aspects of this work. Previous studies did not focus on conditions for the ascent of eclogite-bearing mantle plumes through the whole mantle and thus either used a simplified (Lin and van Keken, 2006a; Lin and van Keken, 2006b) or constant (Farnetani and Samuel, 2005; Kumagai et al., 2008) chemical density contrast, a constant thermal expansivity (Lin and van Keken, 2006a; Lin and van Keken, 2006b; Kumagai et al., 2008; Samuel and Bercovici, 2006) or investigated only the upper (Ballmer et al., 2013) or only the lower (Samuel and Bercovici, 2006) mantle. All parameters used in the model are presented in 2.1. Note that increasing the temperature dependence of viscosity changes the ascent time of LBPs, but does not significantly influence the plume shape, dynamics or surface manifestations (Supplementary Figs. 2.9 and 2.9).

Parameters with physical units.	
Earth's radius	6.371×10^6 m
Mantle thickness	2.870×10^6 m
Initial volume (small plume)	1.22×10^8
Initial volume (intermediate plume)	2.47×10^8
Initial volume (large plume)	3.71×10^8
Thickness of the bottom thermochemical BL (thermochemical models)	430 km
Thickness of the bottom thermochemical BL (thermal models)	100 km
Temperature difference surface–CMB ΔT	3,500 K
Surface temperature T_S	273 K
Temperature increase across the top thermal boundary layer	1,220 K
Temperature increase across the bottom thermal boundary layer	1,200 K
Surface density ρ_0	3,400 kg m^{-3}
Reference viscosity η_0	8.44×10^{21} Pa s
Gravitational acceleration g	10 m^{-2}
Thermal diffusivity (surface) $k_0^\star$	7×10^{-7} m^2 s^{-1}
Thermal expansivity (surface) α_0	4.2×10^{-5} K^{-1}
Specific heat c_p	1,000 J kg^{-1} K^{-1}
Radiogenic heat production rate H	5.9×10^{-12} W kg^{-1}
Mantle compressibility $\xi^{\star\star}$	5.124×10^{-12} Pa^{-1}
Clapeyron slope of the 410-km phase transition γ_{410}	1 MPa K^{-1}
Clapeyron slope of the 660-km phase transition γ_{660}	-1 MPa K^{-1}
Prefactor in the temperature dependence of viscosity $A^{\star\star\star}$	3.9473×10^{-3} resp. 1.3×10^{-2}

Table 2.1: Values of physical parameters and constants.
CMB, core-mantle boundary.
*The thermal diffusivity increases linearly from the surface to the core-mantle boundary by a factor of 2.18 (from Leng and Zhong (2010)).
**We use the Adams–Williamson equation of state, resulting in a depth-dependent density in the form of $\rho_r(z) = \exp(\rho_0 g \chi z)$. Density changes caused by phase transitions are applied additionally.
***We use a viscosity law (Leng and Zhong, 2010) in the form of $\eta(T, z) = \eta_r(z) \exp\left[-A\left(T - T_{\mathrm{adi}}(z)\right)\right]$, with $\eta(z)$ for the average mantle temperature being the viscosity profile shown in Supplementary Fig. 2.6(e). $A = 3.9473 \times 10^{-3}$ (as in ref. 27) corresponds to a viscosity range of six orders of magnitude for $\Delta T = 3,500$ K (temperature difference surface–CMB). To examine the effect of a higher temperature dependence of viscosity on plume dynamics, we also performed computations with a three times higher activation energy (that is, $A = 1.3 \times 10^{-2}$).

2.4.2 Numerical technique

Using the anelastic liquid approximation and treating the mantle as compressible (Leng and Zhong, 2008) leads to the following equations

$$(\rho_r u_i)_{,i} = 0, \tag{2.1}$$

$$\left(\eta\left(u_{i,j} + u_{j,i} - \frac{2}{3}u_{k,k}\delta_{ij}\right)\right)_{,i} - p_{,j}\delta_{ij} = \delta\rho\, g\, \delta_{i3} \tag{2.2}$$

with the density anomaly $\delta\rho = -\alpha\rho(T - T_{\text{adi}}) + p\chi + \delta\rho_{\text{ph}}\psi\delta\rho_{\text{chem}}C$, and

$$\begin{aligned}\rho_r c_p\left(T_{,t} + u_i T_{,i} - \kappa T_{,i,i}\right) = 2\eta\left(\frac{1}{2}u_{i,j} + \frac{1}{2}u_{j,i} - \frac{1}{3}u_{k,k}\delta_{ij}\right) : \\ \left(\frac{1}{2}u_{i,j} + \frac{1}{2}u_{j,i} - \frac{1}{3}u_{k,k}\delta_{ij}\right) \\ - \rho_r\alpha g u_3 T + \rho_r H,\end{aligned} \tag{2.3}$$

which are solved non-dimensionalized and in a cylindrical coordinate system (Zhong and Hager, 2003). ρ_r is the radial density profile, $\mathbf{u}$ is the velocity, η is the viscosity, p is the dynamic pressure, g is the gravitational acceleration, α is the thermal expansivity, T_{adi} is the adiabatic temperature, χ is the compressibility, $\delta\rho_{\text{ph}}$ is the density change across a phase boundary, ψ is the phase function, $\delta\rho_{\text{chem}}$ is the depth-dependent chemical density contrast between eclogite and peridotite, C is the fraction of eclogite, c_p is the specific heat capacity, k is the thermal diffusivity and H is the specific radiogenic heat production rate. Values of all material parameters are given in 2.1.

We use the Adams-Williamson Equation of state, which leads to a radial density profile of

$$\rho_r(z) = \exp(\rho_0 g\chi z) \tag{2.4}$$

with the reference density ρ_0.

The depth dependence of viscosity $\eta_r(z)$ is given in Supplementary Fig. 2.7e, and the temperature dependence (Leng and Zhong, 2010) is

$$\eta(T, z) = \eta_r(z)\exp\left[-A\left(T - T_{\text{adi}}(z)\right)\right] \tag{2.5}$$

The adiabatic temperature profile T_{adi} is computed during the initialization of the model by solving equation

$$\frac{\mathrm{d}T_{\text{adi}}}{\mathrm{d}z} = \frac{\alpha g T_{\text{adi}}}{c_p} \tag{2.6}$$

iteratively, starting from the given surface temperature T_{S} . Citcom uses finite elements, and a multigrid solver using an Uzawa algorithm is incorporated to solve the coupled momentum and mass conservation equation. The resulting velocity is employed to solve the energy equation with a streamline upwind the Petrov–Galerkin scheme. The compositional field is transported by markers and interpolated onto the nodes with a tracer ratio method. A predictor–corrector scheme is used for updating the marker positions.

The surface uplift is calculated using the normal stresses acting on the upper surface:

$$h = \frac{\sigma_{zz}}{g(\rho - \rho_s)} \tag{2.7}$$

with $\sigma_{zz} = 2\eta\left(u_{z,z} - \frac{1}{3}u_{k,k}\right) - p$ and ρ_s being the density contrast at the surface, which is 1 kg m^{-3} where h<0 (water) and 0 where h>0 (air). A feature to note is the self-adaptive coordinate transformation integration scheme that increases the accuracy of the calculated surface topography near the axis of symmetry (Leng and Zhong, 2010).

The plume buoyancy fluxes B are calculated at 200 km depth, integrated over the area with excess temperatures exceeding 25 K and using the following relation:

$$B = -\int_{x=0}^{r} 2\Delta\rho(x) v_y(x) \pi x \mathrm{d}x \tag{2.8}$$

with $\Delta\rho$ being the density difference between the plume and an undisturbed mantle, including effects of both temperature and composition, x the radial direction and y the vertical direction. All changes made to the original version of the code presented in a previous study (Leng and Zhong, 2010) are available from the authors on request.

2.4.3 Model approximations

One assumption we make is that the length scale of chemical heterogeneities within the plume is so small that dense eclogite bodies do not sink in peridotitic material. Estimates based on the Stokes relation for the velocity of a sinking sphere show that for a higher plume viscosity than 10^{17} Pa s this assumption holds if the radii of the spherical eclogite bodies are smaller than 100 m. Note also that we do not include plume–lithosphere interaction or non-linear viscosities in our model. Because of that, any predictions exceeding the first few million years after the plume arrival at the base of the lithosphere and related to mixing of material in the mantle are not as precise as our results regarding the ascent of the plume, which is the focus of this study. In addition, considering these processes strongly accelerates the development and spreading of the plume head in the upper mantle (as demonstrated in two-dimensional Cartesian models (Sobolev et al., 2011)), causing a higher and shorter peak in the buoyancy flux associated with the LIP than what our models show (Fig. 2.5).

Acknowledgments

We are grateful to Nick Arndt, Alex Sobolev, Bernhard Steinberger and Thorsten Becker for carefully and critically reading the manuscript and Elvira Mulykova and Rene Gassmoeller for their help revising the manuscript.

2.A Supplementary figures

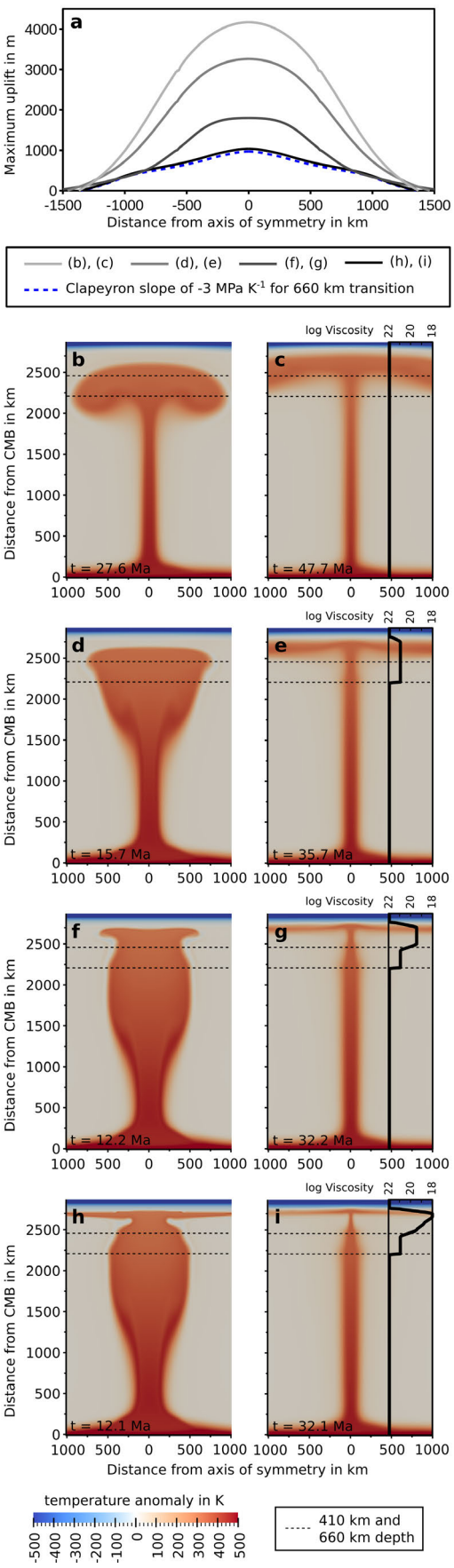

Figure 2.6: Axisymmetric models of thermal mantle plumes and associated surface uplifts. **(a)** Maximal surface uplift versus distance above the spreading plume head computed for different viscosity structures of the upper mantle. All models include major olivine phase transitions. The dashed blue line shows the surface uplift obtained in a model with the viscosity profile of (h,i) and the highly negative Clapeyron slope of the 660 km phase transition used in a previous study (Leng and Zhong, 2010). This is the minimum surface uplift that is expected for a thermal plume of this size and temperature. **(b, c)** Time snapshots of plume excess temperature for the plume rising in a homogeneous mantle. The viscosity model is shown in the inset in the right panel. **(d, e)** Time snapshots of plume excess temperature for the plume rising in a mantle with reduced viscosity in the upper mantle and transition zone. **(f, g)** The same model as in (d, e), but with a low-viscosity upper mantle. **(h, i)** The same model as in (f, g), but with an additional low-viscosity layer in the asthenosphere. All plumes in (a)-(g) have an initial radius of 840 km, an initial excess temperature of 450 K and rise in an adiabatic mantle.

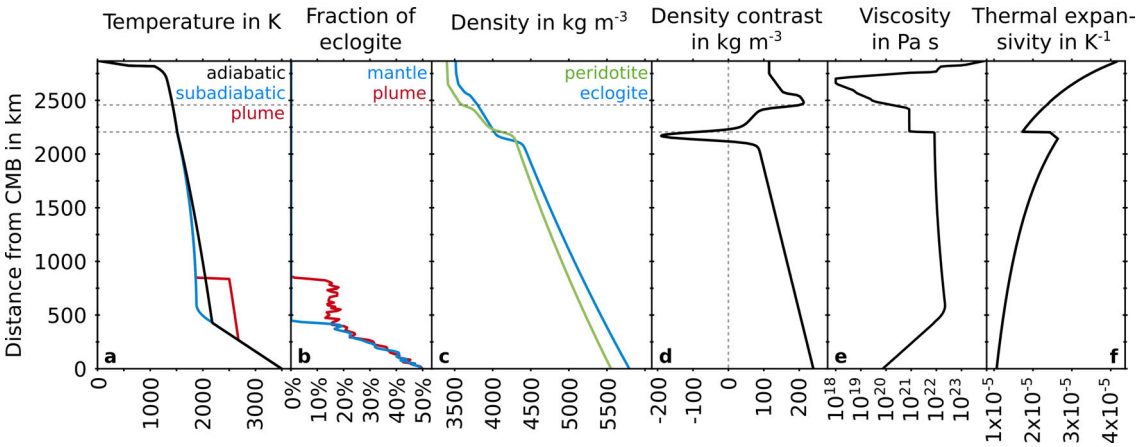

Figure 2.7: Initial conditions and material model. **(a)** Initial temperature profile for mantle abiabaticity (black), subadiabaticity (blue) and exemplary initial temperature perturbation of the starting plume (red). **(b)** Representative profiles of the percentage of eclogite in the mantle (blue) and intersecting the initial temperature perturbation of the starting plume (red). The oscillations in the profiles are due to the probabilistic nature of the method of assigning initial values to the markers that are used for the transport of compositional fields. **(c)** Density profiles of peridotite (green) and eclogite (blue) estimated from experimental data (Aoki and Takahashi, 2004; Litasov and Ohtani, 2005; Hirose et al., 2005). **(d)** Density difference between peridotite and eclogite resulting from subtracting the profiles shown in (c) from each other. Positive values mark a higher eclogite density and negative values mark a higher density of peridotite. **(e)** Mantle viscosity profile modified from a previous study (Leng and Zhong, 2010), including only depth-dependence; for the temperature dependence see 2.1. **(f)** Thermal expansivity profile derived from mineral physics data (Steinberger and Calderwood, 2006).

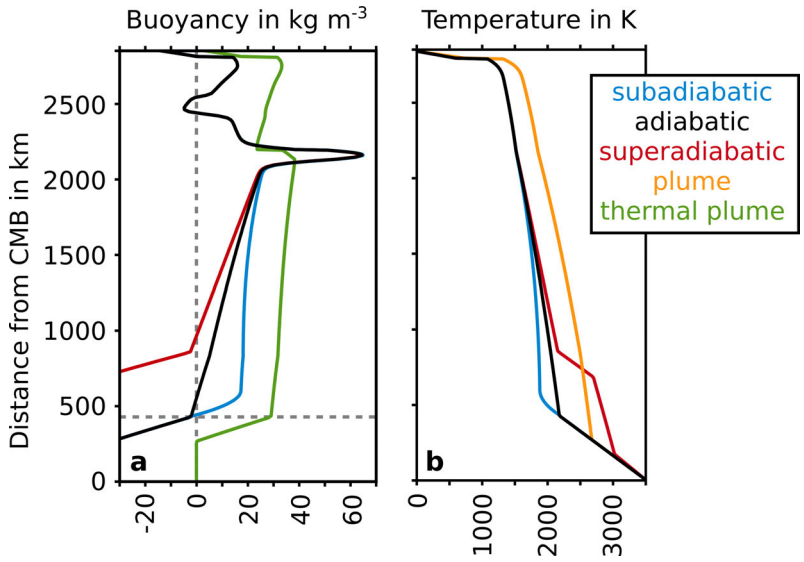

Figure 2.8: (a) Buoyancy in dependence of depth for a thermo-chemical plume containing 15% of eclogite with an initial excess temperature of 450 K in an adiabatic (black line), subadiabatic (blue line) and superadiabatic (red line) mantle and for a thermal plume with an initial excess temperature of 450 K in an adiabatic mantle (green line). The vertical dashed line marks zero buoyancy and the horizontal dashed line marks the top of the thermo-chemical boundary layer in the lowermost mantle. There are two barriers for the ascent of a thermo-chemical plume: one in the lower mantle just above the boundary layer and one in the upper mantle between 300 and 400 km depth. Mantle subadiabaticity increases the plume buoyancy in the lowermost mantle and enables the plume to cross this first barrier. profiles were calculated by adding the thermal buoyancy resulting from the temperatures in (b) and the chemical buoyancy caused by the depth-dependent density difference between peridotite and eclogite as shown in Supplementary Fig. 2.7d. **(b)** Corresponding temperature profiles for the adiabatic (black line), subadiabatic (blue line) and superadiabatic (red line) mantle as well as for a plume following an adiabat with an initial excess temperature of 450 K (yellow line, not including temperature changes due to conduction).

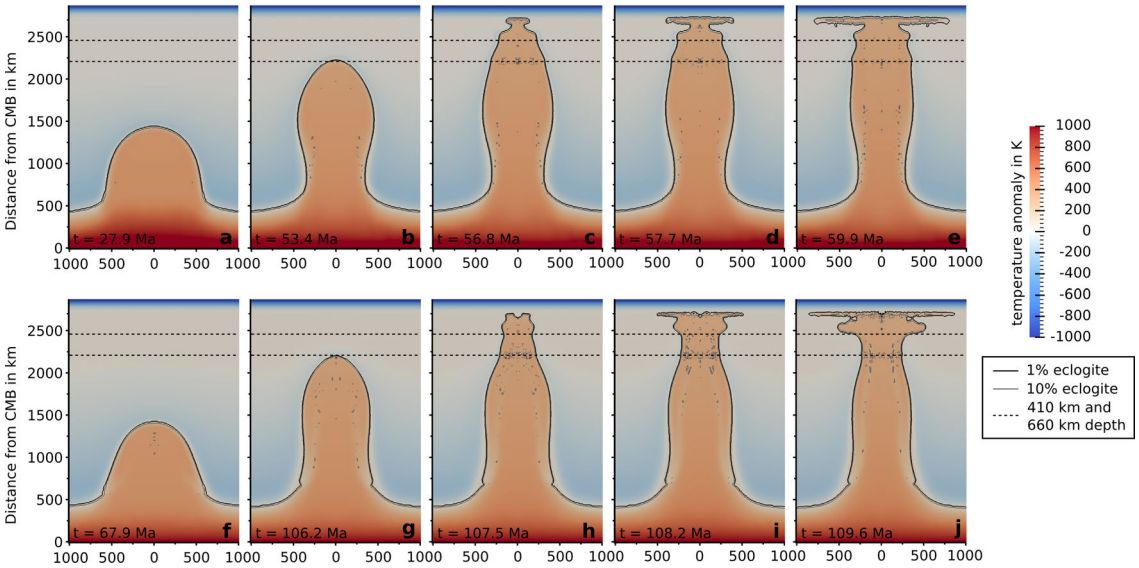

Figure 2.9: Influence of strongly temperature-dependent viscosity on the dynamics of LBPs. Panels **(a-e)** show time snapshots of the model presented in Fig. 2.1 (i.e. the model that fits the Siberian Traps best), panels **(f-j)** show a computation with the similar setup, except for a 30 times stronger temperature dependence of viscosity, achieved by increasing the activation energy by a factor of 3, and an initial excess temperature of 425 K. The comparison shows that the ascent in the lower mantle is delayed because of the increased viscosity in the low-temperature subadiabatic regions. However, there is no significant influence on the plume shape; in particular the wide plume tail in the lower mantle is present in both models.

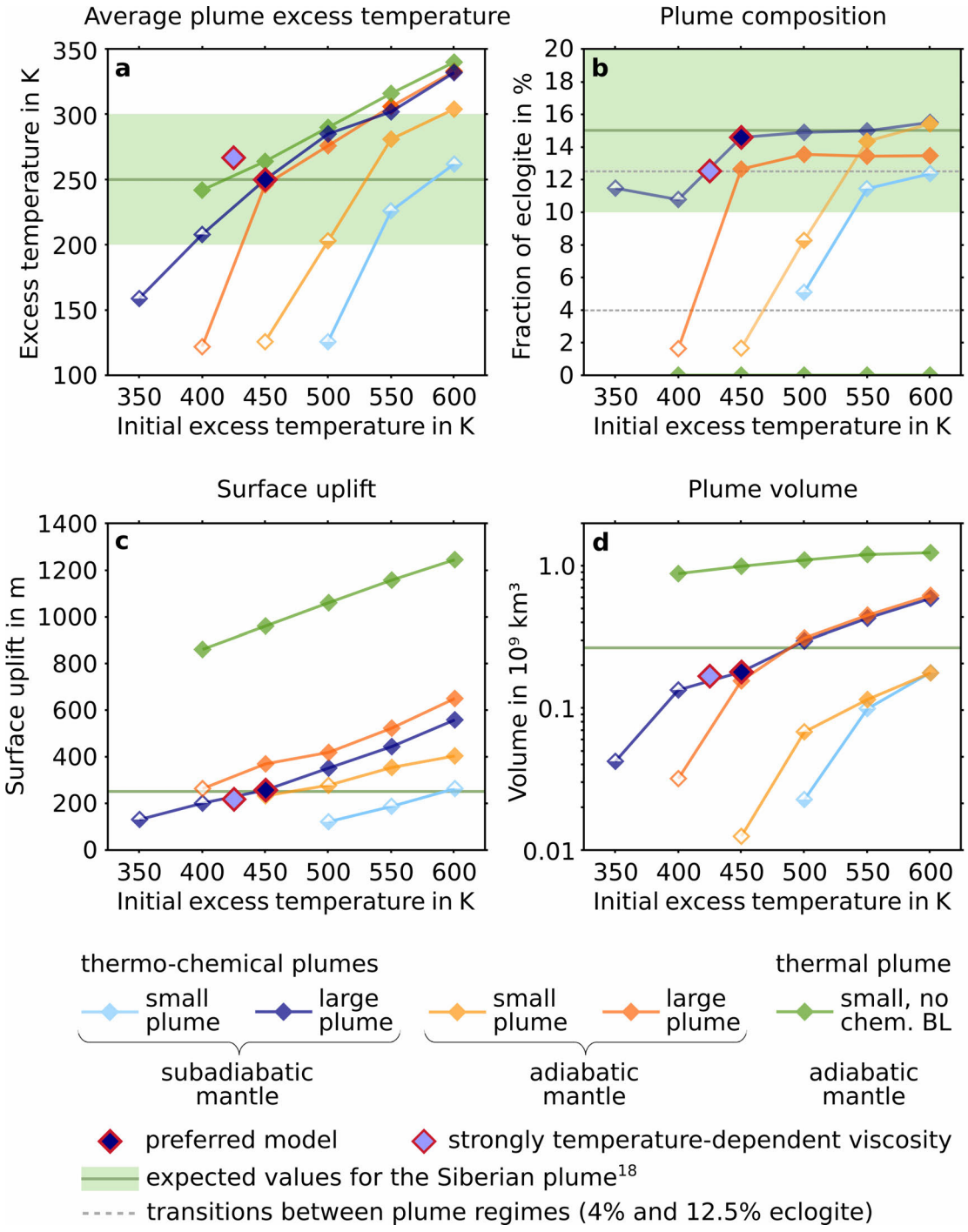

Figure 2.10: Influence of temperature-dependent viscosity on the plume surface manifestations. Shown are the same models as in Fig. 2.3 (with identical colours and symbols), together with an additional model (violet dot) with a "large" initial volume and strongly increased temperature-dependence of viscosity (see Supplementary Fig. 2.9) shortly after arrival at the lithosphere, showing a similar behaviour to the preferred model.

Bibliography

Anderson, D. L. (2000). "The thermal state of the upper mantle; no role for mantle plumes". *Geophysical Research Letters* 27 (22): 3623–3626.

Aoki, I. and E. Takahashi (2004). "Density of MORB eclogite in the upper mantle". *Physics of the Earth and Planetary Interiors* 143: 129–143.

Ballmer, M. D. et al. (2013). "Double layering of a thermochemical plume in the upper mantle beneath Hawaii". *Earth and Planetary Science Letters* 376: 155–164.

Boschi, L, T. W. Becker, and B. Steinberger (2008). "On the statistical significance of correlations between synthetic mantle plumes and tomographic models". *Physics of the Earth and Planetary Interiors* 167 (3): 230–238.

Bunge, H.-P. (2005). "Low plume excess temperature and high core heat flux inferred from non-adiabatic geotherms in internally heated mantle circulation models". *Physics of the Earth and Planetary Interiors* 153 (1): 3–10.

Burke, K. et al. (2008). "Plume generation zones at the margins of large low shear velocity provinces on the core–mantle boundary". *Earth and Planetary Science Letters* 265 (1): 49–60.

Campbell, I. H. and R. W. Griffiths (1990). "Implications of mantle plume structure for the evolution of flood basalts". *Earth and Planetary Science Letters* 99 (1): 79–93.

Christensen, U. R. and A. W. Hofmann (1994). "Segregation of subducted oceanic crust in the convecting mantle". *Journal of Geophysical Research* 99: 19–867.

Czamanske, G. K. et al. (1998). "Demise of the Siberian plume: paleogeographic and paleotectonic reconstruction from the prevolcanic and volcanic record, north-central Siberia". *International Geology Review* 40 (2): 95–115.

Deschamps, F., E. Kaminski, and P. J. Tackley (2011). "A deep mantle origin for the primitive signature of ocean island basalt". *Nature Geoscience* 4 (12): 879–882.

Farnetani, C. and H Samuel (2005). "Beyond the thermal plume paradigm". *Geophysical Research Letters* 32 (7).

Farnetani, C. G. and M. A. Richards (1994). "Numerical investigations of the mantle plume initiation model for flood basalt events". *Journal of Geophysical Research* 99: 13–813.

Foulger, G. R. (2011). *Plates vs Plumes: a geological controversy*. John Wiley & Sons.

Hales, T. C. et al. (2005). "A lithospheric instability origin for Columbia River flood basalts and Wallowa Mountains uplift in northeast Oregon". *Nature* 438 (7069): 842–845.

Herzberg, C. and E. Gazel (2009). "Petrological evidence for secular cooling in mantle plumes". *Nature* 458 (7238): 619–622.

Hirose, K. et al. (2005). "Phase transition and density of subducted MORB crust in the lower mantle". *Earth and Planetary Science Letters* 237 (1): 239–251.

Hofmann, A. W. and W. M. White (1982). "Mantle plumes from ancient oceanic crust". *Earth and Planetary Science Letters* 57 (2): 421–436.

Jellinek, A. M. and M. Manga (2004). "Links between long-lived hot spots, mantle plumes, D", and plate tectonics". *Reviews of Geophysics* 42 (3).

Kumagai, I. et al. (2008). "Mantle plumes: thin, fat, successful, or failing? Constraints to explain hot spot volcanism through time and space". *Geophysical Research Letters* 35 (16).

Leng, W. and S. Zhong (2008). "Viscous heating, adiabatic heating and energetic consistency in compressible mantle convection". *Geophysical Journal International* 173 (2): 693–702.

Leng, W. and S. Zhong (2010). "Surface subsidence caused by mantle plumes and volcanic loading in large igneous provinces". *Earth and Planetary Science Letters* 291 (1): 207–214.

Li, M., A. K. McNamara, and E. J. Garnero (2014). "Chemical complexity of hotspots caused by cycling oceanic crust through mantle reservoirs". *Nature Geoscience* 7 (5): 366–370.

Lin, S.-C. and P. E. van Keken (2005). "Multiple volcanic episodes of flood basalts caused by thermochemical mantle plumes". *Nature* 436 (7048): 250–252.

Lin, S.-C. and P. E. van Keken (2006a). "Dynamics of thermochemical plumes: 1. Plume formation and entrainment of a dense layer". *Geochemistry, Geophysics, Geosystems* 7 (2).

Lin, S.-C. and P. E. van Keken (2006b). "Dynamics of thermochemical plumes: 2. Complexity of plume structures and its implications for mapping mantle plumes". *Geochemistry, Geophysics, Geosystems* 7 (3).

Litasov, K. D. and E. Ohtani (2005). "Phase relations in hydrous MORB at 18–28GPa: implications for heterogeneity of the lower mantle". *Physics of the Earth and Planetary Interiors* 150 (4): 239–263.

McNamara, A. K. and S. Zhong (2004). "Thermochemical structures within a spherical mantle: superplumes or piles?" *Journal of Geophysical Research: Solid Earth (1978–2012)* 109 (B7).

Montelli, R. et al. (2004). "Finite-frequency tomography reveals a variety of plumes in the mantle". *Science* 303 (5656): 338–343.

Peate, I., M. Larsen, and C. Lesher (2003). "The transition from sedimentation to flood volcanism in the Kangerlussuaq Basin, East Greenland: basaltic pyroclastic volcanism during initial Palaeogene continental break-up". *Journal of the Geological Society* 160 (5): 759–772.

Richards, M. A., R. A. Duncan, and V. E. Courtillot (1989). "Flood basalts and hot-spot tracks: plume heads and tails". *Science* 246 (4926): 103–107.

Samuel, H. and D. Bercovici (2006). "Oscillating and stagnating plumes in the Earth's lower mantle". *Earth and Planetary Science Letters* 248 (1): 90–105.

Sobolev, A. V. et al. (2005). "An olivine-free mantle source of Hawaiian shield basalts". *Nature* 434 (7033): 590–597.

Sobolev, A. V. et al. (2007). "The amount of recycled crust in sources of mantle-derived melts". *Science* 316 (5823): 412–417.

Sobolev, S. V. et al. (2011). "Linking mantle plumes, large igneous provinces and environmental catastrophes". *Nature* 477 (7364): 312–316.

Solomatov, V. S., P. Olson, and D. J. Stevenson (1993). "Entrainment from a bed of particles by thermal convection". *Earth and planetary science letters* 120 (3): 387–393.

Steinberger, B. (2000). "Plumes in a convecting mantle – Models and observations for individual hotspots". *Journal of Geophysical Research* 105 (B5): 11–127.

Steinberger, B. and A. R. Calderwood (2006). "Models of large-scale viscous flow in the Earth's mantle with constraints from mineral physics and surface observations". *Geophysical Journal International* 167 (3): 1461–1481.

Sun, Y. et al. (2010). "Dating the onset and nature of the Middle Permian Emeishan large igneous province eruptions in SW China using conodont biostratigraphy and its bearing on mantle plume uplift models". *Lithos* 119 (1): 20–33.

Tackley, P. J. (2007). "7. Mantle dynamics". *Treatise on geophysics*. Edited by D. Bercovici and G. Schubert. New York: Elsevier.

Tan, E. and M. Gurnis (2007). "Compressible thermochemical convection and application to lower mantle structures". *Journal of Geophysical Research: Solid Earth (1978–2012)* 112 (B6).

van Keken, P. E., E. H. Hauri, and C. J. Ballentine (2002). "Mantle mixing: the generation, preservation, and destruction of chemical heterogeneity". *Annual Review of Earth and Planetary Sciences* 30 (1): 493–525.

White, R. and D. McKenzie (1989). "Magmatism at rift zones: the generation of volcanic continental margins and flood basalts". *Journal of Geophysical Research: Solid Earth (1978–2012)* 94 (B6): 7685–7729.

Wolfe, C. J. et al. (2009). "Mantle shear-wave velocity structure beneath the Hawaiian hot spot". *science* 326 (5958): 1388–1390.

Zhong, S. and B. H. Hager (2003). "Entrainment of a dense layer by thermal plumes". *Geophysical Journal International* 154 (3): 666–676.

Chapter 3

Major influence of plume-ridge interaction, lithosphere thickness variations and global mantle flow on hotspot volcanism

A version of this chapter is published as Gassmöller, R., Dannberg, J., Bredow, E., Steinberger, B. and Torsvik, T.H. (2015) Major influence of plume-ridge interaction, lithosphere thickness variations and global mantle flow on hotspot volcanism – the example of Tristan. Geochem. Geophys. Geosyst., 17, 1454–1479 | doi:10.1002/2015GC006177.

Abstract

Hotspot tracks are thought to originate when mantle plumes impinge moving plates. However, many observed cases close to mid-ocean ridges do not form a single age-progressive line, but vary in width, are separated into several volcanic chains, or are distributed over different plates. Here we study plume-ridge interaction at the example of the Tristan plume, which features all of these complexities. Additionally, the South Atlantic formed close to where plume volcanism began, opening from the south and progressing northwards with a notable decrease in magmatism across the Florianopolis Fracture Zone. We study the full evolution of the Tristan plume in a series of three-dimensional regional models created with the convection code ASPECT. We then compute crustal thickness maps and compare them to seismic profiles and the topography of the South Atlantic. We find that the separation of volcanism into the Tristan and Gough chain can be explained by the position of the plume relative to the ridge and the influence of the global flow field. Plume material below the off-ridge track can flow towards the ridge and regions of thinner lithosphere, where decompression melting leads to the development of a second volcanic chain resembling the Tristan and Gough hotspot tracks. Agreement with the observations is best for a small plume buoyancy flux of 500 kg/s or a low excess temperature of 150 K. The model explains the distribution of syn-rift magmatism by hot plume material that flows into the rift and increases melt generation.

3.1 Motivation

Around 175 million years ago, the southern supercontinent Gondwana, which had existed since Late Precambrian times but amalgamated forming Pangea in the Carboniferous (Torsvik and Cocks, 2013), first split into West (including Africa and South America) and East Gondwana. In Late Jurassic-Early Cretaceous times the parts that eventually became Africa and South America started rifting apart, followed by the opening of the South Atlantic around 130 million years ago. How, in broad terms, this process occurred kinematically, is relatively well-known. Already Wegener (1915) reconstructed continents relative to each other in a way rather similar to modern-day reconstructions such as Torsvik et al. (2009) and Torsvik et al. (2010), which are much better constrained through time mainly based on seafloor magnetic anomalies and fracture zones (Müller et al., 2008). The early opening history of the South Atlantic, however, is convoluted by the fact that there are no magnetic anomalies between approximately 121 and 84 million years ago (the Cretaceous Normal Superchron, see Figure 3.1).

Yet the role of mantle plumes during continental breakup remains controversial. In the South Atlantic, in particular the Tristan plume may have played an important role. Many of the features usually associated with mantle plumes are observed in this region: (1) Active intra-plate volcanism occurs on Tristan da Cunha and Gough Island. (2) The Walvis Ridge is a chain of seamounts thought to be generated as volcanic "hotspot track" as the African plate moves over the plume upwelling (Morgan, 1971). (3) Volcanism along the track is age-progressive, with ages getting older further away from the hotspot – see O'Connor and Duncan (1990), O'Connor and Roex (1992), and Rohde et al. (2013) and references cited therein. Geometry and age progression of the track fits with a global model of plate motions over hotspots that are either fixed (Morgan, 1971) or slowly moving (Doubrovine et al., 2012). (4) Apart from the narrow volcanic tracks, there is also a wider topographic swell (Davies, 1988; Sleep, 1990). (5) There is a geochemical anomaly along the nearby ridge (Schilling, 1991). (6) The Paraná-Etendeka flood basalts, a Large Igneous Province (LIP), is thought to represent the eruption of the initial plume head (Richards et al., 1989). Moreover, both the reconstructed location where the Paraná-Etendeka flood basalts initially erupted, and the current hotspot location directly overlie the margin of the African Large-Low-Shear Velocity Province (LLSVP), a likely zone for the generation of plumes in the deepest mantle (Torsvik et al., 2006).

However, the interpretation of observations in terms of the mantle plume model is complicated in particular due to the close proximity of plume and ridge through much of their history. As proposed long ago by Morgan (1978), plumes can interact with ridges in their vicinity: Volcanism may often not (only) occur directly above the plume, rather plume material may flow at the base of the lithosphere towards regions of thinner lithosphere – a process coined "upside-down drainage" (Sleep, 1997). Moreover, plume material may be sucked towards plate boundaries with negative dynamic pressures, resulting from divergent plate motion (such as the mid-oceanic ridge, but also the transtensional Paraná-Etendeka fault zone). Both mechanisms can lead to additional decompression melting and eruptions at the ridge, and could be responsible for the fact that there are roughly parallel volcanic tracks. The one ending at Tristan da Cunha would then correspond to volcanism at or near the ridge, and the one ending at Gough Island would be due to eruptions directly above the plume. Since the onset of continental rifting predates the onset of flood basalt volcanism (de Assis Janasi et al., 2011), the mantle plume cannot have been the cause of rifting. Yet the generation of ocean floor in the South Atlantic only began after the plume head eruption. Therefore, it is possible that the extension of continents concentrates above mantle plumes, which thus may assist in continental breakup (Buiter, 2014;

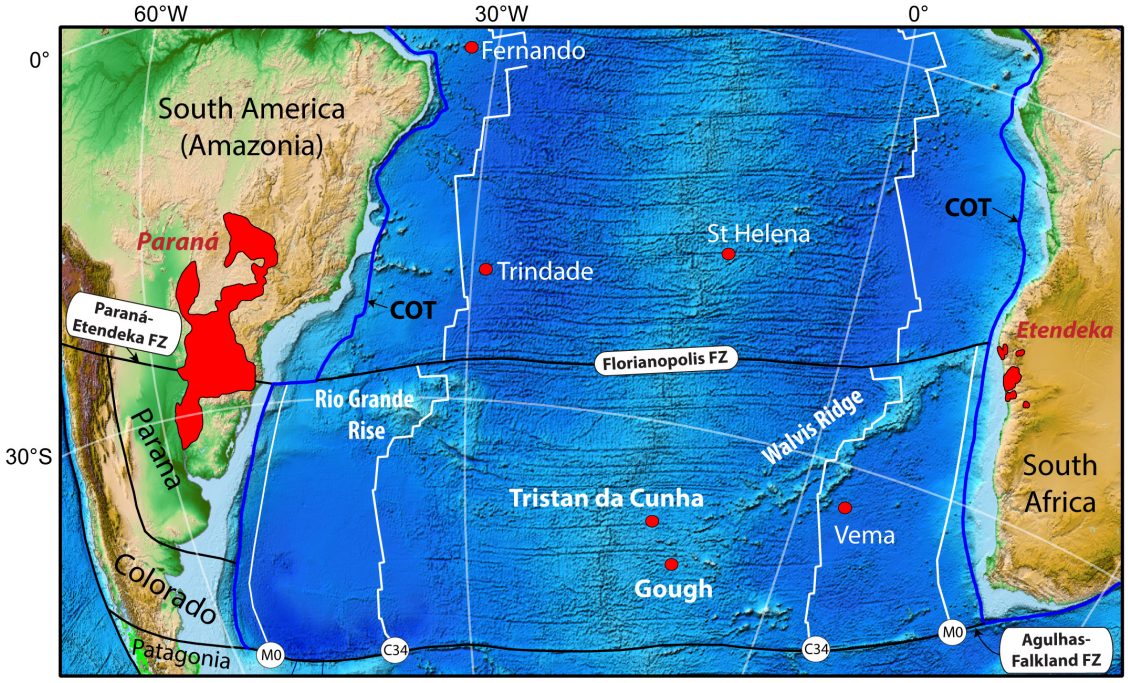

Figure 3.1: Simplified map of the South Atlantic Ocean draped on ETOPO1. The Florianopolis and Agulhas-Falkland Fracture Zones (FZ) are highlighted along with isochrons M0 (c. 121 Ma) and C34 (c. 84 Ma), and we also show some active hotspots and the Paraná-Etendeka large igneous province in Brazil and Namibia. South America is divided into four blocks and the Paraná-Etendeka Fault Zone (active until 126.9 Ma in the model of Torsvik et al. (2009)) separates Amazonia from Paraná and Colorado. Colorado and Patagonia were juxtaposed at about 132 Ma but the bulk of dextral strike-slip faulting ceased at around 160 Ma. COT, Continent Ocean Transition Zone.

Burov and Gerya, 2014).

Recent results have provided more details on volcanics and crustal structure, and their relation to the opening of the South Atlantic and the Tristan plume (also called Tristan-Gough plume): Heit et al. (2015) show that seismic anomalies on the Namibian margin, when interpreted as magmatic underplating, indicate that plume influence was more limited than would be expected if a large plume head impinged the African plate. Similarly, results of deep crustal seismic sounding (Ryberg et al., 2015) suggest a locally confined influence of the plume head affected by pre-existing lithosphere structure. Fromm et al. (2015) show large crustal thickness variations across the Florianopolis Fracture Zone along the Namibia continental margin. O'Connor and Jokat (2015b) discuss how separated segments of age-progressive intraplate volcanics may be related to a single plume. O'Connor and Jokat (2015a) propose that new age dates from ocean drill sites across the Central Walvis Ridge can be explained by interaction of that plume and the South Atlantic Ridge. While theoretical studies indicate that a single plume could be responsible for some of these structures (Sleep, 2002), it is still not clear if and how plume-ridge interaction can explain these observations dynamically.

In order to improve our understanding of these results and the role of the Tristan plume in the context of plume-ridge interaction, we have devised a numerical convection model. This model is not fully dynamic in that a given plate reconstruction is applied as surface boundary condition. We follow an approach previously taken by Mihalffy et al. (2008) for the Iceland plume, setting up a high-resolution box model with boundary conditions obtained from a coarser global model. In particular, the large-scale flow field and the plume position are obtained from a global flow model, which infers its present-day temperature from seismic tomography and is then advected backwards in time. We study the flow of the hot plume material in interaction with the mid-ocean ridge in the regional model and where high temperatures lead to melting and excess crustal production. Finally, we compare our model results with observed locations of volcanism, and by varying important model parameters, such as plume bouyancy flux, lithosphere thickness and the initial plume location, we aim at obtaining an improved agreement. In this way, we can assess whether the plume model is suitable at all to explain the observed distribution of volcanism and crustal thickness, and if so, for which parameters.

3.2 Model setup

3.2.1 Boundary and initial conditions

The model domain is a three-dimensional Cartesian box as shown in Figure 3.2. It comprises the upper mantle and transition zone in vertical direction and extends 3300 km × 3300 km horizontally. The initial conditions correspond to the setting of the South Atlantic 140 million years ago, before the breakup of South America and Africa and approximately 5–10 Ma before the creation of the Paraná-Etendeka flood basalts associated with the arrival of the Tristan plume head at the base of the lithosphere. The initial mantle temperature equals an adiabatic profile with a potential temperature of 1613 K. A cold top boundary layer represents continental lithosphere with a temperature of 273 K at the surface, and a half-space cooling age of 60 Ma. For the material parameters discussed in Section 3.2.3 this results in a depth of approximately 130 km for the 1613 K isotherm – an estimate for the initial lithospheric thickness of our model. Throughout the model evolution (from 140 Ma ago to present day), the temperatures and velocities are prescribed at all boundaries to allow the incorporation of constraints from observations and previous modelling studies. The large-scale flow field on all sides and the bottom of the box is

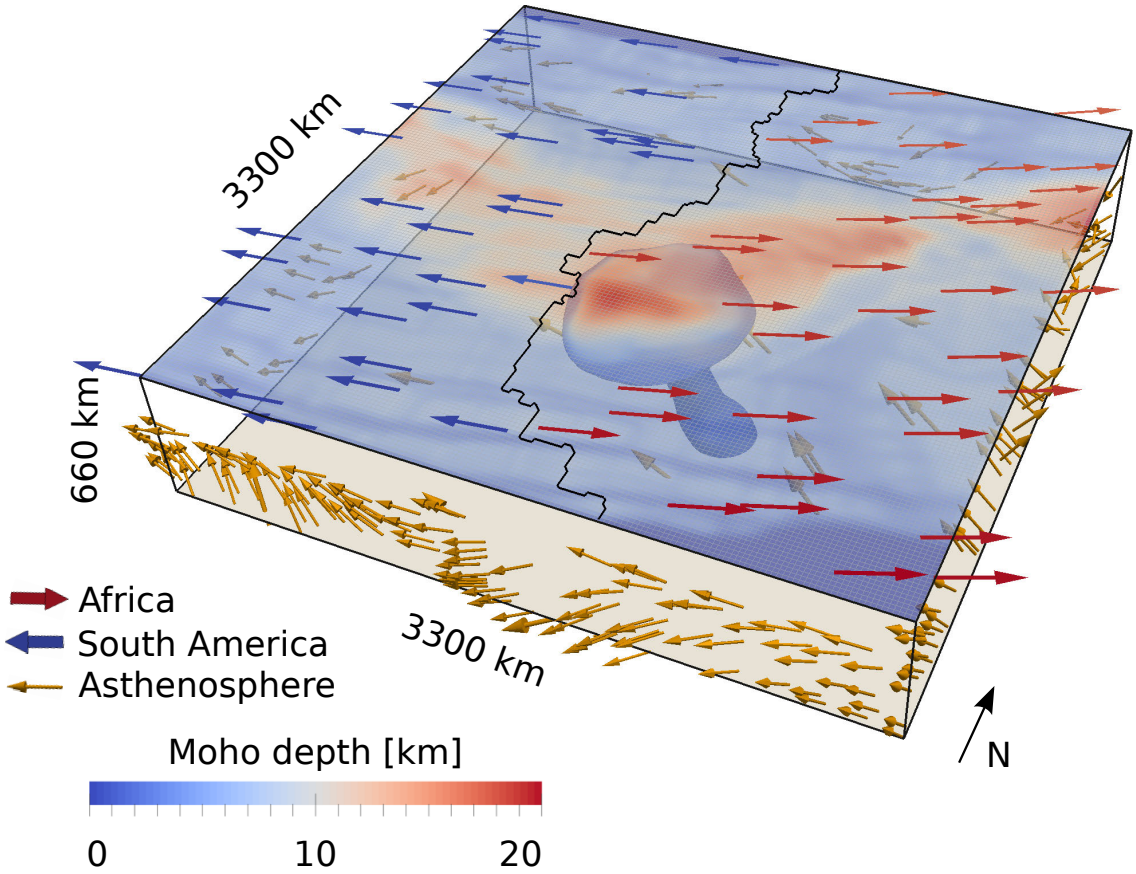

Figure 3.2: Geometry and velocity boundary conditions of the presented convection model. Red and blue arrows denote the prescribed plate motions at the top. Side boundary velocities within the lithosphere are identical to the plate motions, and asthenosphere boundary velocities at the sides and the bottom (yellow arrows) are taken from a global mantle convection model. The transition between plate and asthenospheric velocities is smoothed by an hyperbolic tangent interpolation function. An additional plume inflow is enforced at the bottom boundary.

obtained from a global flow model described in Section 3.2.2 and Supplementary Text S1. We note that in contrast to e.g. Tan et al. (2006) this is a one-way coupling and there is no feedback from the regional to the global model. Moreover, we use a plate reconstruction described in Section 3.2.2 and Supplementary Text S2 to prescribe the plate velocities at the top. We interpolate between these two boundary velocities at the sides of the model to form a gradual transition at the lithosphere–asthenosphere boundary in a depth of approximately 200 km, using a hyperbolic tangent interpolation function. Additionally, the influx of the plume at the bottom of the box is prescribed. At 135 Ma, a spherical temperature perturbation of 300 K and with a radius of 250 km is flowing in, simulating the plume head arriving from the lower mantle. A plume inflow at 135 Ma corresponds to an eruption age of 132 Ma (Doubrovine et al., 2012), but the initial starting age of the LIP could also be a few million years older (Gibson et al., 2006; Thiede and Vasconcelos, 2010; de Assis Janasi et al., 2011). The size is consistent with the LIP volume (Richards et al., 1989; Gladczenko et al., 1997; Peate, 1997; Courtillot et al., 1999), estimates of eruptives vs. total melts (Bryan and Ernst, 2008) and degrees of melting in plume heads (Katz et al., 2003), as well as numerical models (Lin and van Keken, 2006). After the arrival of the plume head, a fixed influx of material following a Gaussian distribution with a maximum velocity of 5 cm/yr, a maximum excess temperature of 200 K and a radius of 130 km is added to the global flow velocity, maintaining a stable plume tail. We choose the colder inflow temperature for the plume tail compared to the plume head to be consistent with observations (Herzberg and Gazel, 2009). These parameters result in a plume buoyancy flux of approximately 1000 kg/s, which is in agreement with estimates for the Tristan hotspot as discussed in Section 3.2.4. An important consequence of adding the plume velocity to the global flow field is that the effective plume buoyancy flux is changing over time. For the reference model this results in an effective flow between 900 and 1250 kg/s.

The plume position is obtained from the global model, which computes the distortion of a plume tail by a combination of buoyant ascent and global mantle flow. This global hotspot motion model is described in Supplementary Text S1. However, the hotspot motion model only provides the location where plume material arrives at the base of the lithosphere and not the inflow position in the regional model. Hence, the position of the inflow of plume material at the bottom of the regional model has to be chosen differently for every individual model. We compute this influx position by iterating the regional model with updated inflow positions and comparing plume arrival below the lithosphere to the global hotspot motion model until they are within a distance of less than 500 km of each other. In general, this required up to three iterations of the model. The temperature at the side and bottom boundaries follows an adiabatic profile with a top thermal boundary layer equivalent to an age of 60 million years, roughly corresponding to the present-day age of the sea floor at the positions of the model boundaries. The temperature at the top is fixed to 273 K.

As our velocity boundary conditions are derived from different sources (i.e. plate reconstruction and global convection model), but are integrated into a single model, it is not guaranteed that the overall in- and outflow of mass is balanced, which would violate the continuity equation. For the purpose of making the equations solvable numerically, this can be fixed by applying a compatibility modification to the right-hand side of Equation 4.5: Adding a small constant value to the compressibility, which has the effect of allowing material to be compressed more (or less) for the same pressures, leads to a different net velocity divergence inside of the model. This approach is useful if the net mass in-/outflow (and hence the correction) is small, but will otherwise result in a non-physical solution. Therefore, an iterative mass flux correction has been applied to all model con-

figurations by computing a first model run with the original velocity boundary condition and then modifying the boundary flux by the integrated in-/outflow for each timestep in a second model iteration. We distributed the correction equally over the asthenosphere and only over the western and eastern boundary – the preferred orientation of flow in the South Atlantic. In all presented models the correction is usually small – less than 0.5 cm/yr.

3.2.2 Plate reconstructions and large-scale mantle flow

As discussed above, we prescribe plate motions as surface boundary conditions in our models, employing plate reconstructions that are derived and discussed in Torsvik et al. (2009). Between 140 and 126.9 Ma (120 Ma in our simplified reconstruction, where the plate velocities are kept constant for 10 Ma intervals) there are four separate plates (Figure 3.3): Africa, South America (originally dubbed Amazonia before 126.9 Ma in Torsvik et al. (2009)), Parana and Colorado. Relative, divergent motion between the African and Parana plate is faster than between the African and South American plate. Since extension is symmetric relative to this plate boundary (the future Mid-Atlantic Ridge), the different extension rates imply that an initially straight plate boundary between African plate (east of the boundary), South American plate (west of the boundary in the north), and Parana plate (west of the boundary further south) develops a transform fault east of the triple junction.

This transform fault corresponds to the offshore Florianopolis Fracture Zone, which continues onshore as Paraná-Etendeka Fault Zone (PEFZ, Torsvik et al., 2009). In their study, the PEFZ was modelled as a transtensional boundary with a lateral offset of about 175 km. Dextral movements ceased at about 126 Ma and this transtensional zone may have provided upside-down drainage of the Tristan plume explaining the large extent of Paraná volcanism compared to that of Etendeka in Namibia. There is no consensus – from either the surface geology or geophysics data – on the exact localization of intraplate deformation in the South American continent, but the PEFZ is recognized in the free air residual gravity field (e.g. from the GOCE satellite) and in crustal and lithospheric thickness maps (Braitenberg, 2015; Assumpção et al., 2013; Chulick et al., 2013).

Another consequence of the different spreading rates is that at 120 Ma, sea floor spreading and the creation of an ocean basin had already begun south of the transform fault, between the African and Parana (and Colorado) plates, while to the north, the plate boundary between the African and South American plate was still in the stage of continental rifting (Müller et al., 2008). Relative motion of the Colorado/Patagonia plates, further to the southwest, is even slightly faster. However, due to the larger distance, this has little effect on the Tristan plume. Accordingly, our numerical model does not distinguish between the Colorado and Patagonia plates. A detailed description of our regional model of plate motions, and how the transformation from spherical to Cartesian coordinates is done, is given in Supplementary Text S2.

The large-scale flow field model used as boundary condition was updated from the one used in Doubrovine et al. (2012) as described in Supplementary Text S1. Cross sections and map views at 1 Ma and 95 Ma are shown in Figure 3.4: There is upward flow above the African LLSVP and downward flow related to subduction beneath South America. These are two limbs of a large-scale convection cell, and consequently, in our region of interest flow is predominantly westward with speeds of several cm/yr, from the upwelling towards the downwelling. Comparison of the two time intervals shows considerably weaker flow for the earlier time interval: This is an artifact caused by the backward-advection procedure, which leads to an increasing stratification with positive density anomalies near the upper

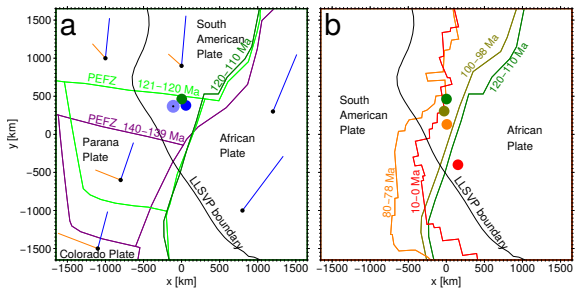

Figure 3.3: Plate reconstructions updated from Torsvik et al. (2010) used as boundary conditions for the geodynamic model for the time periods (a) 140–110 Ma and (b) 110 Ma to present-day. (a) Purple line: Plate boundaries at 140–139 Ma when relative plate motions began. Bright green line: Extrapolated plate boundaries at 121–120 Ma, the final reconstruction with four plates. Dark green line: Plate boundary at 120–110 Ma. The total motion between 140–120 Ma at selected points on each plate is shown as blue lines, motion relative to the African plate as orange lines. PEFZ = Paraná-Etendeka Fault Zone that became the Florianopolis-Fracture Zone (FFZ) offshore. Also shown are the initial plume location at 132 Ma (blue disk) and the plume location at 120 Ma (green disk). For comparison, the bright blue circle with dot marks the reconstructed eruption center of Torsvik et al. (2006) for the Paraná-Etendeka Large Igneous Province in the reconstruction of Doubrovine et al. (2012). However, Paraná flood basalts erupted over a large area on both sides of the PEFZ. The black line marks the boundary of the African LLSVP (1% margin in the SMEAN tomography model (Becker and Boschi, 2002) at depth 2800 km). (b) Plate boundaries at 120–110 Ma (green line), 100–98 Ma (olive green line), 80–78 Ma (orange line) and 10–0 Ma (red line). Plume positions at the times 120 Ma, 100 Ma, 80 Ma and present-day are indicated by green, olive green, orange and red disks.

boundary layer and negative ones near the lower one further back in time.

3.2.3 Numerical implementation

We use the mantle convection code ASPECT (Kronbichler et al., 2012; Bangerth, Heister, et al., 2015) that models thermo-chemical convection in high Rayleigh number flow with adaptive mesh refinement. It solves the equations for the conservation of mass, momentum and energy. Our models include adiabatic heating, shear heating, latent heat, and take into account mantle compressibility in the limit of the Anelastic Liquid Approximation. Specifically, we consider the following set of equations for velocity $\mathbf{u}$, pressure p and temperature T:

$$-\nabla \cdot \left[2\eta\left(\dot{\varepsilon}(\mathbf{u}) - \frac{1}{3}(\nabla \cdot \mathbf{u})\mathbf{1}\right)\right] + \nabla p = \rho \mathbf{g}, \tag{3.1}$$

$$\nabla \cdot (\rho \mathbf{u}) = 0, \tag{3.2}$$

$$\rho C_p \left(\frac{\partial T}{\partial t} + \mathbf{u} \cdot \nabla T\right) - \nabla \cdot k \nabla T = 2\eta\,(\dot{\varepsilon}_s : \dot{\varepsilon}_s) + \alpha T\,(\mathbf{u} \cdot \nabla p) + \rho T \Delta S \frac{DF}{Dt}, \tag{3.3}$$

where η is the viscosity, $\dot{\varepsilon}(\mathbf{u}) = \frac{1}{2}(\nabla \mathbf{u} + \nabla \mathbf{u}^T)$ is the strain rate, ρ is the density, $\mathbf{g}$ is the gravity, C_p is the specific heat capacity, t is time, k is thermal conductivity, $\dot{\varepsilon}_s = \dot{\varepsilon}(\mathbf{u}) - \frac{1}{3}(\nabla \cdot \mathbf{u})\mathbf{1}$ is the shear strain rate, α is the thermal expansivity, ΔS is the entropy change across the solid-melt phase transition for peridotite and F is the melting function.

The radial structure of the viscosity $\eta(z, T)$ in the box (Steinberger and Calderwood, 2006) is the same as was used to compute the large-scale mantle flow field used as a

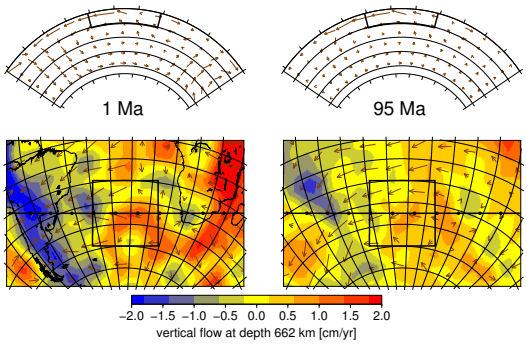

Figure 3.4: Cross sections (top) and map views (bottom) of the large-scale flow field used as boundary condition for the study area of the high-resolution box model (outlined in black) for times 1 Ma before present (left) and 95 Ma before present (right). An arrow length of 10 degrees of an arc (at surface in cross sections) is 5 cm/yr, i.e. the length of arrows corresponds to the total amount of displacement in 22.2 Ma (if flow speed was constant). Cross sections are along the profiles in the map below. In the map views, vertical flow (background colors) is shown at the bottom of the box region (depth 662 km), horizontal flow (arrows) at the transition depth between lithospheric and asthenospheric velocities (212 km).

boundary condition, but additionally lateral variations – derived from the same temperature dependence of viscosity that was used to compute the radial variations – are considered:

$$\eta(z,T) = \eta_r(z) \exp\left(-\frac{H(z)(T - T_{\text{adi}}(z))}{nRTT_{\text{adi}}(z)}\right). \tag{3.4}$$

Here, $H(z)$ corresponds to a depth-dependent activation enthalpy of the temperature dependence of viscosity as described in Steinberger and Calderwood (2006) and ranges from 500 kJ/mol to 700 kJ/mol; n denotes the stress exponent and is set to 3 for the upper mantle, and R is the gas constant. $T_{adi}(z)$ denotes the adiabatic temperature profile. This formulation results in a viscosity change of approximately a factor of two over a temperature range of 100 K or a factor of four between plume material and surrounding asthenosphere for typical upper mantle temperatures (see Supplementary Figure S1 for representative maps and profiles). Because the temperature dependence already introduces a high-viscosity boundary layer at the top, we modified the radial viscosity profile $\eta_r(z)$ to be constant upwards of 200 km depth.

The other material parameters, or more specifically, the density ρ, specific heat C_p, and thermal expansivity α are computed as a function of depth and temperature using the thermodynamic calculation package Perple_X (Connolly, 2005), a published database for mineral properties (Stixrude and Lithgow-Bertelloni, 2011), and assuming a pyrolitic composition (Ringwood and Irifune, 1988). The thermal conductivity k is assumed to be constant at 4.7 W/mK.

We employ a melting parametrization for equilibrium batch melting of anhydrous peridotite (Katz et al., 2003) to compute how much melt is generated in dependence of temperature and pressure during the model evolution. As this melting function $F(p,T)$ considers the change in productivity after the exhaustion of clinopyroxene, it is kinked. The transition from the solid to the melt phase is incorporated in the energy equation as a heat consuming process in the following way:

$$\Delta S \frac{DF}{Dt} = \Delta S \frac{\partial F}{\partial T}\left(\frac{\partial T}{\partial t} + \mathbf{u}\cdot\nabla T\right) + \Delta S \frac{\partial F}{\partial p}\mathbf{u}\cdot\nabla p, \tag{3.5}$$

where the variables are named as described above. The temperature and pressure derivatives of the melting function $\partial F/\partial T$ and $\partial F/\partial p$ are computed analytically. As melting of mantle rock consumes energy, this leads to a colder mantle adiabat than without the consideration of latent heat effects. For a more detailed derivation of the equations we refer the reader to the ASPECT manual (Bangerth, Heister, et al., 2015).

We then use two different methods to track where the melt moves in our model and compute maps of crustal thickness: (1) Melt is passively advected with the mantle flow as a field $F_{\max}$, the maximum degree of melting in every point:

$$\frac{\partial F_{\max}}{\partial t} + \mathbf{u} \cdot \nabla F_{\max} = Q \tag{3.6}$$

$$\text{with } Q = \begin{cases} 0 & \text{if } F(p,T) \leq F_{\max} \\ (F - F_{\max})/\Delta t & \text{if } F(p,T) > F_{\max} \end{cases}$$

The crustal thickness at every point in time is calculated by vertically integrating this quantity from the surface up to a depth of 200 km. (2) Alternatively, generated melt is extracted instantly, added up to yield a crustal thickness and advected with the prescribed plate motions at the top of the model. We emphasize that both methods are implemented as purely passive postprocessing steps. Except for the consumption and release of latent heat upon melting and refreezing of melt, the equations 4.5, 3.2, and 4.21 remain unaffected by the melting process. Both techniques are approximations and represent end-member regimes of how we imagine melt migration in the Earth: a combination of porous flow in the mantle and fast ascent through channels and dikes in the lithosphere (see also Supplementary Text S3). However, modelling two-phase flow in three dimensions and on long time scales is extremely challenging and outside the scope of this paper. Thus, we will show crustal thickness maps generated with both approximations and indicate which method was used in the respective figure captions.

We utilize ASPECT's adaptive mesh refinement to refine regions with high temperature gradients in the lithosphere and in the rising plume. Although we are mostly interested in the region close to the plume and the ridge, the passive advection approach for crustal thickness described above makes it necessary to refine the whole model domain above 200 km depth. The minimal mesh cell size is set to approximately 20 km, which would generate a mesh of $160 \times 160 \times 32$ elements for a uniform resolution, resulting in 34 million degrees of freedom. Adaptively reducing the resolution in the asthenosphere and transition zone outside of the plume region decreases this to 15 million degrees of freedom for the presented models. The use of quadratic finite elements for temperature and composition as well as second order velocity and first order pressure elements (Q2Q1) for the Stokes system allows for higher accuracy compared to the commonly used linear elements, and for a distance between quadrature points of around 10 km. The timespan of 140 Ma is divided into approximately 3100 BDF-2 timesteps (Second order backward differentiation formula, see Kronbichler et al., 2012), which are iteratively solved on average 2 times to account for nonlinearities in the equations (e.g. due to latent heat). This corresponds to 6200 solves of the coupled Stokes–advection system. An average model run on 768 Xeon E5-2860v3 cores at 2.5 GHz takes 16 hours and therefore consumes 12,500 core hours.

3.2.4 Variation of model parameters

We ran a series of models with different plume inflow positions, temperatures and buoyancy fluxes to investigate their respective influence on the evolution of the Tristan hotspot track, the distribution of associated melting events and the thickness of the generated

Model	Plume position	Inflow ΔT in K	Inflow velocity in cm yr^{-1}	Inflow radius in km	Buoyancy flux in kg s^{-1}
Reference	reference (see Figure 3.3)	200	5.0	130	950
East150	150 km east of reference at 132 Ma	200	5.0	130	950
East300	300 km east of reference at 132 Ma	200	5.0	130	950
ΔT150	reference	150	3.75	130	700
ΔT250	reference	250	6.25	130	1500
Flux500	reference	200	3.61	110	500
Flux1700	reference	200	6.66	150	1700
ThinLith	reference	200	5.0	130	950
ThickLith	reference	200	5.0	130	950
RealLithC1	reference	200	5.0	130	950
RealLithC2	reference	200	5.0	130	950
NoGlobalFlow	reference	200	5.0	130	950
NoPlume	–	–	–	–	0.0
RefShift	track towards Gough Island	200	5.0	130	950
Track2	Steinberger et al. (2004)	200	5.0	130	950
Track3	modified Steinberger et al. (2004)	200	5.0	130	950

Table 3.1: Model configurations. Excess temperature ΔT, inflow velocity v and inflow area $A = \pi R^2$ were varied to be consistent with Stokes' law for the rising/sinking velocity in a viscous medium: $\Delta T\, A\, v^{-1} = \text{const}$.

oceanic crust. For this purpose, we varied these model parameters within the bounds of the uncertainty of the relevant observations and reconstructions (see Table 3.1 for a list of model setups):

(1) The excess temperature of the plume tail at the bottom boundary of the model is varied between 150 K and 250 K, with 200 K being the value used in the reference model. As the plume ascends, it loses heat to the surroundings, so that the temperature upon melting is approximately 40 K lower than the maximum inflow temperature. Taking into account this cooling process, the chosen plume temperatures are consistent with estimates for excess temperatures of hotspots in general ($100 - 250$ K, Herzberg and Gazel (2009)) and the Tristan hotspot track in particular ($100 - 180$ K, Herzberg and Asimow (2008), Schilling (1991), and Putirka (2008)).

For varying model parameters between different model configurations, we have to make sure that we retain the consistency of the inflow velocity with the plume velocity inside of the model. Hence, we change the plume excess temperature ΔT, the inflow velocity v and the inflow area $A = \pi R^2$ together, such that $\Delta T\, A\, v^{-1} = \text{const}$. This equation follows from Stokes' law for the rising/sinking velocity of a sphere in a viscous medium.

(2) The setup adapted from Doubrovine et al. (2012) as described in Section 3.2.1 implies a plume buoyancy flux of approximately 1000 kg s^{-1} as estimated inflow from the lower mantle. However, these estimates vary and are not well constrained. Additionally, plume fluxes may be considerably larger, if plumes primarily feed into the asthenosphere as suggested by Morgan et al. (2013). In this case only a small fraction of the total anomalous mass flux is represented by the swell. Accordingly, we vary the plume flux in our model in the range of published estimates from 500 kg s^{-1} (Davies, 1988) to 1700 kg s^{-1} (Sleep, 1990). For this purpose – following the same principle as mentioned under (1) – we change the inflow area and velocity while keeping the plume temperature constant.

(3) Our computed hotspot motion model is described in Section 3.3.1. We use this as a reference case, but also move the position of the arriving plume from the lower mantle 150 km and 300 km to the east: The Doubrovine et al. (2012) reference frame only goes back to 124 Ma, before that there are no strong longitude constraints of plume position relative to the plates because of the large extent of flood basalts. A 300 km shift from 132 Ma to 124 Ma corresponds to ≈ 4 cm/yr additional eastward plate motion, which is not unreasonably fast. Additionally, we employ an alternative hotspot motion model based on Steinberger et al. (2004). This model also implies a different absolute plate motion reference frame, hence different plate boundary locations through time. However, here we do not modify plate boundary locations and instead modify the hotspot motion such that the relative location of hotspot and plate boundary remains the same. Lastly, variations of both this motion model and the reference model are tested, where the youngest part of the plume track is adjusted to end under Gough Island instead of the middle between Tristan and Gough Island.

(4) We varied the initial thickness of the lithosphere to test its influence on the spreading plume head and large igneous province generation. The variations range from a lithosphere half-space cooling age of 40 Ma to 100 Ma, resulting in 1613 K isotherm depths of 110 km to 160 km. In addition, we also used more realistic lithosphere models as described in Supplementary Text S4. These models prescribe a spatially variable lithospheric thickness, derived from the present-day lithosphere structure as seen in seismic tomography models, and then moved backwards in time using the plate reconstruction of our reference model.

(5) We evaluate the influence of the prescribed large-scale flow field on the plume shape and evolution by computing models with no in- and outflow of material (no-slip boundaries) except for the plume influx, the lithospheric plates and the correction to balance the net mass flux as described in Section 3.2.1. We then compare the results

of this model to our reference model with prescribed boundary velocities derived from a global mantle convection model. During this comparison we take into account that the global velocities lead to some additional plume buoyancy flux and therefore the effective averaged buoyancy flux in the model without global flow is lower by 200 kg/s compared to the reference model.

3.3 Results

3.3.1 The hotspot motion model: Geometrical relation of plume and ridge

Before discussing numerical model results, we describe the relative location of plume and ridge in terms of on-ridge and off-ridge track in order to get a first qualitative understanding of the effect of plume-ridge interaction on hotspot tracks.

As a first step we adopted the plume motion model of Doubrovine et al. (2012) as described in Supplementary Text S1. The modelled plume positions in the reference case for selected times are shown in Figure 3.3 together with the plate reconstruction. The initial plume head erupts beneath the South American (Amazonian) plate and near the Paraná-Etendeka Fault Zone (PEFZ). Due to northward plate motion and the opening of the South Atlantic the plume was located south of the transform fault that corresponds to the Florianopolis Fracture Zone after approximately 120 Ma. Subsequently, some time between 100 and 80 Ma, the plume was overridden by the ridge, and has been beneath the African plate since then.

Using this plume motion model and the plate reconstruction described in Section 3.2.2, we can generate a map illustrating ocean-floor ages and plume track geometry (Figure 3.5a). The latter is computed by projecting the predicted plume position to the surface and kinematically advecting it with the plate velocities to create a hotspot track. This also allows us to calculate the distance between the closest ridge segment and the plume-arrival position, making it possible to differentiate between on- and off-ridge tracks.

Technically, an off-ridge track can only occur with hotspot age younger than sea floor age (thick colored line). But one can imagine that the spreading ridge had been at a different location, such that the plume had been beneath the plate on the opposite side of the ridge. The imaginary off-ridge tracks that result from this thought experiment – with ages older than sea floor age (given the true ridge location) – are shown as thin colored lines and are still useful for estimating plume–ridge distance by comparing the colors of the off-ridge track and the background sea floor. If plume and ridge are sufficiently close to each other, volcanism may also occur on nearby ridge segments, leading to thickened crust on both sides of the ridge. The colored centers of the grey, roughly elliptical areas (called “extended on-ridge track” in Figure 3.5 top) mark the sea floor where the hotspot crossed from the South American to the African plate at 90 Ma. The part of the ocean floor generated within less than 300 km of the hotspot approximately corresponds to the Rio Grande Rise and the part of the Walvis ridge with most pronounced topography. After this time, the “on-ridge track” generated on the African plate at the ridge location closest to the hotspot resembles the northwesternmost chain of seamounts within the Walvis ridge. Figure 3.5 shows that our hotspot motion model does not always coincide with the observed volcanic chain. This already indicates that plume-ridge interaction must play a crucial role in determining the melt distribution – an effect we will quantify in the following sections about the dynamic models.

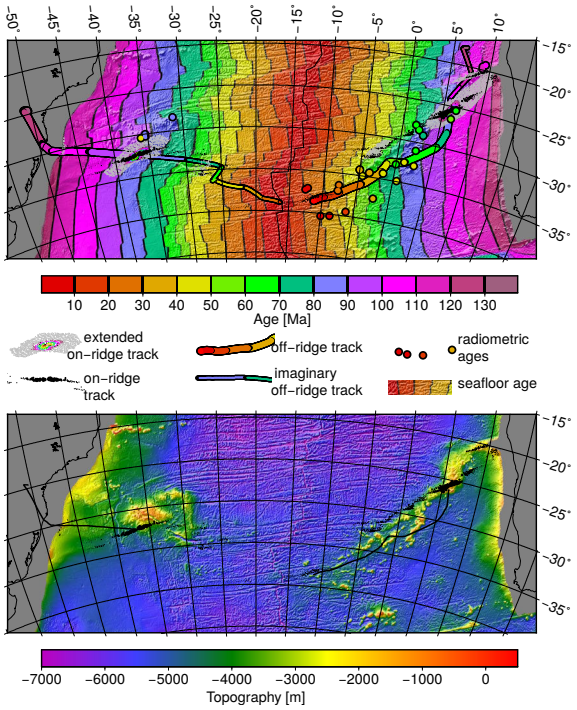

Figure 3.5: Top: Computed Tristan hotspot track for the model of Doubrovine et al. (2012) relative to the South American and the African plate. Also plotted on the same color scale is the ocean floor age grid of Müller et al. (2008) and a compilation of radiometric seamount ages from O'Connor and Duncan (1990), O'Connor and Roex (1992), Rohde et al. (2013), and O'Connor and Jokat (2015a) and references cited therein (circles). The thick colored line is the off-ridge track (classical hotspot track), thin colored lines are imaginary tracks computed from plate and hotspot motions (with ages older than sea floor age). Black dots show the "on-ridge track" (ocean floor generated on the ridge segment closest to the hotspot) if the distance is less than 500 km (dot size inversely proportional to distance if greater than 100 km and constant if less than 100 km) and colored dots surrounded by grey dots show the "extended on-ridge track" (all ocean floor generated at a distance of less than 300 km from the hotspot; colored dots if distance less than 140 km, same color scale for distance [km] as age [Ma]). Bottom: Topography, corrected for the ridge by subtracing 330 m $\cdot(\sqrt{\text{age[Ma]}} - 10)$ for sea floor ages less than 100 Ma for comparison (residual topography).

3.3.2 Time evolution

Large igneous province and opening of the rift

Our interpretation of the high-resolution geodynamic model of the South Atlantic region is structured into two main parts: We first describe the evolution of the reference model in detail, compare it to observations and analyze the occurring physical processes. The model evolution, including melting processes and generated crustal thickness, is shown in Supplementary Movie 1. In a second step we describe the effects of varying essential input parameters as outlined in Section 3.2.4.

We begin the evolution of the reference model at 140 Ma before present day (see also Supplementary Movie 1). The model starts with a uniform lithospheric thickness and prescribed divergent plate motions that thin the lithosphere at the plate boundary and later initiate the rifting. At 136.25 – 135 Ma we prescribe the influx of the plume head at the lower boundary of the model, which corresponds to the arrival of the Tristan plume head at the upper–lower mantle boundary. From there, the plume rises and approaches the base of the lithosphere of the South-American Plate, causing the first melt generation at 134 million years. As the plume head spreads laterally, the melt production increases, reaching a maximum crustal thickness of 4 km above the center of the plume with decreasing thickness towards the edges within 3 million years. The maximum diameter of the melting region is 900 km, which agrees well with estimated areal extensions of the Paraná-Etendeka LIP ($1.5 - 2 \cdot 10^6\,\mathrm{km}^2$, Richards et al., 1989; Peate, 1997; Courtillot et al., 1999).

At 131 Ma, the plume has generated a total melt volume of $10^6\mathrm{km}^3$. Considering that the intrusive or underplated magma volume can be up to 10 times larger than the associated extrusive volume (Bryan and Ernst, 2008), this volume is significantly lower than what is expected for the Paraná-Etendeka flood basalts ($1{\cdot}10^6\mathrm{km}^3 - 2.35{\cdot}10^6\mathrm{km}^3$, Richards et al., 1989; Gladczenko et al., 1997; Peate, 1997; Courtillot et al., 1999). The most plausible explanation for this deviation is that we do not consider thermo-magmatic erosion of the lithosphere in our models, which is known to lead to thinning of the lithosphere, increasing melt generation enormously (Sobolev et al., 2011). At 128 Ma, the plume head has generated the majority of its melt and it has cooled and dissipated a part of its heat so that the melt generation is restricted to three regions: (1) a narrow plume tail with a diameter of 100 km, (2) a 50 km thick ring of minor melting in the spreading outer regions of the plume head, where material is still upwelling and that only grows until 126 Ma and then fades until 121 Ma, and (3) the regions with thinner lithosphere southeast of the plume center where the rift begins to open.

Apart from the plume-influenced region around the FFZ, the first purely rift-related melts are generated at 128 Ma in the southernmost part of the rift, where it opens first. From there, the melting region propagates northwards until it reaches the Florianopolis Fracture Zone at 124 Ma. This opening process is strongly influenced by the plume head intruding into the rift around the FFZ and generating melt, which starts at 130 Ma and reaches its maximum melt production at 122 Ma, leading to a crustal thickness of up to 19 km. We emphasize that at this time the plume tail reaches the base of the lithosphere around 260 km northwest of the zone of maximum melt production and most of its material flows northwestward with the plate (only a small amount intrudes into the landward PEFZ). Therefore, the majority of the additional decompression melting in the rift is caused by the older but still hot plume head material that now ascends into the opening rift. The part of the rift north of the fracture zone opens later at 118 Ma, and is largely unaffected by the plume head material. In our model, the average oceanic crustal thickness

without plume influence amounts to 5 –7 km – depending on the spreading rate – which agrees well with observations in this region (Fromm et al., 2015).

Plume shape in dependence of its position relative to the ridge

While the plume tail is still reaching the surface west of the rift, it generates a hotspot track with a maximum crustal thickness of 21 km (up to ≈ 60 km plume-generated crust along a narrower track, if melts are tracked with plate motions; Figure 3.6), and the maximum melt fraction inside of the plume is approximately 28%. The melting region is influenced by the fast movement of the South American plate, shaping it to a fan elongated in the direction of the plate motion (Supplementary Movie 1, at 95 Ma). Once the plume reaches the rift at approximately 90 Ma, it is focused to a thin column and melting is concentrated at the ridge. In the following 10 Ma, the plume tail and the African plate move eastwards with approximately the same speed so that their positions relative to each other are unaffected. The melting region remains close to the ridge and broadens, leading to a high melt production and a calculated plume-generated crustal thickness even exceeding 100 km in a small area (Figure 3.6, 5° E, 27° S). Such thick crust is at odds with observations and we refer to Section 3.4 for a discussion of mechanisms that could reduce melt generation when the plume crosses the ridge. At 70 – 60 Ma, the plume tail starts to move south, and the African plate accelerates, with the South American plate also changing its absolute movement direction from westwards to eastwards. The associated change in the global flow field leads to a fast movement of the upper part of the plume away from the ridge, shaping it to a shallow, thin pancake with a maximum melt fraction of less than 15%, and a lower additional crustal thickness of less than 10 km. At 60 Ma, the African plate changes direction again, moving towards the southeast, and at 50 Ma also the South American plate begins to move westwards again. This draws the upper part of the plume back to the ridge, whereas between 40 and 30 Ma, when the African plate moves faster again, the plume straightens up again, changing its shape back to a columnar structure. This cycle is repeated as the plume accelerates southward relative to the plate between 30 and 10 Ma, slowly tilting towards the ridge again. It then remains more or less constant in place until present-day.

In general, thicker crust is produced when the global mantle flow favors a stable plume tail and melting region relative to the plate, while the plume forms a flat pancake and produces less additional crust while it moves relative to the plate. Additionally, a faster plate movement drags the plume away from the ridge, and therefore not only the lateral motion of the plume tail, but also the distance between plume track and ridge is correlated with the speed of the African plate. This distance, however, also controls the age and thickness of the overlying lithosphere. Hence, the amount of generated crust is anti-correlated with the distance between plume track and ridge (shown by the distance between off-ridge and on-ridge track in Figure 3.6). Regions where the plume reaches the lithosphere close to the ridge like 5° E, 4° W, and 10° W have much higher crustal thickness than regions with a larger distance at 0° and 7° W. For the full time evolution of the model we refer to Supplementary Movie 1 and a more detailed visualization of the crustal production in dependence of the distance to the ridge is shown in Supplementary Movie 2.

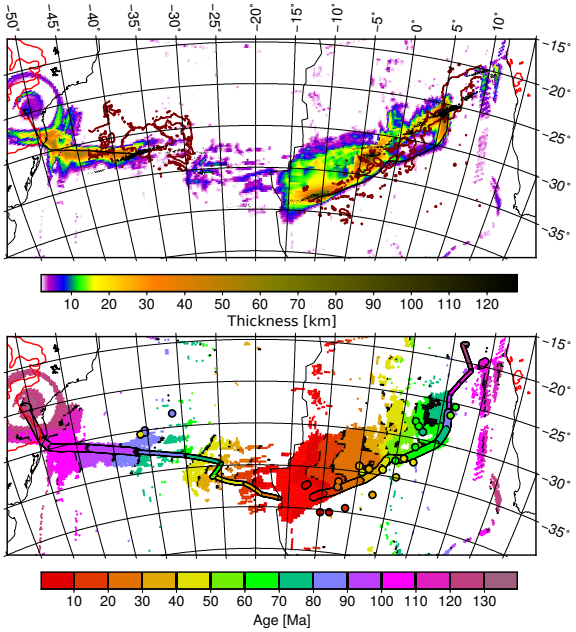

Figure 3.6: Top: Plume-generated crust in the reference model at the present-day state, computed as the difference between models with and without plume. Also shown are the assumed off-ridge track (continuous black line) and on-ridge track (dots, as in Figure 3.5, top) for comparison. The observed hotspot track is represented by dark red contours (often only appearing as isolated dots) of -3700 m ridge-corrected topography (as in Figure 3.5, bottom). LIP outlines are shown on land in bright red. Bottom: Age of the additional crust (youngest layer with thickness larger than 50 m generated in a 0.25 million year time interval). Thin and thick colored lines and colored dots are as in Figure 3.5 top. Both plots can be directly compared to Figure 3.5 and crustal thickness is tracked by instant melt extraction and advection with the plate velocities.

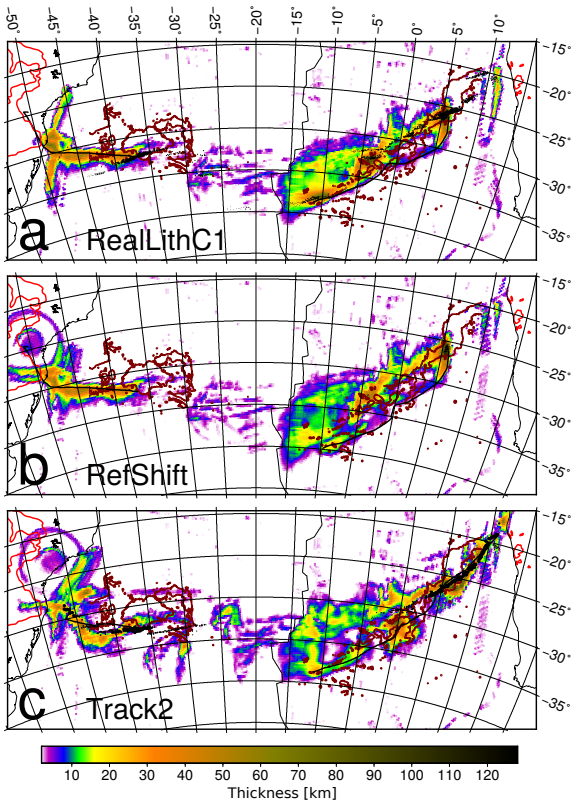

Figure 3.7: Plume generated crust (melt advected with plate motions) at the present-day state for the three model cases RealLithC1, RefShift and Track2. Other features shown as in Figure 3.6.

3.3.3 Present-day crustal thickness distribution and influence of hotspot motion model

From the model evolution described in Section 3.3.2 we compute crustal thickness and age maps by extracting all generated melt to the surface immediately and moving it with the plate velocities (Figure 3.6). We then compare the modelled crustal thickness to the residual topography of the South Atlantic region (Figure 3.5 bottom), assuming that the topography strongly correlates with the crustal thickness. We start with the oldest part of the hotspot track and progress in time towards the present day.

The general pattern of thickened crust in our model resembles observations in the South Atlantic. On the South-American margin, the position and age of the generated crust agrees with the observed hotspot track and the Rio Grande rise. After the plume jumps to the African side of the ridge, it generates several segments of the hotspot track with varying width and thickness, depending on the proximity to the ridge (black dots in Figure 3.6 top mark the on-ridge track of the hotspot) and speed of the African plate, as discussed in Section 3.3.2. Overall, these segments correspond to topographic features of the Walvis Ridge. Examples are the broad regions of thickened oceanic crust at the beginning of the track at 5° E and between 0 and 5° W, and the narrow segment at 0−5° E.

In the youngest part of the hotspot track our models show a steep slope from thickened crust to “normal” ocean floor towards the south, but a more gradual transition towards the north and west, where the mid-ocean ridge lies. The smooth transition is caused by the channelling of plume material that arrives at the base of the lithosphere towards the ridge, which leads not only to a lateral movement, but also to a slow ascent while the lithosphere gradually decreases in thickness towards the ridge. This process allows additional melt to

be generated between the primary melting regions at the hotspot track and the mid-ocean ridge, especially in regions where the lithosphere is thinned by transform faults. It leads to the development of a broad region of thickened crust with a width of up to 500 km. Moreover, this mechanism provides an explanation for the observations of O'Connor and Jokat (2015b), who find that the south-eastward transition between Walvis ridge and Cape Basin is much more abrupt than the smoother transition to the Angola Basin in the northwest.

Employing variations of the hotspot motion model (as described in Section 3.2.4) to compute the plume position, reveals that in some models two parallel lines of volcanism with similar ages are generated (like Figure 3.7b,c). These lines approximately correspond to the observed Tristan and Gough volcanic chains. Figure 3.6 top and Figure 3.7 also show that these two tracks represent a separation of the off-ridge track (directly above the plume, continuous black lines in the figures) and the on-ridge track (at the ridge, closest to the hotspot, black dots in the figures). The areal extent of the region where melt is generated at any given time (Supplementary Movie S2) is broadly similar to the observed spread of volcanism with similar radiometric age (Supplementary Figure S2) – about 5 degrees in longitude.

Multiple parallel tracks or one broad track are generated mainly when the plume was in an intra-plate location on the African plate: After it was at the ridge at $\approx$ 90 Ma (creating thick crust now around 5° E 27° S in the reference case) and started to move away, on-ridge volcanism was dominant. Hence, the single track observed between $\approx$ 5°E 27°S and 3°E 29°S in a similar location to our model track could be an on-ridge track, whereas during that time the off-ridge track directly above the hotspot could be entirely absent.

3.3.4 Plume head position and post-rift ocean floor thickness

In addition to analyzing the model evolution in general and comparing it to the present-day South Atlantic, we vary the position of the modelled plume head and the thickness of the lithosphere as described in Section 3.2.4. We then investigate under which conditions our model reproduces the observed LIP magmatism associated with the Tristan plume head and if that allows us to constrain the plume head properties. To quantify the spatial pattern and volume of melt generation, we also compute a model without plume and identify the region where melt is produced. We define melt generated within this region in all models as purely rift-associated melts, but melt generated outside of this region in the presence of a plume as LIP-associated melts that are attributed to their respective continents. We here only take into account melt accumulated in the first 20 Ma after the plume reaches the surface (equivalent to 135 to 115 Ma).

All models that include a plume predict melting where the plume head impinges on the lithosphere, and at the PEFZ and FFZ, as well as increased melt generation at the mid-ocean ridge compared to a model without plume influence (Figure 3.8). Moreover, the generated oceanic crust is significantly thicker directly south of the FFZ, where the rift opens first. The amount of melt generated north of the FFZ is much smaller, as the plume head has cooled once the spreading begins in this area. For a detailed comparison between our models and a seismic profile we refer to Supplementary Text S5 and Supplementary Figure S3.

An eastward shift of the plume head by 150 km respectively 300 km only changes the east/west distribution of the generated melt by less than five percent of the total volume. The majority of more than 75% of the melt is still produced on the South American side (Figure 3.9a, 3.8b-d). Presumably only an arrival at the African side of the rift

would lead to a significantly larger amount of melt produced there. The same is true for computations employing different models of the hotspot track (Figure 3.7b,c and 3.9a, Track2 and Track3). However, all presented models agree with the observed melt distribution of the Paraná-Etendeka LIP, for which up to 90 % of the magmatic volume is observed on the South American side (Richards et al., 1989). Becker et al. (2014) pointed out that this pattern is at odds with the distribution of possibly magmatically underplated crust below the continental margin, which is between 1.5 and three times more voluminous in Africa compared to South America. Hence we conclude that the LIP distribution can be explained by a plume head arriving mainly below South America, but the thicker African margin might be more easily explained by processes not covered in our model, such as asymmetric rifting (Brune et al., 2014). This also implies that our models do not allow us to further constrain the position of the plume head arrival.

The initial thickness of the lithosphere, on the other hand, has an important influence on the accumulated melt volume the plume head produces below the continents. While a thin lithosphere of 110 km increases the amount of plume-related melts by a factor of three in comparison to the reference of 130 km, a 160 km thick lithosphere leads to virtually no melt being generated apart from the mid-ocean ridge (Figure 3.9b). The models using lithospheric thickness models derived from seismic tomography and plate motions (RealLithC1 and C2, see Supplementary Figure S4 and Supplementary Text S4) generate a similar crustal volume as the reference model, but feature a different melt distribution (Figure 3.8g,h). Due to the large contrast between the thick continental lithosphere of approximately 250 km and the only 80 km thin lithosphere close to the future rift, melt is focused towards the rift, resulting in a more elongated shape of the produced thickened magmatic crust. Considering the increased but still minor melt generation on the African side of the rift especially lithosphere model C2 creates a more realistic pattern for the Etendeka LIP (Figure 3.8h, 7° W, 33° S). However, due to a thicker lithosphere in the region of the PEFZ on the South American side, it does not reproduce the large westward extent of the Paraná LIP.

These results demonstrate how important the properties of the overlying lithosphere are for the spatial extent and distribution of large igneous provinces. Despite its more realistic approach, the overall thickness of the lithosphere in the model derived from tomographic data depends on the conversion between seismic velocities and temperatures, and therefore might be slightly higher or lower, changing the total melt volume compared to Figure 3.9b. Also, seismic tomography provides a snapshot at present-day and lithosphere thickness may have changed with time. But although the model with a thin lithosphere of only 110 km results in a melt volume that is closest to the observations, we can not certainly rule out a thicker initial lithosphere because a number of processes that can lead to lithospheric thinning and increase the volume of generated melts are not included in the model. Examples are viscosity reduction due the presence of melt or water, dislocation creep as dominant deformation mechanism, melt migration and freezing, and plasticity, some of which are discussed in previous studies (e.g. Howell et al., 2014; Nielsen and Hopper, 2004).

3.3.5 Constraining plume properties by comparing the associated crustal thickness variations

Due to the overall agreement of generated crustal thickness and observed topography (Section 3.3.3), it seems plausible to constrain the plume properties by comparing the results of models with different plume excess temperatures and buoyancy fluxes to these observations. As expected, our models show an increase of hotspot activity with both

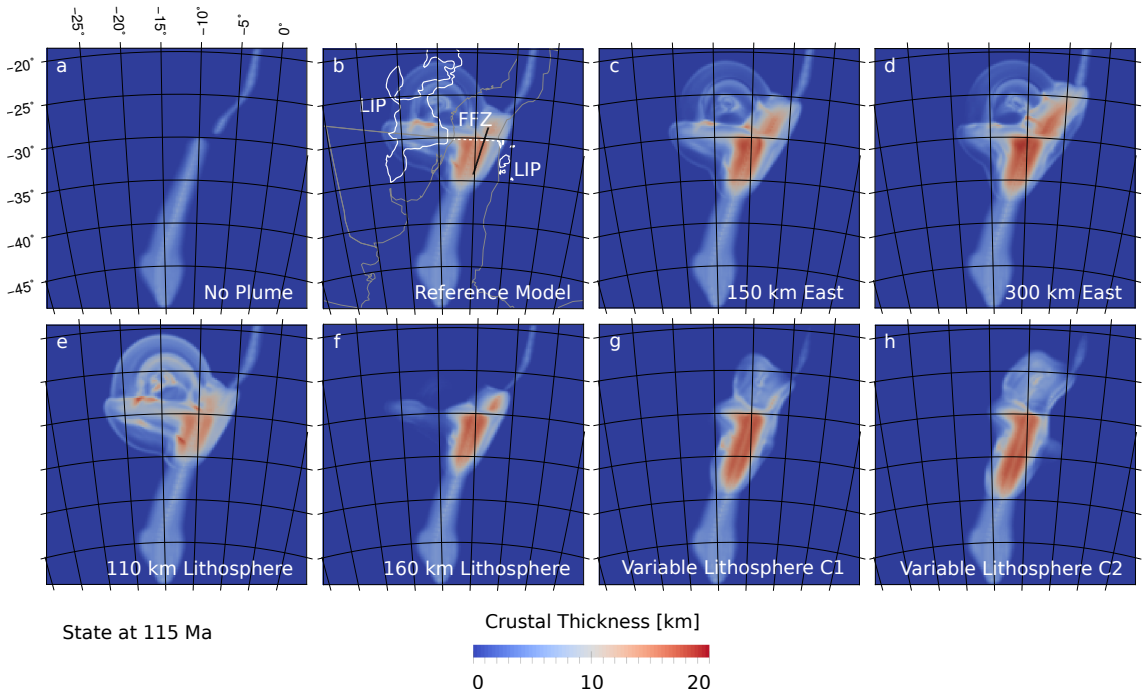

Figure 3.8: Computed crustal thickness distribution in the rifting and post-rift phase at 115 Ma for different initial plume head positions (b-d) and lithosphere properties (e-h). The top row displays a model without plume (a), the reference case (b) and a plume head that is shifted eastwards by 150 km (c) and 300 km (d), respectively, compared to the initial reconstruction of the hotspot track. The bottom row features models with a lithosphere thickness that is reduced to 110 km (e), increased to 160 km (f), or prescribed according to two different more realistic lithosphere models described in Supplementary Text S4 (g, h), with (h) featuring stronger lithospheric thickness variations. In addition, (b) includes the outlines of the continents and former plate boundaries (gray lines) and the Paraná-Etendeka LIP (Coffin et al., 2006, white line), the position of the FFZ (dashed line) and the crustal thickness profile shown in Supplementary Figure S3 (solid black line), all reconstructed to their 115 Ma location. Crustal thickness is computed by passive advection of melt.

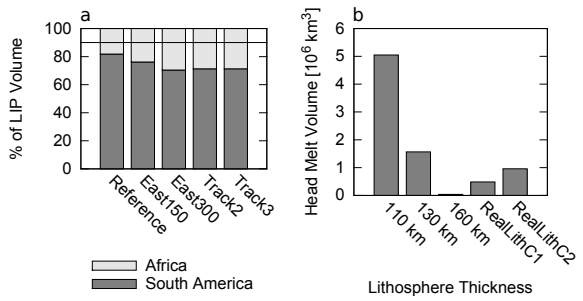

Figure 3.9: (a) Volume distribution of plume-related melts at 115 Ma for different plume positions. East150 and East300 shift the plume head by 150 km and 300 km respectively, and Track2 uses an alternative hotspot motion model by Steinberger et al. (2004). Track3 is a modified version of Track2 as described in Section 3.2.4. The overall melt volume is approximately $5.5 \cdot 10^6 \text{km}^3$ for all models. The black line marks the observed distribution of flood basalts between the Paraná and Etendeka provinces (Peate, 1997).
(b) Total melt volume generated by the plume head in dependence of the initial lithosphere thickness in the model. The two models RealLithC1 and RealLithC2 shown in the last two columns are initialized with variable lithosphere models that are derived from today's lithosphere thickness rotated back to the beginning of the model runtime, see Supplementary Text S4 for details. All melt volumes are computed by passive advection of melt.

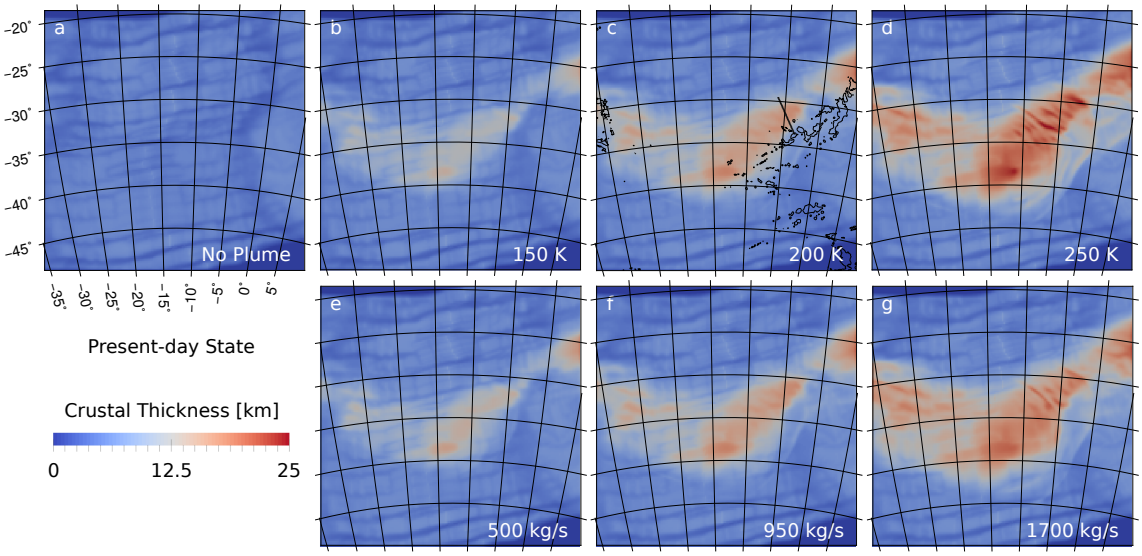

Figure 3.10: Maps of crustal thickness at present day for models with different plume tail properties and compared to a model without plume influx. The top row displays a model without plume (a), plume excess temperatures of 150 K (b), 200 K (c, the reference case) and 250 K (d), and the bottoms row shows models with plume buoyancy fluxes of 500 kg/s (e), 1000 kg/s (f, the reference case) and 1500 kg/s (g). The profile through the convection models shown in Figure 3.11 is marked with a thick black line. The -3300 m contour of topography representing the hotspot track and modified as in Figure 3.5 are given as thin black lines in (c). Crustal thickness is computed by passive advection of melt.

increasing buoyancy flux and excess temperature of the plume (Figure 3.10). In addition, we find that the temperature seems to have a stronger influence than the inflow volume. While varying the temperature also implies a change in buoyancy flux, a plume with an excess temperature of 150 K and a buoyancy flux of 700 kg/s (Figure 3.10b) produces less melt than one with an excess temperature of 200 K and a buoyancy flux of 500 kg/s (Figure 3.10e). The same relation is valid for higher plume excess temperatures. Fitting a linear trend to the integrated crustal thickness in dependence of the buoyancy flux reveals that the temperature change has more than twice the effect than a change of the buoyancy flux alone. For a more complete description of deriving scaling relationships between excess temperature, buoyancy flux and melt flux, we refer to Ribe and Christensen (1999).

Comparing profiles of crustal thickness across the hotspot track to seismic profiles (Figure 3.11) reveals that models with excess temperature of 200 K or higher and buoyancy fluxes of 1000 kg/s or higher significantly overestimate the produced melt volume. Due to the limited resolution and simplification of melt migration processes, our models are not able to reproduce small-scale features visible in the observations. However, the maximum magmatic crustal thickness of 13 km–17 km suggested by the seismic profiles indicates that the properties of the Tristan plume tail tend towards the lower end of predicted values for temperature and buoyancy flux. Values of at most 150 – 200 K respectively 500 – 700 kg/s achieve reasonable agreement with the profile P150, but are still too high to match profile P20060600. We emphasize that the profile P20060600 by Kessling (2008) from 5.5° W, 33.5° S to 2° W, 35.5° S samples a part of the hotspot track that is closer to our model profiles. The profile P150 of Fromm et al. (2015) on the other hand (9.2° E, 22.2° S to 5° E, 20.2° S) samples a very thick segment close to the plume-ridge crossing and therefore represents an upper limit on the possible crustal thickness.

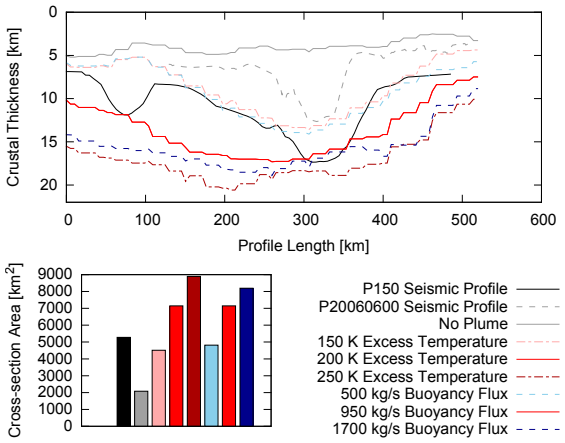

Figure 3.11: (top) Crustal thickness across the hotspot track for models with different plume tail excess temperatures (lines in different shades of red) and buoyancy fluxes (lines in different shades of blue), compared to a model without plume influx (gray line) and to the crustal thickness derived from seismic models (Profile P150 of Fromm et al. (2015) and Profile 20060600 of Kessling (2008)). The position of the model profiles is shown in Figure 3.10c.
(bottom) Integrated area of the crustal thickness along the profile. Note that the reference model with 950 kg/s buoyancy flux and 200 K excess temperature appears twice for better comparison. Values in excess of the one in the model without plume reveal the plume influence and how it depends on the plume properties.
Crustal thickness is computed by passive advection of melt.

3.3.6 Influence of global flow field

Regional studies of plume–lithosphere interaction usually do not take into account the global mantle flow field (e.g. Ribe, 1996; Ito et al., 1997; Albers and Christensen, 2001; Ruedas et al., 2004; Schmeling and Marquart, 2008; Howell et al., 2014). Here, we investigate this influence on plume-ridge interaction by comparing the reference model to a model without prescribed global flow (as described in Section 3.2.4).

As both model setups are chosen in such a way that the plume arrival position at the surface agrees with the observed hotspot track (Section 3.2.1), the geometrical pattern of the computed hotspot track is similar in both models. However, there are significant differences in the detailed structure and overall volume of the generated magmatic crust (see Figure 3.12b). The maximum plume-related crustal thickness is reduced by 30% (across the profile in Figure 3.12) without the influence of the global flow, and the overall plume-related melt volume in the model region is lower by 40%. This effect can be partly explained by the lower effective buoyancy flux in the model without global flow. However, when correcting for this effect by linear interpolation between the models with different buoyancy fluxes, a contribution of 20% remains that is purely related to the horizontal global flow.

A cross-section of the plume (Figure 3.12a) shows how the global flow can explain the significant deviation in crustal thickness: In the reference model, the westward mantle flow forces the plume material to spread asymmetrically below the lithosphere, supporting westward material transport and hindering eastward transport. This influence increases the tendency of plume material to flow towards the ridge, and therefore to regions with thinner lithosphere. Hence, plume temperatures in the western, shallower part of the plume head are increased by 15–50 K compared to the model without global flow, leading to a higher melt production. Omitting the influence of the global flow field results in a

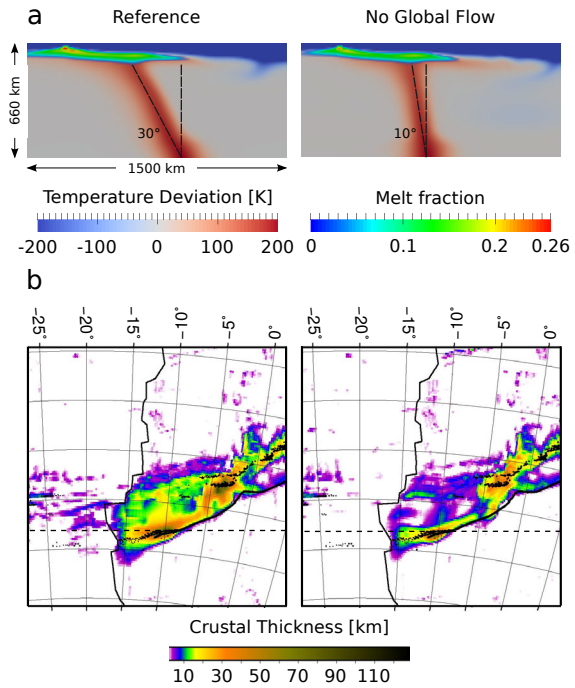

Figure 3.12: (a) Cross sections through the reference model (left) and a model without global flow, but otherwise unchanged parameters (right) at present day, illustrating the tilt of the plume tail and the melt distribution in the plume head. Temperatures are shown in shades of blue–red and the melt fraction is colored in a different scale, which becomes transparent below melt fractions of 5 %. (b) Comparison of crustal thickness maps for the corresponding plume models. The dashed line marks the position of the profile shown in (a). Crustal thickness is computed by instant melt extraction.

much more symmetrical spreading of plume material. Therefore, more material is pushed eastward into regions of thicker and colder lithosphere, which prevents extensive melting despite the elevated temperatures.

While the position of the transition of the hotspot track into the south-eastward Cape Basin is nearly identical in both models, the thickness of the hotspot track itself is reduced significantly and the transition region into the north-westward Angola Basin is nearly removed in the model without global flow. Instead of producing a wide area or two parallel lines of thickened magmatic crust, mainly the southern line – corresponding to the Gough volcanic chain – is present in the model without global flow, whereas further to the north – corresponding to the Tristan hotspot track – only a rather thin, E-W trending ridge is present. In addition, the models reveal differences in the plume tail position at the base of the upper mantle and in particular in plume shape and tilt: While the present-day plume tail of the reference model is tilted by 30° by the combined effect of plate motion, nearby ridge and global flow (equivalent to a lateral deflection of approximately 300 km), the model without global flow generates a plume tail with a tilt of only 10° (see Figure 3.12a).

This shows that the influence of global processes on the behavior of regional models are not negligible in regions of strong mantle flow and can lead to differences in predicted melt volumes of up to 40%.

3.4 Discussion

We explain the distribution of magmatic crust in the South Atlantic by the arrival of a hot mantle plume. Melting in the plume head generates the LIP volcanism, and melting in the plume tail, in interaction with the Mid-Atlantic Ridge, leads to one broad or two smaller lineaments of thickened crust – the hotspot track. When the plume reaches the base of the lithosphere in a sufficient distance from the ridge, two separate regions of upwelling and significant melting are created (see also Supplementary Figure S5a): One where the plume tail arrives (the off-ridge track), and another one when the plume material that is sucked towards the ridge reaches the ridge and flows upwards (the on-ridge track). This can lead to two parallel lines of volcanic islands, but if one of these melting regions is absent, only one track is generated.

In general, this model fits the observation on a first order. It is able to reproduce and explain the melt distribution and volume in the LIP and hotspot track. However, our plume model generates overall thicker and more prominent hotspot tracks than the maximum width of 100 km of thickened crust observed by O'Connor and Jokat (2015b). On the other hand, the volume of LIP-related melts is relatively low compared to observations. And although several models feature two parallel lines of increased magmatic activity with similar spacing as the Tristan and Gough tracks, melt is always distributed over a wide area, where observations show the focusing into several distinct, narrower tracks.

3.4.1 Limitations of the geodynamic model

A number of limitations of our modelling approach can explain these differences. While separated melting regions within a distance of a few hundred kilometers are generated in our model, no mechanisms for focusing of melt on a smaller scale of several tens of kilometers are included. Different processes related to porous flow and fracturing have the potential to focus melt into more distinct structures, such as ascent through fractures in the lithosphere, channelized flow due to upwelling melting in a heterogeneous mantle

(Katz and Weatherley, 2012; Weatherley and Katz, 2012) or flexural stresses due to volcanic loading (Hieronymus and Bercovici, 2001). In addition, viscosities in our model plume are higher than in reality to be consistent with the global model that provides the boundary conditions; and resolution is limited to 10 km. This causes larger structures of hot plume material and broader melting regions than expected for a plume of this temperature. Furthermore, these model properties inhibit small-scale convection and viscous fingering instabilities, which can lead to focussing of melt into distinct chains of volcanic activity (e.g. Ballmer et al., 2011).

The comparatively low LIP melt volumes in our model can be explained by a number of mechanical and magmatic processes that have the potential to thin the lithosphere, and are not included in the present models. Lower viscosities due to a strong temperature-dependence, the presence of melt or water, and dislocation creep as an important deformation mechanism all enhance small-scale convection within the hot plume material at the base of the lithosphere (Moore et al., 1998; Moore et al., 1999). Furthermore, the fast transport of magma and the associated latent heat can lead to thermomagmatic erosion of the lithosphere. Freezing melt has a higher density than the surrounding mantle, providing an additional destabilizing effect. Finally, extension during the rifting phase results in faults and thinning of the lithosphere and crust, which is not captured in models without plasticity. All these processes of lithospheric thinning increase the volume of melt produced significantly when hot material rises to regions of shallower depth. Hence, they could easily explain the larger observed magma volumes and igneous crustal thickness for the Paraná-Etendeka LIP compared to our model results.

Two-phase models of magma/mantle dynamics with the capability to simulate plastic and elastic deformation in addition to viscous flow will allow a more detailed investigation of magmatic features of the crust developing in interaction with tectonic processes and the small-scale mechanical structure of the lithosphere as well as more realistic estimates of melt volumes. For example extracting the generated thick crust could lead to a downward compaction flow that reduces decompression melting (Schmeling and Marquart, 2008). In addition, we neglect any changes in material properties related to retained melt or depletion of the residue. Positive buoyancy of melt and depleted material, low-viscosity channels due to focusing of melt, stiffening of the material due to the extraction of water in the melting process, or changes in chemical composition of the mantle residue from asthenospheric mantle to depleted oceanic lithosphere may further influence the model dynamics. In particular, stiffening of the depleted residue has been suggested to reduce the thickness of crust generated by a plume in interaction with a mid-ocean ridge significantly (Ito et al., 1999; Howell et al., 2014). This is a likely explanation for the overly thick modelled crust for times when the plume was located directly below the ridge, while it may not have such an important influence on the volume of LIP-generated melts further away from the ridge.

Another important factor for the amount of melt generated in a geodynamic model is the choice of parametrization for melting in dependence of temperature and pressure, and the assumed composition of the source material. We use the parametrization of Katz et al. (2003) for anhydrous peridotite, but other melting models predict different melting rates: Gregg et al. (2009) reveal absolute differences in melt fraction of up to 10% between models for a mid-ocean ridge setup. Moreover, both a higher content of water (Katz et al., 2003) and recycled crustal material (Sobolev et al., 2007; Sobolev et al., 2011) are known to enhance melt production by several percent. This means that there is a considerable uncertainty in the computed melt volume related to the employed data for mantle melting and the composition of the Tristan plume alone. Nevertheless, the patterns of melt distribution and the general structures of the produced igneous crust

should remain largely unaffected.

Moreover, our kinematic surface boundary condition may not appropriately represent rift migration, a possible cause for continental margin asymmetry and crustal hyperextension (Brune et al., 2014). Accordingly, these processes may influence the asymmetry of volcanic rocks generated in the rift between South American and African plates, which may hence not be accurate in our model. Kinematic surface boundary conditions combined with a stress-independent viscosity formulation (as used here), can lead to artificial dissipative heating at the ridge that potentially influences the thermal structure of the lithosphere. We ensured that this effect is small in our models and that the resulting lithospheric temperature profile is consistent with published estimates (e.g. McKenzie et al., 2005).

Our models provide an explanation for the crustal-thickness jump that is observed across the FFZ: Ascending plume material flowing into the opening rift leads to higher melt generation south of the fracture zone. However, it is important to note that the seismic profile is located within the continent ocean transition (COT) south of the ridge (in the cape basin) and at normal oceanic crust north of it in the Angola Basin. The nature of the thick COT crust is still debated. Hence, part of the north–south variation of crustal thickness might be due to the presence of a significant portion of continental crust in the profile south of the ridge. This could be one reason for the smaller crustal thickness jump in our models when compared to seismic profiles.

3.4.2 Limitations of the hotspot motion model

Other detailed features, such as the timing of the ridge jump and the associated separation of the hotspot track to the two continents, and the precise position of the generated crust are linked to the accuracy of the employed hotspot motion model. However, we only used the position of the Paraná-Etendeka LIP and large-scale mantle flow based on tomographic models to reconstruct the plume position. This allows for different scenarios, each explaining certain features of the hotspot track (Figure 3.7).

For example, before the ridge crossing the hotspot presumably was closer to the ridge than it is simulated in our reference model. Thus, the model does not reproduce the beginning of the observed Walvis Ridge on the African side, and the prominent area of very thick magmatic crust related to this crossing is generated approximately 2° further to the west and south, respectively. Related to that, on the South American side, the Rio Grande Rise is clearly separated from the continent in the observations, whereas our results predict a more continuous track from the continent, because in our model the plume was initially beneath the South American plate.

Nevertheless, some features are fit better by some of our models than others (Figure 3.7): Model Track2 explains the older part of the Walvis Ridge on the African plate – a single ridge reaching all the way to the continent, including the position of the strongly thickened crust related to the plume–ridge crossing – better, because in this hotspot motion model the plume has remained close to the ridge before 90 Ma. In contrast, the reference plume location further west in combination with westward large-scale flow leads to much less volcanism and no continuous track on the African plate before 90 Ma. Model RefShift explains the location of the younger part of the track much better. This may indicate a plume location closer to Gough Island, whereas the generation of Tristan da Cunha would be due to plume-ridge interaction. Consequently, none of our models fits all of the observed volcanism, but different models fit different parts. Fitting the position of the inflowing plume material to the hotspot track (possibly closer to Gough Island) would presumably lead to even better agreement of small-scale structures.

However, reconstructing the plume position is not straightforward. One effect that needs to be considered – for example when devising hotspot reference frames – is that volcanism may occur several million years after lithosphere has passed over the plume. For example, in Figure 3.6 bottom, the hotspot track age for the lithosphere generated around 5° E 27° S during plume-ridge crossing at ≈ 90 Ma is only 70-80 Ma, because melts continued to be generated beneath that lithosphere. These younger model ages help to explain the discrepancy between measured ages near that location and the hotspot track of Doubrovine et al. (2012).

Moreover, we have shown that a single plume can cause several volcanic chains, and that the observed magmatic activity does not always have to be directly above the plume conduit. If the plume tail reaches the base of the lithosphere close to the mid-ocean ridge, and global mantle flow supports flow towards the ridge, plumes may temporarily only generate an on-ridge track, whereas the off-ridge track directly above the hotspot can be entirely absent during that time. This means that discrepancies between hotspot motion models and observed volcanism may hence not be due to a deficiency of the model reference frame but due to plume-ridge interaction. One example in our model could be the track on the African side, directly after the plume crossed (and while it is still close to) the ridge: The predicted track of Doubrovine et al. (2012) is southeast of the observed track in that area, but the distribution of generated melt in our model agrees well with the observations. This shows the importance of our results for hotspot motion models and hotspot reference frames, which are usually constructed under the assumption that the plume is directly beneath the track.

3.4.3 Alternative models

Our model explains the generation of separate volcanic chains close to mid-ocean ridges by disconnected melting regions below the lithosphere while the plume material is spreading preferentially towards the ridge. Other mechanisms have been proposed to explain the observed splitting of hotspot tracks in other regions. Small-scale convection could lead to a separation of melt upwelling with a characteristic length scale. However, small-scale convection usually only occurs below plates older than 70 Ma (Ballmer et al., 2011), while the oceanic plate above the Tristan plume is much younger. Nevertheless, the reduced viscosity in the plume head enhances small-scale convection and can lead to a shear-aligned roll regime of material flow with a spacing of a few hundred kilometres (Moore et al., 1998). For the Tristan plume, which has a low excess temperature of <180 K and impinges on a young plate plate with an age of approximately 20 Ma, convection rolls are not expected to occur closer than 500 km downstream of the plume center (Moore et al., 1998; Agrusta et al., 2013). This would require the plume tail to be at least 500 km upstream of the centers of volcanic activity. For the current position of Tristan, upstream with respect to the local flow field would mean a distance of at least 1000 km from the mid-ocean ridge, which would presumably be too large for the plume material to still flow towards the ridge. Upstream with respect to the plate motion would mean a plume position directly below the ridge, which would be visible in numerous observations. Alternatively, several smaller, separated plumes have been suggested by O'Connor et al. (2012). Yet a consistent dynamic model, a potential mechanism, or an estimate for the forces required to prevent such small plumes from merging during their ascent are still missing. For other volcanic chains, volcanic loading and lithospheric flexure have been suggested as mechanisms for splitting the volcanism caused by a single plume into a dual line (Hieronymus and Bercovici, 1999). However, this causes volcanic lines with a much closer spacing (≈70 km) than the Tristan-Gough chains (≈500 km). Another mechanism

for the formation of seamount chains and the material transport from an off-ridge plume to the mid-ocean ridge are viscous fingering instabilities – formed when low-viscous plume material is injected into the asthenosphere (Weeraratne et al., 2007) – and the associated shear-driven upwelling (Ballmer et al., 2013). But while these instabilities might generate volcanic chains with the observed spacing, they are expected to lead to much faster age progression than observed for the Tristan and Gough tracks. Moreover, over the last 90 Ma, the closest ridge segment from the plume tail, and therefore the expected direction of fingering instabilities, was located in north-westward direction – perpendicular to the direction of the Tristan–Gough lineaments and the absolute plate motion. Lastly, an additional depleted/dehydrated mantle region can form below an active hotspot due to the continuous melting and lead to a shift of the melting region to both sides of this "plug" (Kundargi and Hall, 2014), but the continuous plate movement should transport this 'plug' away and lead to an oscillating behavior of the hotspot tracks.

Therefore, we think that our mechanism is a likely explanation for the separation of the Tristan and Gough volcanic chains. In addition, it does not contradict the observation of a distinct geochemical signature for each of the two tracks (Hoernle et al., 2015), because a single plume can carry two distinct chemical components from the CMB to the surface without significant mixing (Farnetani and Hofmann, 2010). But even though we rule out the discussed alternative models as the main mechanism for separating the Tristan plume into the Tristan and Gough track, they might still have an influence on focussing melt into more distinct structures.

Although we specifically study the Tristan hotspot and its interaction with the South Atlantic opening, some of our results – in particular the strong influence of large-scale mantle flow on plume-ridge interaction – can be readily generalized. Our method can be easily adopted to study plume-ridge interaction for other hotspots close to mid-ocean ridges, like Galápagos, Réunion, Kerguelen or Iceland. All of these hotspots are very promising candidates for further studies due to their complex histories of interactions with close-by ridges. These investigations could help to understand the behavior of plumes below fast-moving plates, forces exchanged between plumes and plates, the role of plumes in subduction initiation, the generation of new plate boundaries on top of mantle plumes and the history of plumes over longer periods of time.

3.5 Conclusion

We have studied the evolution of the Tristan plume and its interaction with the Mid-Atlantic Ridge in a series of three-dimensional regional convection models, and in particular the influence of the global flow field on the distribution of magmatism. Our comparison of computed crustal thickness to maps of residual topography and seismic profiles has shown that a convection model that takes into account plate motion, mantle flow, plume movement and decompression melting of peridotite resembles both the current-day geometry of the hotspot track and the distribution of syn-rift magmatism. This includes the correct timing of the ridge overriding the plume, the east–west distribution of melts of the Paraná-Etendeka flood basalts, with a majority of the plume-related melt being generated on the South American plate, and differences in crustal thickness across the Florianopolis Fracture Zone. Moreover, the comparison to seismic profiles allowed us to further constrain the physical properties of the Tristan mantle plume within the existing uncertainties.

Our key findings are as follows:

1. The broadening of the Tristan hotspot track and the apparent separation into the

Tristan and Gough volcanic chains can be explained by the interaction of a single plume with the nearby ridge. The global flow field enhances material motion from below the off-ridge track towards the ridge and regions of thinner lithosphere, where decompression melting leads to the development of a broad region of volcanic activity, which can be focussed into additional volcanic chains.

2. The jump in crustal thickness north and south of the Florianopolis Fracture Zone is well reproduced by hot plume material in the asthenosphere feeding into the already opening southern part of the rift. 10–15 Ma later – when the northern part opens – the plume head has cooled and has been transported away from the rift, leading to a lower crustal production north of the FFZ.

3. An excess temperature of 150 K and a buoyancy flux of around 500 kg/s – consistent with the lower end of previously published estimates for the Tristan hotspot – lead to a crustal production comparable to seismic observations for the Tristan hotspot track. Larger plumes overpredict the generated crustal thickness in our models.

4. A back-rotated lithosphere model explains the size and extent of the Etendeka LIP better than a constant lithosphere thickness. However, in this model the thick lithosphere north of the PEFZ prevents the Paraná LIP from extending west- and northward, as it is observed for the LIP today. Additional high-resolution studies are needed to investigate if a more advanced simulation of the fault zone with a stronger and more localized thinning of the lithosphere would produce a better agreement between model and observation.

5. The position and shape of the generated large igneous province is an additional constraint for the plate reference frame used: Our reference model approximately fits the Paraná LIP location; with the same reference frame and strong initial lithosphere thickness variations, volcanism occurs near the Etendeka LIP.

6. Neglecting global mantle flow can influence the estimates of plume temperature by up to 50 K and mispredict the plume tilt by up to 20°. This can prevent the development of two separate volcanic chains in the geodynamic model. Additionally incorporating global flow changes (in this case increases) the overall volume of plume-related melt by 40 %, with 20 % being purely caused by the westward lateral flow.

The current models are simplified and neglect plastic behavior of the lithosphere and melt segregation, which limits focusing of melt and prevents thinning of the lithosphere by thermo-magmatic erosion. Despite these limitations, the results presented here indicate that regional convection models incorporating plate motion and global mantle flow can resemble the melt distribution both of the large igneous province and the hotspot track, including small-scale features such as the development of several distinct volcanic chains. Hence, this method promises to be a useful tool to investigate unresolved questions surrounding other hotspots with a complex history of origins.

Acknowledgments

The geodynamic models were computed with the open-source software ASPECT (*http://aspect.dealii.org*) and visualized with the open-source programs ParaView (*http://www.paraview.org*) and GMT (Wessel et al., 2013). The necessary data to reproduce the models is included in the supplementary material. We are grateful to Tanja

Fromm, Wolfgang Bangerth and Thorsten Becker for carefully and critically reading the manuscript and providing suggestions for improvement. We would also like to thank Maxim Ballmer, Harro Schmeling, Mike Gurnis and an anonymous reviewer for their helpful comments. This project was funded by the Deutsche Forschungsgemeinschaft (DFG) under grant STE 907/8-2 as part of the DFG Priority Program SPP 1375 "South Atlantic Margin Processes and Links with onshore Evolution" and grant STE 907/11-1 to BS. The computational resources were provided by the North-German Supercomputing Alliance (HLRN) as part of the project "Plume-Plate interaction in 3D mantle flow – Revealing the role of internal plume dynamics on global hot spot volcanism". THT and BS also acknowledge the European Research Council under the European Union's Seventh Framework Programme (FP7/2007-2013)/European Research Council Advanced Grant Agreement 267631 (Beyond Plate Tectonics) and the Research Council of Norway through its Centres of Excellence funding scheme (Centre for Earth Evolution and Dynamics, 223272) for financial support. JD acknowledges the support of the Computational Infrastructure in Geodynamics (CIG-II) grant (National Science Foundation Award No. EAR-0949446, via The University of California – Davis) and the Helmholtz graduate research school GeoSim.

3.A Additional Supporting Information

1. Text S1 to S5
2. Captions for Datasets S1 to S5
3. Captions for Movies S1 and S2
4. Figures S1 to S5
5. Table S1

Text S1: Hotspot motion and large-scale mantle flow

The computation of Doubrovine et al. (2012) essentially assumes that an initially (at the time when the Paraná–Etendeka LIP erupted, at 132 Ma) vertical conduit gets subsequently tilted and distorted through a combination of buoyant rising and advection in large-scale mantle flow. Doubrovine et al. (2012) assumed an anomalous mass flux of 1000 kg/s, which is the order of magnitude derived from hotspot swell size (Davies, 1988; Sleep, 1990) and the interaction with the Mid-Atlantic Ridge (Schilling, 1991).

The location where the conduit reaches the surface as a function of time is taken as hotspot location. For the present-day, large-scale mantle flow in the model of Doubrovine et al. (2012) is based on a mantle density model, which is derived from seismic tomography, a surface boundary condition consistent with prescribed plate motions, and a radial viscosity structure (Steinberger and Calderwood, 2006) derived from a model of pressure- and temperature dependent viscosity. Lateral viscosity variations were not considered in the large-scale flow model of Doubrovine et al. (2012).

Large-scale mantle flow was also used as a boundary condition for the Cartesian box model presented in this study. Mantle flow in the geologic past was computed by backward-advecting density anomalies with prescribed global plate motion surface velocity boundary conditions back to 68 Ma. Before 68 Ma, density anomalies used to compute the flow are left constant, because reconstructing density anomalies by backward advection becomes increasingly inappropriate further back in time, due to neglecting diffusion. However, the plate motion boundary conditions (as described in Section 3.2.2) are still time-dependent when computing mantle flow before 68 Ma. The time-dependent flow model applied here as boundary condition is an update of Doubrovine et al. (2012) and similar to the one described in Steinberger et al. (2015), corresponding to Figure 3A-C in that paper, but with the difference that here we treat LLSVPs also as chemically distinct: We add 1.2% density wherever seismic velocity anomaly is more than 1% negative below a depth of 2600 km, because with this addition, Steinberger and Holme (2008) obtained a relatively good fit to CMB excess ellipticity and topography.

Text S2: Model of plate motions used as surface boundary condition

All our plate reconstructions are available online as Data Supplement S2. The plate stage rotation vectors and boundaries are based on Torsvik et al. (2010) but were modified in two steps:

First, absolute plate rotations were updated in the time interval 0-120 Ma to the reference frame of Doubrovine et al. (2012), which is obtained by optimally fitting the five best-constrained hotspot tracks globally: Hawaii, Louisville, Tristan, Réunion and New England. The reference frame also considers the calculated motion of hotspots in a convecting mantle. Since the Tristan track is among those five tracks, it is important for the sake of consistency to use the same model of hotspot motion that was used to devise the reference frame. Given the age span of available hotspot tracks, the Doubrovine et al.

(2012) model only goes back to 124 Ma, and is used here only after 120 Ma. For 130-150 Ma, plate motions are based on paleomagnetism, but corrected for true polar wander. The transition in the time interval 120-130 Ma is made in such a way that the African plate has, on average, no eastward or westward component of motion. Motions of South American, Parana and Colorado plates relative to the African plate were not changed, but locations of plate boundaries were shifted accordingly. This update was performed with a routine described in Torsvik et al. (2010), and it also affects finite plate rotations, and hence the location of plate boundaries before 120 Ma. Plate rotations are listed in Supplementary Table S1.

Second, plate reconstructions were converted to the Cartesian box, and, if necessary, plate boundaries were interpolated to shorter time intervals of 5, 2 or 1 million years, in order to avoid apparent jumps that do not correspond to presumed real jumps of the plate boundary: This is necessary, because Torsvik et al. (2010) only give plate boundaries from 150 Ma to present-day in 10 million year time intervals. The conversion uses a Lambert azimuthal equal-area projection centered on 13° W, 35° S, corresponding to the center of the Cartesian box. Spherical plate rotation vectors were also used to compute motion and rotation, in Cartesian coordinates, at the projection center. This (2-D) motion combined with rotation is then applied to all points on the corresponding plates. In this way, internal deformation of the plates in the Cartesian coordinate system is avoided.

Figure 3.3 shows that, besides relative plate motions, there is also a rather strong northward motion of all plates in the reference frame used. Since this occurs before 120 Ma, i.e. before we use hotspot tracks to derive plate motions, this is based on paleomagnetic data: Under the geocentric axial dipole hypothesis, the paleomagnetic axis, after secular variations have been averaged out, is assumed to represent the Earth's spin axis. Hence a northward motion in the paleomagnetic reference frame could be either plate motion over the underlying mantle, or a re-orientation of the entire mantle–lithosphere system relative to the spin axis, so-called true polar wander. The procedure applied to separate off the true polar wander component follows Steinberger and Torsvik (2008): Essentially, coherent rotations of all plates around an axis close to their center of mass are interpreted as true polar wander. However, in the interval 140-120 Ma, the remaining plate motions still have a strong coherent northward component, which is interpreted as plate motions over the mantle beneath. The rationale for this is that the alternative interpretation of coherent north–south motion as true polar wander would also move the Large Low Shear Velocity Provinces (LLSVPs) in the lowermost mantle north and south. Yet these are believed to correspond to long-term stable geoid highs, which should remain near the equator under true polar wander. While this is a first-order approximation, reconstructions for more recent time intervals where also hotspot tracks are available show that due to true polar wander the pole does in fact move up to about ten degrees towards and away from the LLSVPs. So we cannot exclude that the $\approx$ 500 km southward motion in that time interval may in fact be partly or fully due to true polar wander. Likewise, east–west motion is not constrained by paleomagnetism. Because of these uncertainties, we will use here a couple of different assumptions of where the plume, and in particular the plume head, was relative to the plate boundaries before 120 Ma. We expect that allowing for such model variablility, and optimizing the agreement of model output with observations can in fact help to further constrain the absolute plate reconstructions before 120 Ma.

Here we interpolate and extrapolate plate boundaries of Torsvik et al. (2010) in 1 Ma intervals from 140 to 121 Ma. Figure 3.3 shows the 140 Ma reconstruction, the 121 Ma extrapolation (the youngest time for which Parana and Colorado exist as separate plates in our model) and the 120 Ma reconstruction with only African and South American plates. In the reconstructions, the length of the transform fault east of the triple junction grows

continuously and rather uniformly.

The following time interval 120 − 80 Ma falls mostly within the Cretaceous superchron 121 − 84 Ma, therefore plate reconstructions are comparatively poorly constrained. By comparing magnetic anomalies before and after, we know that considerable plate reorganizations must have occurred in the meantime, especially the transform fault corresponding to the Florianopolis Fracture Zone disappeared, and a number of other transform faults appeared. In our plate reconstruction, we keep the transform fault generated at the triple junction until 100 Ma. At 100 Ma, we adopt a rather simple, straight plate geometry. We then interpolate from the simple 100 Ma geometry to the much better constrained and therefore much more complicated 80 Ma geometry. After 80 Ma, plate boundaries were interpolated from the 10 million year intervals to shorter intervals if necessary to avoid apparent ridge jumps.

Text S3: Melt extraction methods

As mentioned in the main text, our model does not include two-phase flow. This would allow it to simulate melt segregation, but is numerically extremely challenging and computationally expensive, especially in three dimensions. Instead, we use two different methods to track where the melt moves in our model and to compute maps of crustal thickness:

(1) Melt is passively advected with the mantle flow as a field $F_{\max}(x)$, the maximum degree of melting in every point. The crustal thickness at every point in time is calculated by vertically integrating this quantity from the surface up to a depth of 200 km. This method assumes that while melt is below the lithosphere, lateral movements of the solid flow influence melt migration, and once it reaches the lithosphere, it moves with the plate.

(2) Alternatively, generated melt is extracted instantly, added up to yield a crustal thickness and advected with the prescribed plate motions at the top of the model.

Both methods are simplifications of our concept of melt migration in the Earth: a combination of porous flow in the mantle and fast ascent through channels and dikes in the lithosphere.

Melt ascent through channels and dikes happens on much shorter time scales than motion in the mantle, so for these processes it is a good approximation to neglect any lateral movement of melt and assume that magmatic crust is produced vertically above the melting region (Approximation 2). However, for porous flow in the mantle, the velocities of the solid matrix can have an important influence on the migration of melt, dependent on the material properties. For example, melt close to mid-ocean ridges is expected to be focused towards the ridge (e.g. Katz, 2008; Katz, 2010) instead of being extracted through the lithosphere above, and it has been argued that similar processes can apply to plume-ridge interaction and the relevant distances of several hundred kilometers (Braun and Sohn, 2003). This is also what happens to the plume material in our models when it reaches the base of the lithosphere close to the ridge (Supplementary Figure S5a): Flow within the melting region (black outline) in the plume is partly pointed upwards and away from the ridge, and partly pointed towards the ridge and upwards once it reaches the ridge. Above the melting region, the flow field is aligned with the direction of plate motion, due to the high viscosity of the cold lithosphere. Hence, in Approximation (1), after the field $F_{\max}(x)$ has reached the ridge and moved upwards, it is advected with velocities very similar to the plate motion, and thus similar velocities as in method (2). Integrating $F_{\max}(x)$ over the uppermost 200 km as a final step for computing the thickness of generated crust is based on the assumption that once melt is within the lithosphere, it ascends to the surface through fractures and channels, but as the whole lithosphere moves with the same speed, it is irrelevant if we do this integration when melt reaches

the lithosphere or all at once at the end of the model evolution.

However, it is clear that velocities of porous flow are not equal to the solid velocities. Hence, we see Approximation (1) only as an end-member, valid in the limit of very low porosities. On the other hand, instantaneous extraction (2) becomes an increasingly appropriate approximation with higher melt fractions and permeabilities.

Another disadvantage of the passive advection approach is that it does not guarantee that all melt ends up in the uppermost, high-viscous layer of the model that moves with the plates, in particular for melt that is generated within the plume, but on the far side of the ridge. Moreover, if the melt is advected within the asthenosphere, velocities are still in the direction of plate motion, but might have different amplitudes or a more chaotic behaviour, leading to mixing of the field $F_{\max}(x)$ with the surrounding mantle. Therefore, Approximation (1) becomes less appropriate the further away melt is advected from its source region. We show a comparison between the two methods in Supplementary Figure S5b,c. While the general structures of generated crust are similar, the immediate extraction (2) results in much more focused features with steeper slopes, while method (1) reveals broader structures influenced by lateral movement and mixing of melt with the surrounding material. In addition, melt focused towards the ridge results in crustal production on both sides of the ridge, while this is not the case for method (2), where crust is only produced directly above the melting region. The track on the African plate is slightly shifted towards the ridge when method (1) is used, in accordance with the flow shown in Supplementary Figure S5a.

Furthermore, the passive advection method (1) is more consistent with the formulation of the mass and energy conservation equations in our model. Extracting melt without accounting for the missing material would violate mass conservation by the extracted melt fraction – in some model cells up to 25 % of the overall material. Moreover, our energy conservation equation includes the latent heat of melting and freezing, so removing melt from the model that might otherwise crystallize would also extract energy from the model. While melt extraction has been proposed to form an important cooling mechanism for continental rifting (Schmeling and Wallner, 2012), we here decided to stay consistent with our mass conservation equation and neither remove the mass nor the energy of melt.

For these reasons, we believe that the passive advection method (1) is suitable to compute a distribution of generated crust shortly after the melting process, such as in Figures 3.8 and 3.10. For analyzing the generated hotspot track over the whole history of the plume, however, such as in Figures 3.7 and 3.12, the immediate extraction method (2) is more appropriate.

Text S4: Lithosphere thickness model

Present-day lithosphere thickness is inferred from seismic tomography using a combination of the tomography models by Schaeffer and Lebedev (2013) above 200 km depth and a 2010 update of Grand (2002) below. This combination was chosen because the former model does not cover the entire mantle, and its quality is highest in the upper 200 km. At each location, lithosphere thickness is determined by finding the intersection of the vertical profile of relative S-wave anomaly with a cutoff function

$$\delta v_s/v_s|_L = 3.1\% - C \cdot \left(1 - \operatorname{erf}\left(\frac{z}{z_0}\right)\right) \tag{3.7}$$

that is meant to take into account both the presence of a thermal boundary layer and the effect of chemical anomalies within the continental lithosphere. This cutoff function is calibrated by adjusting parameters C and z_0 such that the thickness of oceanic lithosphere determined approximately matches, on average, thickness inferred from age. A detailed

description of the procedure is given in Steinberger (2016). As a more extreme alternative, we also use the cutoff function

$$\delta v_s/v_s|_{L2} = C \cdot \left(\mathrm{erf}\left(\frac{z}{z_0}\right) - 0.843 \right), \tag{3.8}$$

which yields much stronger lithosphere thickness variations – in particular regions of thick lithosphere are even thicker, up to ≈ 380 km, whereas in the previous case thickness does not exceed ≈ 250 km. Supplementary Figure S4 shows the thickness models for both cases, rotated back to 140 Ma using the parameters of Supplementary Table S1.

Text S5: Coast parallel profiles

One observation that can help to constrain plume properties is the jump in igneous crustal thickness across the Florianopolis Fracture Zone. It is reproduced for all tested plume excess temperatures (150 K to 250 K) and buoyancy fluxes (500 kg/s to 1700 kg/s) tested in our models. However, comparing the different models (Supplementary Figure S3), we find that the jump increases with the thickness of the lithosphere, and decreases for a plume position further towards the east (and closer to the rift). Nevertheless, all models with an initially constant thickness of the lithosphere show similar differences of 3-5 km between the regions north and south of the fracture zone, which is much smaller than the 30 km suggested by seismic models. Employing the more realistic structure of the lithosphere that was reconstructed from the present-day state, however, leads to a significantly higher contrast in crustal thickness of 12 km and also resembles the absolute values much better (green profiles in Supplementary Figure S3). This is notable in particular for RealLithC2, where the lithospheric thickness variations are bigger (see Supplementary Text S4). Nevertheless, there is still a considerable deviation from the seismic profile, which can be explained by the fact that both our model for the initial lithospheric thickness and the geodynamic model do not capture the behavior of faults or thinning of lithosphere and crust during the rifting phase accurately.

Data Set S1. The presented models were computed with an extended version of the ASPECT modelling software. The core functionality remains unchanged, but is extended by specific initial and boundary conditions as well as an individual material model and a new postprocessing plugin. The used source code is available online at: *https://github.com/gassmoeller/aspect/tree/tristan_plume_model*. Alternatively, we provide a patch file in this data supplement that can be applied to git commit f710e23a8bf204512cbc8fb33235fe31b818970b of the official ASPECT repository and modifies the code to exactly the state used for this study.

Data Set S2.

Plate boundary reconstructions for the time interval as indicated in the file name.

Data files: 'plates' files represent ASCII maps of the model region (165 x 165 characters) for the time indicated in the file name. Each character determines on which plate the according model position is located and changes of neighboring characters denote the plate boundaries (S = South America, A = Africa, C = Colorado, P = Parana). The 'velocities' file is a map between plate identification character (C), and velocity (v), thereby velocity is defined as:

$$v_x(\vec{x}, t) = v_{EC} - \omega * y \tag{3.9}$$

$$v_y(\vec{x}, t) = v_{NC} + \omega * x \tag{3.10}$$

Velocities are given in units of cm/yr, positions ($\vec{x}$ with $\vec{x} = x * \vec{e}_x + y * \vec{e}_y$) in units of km.

Figure files: Contours show plate boundaries. Blue means old end, red means young end. Also shown are hotspot positions (blue at the beginning, red at the end, for map_100_80.jpg violet at 90 Ma). Black, green, olive green and orange lines indicate plate velocities corresponding to the center of the box (i.e. v_E and v_N in file velocities) with length of lines corresponding to total displacement in 10 Myr, for African, South American (Amazonian), Parana and Colorado plates, respectively.

Data Set S3. Global mantle flow that was computed by a coarser global mantle convection model as described in Supplementary text S1 and the main manuscript. This boundary velocity is used in all models except NoGlobalFlow. Files are named according to their boundary and time in Ma BP, and contain two coordinate columns in the order x,y,z (whichever 2 apply for the respective boundary) and three columns containing the velocity components in cm/yr.

Data Set S4. Plume motion data as used in the different models ordered by time in Ma BP,x,y. Files are named according to the used model. The '.surface' files contain the original plume motion model from the cited references. The '.bottom' files contain the used motion model, which is modified as described in the main manuscript to ensure that prescribing the plume at this position at the bottom of the model will lead to a plume arrival close to the position described in the '.surface' files.

Data Set S5. Time snapshots of the reference model in 5 Ma intervals. For a description of the panels see the caption of Supplementary Movie S1.

Movie S1.

Time evolution of the reference model. The top left panel shows a temperature isosurface 50 K hotter than the surrounding mantle and the view is from south to north. The bottom left panel shows the same isosurface from west to east. Mid top panel shows the depth of the 1613 K isosurface, which we interpret here as a proxy for the depth of the lithosphere. Mid bottom panel shows transparent isosurfaces of melt fraction, in a top view and colored by melt fraction (isosurfaces are: 5%, 10%, 15%, 20%). Top right panel shows an approximation of isostatic topography by assuming that one eighth of the crustal thickness is compensated by topography and neglecting dynamic topography and elastic compensation. This panel is meant as proxy for real topography, small wavelength features would likely be modified when considering elastic effects. The panel uses a vertical exaggeration factor of 80. Bottom right panel shows a map view of crustal thickness, identical to the ones shown in Figure 3.8 and 3.10. Lineations of reduced crustal thickness in this panel originate at regions of reduced melt productivity at transform faults in the ridge geometry. They preferentially form at times of oblique rifting (ridge geometry and plate motions are prescribed in our model) and align with the plate motions after their creation.

Movie S2.

Time evolution of the crust generation and region of melting in the reference model. The left panel shows the new plume-generated crust during the last output interval (250,000 years). We calculate the plume-related crust as the difference in crust production between the reference model and the model without plume. Note the change between off-ridge and on-ridge plume arrival around 45 Ma. The right panel shows corresponding East-West

slices approximately through the center of melt generation. Colors show temperature difference to an adiabatic profile and the black contour line shows the region of melting. Note that the contour shows the region of melting for undepleted material, while the left panel shows the position of actual crust generation (i.e. where the melt fraction exceeds the depletion).

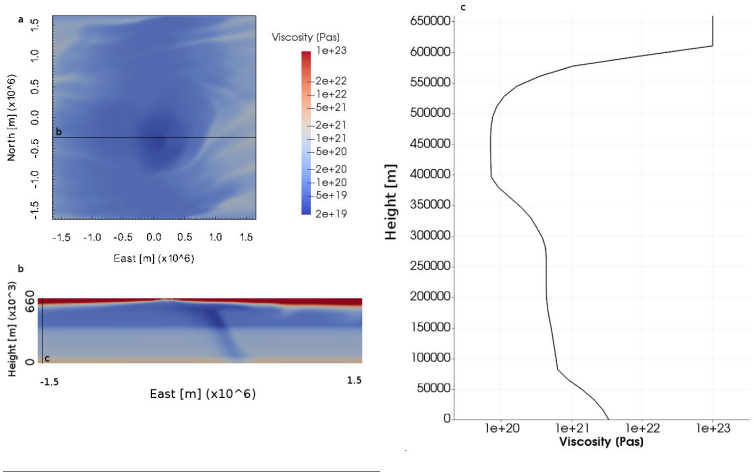

Figure S1: Viscosity distribution in the geodynamic model. (a) Map view of the viscosity distribution in the reference model in 110 km depth. The cross section shown in (b) is marked as a solid line. (b) Cross section through the reference model, showing the viscosity distribution. The plume reduces the viscosity by approximately a factor of four. The profile shown in (c) is marked as a solid line. (c) Viscosity profile through the reference model in a part of the model not influenced by the plume or ridge. Viscosity in the lithosphere is 10^{23} Pas, decreasing to $7 \cdot 10^{19}$ Pas in the asthenosphere, and increasing again towards the lower mantle.

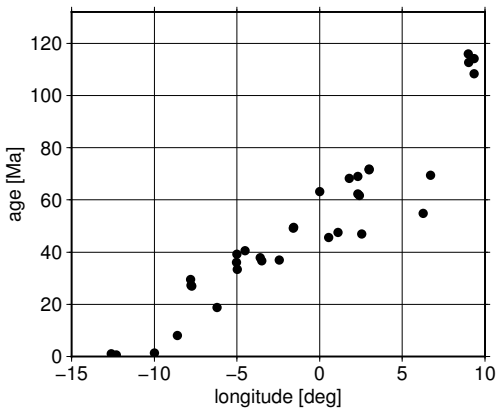

Figure S2: Radiometric seamount ages as in Figure 3.5 along Walvis Ridge versus longitude. Data fall within a band about 5 degrees wide for given age. This spread can be compared with the extent of the area of melt generation at any given time in Supplementary Movie S2.

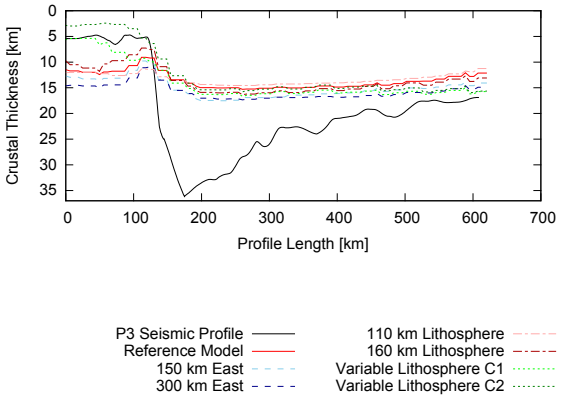

Figure S3: Crustal thickness across the Florianopolis Fracture Zone for models with different plume head position (lines in different shades of blue) and lithosphere thickness (lines in different shades of red), compared to the crustal thickness derived from seismic models (solid black line, Profile P3 of Fromm et al. (2015)). The position of the profiles is shown in Figure 3.8b. Crustal thickness is computed by passive advection of melt.

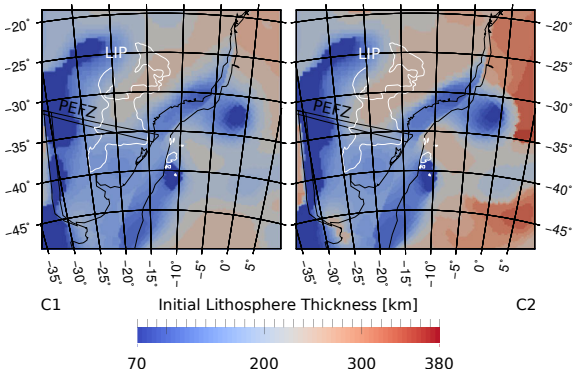

Figure S4: Initial lithosphere thickness models for model RealLithC1 (left) and RealLithC2 (right). The models were created by reconstructing present-day lithosphere thicknesses determined with the two cutoff functions in Equation 3.7 and 3.8 to 140 Ma by using the plate reconstruction listed in Supplementary Table S1. For orientation we show coastlines, Paraná-Etendeka Fault Zone (PEFZ) and Paraná-Etendeka LIPs (outlined in white) also rotated back to 140 Ma.

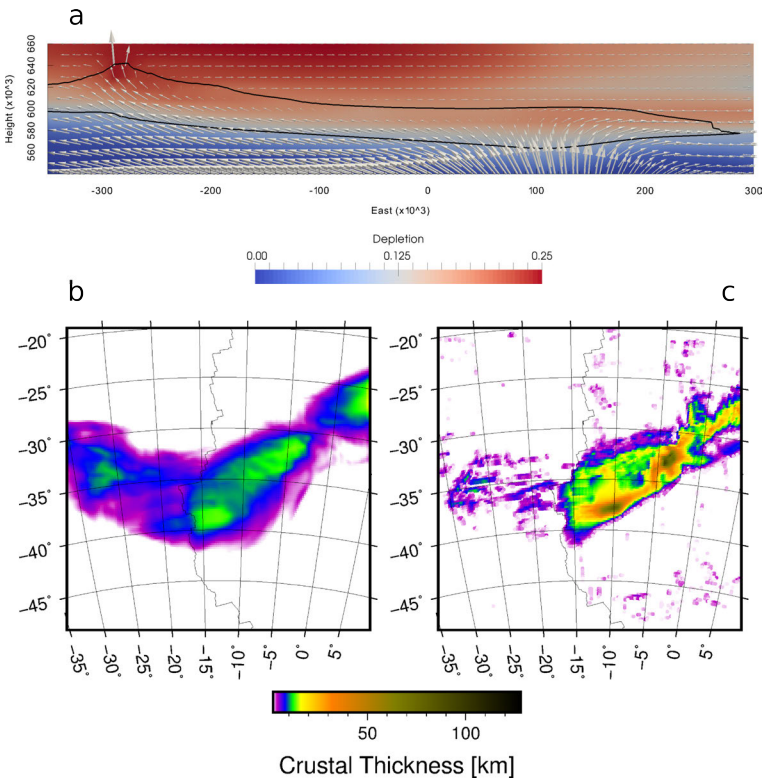

Figure S5: (a) Cross section through the reference model, illustrating the flow field (gray arrows), the melting region (outlined in black) and the depletion field $F_{\max}(x)$ (background color) close to the plume. Where melting takes places close to the mid-ocean ridge, the depletion field is focused towards the ridge, where it moves upwards and becomes part of the highly viscous layer on top of the model that moves with the plate velocity. (b) Crustal thickness computed by passive advection for the reference model. (c) Crustal thickness computed by instant melt extraction for the reference model. In both cases (b) and (c), only the additional crustal thickness relative to the case without plume is shown. Note that the figure suggests a difference in integrated melt volume. This conception is caused by lower but more widely distributed crustal thickness in (b), while the quantitative difference is only 10-15%.

Table S1: Plate rotations used in this paper. Time intervals in Ma, longitude and latitude of stage rotation poles in degrees, rotation rates in degrees per million years.

Plate	African			South American			Parana			Colorado		
time	long	lat	rate	long	lat	rate	long	lat	rate	long	lat	rate
150-140	171.27	47.65	.247									
140-130	-25.62	19.71	.491	-29.04	20.45	.471	-28.27	28.09	.397	-33.11	24.65	.334
130-120	137.18	32.55	-.846	115.49	39.55	-.770	105.67	43.55	-.641	100.18	47.20	-.664
120-110	-24.11	24.00	.191	-0.36	42.75	-.114						
110-100	-24.11	24.00	.191	-12.56	40.01	-.484						
100-90	147.52	21.31	-.367	3.53	67.01	-.572						
90-80	147.52	21.31	-.367	5.43	73.55	-.573						
80-70	158.55	22.06	-.723	161.12	62.02	-.837						
70-60	-33.84	37.48	.447	-33.94	0.94	.269						
60-50	122.90	70.71	.307	-67.91	18.52	-.119						
50-40	48.98	84.52	.113	-21.69	52.35	-.298						
40-30	-44.91	39.96	.332	60.98	61.28	-.202						
30-20	-30.18	37.17	.234	-22.21	70.60	-.235						
20-10	-15.31	33.88	.194	-64.98	68.78	-.257						
10-0	146.72	-36.66	-.161	-67.03	80.98	-.198						

Bibliography

Agrusta, R. et al. (2013). "Small-scale convection in a plume-fed low-viscosity layer beneath a moving plate". *Geophysical Journal International* 194 (2): 591–610.

Albers, M. and U. R. Christensen (2001). "Channeling of plume flow beneath mid-ocean ridges". *Earth and Planetary Science Letters* 187 (1-2): 207–220.

Assumpção, M. et al. (2013). "Models of crustal thickness for South America from seismic refraction, receiver functions and surface wave tomography". *Tectonophysics* 609: 82–96.

Ballmer, M. D. et al. (2011). "Spatial and temporal variability in Hawaiian hotspot volcanism induced by small-scale convection". *Nature Geoscience* 4: 457–460.

Ballmer, M. D. et al. (2013). "Non-hotspot volcano chains produced by migration of shear-driven upwelling toward the East Pacific Rise". *Geology* 41 (4): 479–482.

Bangerth, W., T. Heister, et al. (2015). ASPECT*: Advanced Solver for Problems in Earth's ConvecTion*. Computational Infrastructure for Geodynamics.

Becker, K. et al. (2014). "Asymmetry of high-velocity lower crust on the South Atlantic rifted margins and implications for the interplay of magmatism and tectonics in continental breakup". English. *Solid Earth* 5 (2): 1011–1026.

Becker, T. W. and L. Boschi (2002). "A comparison of tomographic and geodynamic mantle models". *Geochemistry, Geophysics, Geosystems* 3 (1).

Braitenberg, C. (2015). "Exploration of tectonic structures with GOCE in Africa and across-continents". *International Journal of Applied Earth Observation and Geoinformation* 35: 88–95.

Braun, M. G. and R. A. Sohn (2003). "Melt migration in plume–ridge systems". *Earth and Planetary Science Letters* 213 (3): 417–430.

Brune, S. et al. (2014). "Rift migration explains continental margin asymmetry and crustal hyper-extension". *Nature Communications* 5: 4014.

Bryan, S. E. and R. E. Ernst (2008). "Revised definition of Large Igneous Provinces (LIPs)". *Earth-Science Reviews* 86 (1-4): 175–202.

Buiter, S. (2014). "Geodynamics: How plumes help to break plates". *Nature* 513: 36–37.

Burov, E. and T. Gerya (2014). "Asymmetric three-dimensional topography over mantle plumes." *Nature* 513 (7516): 85–9.

Chulick, G. S., S. Detweiler, and W. D. Mooney (2013). "Seismic structure of the crust and uppermost mantle of South America and surrounding oceanic basins". *Journal of South American Earth Sciences* 42: 260–276.

Coffin, M. F. et al. (2006). "Large igneous provinces and scientific ocean drilling: Status quo and a look ahead". *Oceanography* 19 (4): 150–160.

Connolly, J. A. D. (2005). "Computation of phase equilibria by linear programming: A tool for geodynamic modeling and its application to subduction zone decarbonation". *Earth and Planetary Science Letters* 236 (1-2): 524–541.

Courtillot, V et al. (1999). "On causal links between flood basalts and continental breakup". *Earth and Planetary Science Letters* 166 (3-4): 177–195.

Davies, G. F. (1988). "Ocean bathymetry and mantle convection: 1. Large-scale flow and hotspots". *Journal of Geophysical Research* 93 (B9): 10467–10480.

de Assis Janasi, V., V. A. de Freitas, and L. H. Heaman (2011). "The onset of flood basalt volcanism, Northern Paraná Basin, Brazil: A precise U-Pb baddeleyite/zircon age for a Chapecó-type dacite". *Earth and Planetary Science Letters* 302 (1–2): 147–153.

Doubrovine, P. V., B Steinberger, and T. H. Torsvik (2012). "Absolute plate motions in a reference frame defined by moving hot spots in the Pacific, Atlantic, and Indian oceans". *Journal of Geophysical Research* 117 (B9).

Farnetani, C. G. and A. W. Hofmann (2010). "Dynamics and internal structure of the Hawaiian plume". *Earth and Planetary Science Letters* 295 (1-2): 231–240.

Fromm, T. et al. (2015). "South Atlantic opening: A plume-induced breakup?" *Geology* 43 (10): 931–934.

Gibson, S. A., R. N. Thompson, and J. A. Day (2006). "Timescales and mechanisms of plume–lithosphere interactions: 40 Ar/39 Ar geochronology and geochemistry of alkaline igneous rocks from the Paraná–Etendeka large igneous province". *Earth and Planetary Science Letters* 251 (1-2): 1–17.

Gladczenko, T. P. et al. (1997). "South Atlantic volcanic margins". *Journal of the Geological Society* 154: 465–470.

Grand, S. P. (2002). "Mantle shear-wave tomography and the fate of subducted slabs". *Philosophical Transactions of the Royal Society A* 360: 2475–2491.

Gregg, P. M. et al. (2009). "Melt generation, crystallization, and extraction beneath segmented oceanic transform faults". *Journal of Geophysical Research* 114 (B11): B11102.

Heit, B. et al. (2015). "Crustal thickness and Vp/Vs ratio in NW Namibia from receiver functions: Evidence for magmatic underplating due to mantle plume-crust interaction". *Geophysical Research Letters* 42 (9): 3330–3337.

Herzberg, C. and P. D. Asimow (2008). "Petrology of some oceanic island basalts: PRIMELT2.XLS software for primary magma calculation". *Geochemistry, Geophysics, Geosystems* 9 (9): Q09001.

Herzberg, C. and E. Gazel (2009). "Petrological evidence for secular cooling in mantle plumes". *Nature* 458: 619–622.

Hieronymus, C. F. and D. Bercovici (1999). "Discrete alternating hotspot islands formed by interaction of magma transport and lithospheric flexure". *Nature* 397: 604–607.

Hieronymus, C. F. and D. Bercovici (2001). “A theoretical model of hotspot volcanism: Control on volcanic spacing and patterns via magma dynamics and lithospheric stresses”. *Journal of Geophysical Research* 106 (B1): 683–702.

Hoernle, K. et al. (2015). “How and when plume zonation appeared during the 132 Myr evolution of the Tristan Hotspot”. en. *Nature Communications* 6.

Howell, S. M. et al. (2014). “The origin of the asymmetry in the Iceland hotspot along the Mid-Atlantic Ridge from continental breakup to present-day”. *Earth and Planetary Science Letters* 392: 143–153.

Ito, G., J. Lin, and C. W. Gable (1997). “Interaction of mantle plumes and migrating mid-ocean ridges: Implications for the Galápagos plume-ridge system”. *Journal of Geophysical Research* 102 (B7): 15403–15417.

Ito, G. et al. (1999). “Mantle flow, melting, and dehydration of the Iceland mantle plume”. *Earth and Planetary Science Letters* 165 (1): 81–96.

Katz, R. F. (2008). “Magma Dynamics with the Enthalpy Method: Benchmark Solutions and Magmatic Focusing at Mid-ocean Ridges”. *Journal of Petrology* 49 (12): 2099–2121.

Katz, R. F. (2010). “Porosity-driven convection and asymmetry beneath mid-ocean ridges”. *Geochemistry, Geophysics, Geosystems* 11 (11): Q0AC07.

Katz, R. F. and S. M. Weatherley (2012). “Consequences of mantle heterogeneity for melt extraction at mid-ocean ridges”. *Earth and Planetary Science Letters* 335–336: 226–237.

Katz, R. F., M. Spiegelman, and C. H. Langmuir (2003). “A new parameterization of hydrous mantle melting”. *Geochemistry, Geophysics, Geosystems* 4 (9): 1073.

Kessling, S. (2008). “Die Tiefenstruktur der Kruste des Discovery Seamounts und des südlichen Walfischrückens im Südatlantik”. Master’s thesis. Germany: Friedrich-Schiller-Universität Jena.

Kronbichler, M., T. Heister, and W. Bangerth (2012). “High accuracy mantle convection simulation through modern numerical methods”. *Geophysical Journal International* 191 (1): 12–29.

Kundargi, R. and P. S. Hall (2014). “Geographic Patterns of Volcanism at Intraplate Hotspots”. *AGU Fall Meeting Abstracts*.

Lin, S.-C. and P. E. van Keken (2006). “Dynamics of thermochemical plumes: 1. Plume formation and entrainment of a dense layer”. *Geochemistry, Geophysics, Geosystems* 7 (2).

McKenzie, D, J Jackson, and K Priestley (2005). “Thermal structure of oceanic and continental lithosphere”. *Earth and Planetary Science Letters* 233 (3-4): 337–349.

Mihalffy, P., B. Steinberger, and H. Schmeling (2008). “The effect of the large-scale mantle flow field on the Iceland hotspot track”. *Tectonophysics* 447: 5–18.

Moore, W. B., G. Schubert, and P. Tackley (1998). “Three-dimensional simulations of plume-lithosphere interaction at the Hawaiian swell”. *Science* 279: 1008–1011.

Moore, W. B., G. Schubert, and P. J. Tackley (1999). “The role of rheology in lithospheric thinning by mantle plumes”. *Geophysical Research Letters* 26 (8): 1073–1076.

Morgan, J. P., J. Hasenclever, and C Shi (2013). "New observational and experimental evidence for a plume-fed asthenosphere boundary layer in mantle convection". *Earth and Planetary Science Letters* 366: 99–111.

Morgan, W. J. (1971). "Convection Plumes in the Lower Mantle". *Nature* 230: 42–43.

Morgan, W. J. (1978). "Rodriguez, Darwin, Amsterdam, ..., A second type of Hotspot Island". *Journal of Geophysical Research* 83 (B11): 5355–5360.

Müller, R. D. et al. (2008). "Age, spreading rates, and spreading asymmetry of the world's ocean crust". *Geochemistry Geophysics Geosystems* 9 (4): Q04006.

Nielsen, T. K. and J. R. Hopper (2004). "From rift to drift: Mantle melting during continental breakup". *Geochemistry, Geophysics, Geosystems* 5: Q07003.

O'Connor, J. M. and R. A. Duncan (1990). "Evolution of the Walvis Ridge - Rio Grande Rise Hot Spot System: Implications for African and South American Plate motions over plumes". *Journal of Geophysical Research* 95: 17475–17502.

O'Connor, J. M. and W. Jokat (2015a). "Age distribution of Ocean Drill sites across the Central Walvis Ridge indicates plate boundary control of plume volcanism in the South Atlantic". *Earth and Planetary Science Letters* 424: 179–190.

O'Connor, J. M. and W. Jokat (2015b). "Tracking the Tristan-Gough mantle plume using discrete chains of intraplate volcanic centers buried in the Walvis Ridge". *Geology* 43 (8): 715–718.

O'Connor, J. M. and A. P. le Roex (1992). "South Atlantic hot spot-plume systems: 1. Distribution of volcanism in time and space". *Earth and Planetary Science Letters* 113 (3): 343–364.

O'Connor, J. M. et al. (2012). "Hotspot trails in the South Atlantic controlled by plume and plate tectonic processes". *Nature Geoscience* 5: 735–738.

Peate, D. W. (1997). "The Paraná-Etendeka Province". *Large Igneous Provinces: Continental, Oceanic, and Planetary Flood Volcanism*. Edited by J. J. Mahoney and M. F. Coffin. American Geophysical Union: 217–245.

Putirka, K. (2008). "Excess temperatures at ocean islands: Implications for mantle layering and convection". *Geology* 36 (4): 283–286.

Ribe, N. M. (1996). "The dynamics of plume-ridge interaction: 2. Off-ridge plumes". *Journal of Geophysical Research* 101 (B7): 16195–16204.

Ribe, N. M and U. R Christensen (1999). "The dynamical origin of Hawaiian volcanism". *Earth and Planetary Science Letters* 171 (4): 517–531.

Richards, M. A., R. A. Duncan, and V. E. Courtillot (1989). "Flood Basalts and Hot-Spot Tracks: Plume Heads and Tails". *Science* 246 (4926): 103–107.

Ringwood, A. E. and T. Irifune (1988). "Nature of the 650-km seismic discontinuity: implications for mantle dynamics and differentiation". *Nature* 331: 131–136.

Rohde, J. K. et al. (2013). "Evidence for an age progression along the Tristan-Gough volcanic track from new 40Ar/39Ar ages on phenocryst phases". *Tectonophysics* 604: 60–71.

Ruedas, T. et al. (2004). "Temperature and melting of a ridge-centred plume with application to Iceland. Part I: Dynamics and crust production". *Geophysical Journal International* 158 (2): 729–743.

Ryberg, T. et al. (2015). "Crustal structure of northwest Namibia: Evidence for plume-rift-continent interaction". *Geology* 43 (8): 739–742.

Schaeffer, A. J. and S. Lebedev (2013). "Global shear speed structure of the upper mantle and transition zone". *Geophysical Journal International* 194: 417–449.

Schilling, J.-G. (1991). "Fluxes and excess temperatures of mantle plumes inferred from their interaction with migrating mid-ocean ridges". *Nature* 352: 397–403.

Schmeling, H. and G. Marquart (2008). "Crustal accretion and dynamic feedback on mantle melting of a ridge centred plume: The Iceland case". *Tectonophysics* 447 (1-4): 31–52.

Schmeling, H. and H. Wallner (2012). "Magmatic lithospheric heating and weakening during continental rifting: A simple scaling law, a 2-D thermomechanical rifting model and the East African Rift System". *Geochemistry, Geophysics, Geosystems* 13 (8). Q08001: n/a–n/a.

Sleep, N. H. (1990). "Hotspots and Mantle Plumes: Some Phenomenology". *Journal of Geophysical Research* 95 (B5): 6715–6736.

Sleep, N. H. (1997). "Lateral flow and ponding of starting plume material". *Journal of Geophysical Research* 102 (B5): 10001–10012.

Sleep, N. H. (2002). "Ridge-crossing mantle plumes and gaps in tracks". *Geochemistry, Geophysics, Geosystems* 3 (12): 8505.

Sobolev, A. V. et al. (2007). "The Amount of Recycled Crust in Sources of Mantle-Derived Melts". *Science* 316 (5823): 412–417.

Sobolev, S. V. et al. (2011). "Linking mantle plumes, large igneous provinces and environmental catastrophes". *Nature* 477: 312–316.

Steinberger, B. (2016). "Topography caused by mantle density variations: Observation-based estimates and models derived from tomography and lithosphere thickness". *Geophysical Journal International* in press.

Steinberger, B. and A. R. Calderwood (2006). "Models of large-scale viscous flow in the Earth's mantle with constraints from mineral physics and surface observations". *Geophysical Journal International* 167 (3): 1461–1481.

Steinberger, B. and R. Holme (2008). "Mantle flow models with core-mantle boundary constraints and chemical heterogeneities in the lowermost mantle". *Journal of Geophysical Research* 113: B05403.

Steinberger, B. and T. H. Torsvik (2008). "Absolute plate motions and true polar wander in the absence of hotspot tracks". *Nature* 452: 620–623.

Steinberger, B., R. Sutherland, and R. J. O'Connell (2004). "Prediction of Emperor-Hawaii seamount locations from a revised model of global plate motion and mantle flow." *Nature* 430 (6996): 167–173.

Steinberger, B. et al. (2015). "The key role of global solid-Earth processes in preconditioning Greenland's glaciation since the Pliocene". *Terra Nova* 27 (1): 1–8.

Stixrude, L. and C. Lithgow-Bertelloni (2011). "Thermodynamics of mantle minerals - II. Phase equilibria". *Geophysical Journal International* 184 (3): 1180–1213.

Tan, E et al. (2006). "GeoFramework: Coupling multiple models of mantle convection within a computational framework". *Geochemistry, Geophysics, Geosystems* 7 (6).

Thiede, D. S. and P. M. Vasconcelos (2010). "Paraná flood basalts: Rapid extrusion hypothesis confirmed by new 40Ar/39Ar results". *Geology* 38 (8): 747–750.

Torsvik, T. H. and L. R. M. Cocks (2013). "Gondwana from top to base in space and time". *Gondwana Research* 24 (3–4): 999–1030.

Torsvik, T. H. et al. (2006). "Large igneous provinces generated from the margins of the large low-velocity provinces in the deep mantle". *Geophysical Journal International* 167 (3): 1447–1460.

Torsvik, T. H. et al. (2009). "A new scheme for the opening of the South Atlantic Ocean and the dissection of an Aptian salt basin". *Geophysical Journal International* 177 (3): 1315–1333.

Torsvik, T. H. et al. (2010). "Plate tectonics and net lithosphere rotation over the past 150 My". *Earth and Planetary Science Letters* 291 (1-4): 106–112.

Weatherley, S. M. and R. F. Katz (2012). "Melting and channelized magmatic flow in chemically heterogeneous, upwelling mantle". *Geochemistry, Geophysics, Geosystems* 13 (5).

Weeraratne, D. S. et al. (2007). "Rayleigh wave tomography beneath intraplate volcanic ridges in the South Pacific". *Journal of Geophysical Research* 112 (B6).

Wegener, A. (1915). "Die Entstehung der Kontinente und Ozeane (first edition)". *Friedr. Vieweg & Sohn, Braunschweig.*

Wessel, P. et al. (2013). "Generic Mapping Tools: Improved Version Released". *Eos, Transactions American Geophysical Union* 94 (45): 409–410.

Chapter 4

3D Compressible Melt Transport with Mesh Adaptivity

A version of this chapter is submitted to Geophysical Journal International as Dannberg, J., Heister, T. (2015) 3D Compressible Melt Transport with Mesh Adaptivity.

Abstract

Melt generation and migration are important processes for the evolution of the Earth's interior and impact the global convection of the mantle. While they have been the subject of numerous investigations, the typical time and length-scales of melt transport are vastly different from global mantle convection, which determines where melt is generated. This makes it difficult to study mantle convection and melt migration in a unified framework. The equations that describe coupled Stokes-Darcy flow have been derived a long time ago and they have been successfully implemented and applied in numerical models. However, modelling magma dynamics poses the challenge of highly non-linear and spatially variable material properties, in particular the viscosity. In addition, previous models neglected the individual compressibilities of the solid and the fluid phase. However, experiments have shown that the melt density change from the depth of melt generation to the surface leads to a volume increase of up to 20%. Considering these volume changes in both phases also ensures self-consistency of models that strive to link melt generation to processes in the deeper mantle, where the compressibility of the solid phase becomes more important. Here, we describe our extension of the finite element mantle convection code ASPECT that adds equations describing the behaviour of silicate melt percolating through and interacting with a viscously deforming host rock. We use the original compressible formulation of the McKenzie equations, augmented by an equation for the conservation of energy. This approach includes both melt migration and melt generation with the accompanying latent heat effects. Applying adaptive mesh refinement to this type of problems is particularly advantageous, as the resolution can be increased in mesh cells where melt is present and viscosity gradients are high, whereas a lower resolution is sufficient in regions without melt. Together with a high-performance, massively parallel implementation, this allows for high resolution, 3d, compressible, global mantle convection simulations coupled with melt migration. We evaluate the functionality and potential of this method using a series of benchmarks and model setups relevant for applications, compare results of the compressible and incompressible formulation and show the effectiveness of adaptive mesh refinement when applied to melt migration. Our model of magma dynamics

provides a framework for modelling processes on different scales and investigating links between processes occurring in the deep mantle and melt generation and migration. This approach could prove particularly useful applied to modelling the generation of komatiites or other melts originating in greater depths. The ASPECT code, including all presented modifications, is available online under an Open Source license[1].

[1]Note: The modifications are currently available at `https://github.com/tjhei/aspect/tree/melt_reorder_fields` and will be incorporated into the official ASPECT release in the very near future. All model input files, scripts and data files that are required to reproduce the presented results are available at `https://github.com/jdannberg/melt-transport-data`.

4.1 Introduction

Mantle convection and melt migration are important processes for our understanding of the physics of the Earth's interior and how it is linked to observations at the surface. Both processes have been studied in much detail individually, however, most studies of solid-state creep in the Earth's mantle such as in mantle plumes, subduction zones or mantle convection in general either do not consider melting and melt migration, or treat it in a simplified way, only computing the melting rate and extracting the melt from the model, neglecting (e.g. Sobolev et al., 2011; Ballmer et al., 2013; Gerya, 2011, and references therein) or approximating (Ruedas et al., 2004; Schmeling and Marquart, 2008; Cagnioncle et al., 2007; Mittelstaedt et al., 2011) the physics of two-phase flow and the effects of compaction. Previous modelling studies of magma dynamics comprise a wide range of applications, such as solitary waves (Simpson and Spiegelman, 2011), channelling instabilities (Weatherley and Katz, 2012), rifting (Schmeling, 2010), mid-ocean ridges (Spiegelman, 1996; Katz, 2008; Katz, 2010), melt shear bands in partially molten rocks (Spiegelman, 2003; Katz, 2006) and magma dynamics in a host rock undergoing both fracture and flow (Keller et al., 2013). However, these models often do not include the feedback of the melt on the solid mantle flow, they have only been carried out in two dimensions, and although they take into account the compaction of the solid matrix by changes in melt fraction, they treat both individual phases as incompressible.

These simplifications are valid on small scales, but become more limiting when linking surface observation to the deeper mantle and studying the interaction of mantle and magma dynamics in the context of larger-scale structures such as mantle plumes, subduction zones, and mid-ocean ridges. Typical compressibilities of mantle melts are in a range of $3.1 \cdot 10^{-11}$ to $5.3 \cdot 10^{-11}\mathrm{Pa}^{-1}$ (Agee and Walker, 1993; Ohtani and Maeda, 2001; Suzuki and Ohtani, 2003; Sanloup et al., 2013), implying that their volume can increase 7–11% per 100 km they ascend from the melting region. This volume change is especially important for melt generated in greater depths, such as komatiites.

Moreover, the geometry of geologic structures is not limited to two dimensions, examples being transform faults at mid-ocean ridges, plate velocities and lateral variations in the thickness of the overlying plate when a mantle plume impinges on the base of the lithosphere, and bent subduction zones or along-trench variations of oceanic crustal thickness. The three-dimensional structure of these settings has implications for the processes of melt migration, focusing and distribution of melt, and eventually the associated volcanism at the surface.

Nevertheless, several numerical challenges have prevented joint modelling of coupled magma and mantle dynamics in three dimensions so far: (1) Melt migration and mantle convection occur on widely different time and length scales, which makes it very difficult to study both processes together, as melt migration can only be resolved on a much higher resolution and using smaller time steps. (2) Important material properties strongly depend on temperature, pressure and in particular the porosity, leading for example to high viscosity contrasts of potentially more than 5 orders of magnitude often on very small length scales, which poses a challenge for iterative solvers. (3) These dependencies of the material parameters on the solution variables are strongly nonlinear, calling for advanced nonlinear solvers. All the previous points combined make it impossible to study these processes without using advanced numerical techniques and the ability to do large-scale parallel computations. We address these challenges in the following way:

1. Adaptive mesh refinement allows us to refine the mesh where melt is present and viscosity contrasts are high, and to use a coarser mesh in regions without melt,

where velocities and gradients of material properties are lower. For reaching the same accuracy overall fewer degrees of freedom and computational resources are required compared to a model with uniform mesh.

2. Parallelization of the code, scaling up to 10,000s of processors makes it possible to run models with several tens of millions of degrees of freedom, allowing for large-scale models in three dimensions that still resolve processes on the length scale of melt migration.

3. We use an iterated IMplicit Pressure Explicit Saturation (IMPES) scheme to resolve the strong non-linearity in the system, alternating the solution of the Stokes system and the advection systems until convergence is reached. We employ a generalized minimal residual method with a Wathen style block preconditioner for the Stokes part of the problem, allowing for high local and global viscosity contrasts.

The melt migration is integrated into the open source mantle convection code ASPECT (Kronbichler et al., 2012; Bangerth, Heister, et al., 2015), which is based on the deal.II finite element library (Bangerth et al., 2015). The massively parallel, adaptive computing capabilities of the underlying deal.II library (Bangerth et al., 2011) enable the computations done for this paper.

Here, we present our extension of ASPECT that models coupled magma/mantle dynamics in two and three dimensions, employing adaptive mesh refinement. It includes all of the terms of the original formulation of two-phase flow of McKenzie (1984), taking into account the compressibility of both individual phases, which makes this formulation (hereafter called fully compressible formulation) consistent also for higher pressures. Moreover, energy conservation, pressure-, temperature- and composition-dependent melt generation and latent heat effects are considered. We demonstrate the correctness and accuracy of the code by showcasing several benchmarks and convergence tests (Sections 4.4.1 and 4.4.3). Moreover, we show the effectiveness of adaptive mesh refinement using a test case that features structures expected in applications, but has an analytical solution (Sections 4.4.4). Finally, we present two- and three-dimensional application cases in earth-like settings, including mantle plumes, global mantle convection and magmatic shear bands (Sections 4.4.2, 4.4.5 and 4.4.6). The code used to generate these results is available online (Dannberg and Heister, 2015), and required input files, data files, and scripts for creating the analytic solutions are provided in the Supplementary Material (Appendix 4.C).

4.2 Problem Setup

4.2.1 Physical model

The original ASPECT mantle convection code (Kronbichler et al., 2012) models the movement of solid mantle material. These computations also allow for taking into account how partially molten material changes the material properties and the energy balance through the release of latent heat. However, this does not include melt extraction or any relative movement between melt and solid. Here, we adapt ASPECT to solve additional equations describing the behaviour of silicate melt percolating through and interacting with a viscously deforming host rock. This is implemented based on the approach of Keller et al., 2013 in the viscous limit, extended to a compressible formulation.

Our model includes two material phases: The solid matrix (denoted with index s) and the fluid melt phase (denoted with index f). The melt fraction ϕ defines averaged

Table 4.1: Explanation of some important symbols used in the paper.

Symbol	Quantity	Expression	Unit
ϕ	porosity		volume fraction
p_f	fluid pressure	$p_f = p_s - \frac{p_c}{1-\phi}$	Pa
p_s	solid pressure	$p_s = p_f + \frac{p_c}{1-\phi}$	Pa
p_c	compaction pressure	$p_c = (1-\phi)(p_s - p_f)$ $p_c = -\xi(\nabla \cdot \mathbf{u}_s)$	Pa
$\mathbf{u}_s$	solid velocity		m/yr
$\mathbf{u}_f$	fluid velocity	$\mathbf{u}_f = \mathbf{u}_s - \frac{K_D}{\phi}(\nabla p_f - \rho_f \mathbf{g})$	m/yr
$\dot{\varepsilon}$	strain rate	$\dot{\varepsilon}(\mathbf{u}_s) = \frac{1}{2}(\nabla \mathbf{u}_s + \nabla \mathbf{u}_s^T)$	1/yr
η	shear viscosity (solid)		Pa s
ξ	bulk viscosity (solid)		Pa s
η_f	shear viscosity (melt)		Pa s
K_D	Darcy coefficient	$K_D = \frac{k_\phi}{\eta_f}$	Pa

quantities $\bar{X}$ out of solid (X_s) and fluid (X_f) quantities:

$$\bar{X} = (1-\phi)X_s + \phi X_f. \tag{4.1}$$

We start from the McKenzie equations, which are derived in Appendix A of McKenzie, 1984. The mass and momentum conservation for solid and fluid are:

$$\frac{\partial}{\partial t}\left[\rho_f \phi\right] + \nabla \cdot \left[\rho_f \phi \mathbf{u}_f\right] = \Gamma, \tag{4.2}$$

$$\frac{\partial}{\partial t}\left[\rho_s (1-\phi)\right] + \nabla \cdot \left[\rho_s (1-\phi)\mathbf{u}_s\right] = -\Gamma, \tag{4.3}$$

$$\phi\left(\mathbf{u}_f - \mathbf{u}_s\right) = -K_D\left(\nabla p_f - \rho_f \mathbf{g}\right), \tag{4.4}$$

$$-\nabla \cdot \left[2\eta\left(\dot{\varepsilon}(\mathbf{u}_s) - \frac{1}{3}(\nabla \cdot \mathbf{u}_s)\mathbf{1}\right) + \xi(\nabla \cdot \mathbf{u}_s)\mathbf{1}\right] + \nabla p_f = \bar{\rho}\mathbf{g}, \tag{4.5}$$

where ρ is the density (with the index denoting solid or fluid phase), $\mathbf{g}$ is the gravitational acceleration, Γ is the melting rate, and the other symbols are as given in Table 4.1. In order to eliminate the time derivatives, and under the assumption that the flow field is in equilibrium ($\partial \rho_{s,f}/\partial t = 0$), we rewrite the first two equations to:

$$\frac{\partial \phi}{\partial t} + \nabla \cdot \left[\phi \mathbf{u}_f\right] = \frac{\Gamma}{\rho_f} - \frac{\phi}{\rho_f}\mathbf{u}_f \cdot \nabla \rho_f, \tag{4.6}$$

$$-\frac{\partial \phi}{\partial t} + \nabla \cdot \left[(1-\phi)\mathbf{u}_s\right] = -\frac{\Gamma}{\rho_s} - \frac{1-\phi}{\rho_s}\mathbf{u}_s \cdot \nabla \rho_s. \tag{4.7}$$

Now we can add (4.6) and (4.7) and get

$$\nabla \cdot \left[\phi \mathbf{u}_f + (1-\phi)\mathbf{u}_s\right] = \Gamma\left(\frac{1}{\rho_f} - \frac{1}{\rho_s}\right) - \frac{\phi}{\rho_f}\mathbf{u}_f \cdot \nabla \rho_f - \frac{1-\phi}{\rho_s}\mathbf{u}_s \cdot \nabla \rho_s. \tag{4.8}$$

To eliminate the fluid velocity $\mathbf{u}_f$ from the equations, we replace it by using Darcy's law (Equation 4.4):

$$\phi \mathbf{u}_f = \phi \mathbf{u}_s - K_D\left(\nabla p_f - \rho_f \mathbf{g}\right) \tag{4.9}$$

and get

$$\begin{aligned}\nabla \cdot \mathbf{u}_s - \nabla \cdot [K_D(\nabla p_f - \rho_f \mathbf{g})] = \Gamma \left(\frac{1}{\rho_f} - \frac{1}{\rho_s}\right) \\ - \frac{\phi}{\rho_f}\mathbf{u}_s \cdot \nabla \rho_f + \frac{K_D}{\rho_f}(\nabla p_f - \rho_f \mathbf{g}) \cdot \nabla \rho_f \\ - \frac{1-\phi}{\rho_s}\mathbf{u}_s \cdot \nabla \rho_s.\end{aligned} \tag{4.10}$$

Rearranging terms, we get

$$\begin{aligned}\nabla \cdot \mathbf{u}_s - \nabla \cdot K_D \nabla p_f - K_D \nabla p_f \cdot \frac{\nabla \rho_f}{\rho_f} = -\nabla \cdot (K_D \rho_f \mathbf{g}) \\ + \Gamma \left(\frac{1}{\rho_f} - \frac{1}{\rho_s}\right) \\ - \frac{\phi}{\rho_f}\mathbf{u}_s \cdot \nabla \rho_f - \frac{1-\phi}{\rho_s}\mathbf{u}_s \cdot \nabla \rho_s \\ - K_D \mathbf{g} \cdot \nabla \rho_f \qquad \text{in } \Omega.\end{aligned} \tag{4.11}$$

To avoid the density gradients, we can assume that the change in density (for both the solid and the fluid phase) is dominated by the change in static pressure, which can be written as $\nabla p_{s,f} \approx \nabla p_{\text{static}} \approx \rho_{s,f}\mathbf{g}$. This finally allows us to write

$$\frac{1}{\rho_{s,f}}\nabla \rho_{s,f} \approx \frac{1}{\rho_{s,f}}\frac{\partial \rho_{s,f}}{\partial p_{s,f}}\nabla p_{s,f} \approx \frac{1}{\rho_{s,f}}\frac{\partial \rho_{s,f}}{\partial p_{s,f}}\nabla p_{\text{static}} \approx \frac{1}{\rho_{s,f}}\frac{\partial \rho_{s,f}}{\partial p_{s,f}}\rho_{s,f}\mathbf{g} = \kappa_{s,f}\rho_{s,f}\mathbf{g}, \tag{4.12}$$

where $\kappa_{s,f}$ are the compressibilities of solid and fluid, respectively. We can now replace Equation (4.11) by

$$\begin{aligned}\nabla \cdot \mathbf{u}_s - \nabla \cdot K_D \nabla p_f - K_D \kappa_f \rho_f \nabla p_f \cdot \mathbf{g} = -\nabla \cdot (K_D \rho_f \mathbf{g}) \\ + \Gamma \left(\frac{1}{\rho_f} - \frac{1}{\rho_s}\right) \\ - (\mathbf{u}_s \cdot \mathbf{g})\left[\phi \kappa_f \rho_f + (1-\phi)\kappa_s \rho_s\right] \\ - K_D \kappa_f \rho_f^2 \mathbf{g} \cdot \mathbf{g}.\end{aligned} \tag{4.13}$$

The original McKenzie formulation of the momentum equation (Equation 4.5, Equations (A16) - (A18) in McKenzie, 1984) only contains the fluid pressure. However, analogous to Keller et al., 2013 we can define a new variable, the compaction pressure, as

$$p_c = (1-\phi)(p_s - p_f).$$

The viscous constitutive law for the compaction stress in the host rock (see Keller et al., 2013, viscous limit) is

$$p_c = -\xi(\nabla \cdot \mathbf{u}_s), \tag{4.14}$$

which allows us to replace the compaction term in (4.5) by the compaction pressure:

$$-\nabla \cdot \left[2\eta\left(\dot{\varepsilon}(\mathbf{u}_s) - \frac{1}{3}(\nabla \cdot \mathbf{u}_s)\mathbf{1}\right)\right] + \nabla p_f + \nabla p_c = \bar{\rho}\mathbf{g}. \tag{4.15}$$

The final set of equations are (4.15), (4.13) and (4.14):

$$
\begin{aligned}
-\nabla\cdot\left[2\eta\left(\dot{\varepsilon}(\mathbf{u}_s)-\frac{1}{3}(\nabla\cdot\mathbf{u}_s)\mathbf{1}\right)\right]+\nabla p_f+\nabla p_c &= \bar{\rho}\mathbf{g},\\
\nabla\cdot\mathbf{u}_s-\nabla\cdot K_D\nabla p_f-K_D\kappa_f\rho_f\nabla p_f\cdot\mathbf{g} &= -\nabla\cdot(K_D\rho_f\mathbf{g})\\
&\quad+\Gamma\left(\frac{1}{\rho_f}-\frac{1}{\rho_s}\right)\\
&\quad-(\mathbf{u}_s\cdot\mathbf{g})\left[\phi\kappa_f\rho_f+(1-\phi)\kappa_s\rho_s\right]\\
&\quad-K_D\kappa_f\rho_f^2\mathbf{g}\cdot\mathbf{g},\\
\nabla\cdot\mathbf{u}_s+\frac{p_c}{\xi} &= 0.
\end{aligned}
$$

The equations are solved for the solid velocity $\mathbf{u_s}$, the fluid pressure p_f, and the compaction pressure p_c. Without the presence of melt ($\phi = 0$), the equations reduce to the standard compressible Stokes system used in ASPECT. For the material properties used in the equations, there are many different parametrisations provided in the literature, so in ASPECT these material description can be set in a material model module that can be easily modified by the user, and we will use different formulations for the various models presented in this manuscript. Through the permeability, which is often parametrized as $k_\phi = k_0\phi^n$, the Darcy coefficient K_D depends on the solution variables, as well as the shear, and compaction viscosities η and ξ, which can depend on the porosity, temperature, pressure, strain rate and composition. Common formulations for the dependence on porosity are $\eta = (1-\phi)\eta_0 e^{-\alpha_\phi\phi}$ with $\alpha_\phi \approx 25...30$ and $\xi = \eta_0\zeta\phi^{-n}$ with $n \approx 1$ and $\zeta \approx 1...10$ (e.g. Katz, 2008; Katz, 2010; Keller et al., 2013, and references therein). These dependencies introduce strong non-linearities in the equations, which have to be considered when solving the system. Note that we use a three-field instead of a two-field system of equations here, based on the results of previous studies (Rhebergen et al., 2014; Rhebergen et al., 2015) showing that the construction of a uniform preconditioner with respect to the model parameters is difficult for the two-field formulation, while preconditioners are less sensitive to these parameters for the three-field problem.

We use Dirichlet boundary conditions for the velocity and Neumann boundary conditions for the fluid pressure:

$$\mathbf{u}_s = \mathbf{f}_1 \text{ on } \partial\Omega, \tag{4.16}$$

$$\nabla p_f = \mathbf{f}_2 \text{ on } \partial\Omega. \tag{4.17}$$

Prescribing the lithostatic pressure gradient $\mathbf{f}_2 = \rho_s\mathbf{g}$ leads to melt flowing in only due to variations in the dynamic pressure, whereas $\mathbf{f}_2 = \rho_f\mathbf{g}$ together with $\mathbf{f}_1\cdot\vec{n} = 0$ leads to no in- and outflow of melt or solid. Arbitrary melt fluxes can be prescribed in addition to these options. Note that the compatibility condition implies $\int_\Omega \frac{p_c}{\xi}\,\mathrm{d}x = 0$.

Here, we do not use the visco-elasto-plastic rheology of the Keller et al. (2013) formulation. Hence, we do not consider the elastic deformation terms that would appear on the right hand side of Equation 4.15 and Equation 4.14 and that include the elastic and compaction stress evolution parameters ξ_τ and ξ_p. Moreover, our viscosity parameters η and ξ only cover viscous deformation instead of combining visco-elasticity and plastic failure.

In addition to the previously derived conservation equations for total mass and momentum (Equations 4.13 – 4.15), melt transport requires an advection equation that governs the evolution of the porosity field ϕ and an equation for the conservation of energy. Under

the assumption of equilibrium ($\partial\rho_{s,f}/\partial t = 0$) we can write Equation 4.3 as:

$$\rho_s \frac{\partial(1-\phi)}{\partial t} + \nabla\cdot[\rho_s(1-\phi)\mathbf{u}_s] = -\Gamma. \tag{4.18}$$

To bring this equation in the same form as the other advection equations in ASPECT, we replace the second term of the equation by

$$\nabla\cdot[\rho_s(1-\phi)\mathbf{u}_s] = (1-\phi)\left(\rho_s\nabla\cdot\mathbf{u}_s + \nabla\rho_s\cdot\mathbf{u}_s\right) - \nabla\phi\cdot\rho_s\mathbf{u}_s.$$

Then we use the same method as for the mass conservation and assume the change in density is dominated by the change in static pressure. This finally allows us to use Equation 4.12 to replace $\nabla\rho_s/\rho_s = \kappa_s\rho_s\mathbf{g}$ and write

$$\frac{\partial\phi}{\partial t} + \mathbf{u}_s\cdot\nabla\phi = \frac{\Gamma}{\rho_s} + (1-\phi)(\nabla\cdot\mathbf{u}_s + \kappa_s\rho_s\mathbf{g}\cdot\mathbf{u_s}). \tag{4.19}$$

In order to model melting and freezing of melt, we also need a solution for the temperature T and thus include an energy conservation equation in our model that includes radiogenic heat production, shear heating, adiabatic heating, and release and consumption of latent heat of melting/freezing:

$$\begin{aligned}\rho_s C_p\left(\frac{\partial T}{\partial t} + \mathbf{u}_s\cdot\nabla T\right) - \nabla\cdot k\nabla T = \rho_s H & \\ + 2\eta\left(\dot{\varepsilon_s} : \dot{\varepsilon_s}\right) & \\ + \alpha T\left(\mathbf{u}_s\cdot\nabla p_s\right) & \\ + T\Delta S\,\Gamma, &\end{aligned} \tag{4.20}$$

with the shear strain rate $\dot{\varepsilon_s} = \dot{\varepsilon}(\mathbf{u}_s) - \frac{1}{3}(\nabla\cdot\mathbf{u}_s)\mathbf{1}$. This formulation assumes thermal equilibrium in the whole model domain. As our emphasis is on the mechanical modelling, we do not include the effect of melt migration on the energy equation – except for the latent heat of melting and freezing $T\Delta S\,\Gamma$, which is determined by the entropy change ΔS upon melting the material completely and the melting rate Γ – and use phase-independent parametrisations for thermal expansivity α, specific heat C_p and thermal conductivity k.

4.2.2 Weak formulation

To apply the finite element method we need to derive the weak form of the equations (4.13), (4.14), and (4.15). We multiply by test functions, integrate over the domain, and integrate by parts:

$$(2\eta\dot{\varepsilon}(\mathbf{u}_s), \dot{\varepsilon}(\mathbf{v}_s)) - \frac{2}{3}\eta\left(\nabla\cdot\mathbf{u}_s, \nabla\cdot\mathbf{v}_s\right) + (\nabla p_f, \mathbf{v}_s) + (\nabla p_c, \mathbf{v}_s) = (\bar{\rho}\mathbf{g}, \mathbf{v}_s)\,, \tag{4.21}$$

$$\begin{aligned}(\nabla\cdot\mathbf{u}_s, q_f) - (\nabla\cdot K_D\nabla p_f, q_f) - (K_D\kappa_f\rho_f\nabla p_f\cdot\mathbf{g}, q_f) = & -(\nabla\cdot(K_D\rho_f\mathbf{g}), q_f) \\ & + \left(\frac{1}{\rho_f} - \frac{1}{\rho_s}\right)(\Gamma, q_f) \\ & - \left[\phi\kappa_f\rho_f + (1-\phi)\kappa_s\rho_s\right](\mathbf{u}_s\cdot\mathbf{g}, q_f) \\ & - \left(K_D\kappa_f\rho_f^2\mathbf{g}\cdot\mathbf{g}, q_f\right),\end{aligned} \tag{4.22}$$

$$(\nabla\cdot\mathbf{u}_s, q_c) + \left(\frac{1}{\xi}p_c, q_c\right) = 0. \tag{4.23}$$

For the first equation we do integration by parts on the pressure terms ($\mathbf{v} = 0$ on the boundary, so the boundary integral vanishes):

$$(2\eta\dot{\varepsilon}(\mathbf{u}_s), \dot{\varepsilon}(\mathbf{v}_s)) - \left(\frac{2}{3}\eta\nabla\cdot\mathbf{u}_s, \nabla\cdot\mathbf{v}_s\right) - (p_f, \nabla\cdot\mathbf{v}_s) - (p_c, \nabla\cdot\mathbf{v}_s) = (\bar{\rho}\mathbf{g}, \mathbf{v}_s)\,. \tag{4.24}$$

We aim to include only material properties and not their derivatives in the equations, because these material descriptions are provided by ASPECT's user-defined plugins, which are designed to be easily comprehensible and extensible. Thus, we integrate the first part on the right hand side of the second equation by parts (and pick up a boundary term):

$$(\nabla\cdot(K_D\rho_f\mathbf{g}), q_f) = -(K_D\rho_f\mathbf{g}, \nabla q_f) + \int_\Gamma q_f K_D\rho_f\mathbf{g}\cdot\vec{n}\,\mathrm{d}s.$$

We reverse the sign to later have a symmetric system:

$$\begin{aligned} -(\nabla\cdot\mathbf{u}_s, q_f) + (\nabla\cdot K_D\nabla p_f, q_f) + (K_D\kappa_f\rho_f\nabla p_f\cdot\mathbf{g}, q_f) = &-(K_D\rho_f\mathbf{g}, \nabla q_f) \\ &+ \int_\Gamma q_f K_D\rho_f\mathbf{g}\cdot\vec{n}\,\mathrm{d}s \\ &- \left(\frac{1}{\rho_f} - \frac{1}{\rho_s}\right)(\Gamma, q_f) \\ &+ \left[\phi\kappa_f\rho_f + (1-\phi)\kappa_s\rho_s\right](\mathbf{u}_s\cdot\mathbf{g}, q_f) \\ &+ \left(K_D\kappa_f\rho_f^2\mathbf{g}\cdot\mathbf{g}, q_f\right). \end{aligned} \tag{4.25}$$

The second term on the left needs to be integrated by parts to get

$$(\nabla\cdot K_D\nabla p_f, q_f) = -(K_D\nabla p_f, \nabla q_f) + \int_\Gamma q_f K_D\nabla p_f\cdot\vec{n}\,\mathrm{d}s.$$

We can use the boundary integral to prescribe Neumann boundary conditions for p_f (Equation 4.17), and with $\nabla p_f = \mathbf{f}_2$ on the boundary we can move the boundary term to the right-hand side and get:

$$\int_\Gamma q_f K_D\rho_f\mathbf{g}\cdot\vec{n}\,\mathrm{d}s - \int_\Gamma q_f K_D\nabla p_f\cdot\vec{n}\,\mathrm{d}s = -\int_\Gamma q_f K_D(\rho_f\mathbf{g} - \mathbf{f}_2)\cdot\vec{n}\,\mathrm{d}s.$$

For the third equation we also flip the sign to get

$$-(\nabla\cdot\mathbf{u}_s, q_c) - \left(\frac{1}{\xi}p_c, q_c\right) = 0. \tag{4.26}$$

Finally, the weak form reads:

$$\begin{aligned} (2\eta\dot{\varepsilon}(\mathbf{u}_s), \dot{\varepsilon}(\mathbf{v}_s)) - \left(\frac{2}{3}\eta\nabla\cdot\mathbf{u}_s, \nabla\cdot\mathbf{v}_s\right) & \\ -(p_f, \nabla\cdot\mathbf{v}_s) - (p_c, \nabla\cdot\mathbf{v}_s) = (\bar{\rho}\mathbf{g}, \mathbf{v}_s)\,, & \end{aligned} \tag{4.27}$$

$$\begin{aligned} -(\nabla\cdot\mathbf{u}_s, q_f) - (K_D\nabla p_f, \nabla q_f) & \\ + (K_D\kappa_f\rho_f\nabla p_f\cdot\mathbf{g}, q_f) = &-(K_D\rho_f\mathbf{g}, \nabla q_f) \\ &- \int_\Gamma q_f K_D(\rho_f\mathbf{g} - \mathbf{f}_2)\cdot\vec{n}\,\mathrm{d}s \\ &- \left(\frac{1}{\rho_f} - \frac{1}{\rho_s}\right)(\Gamma, q_f) \\ &+ \left[\phi\kappa_f\rho_f + (1-\phi)\kappa_s\rho_s\right](\mathbf{u}_s\cdot\mathbf{g}, q_f) \\ &+ \left(K_D\kappa_f\rho_f^2\mathbf{g}\cdot\mathbf{g}, q_f\right), \end{aligned} \tag{4.28}$$

$$-(\nabla\cdot\mathbf{u}_s, q_c) - \left(\frac{1}{\xi}p_c, q_c\right) = 0. \tag{4.29}$$

4.3 Discretization and Linear Solvers

Let $(\mathbf{u}_s, p_f, p_c) \in V^u \times V^{p_f} \times V^{p_c}$ be the continuous solutions of the weak form (4.27)–(4.29). While $V^u = \left[H_0^1(\Omega)\right]^d$ is natural (we assume homogeneous boundary conditions for simplicity here), the choice for V^{p_f} and V^{p_c} require more thought:

Unique solvability can only be expected with an additional normalization condition like $\int_\Omega p_f = 0$. If we assume $K_D > 0$ at all times, the natural space for the fluid pressure would be

$$V^{p_f} = H_*^1(\Omega) = H^1(\Omega) \cap L_*^2(\Omega),$$

while for $K_D = 0$ it reduces to $L_*^2(\Omega) = \{q \in L^2(\Omega) \mid \int_\Omega q = 0\}$ and we experience a standard inf-sup condition known from the Stokes equation.

Assuming ξ is finite, the constant in the compaction pressure p_c is already uniquely determined due to (4.29), which is essentially an L^2 projection of the divergence into p_c. The correct space here is $V^{p_c} = L^2(\Omega)$.

We now discretize using conforming finite elements on quadrilaterals. An example for a stable discretization is given by

$$V_h^u \times V_h^{p_f} \times V_h^{p_c} = Q_k^d \times Q_{k-1} \times Q_{k-1} \subset V^u \times V^{p_f} \times V^{p_c}$$

with $k \geq 2$ where Q_k is the standard continuous space of tensor-product polynomials of degree k on the reference cell. For $k = 2$ this results in the standard Taylor-Hood pair $Q_2^d \times Q_1$ for both velocity/pressure pairs. For the evolution of the melt fraction, we achieve the best results when choosing elements of degree $k-1$ for the porosity field. In this case, the divergence of the velocity, which is contained in the advection equation as a source term, and the porosity are in the same function space, and no interpolation is necessary. This guarantees that no melt is generated for a divergence-free velocity field.

As we use stable finite elements, we do not have to impose a minimum permeability to avoid stability problems, which has been done in previous finite element magma dynamics implementations. Instead, there is a continuous transition to Stokes flow for zero porosity. Nevertheless, we have to limit the compaction viscosity for low porosities to guarantee $\xi < \infty$, which would technically be possible by setting $1/\xi = 0$ and, but would make Equations 4.28 and 4.29 linear dependent.

4.3.1 Linear System

Discretizing (4.27)–(4.29), we obtain the linear system

$$\begin{pmatrix} \mathbf{A} & \mathbf{B}^T & \mathbf{B}^T \\ \mathbf{B} & \mathbf{N} & \mathbf{0} \\ \mathbf{B} & \mathbf{0} & \mathbf{K} \end{pmatrix} \begin{pmatrix} \mathbf{U}_s \\ \mathbf{P}_f \\ \mathbf{P}_c \end{pmatrix} = \begin{pmatrix} \mathbf{F} \\ \mathbf{G} \\ \mathbf{0} \end{pmatrix}. \tag{4.30}$$

Where $\mathbf{N}$ is the discretization of $(K_D \nabla p_f, \nabla q_f)$ in the incompressible case and $\mathbf{K}$ is given by $\left(\frac{1}{\xi} p_c, q_c\right)$. For compressible computations, $\mathbf{N}$ also contains the non-symmetric, third term from (4.28).

Based on the solver strategy in Rhebergen et al., 2015, we solve the block system (4.30) using flexible GMRES with the upper block triangular preconditioner (preconditioned from the right)

$$\mathbf{P}^{-1} = \begin{pmatrix} \mathbf{A} & \mathbf{B}^T & \mathbf{B}^T \\ \mathbf{0} & \mathbf{X} & \mathbf{0} \\ \mathbf{0} & \mathbf{0} & \mathbf{Y} \end{pmatrix}^{-1}.$$

For the Schur complement approximations we choose

$$\mathbf{X} = \mathbf{B}\mathbf{A}^{-1}\mathbf{B}^T + \mathbf{N} \approx \frac{1}{\eta}\mathbf{M}_{p_f} + K_D\mathbf{L}_{p_f} = \hat{\mathbf{X}}$$

and

$$\mathbf{Y} = \mathbf{B}\mathbf{A}^{-1}\mathbf{B}^T + \mathbf{K} \approx (\frac{1}{\eta} + \frac{1}{\xi})\mathbf{M}_{p_c} = \hat{\mathbf{Y}},$$

where $\mathbf{M}_*$ and $\mathbf{L}_*$ are mass and stiffness matrices, respectively. While the preconditioner $\mathbf{P}$ is only defined for constant coefficients this way, varying coefficients can be treated by pulling them into the integration for the mass and stiffness matrices in $\hat{\mathbf{X}}$ and $\hat{\mathbf{Y}}$.

The approximation for $\mathbf{A}^{-1}$ is done using an inner CG solver with a relative tolerance of 10^{-2} preconditioned by Trilinos ML applied to the diagonal blocks of $\mathbf{A}$. The Schur complement solves for $\hat{\mathbf{X}}^{-1}$ and $\hat{\mathbf{Y}}^{-1}$ are also done using CG preconditioned by a block ILU(0).

4.4 Numerical Results

In the following, we will demonstrate the accuracy and versatility of our code at the example of a number of benchmark cases and relevant setups for coupled magma/mantle dynamics applications.

4.4.1 Incompressible solitary wave benchmark

The support of non-linear solitary waves is a well-known feature of the melt migration equations, resulting from the ability of the solid matrix to compact and dilate (Barcilon and Richter, 1986; Barcilon and Lovera, 1989) and this problem has become a standard for benchmarking magma migration codes (Simpson and Spiegelman, 2011; Keller et al., 2013; Schmeling, 2000). Moreover, solitary waves have been suggested as a way of magma transport in the mantle, contributing to its episodic behaviour (Scott and Stevenson, 1986; Wiggins and Spiegelman, 1995). For 1D solitary waves, assuming constant shear and compaction viscosities and using a permeability law in form of

$$k_\phi = k_0\phi^3, \qquad \text{implying a Darcy coefficient } K_D(\phi) = \frac{k_0}{\eta_f}\phi^3,$$

and the non-dimensionalization

$$\begin{aligned} x &= \delta x' && \text{with the compaction length } \delta = \sqrt{K_D(\phi_0)(\xi + \frac{4}{3}\eta)}, \\ \phi &= \phi_0\phi' && \text{with the background porosity } \phi_0, \\ (\mathbf{u}_s, \mathbf{u}_f) &= u_0(\mathbf{u}_s, \mathbf{u}_f)' && \text{with the separation flux } \phi_0 u_0 = K_D(\phi_0)\Delta\rho g, \\ t &= \frac{\delta}{u_0}t', \end{aligned}$$

there is an analytical solution for the shape of the solitary wave, which can be written in the implicit form:

$$x(\phi) = \pm(A + 0.5)\left[-2\sqrt{A-\phi} + \frac{1}{\sqrt{A-1}}\ln\frac{\sqrt{A-1}-\sqrt{A-\phi}}{\sqrt{A-1}+\sqrt{A-\phi}}\right],$$

with $A > 1$ being the non-dimensional amplitude of the wave (Barcilon and Richter, 1986). When scaled back to physical units, this equation describes a wave with the amplitude

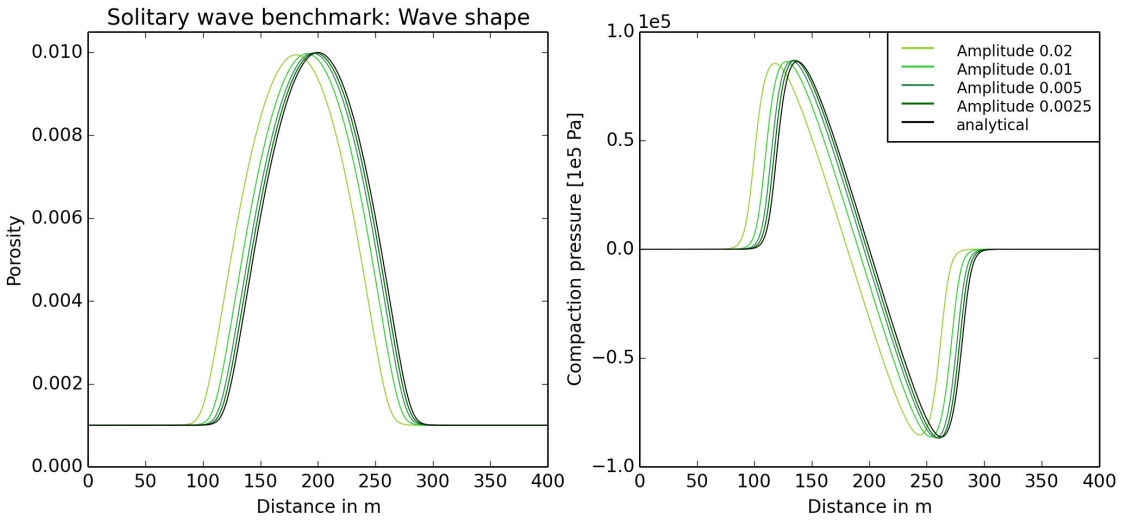

Figure 4.1: *Shape of the solitary wave in porosity (left) and compaction pressure (right) for the same resolution, but different wave amplitudes, still retaining the same non-dimensional problem, after propagating five times its wave length. The porosity is scaled according to the wave amplitude to make the plots comparable, and the end time of each model is chosen according to the phase speed of the wave (proportional to the wave amplitude) with a model time of* $t = 6 \cdot 10^6$ *years for* $A = 0.01$*. Both porosity and compaction pressure illustrate how the model result approaches the analytical solution with decreasing porosity.*

A/ϕ_0 propagating with a fixed shape and constant phase speed $c = u_0(2A/\phi_0 + 1)$ in a uniform porosity ($\phi = \phi_0$) background. This is only valid in the limit of small porosity $\phi_0 \ll 1$.

For running this 1D benchmark problem, we use a pseudo-1-D profile with only a few elements in the horizontal direction and a vertical extension of 400 m, chosen in such a way that the deviation from background porosity $\phi/\phi_0 - 1 < 10^{-7}$. The resolution in this direction is varied as multiples of two of the coarsest grid with $n_z = 160$, resulting in a resolution of 2.5 m ... 0.3 m. We apply the negative phase speed of the solitary wave $\mathbf{u}_s = -c\,\mathbf{e}_z$ as velocity boundary condition, so that the wave will stay at its original position while the background is moving, and set the end time of the model to $t = 6 \cdot 10^6$ years to allow the wave to propagate five times its wavelength. The parameters used for the model are taken from Keller et al. (2013) and are given in Table 4.2. Figure 4.1 displays the shape of the solitary wave for both porosity and compaction pressure in the final time step for different models as well as the analytical solution.

We evaluate the accuracy of our model results by comparing both the phase speed and the shape of the wave after the model runtime to this analytical solution. In order to do this, we calculate the deviation of the position of the computed wave from the analytical solution (the phase shift Δz). This is done by averaging over the the distance between points with the same porosity in both solutions:

$$\Delta z = \sum_{\phi=\phi_0}^{A/\phi_0} \frac{z_{num}(\phi) - z_{ana}(\phi)}{n}.$$

We can then use the phase shift to calculate the phase speed error

$$e_c = \left| \frac{c_{num}}{c_{ana}} - 1 \right|$$

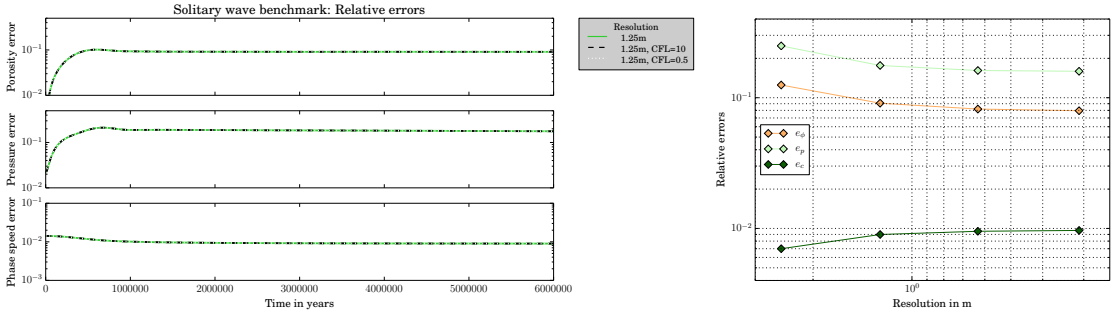

Figure 4.2: *Results of temporal (left) and spatial (right) convergence tests, plotted are the errors of the porosity e_ϕ, compaction pressure e_p and phase speed e_c relative to the 1-D analytical solution against model time and resolution, respectively. Grid resolution is chosen as multiples of two of the coarsest grid with* 160 *grid cells in vertical direction, corresponding to a cell size of* 2.5 *m ...* 0.3 *m or approximately* 1/80...1/640 *of the wavelength of the solitary wave. Time step lengths are chosen according to the CFL condition for the respective phase speed c.*

and the porosity and pressure shape errors

$$e_\phi = \frac{\|\phi_{num}(z) - \phi_{ana}(z - \Delta z)\|_2}{A},$$
$$e_p = \frac{\|p_{c_{num}}(z) - p_{c_{ana}}(z - \Delta z)\|_2}{A_p}.$$

Figure 4.2 illustrates the time evolution of these errors for simulations with different resolutions and time step sizes. After an initial transient stage, the shape and phase speed errors remain constant. This demonstrates that the code is able to capture the expected behaviour of a solitary wave that moves with a constant phase speed without changing its shape. However, the errors do not seem to converge to zero with increasing resolution. This is expected, as solitary waves are the solution of a simplified formulation of the porous flow equations that is only valid in the limit of small porosity. To show how the solution depends on the amplitude of the wave A and the background porosity ϕ_0, we performed a series of models with the same parameters as given in Table 4.2, but varying ϕ_0, and accordingly changed the reference permeability, background velocity and maximum porosity A/ϕ_0 to retain the same non-dimensional problem, only modifying the scaling. The results (Figure 4.3) show that all errors decrease with decreasing porosity. This is also visible in Figure 4.1, where the shape of the solitary wave approaches the one of the analytical solution for small wave amplitudes. The results show no dependence on time step size (Figure 4.2), and we attribute this to the fact that the position of the solitary wave – and the numerical solution for each time step – only changes very slowly with time because we prescribe the negative wave speed at the model boundaries.

4.4.2 Magmatic shear bands

It has been suggested and shown both numerically and experimentally that shear bands are a typical feature emerging when simple shear is applied to a partially molten rock (Stevenson, 1989; Holtzman and Kohlstedt, 2007). These shear bands are predicted to grow fastest under an angle of 45° to the orientation of highest shear stress if the rheology of the host rock is Newtonian and porosity-dependent (Spiegelman, 2003), but to develop at much smaller angles in case of a combination of porosity-dependent and power-law viscosity (Katz, 2006). We present shear band models analogous to the setup of Katz,

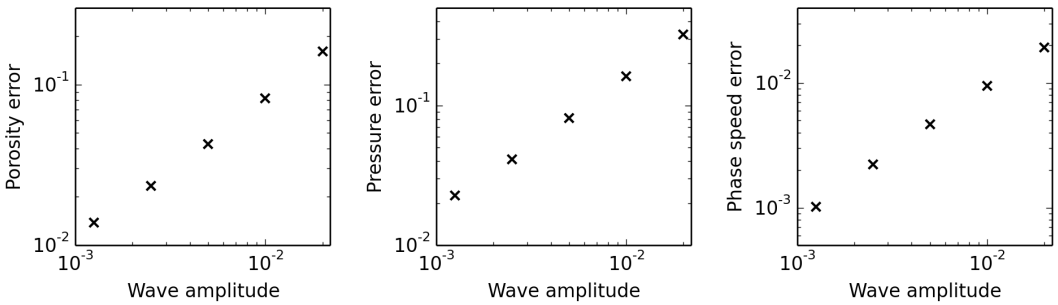

Figure 4.3: *Accuracy of the solution in dependence of the solitary wave amplitude resp. background porosity. Plotted are the shape error of porosity (left), compaction pressure (middle) and the phase speed error (right) in the final time step compared to the 1-D analytical solution. All model runs are performed with a grid resolution of* 0.625 *m and the model end time is inversely proportional to the wave speed (proportional to the wave amplitude) with a model time of* $t = 6 \cdot 10^6$ *years for* $A = 0.01$*. All errors converge to zero as the porosity approaches zero.*

Table 4.2: Parameters and scaling used for the solitary wave benchmark.

Symbol	Expression
ξ	10^{20} Pa s
η	10^{20} Pa s
η_f	100 Pa s
ρ_{s_0}	3000 kg/m^3
ρ_{f_0}	2500 kg/m^3
k_0	5×10^{-9} m^2
ϕ_0	1^{-3} (convergence tests)
	$2.5^{-4}...2^{-3}$ (porosity-dependence)
A	10
δ_0	3.41565 m
u_0	2.5×10^{-13} m/s= 7.8894×10^{-6} m/yr
c	1.656774×10^{-4} m/yr
CFL	1, 0.5, 0.25, 0.125
n_z	160, 320, 640, 1280
resolution	2.5 m, 1.25 m, 0.625 m, 0.3125 m

2006, using a power-law relation in the form

$$\eta(\phi, \dot{\varepsilon}) = \eta_0 e^{\alpha(\phi-\phi_0)} \dot{\varepsilon}_{II}^{\frac{1-n}{n}} \tag{4.31}$$

for both the porosity and strain rate dependence of viscosity with an exponent of $\alpha = -27$ for the porosity and $n = 6$ for the strain rate. The permeability is parametrised using the common formulation $k_\phi = k_0\phi^3$. The model geometry is a $4\,\text{mm} \times 1\,\text{mm}$ 2D box periodic in the horizontal direction, starting from a background porosity $\phi_0 = 0.05$ with a white noise perturbation with an amplitude of 0.0005. A constant horizontal velocity $u_s = (\pm 32\,\text{m yr}^{-1}, 0)$ in opposite directions is applied at the top and bottom boundaries, leading to a strain rate of $\dot{\varepsilon} = 1.434\ \text{s}^{-1}$, and the vertical gradients of pressure and porosity are required to be zero at these boundaries. A comprehensive list of model parameters and the material description can be found in Table 4.3. During the model evolution, elongated melt bands develop due to the applied shear; and we measure the angle of these bands after a strain of $\gamma = 1$ is reached (Figure 4.4, top). We apply a fourier transform to the porosity field of the final time step and analyse the amplitude of the resulting frequencies in dependence of their angle. Figure 4.4 (middle left) shows a histogram of these values binned by band angle. The average angle of the shear bands is then computed by fitting a log-normal to the band angle distribution. Computations with varying resolutions (Figure 4.4, middle right) show that the band angle converges to a value of approximately 17.5°, being in the range of predictions from experiments and other numerical models, where 15° – 25° to the plane of shear are reported (Katz, 2006). A model of magmatic shear bands in three dimensions, but otherwise identical setup (Figure 4.4, bottom) reveals that the modelled shear bands are indeed planar features also in 3D. They still emerge in a certain angle determined by the applied shear, while the white noise – initially randomly distributed in all three dimensions – only modulates the concentration of porosity in the band along its extension. The model has a resolution of $8\,\mu$m, which corresponds to 45 million degrees of freedom, and the full model evolution is shown in Supplementary Movie S1.

4.4.3 Compressible convergence

To set up a 2D test for melt transport including compressiblity, we developed a new benchmark with an analytical solution, choosing the velocity, density and gravity in such a way that the laterally averaged products $\rho_{f,s}\,\mathbf{u}_s$ as well as $\rho_{f,s}\,\mathbf{g}$ are constant, but the divergence of the velocity is not zero:

$$\begin{aligned}
\mathbf{u}_s(x,z) &= (0.1e^z, -0.075e^z),\\
\rho_s(x,z) &= 1.2e^{-z},\\
\rho_f(x,z) &= e^{-z},\\
\mathbf{g}(x,z) &= (0, -e^z),
\end{aligned}$$

which also leads to all the terms $\frac{\nabla\rho}{\rho}$ being constant. The remaining material parameters are constructed to create a zero horizontal component of the fluid pressure, a vertical

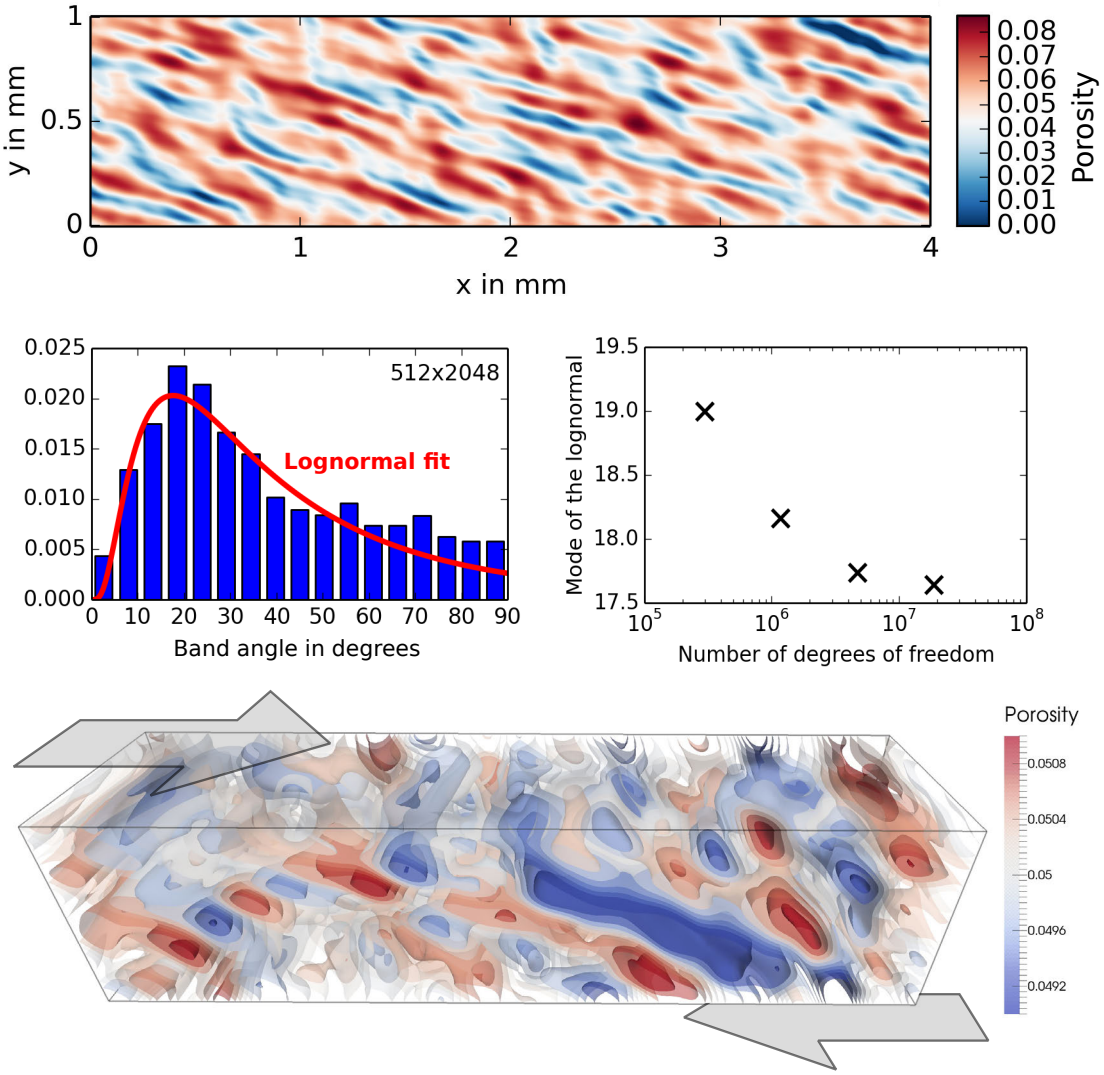

Figure 4.4: *Band angle of magmatic shear bands after a strain of $\gamma = 1$. (top) Porosity field after the final time step for a model with 512×2048 cells. (middle left) Histogram of the band angle distribution of the model shown at the top after binning in 5-degree intervals. The red line shows the best fit of a log-normal distribution to the band angle distribution. (middle right) Dominant band angle (i.e. mode of the log-normal distribution shown on the left) for models with different resolution, showing convergence to a value of $\approx 17.5°$. (bottom) Shear bands in three dimensions.*

Table 4.3: Parameters and scaling used for the shear bands, plume and global convection model.

Quantity	Shear bands model	Plume model	Global convection model
ξ_0	1.41176×10^8 Pa s	5^{18} Pa s	10^{19} Pa s
η_0	1.41176×10^7 Pa s	5^{19} Pa s	5^{21} Pa s
η_f	100 Pa s	10 Pa s	10 Pa s
ρ_{s_0}	3000 kg/m^3	3400 kg/m^3	3400 kg/m^3
ρ_{f_0}	3000 kg/m^3	3000 kg/m^3	3000 kg/m^3
k_0	5×10^{-9} m^2	5^{-9} m^2	10^{-8} m^2
n_{dis}	6	–	–
ϕ_0	0.05	0.05	– $\left(\xi \sim e^{\alpha\phi}\right)$
α	-27	-10	-10
β	–	5	7
α_{thermal}	–	3.5×10^{-5} 1/K	2×10^{-5} 1/K
T_{ref}	–	1600 K	1600 K
k_{thermal}	–	4.7 W/(m K)	4.7 W/(m K)
κ_s	–	3.2×10^{-12} 1/Pa	4.2×10^{-12} 1/Pa
κ_f	–	3.8462×10^{-11} 1/Pa	1.25×10^{-11} 1/Pa
$\frac{\partial \kappa_f}{\partial p}$	–	1.6	0
X extent	0.004 m	600 km	8700 km
Z extent	0.001 m	300 km	2900 km
u_s	$(\pm 32\text{m yr}^{-1}, 0)$	–	–
γ	1	–	–
CFL	1	1	1
n_x	128, 256, 512, 1024, 2048	adaptive (128–512)	adaptive (64–512)

component that depends only on z, and to satisfy our previous assumption that $\frac{\nabla\rho}{\rho} \approx \kappa\rho\mathbf{g}$:

$$\begin{aligned}
\eta(x,z) &= \frac{1}{2}e^{2x}, \\
\xi(x,z) &= e^{-z} + \frac{2}{3}e^{2x} + 1, \\
K_D(x,z) &= \frac{149}{45} + \frac{1}{30}e^{z}, \\
\kappa_s &= \frac{5}{6}, \\
\kappa_f &= 1, \\
\Gamma &= \frac{1}{37}e^{z},
\end{aligned}$$

This leads to the following solution for the porosity, fluid pressure, compaction pressure and fluid velocity:

$$\begin{aligned}
\phi(x,z) &= 1 - 0.3e^{z}, \\
\nabla p_f &= (0, -0.135e^{z} - 1), \\
p_c(x,z) &= 0.075\xi e^{-z}, \\
\mathbf{u}_f(x,z) &= (0.1e^{z}, -0.075e^{z} - 2.2\frac{K_D}{\phi}e^{z}).
\end{aligned}$$

The results are shown in Figure 4.5. In the top part, velocity u and porosity ϕ are converging as expected with order $k+1$ in the L^2 norm, except that we can not explain why u for $k=2$ is only converging quadratically (but the correct order is attained when discretizing with $k=3$). The melt velocity is computed as a postprocess from u and the gradient of the pressure solutions, which explains the almost linear convergence order. This is not a problem in practice, because the melt velocity is not used in the computation and is only used for visualization. The bottom half of Figure 4.5 shows convergence of the three pressures with optimal orders. Altogether, these results demonstrate the functionality and accuracy of our solver for the fully compressible formulation of two-phase flow.

4.4.4 Adaptive convergence

To demonstrate the effectiveness of adaptive mesh refinement when applied to problems of melt migration, we have set up a test case with an incompressible, analytical solution featuring a vein of high porosity standing out against a low-porosity background (Figure 4.6), and including a compaction viscosity with a Gaussian in the middle of the domain. We constructed the boundary conditions, the source term and the gravity in such a way that the the solution is:

$$\begin{aligned}
\phi &= 0.01 + 0.2\exp\left(-20(x+2z)^2\right), \\
\xi &= 0.1 + 0.1\exp\left(1 - 20(x^2+z^2)\right), \\
K_D &= \phi, \\
\mathbf{u}_s &= (x, e^{z} - z), \\
p_s &= 1 - z, \\
p_c &= -\xi\nabla\cdot u = -0.1e^{z} - 0.1e^{z}\exp\left(1 - 20(x^2+z^2)\right).
\end{aligned}$$

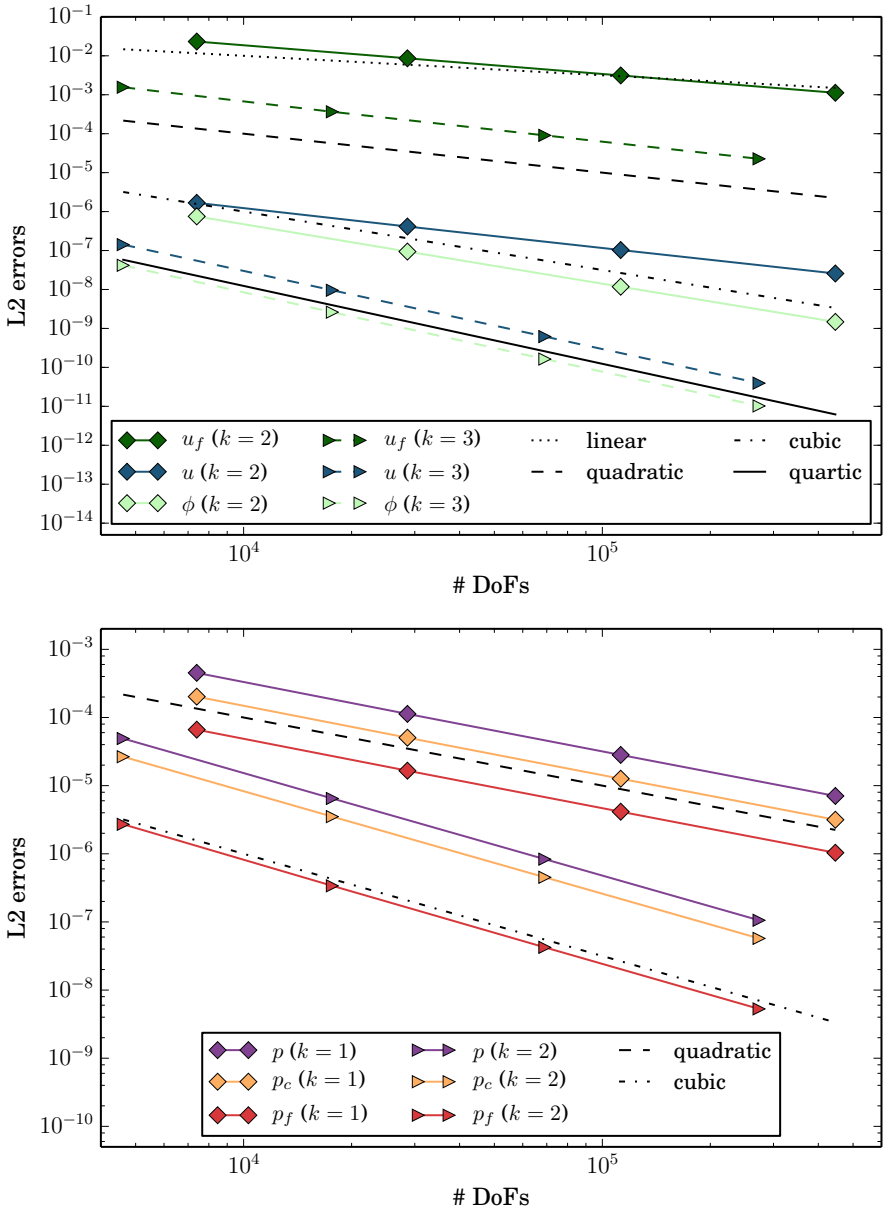

Figure 4.5: *Results of spatial convergence test for different polynomial degrees k (diamonds: $Q_2 \times Q_1$, triangles: $Q_3 \times Q_2$) Plotted are the L2 errors relative to the compressible, 2D, analytical solution. Linear, quadratic, cubic and quartic trends are shown for reference as dotted and dashed lines.*

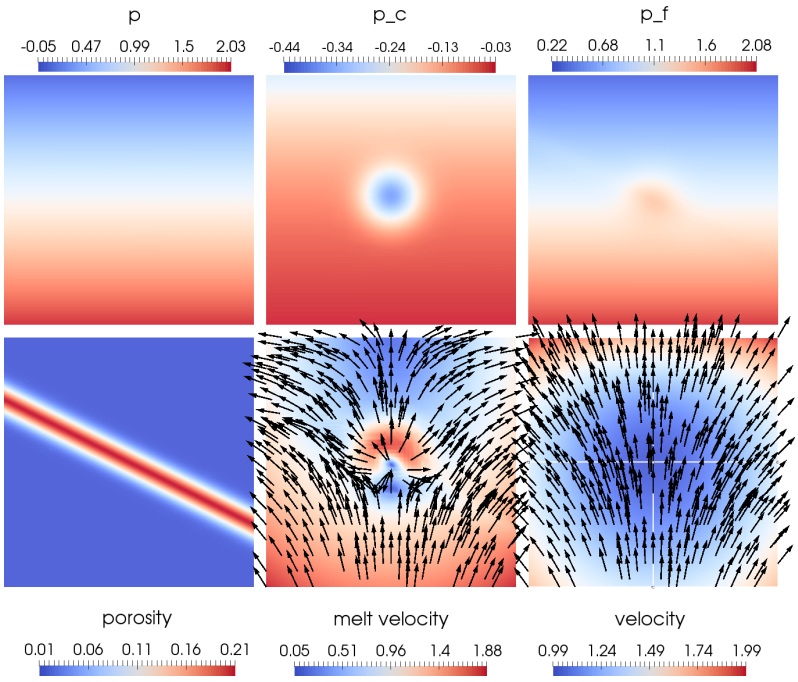

Figure 4.6: *Setup of the convergence test for adaptive mesh refinement. Top row is solid pressure, compaction pressure, and fluid pressure. Bottom row shows porosity, melt velocity, and solid velocity. The main feature is a vein of increased porosity standing out against a low-porosity background.*

A script to generate the constructed material parameters, source terms and boundary conditions can be found in the supplementary material.

In this example we use a refinement criterion employing a gradient jump estimator based on the porosity and the compaction pressure. An example mesh can be seen in Figure 4.7 and the refinement clearly captures the region of interest for the two fields in the estimator. Note that the refinement does not match the features of the velocity or solid pressure, so we can not expect superior performance compared to global refinement. While it would have been easy to improve the adaptive convergence by changing the setup to concentrate the features of every variable in the vein, we think this is a more realistic setup. Even then, the improvements in the error over global refinement are convincing and highlight how useful adaptive refinement in the setting of melt migration can be, see Figure 4.8.

In this model global refinement requires two to four times as many degrees of freedom compared to adaptive refinement (for quantities like compaction pressure, porosity, and derived quantities like melt velocity). While quantities like solid velocity see no improvement here, the errors are very small to begin with because the field is relatively smooth compared to the melt velocity. This is likely also true for most realistic problems. For realistic models we propose to combine one of these criteria with refinement based on other solution variables or material properties such as temperature or viscosity.

4.4.5 Melt transport in a rising mantle plume

When hot buoyant material in form of a mantle plume approaches the surface, the temperatures inside of the plume exceed the solidus and material starts to melt. We use this example as an application for our coupled magma/mantle dynamics code. We present two- and three-dimensional plume models, and employ both the incompressible and com-

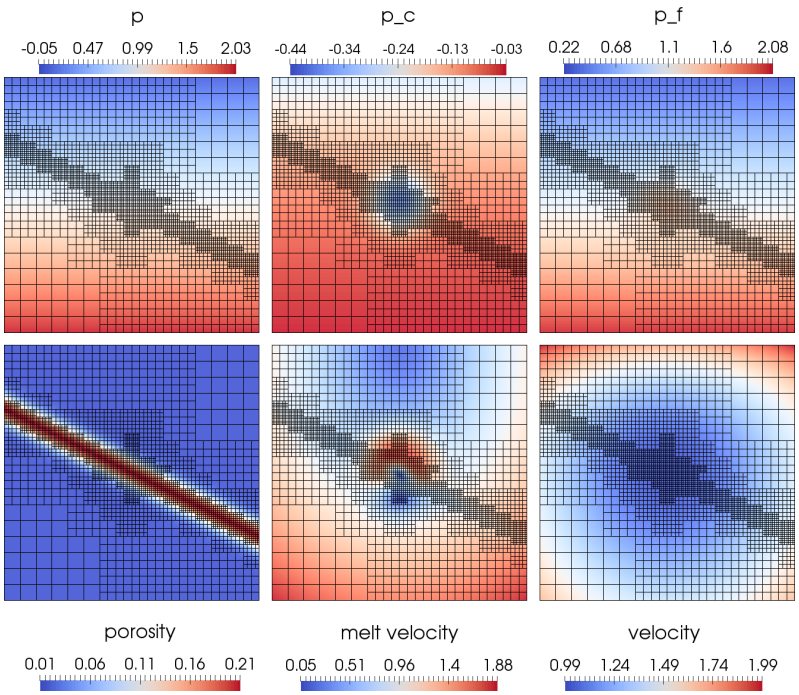

Figure 4.7: *Fields like in Figure 4.6, but showing the mesh refined using an error indicator based on a combination of porosity and compaction pressure gradient jumps. The algorithm clearly detects the peak in the compaction pressure and the vein and resolves them using small cells.*

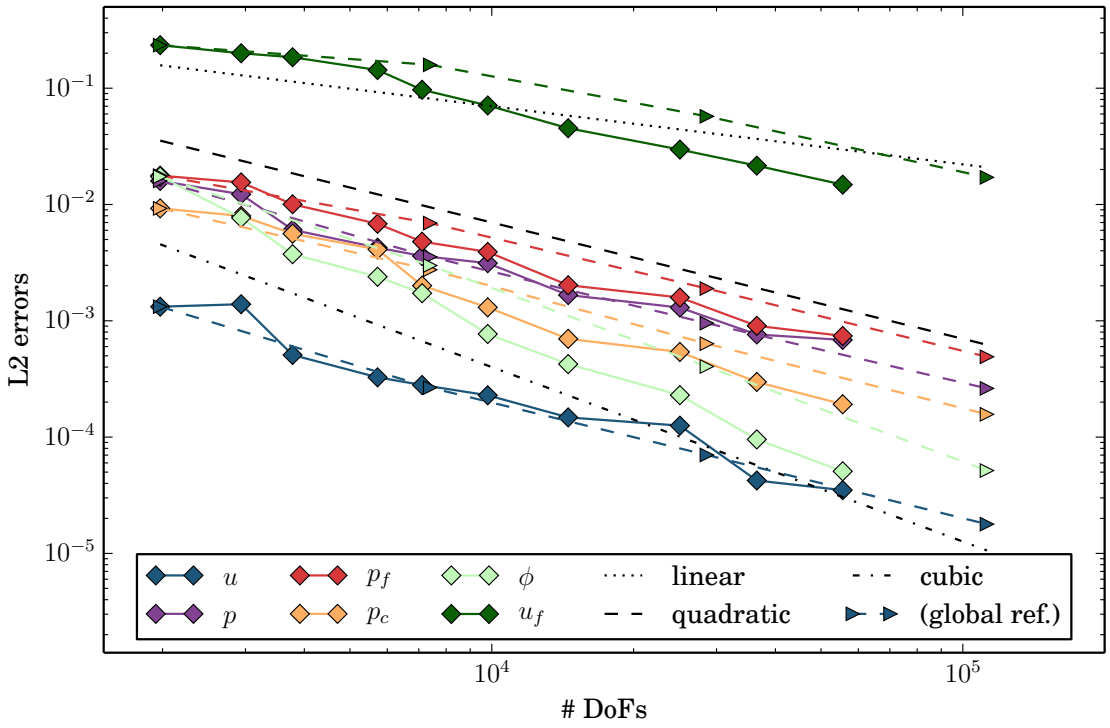

Figure 4.8: *Convergence plot of L2 errors of various quantities with adaptive refinement (solid lines with diamonds) compared to global refinement (dashed lines with triangles). As expected from the refinement in the porosity vein, the errors for porosity, compaction pressure, and fluid velocity are clearly superior, while other errors are comparable to global refinement. Linear, quadratic and cubic trends are shown for reference as dotted and dashed lines.*

pressible formulation of two-phase flow. The model domain is a Cartesian box, extending from the Earth's surface to 300 km depth and 600 km horizontally. The initial temperature profile is adiabatic with a potential temperature of 1600 K, with a cold top thermal boundary layer corresponding to oceanic lithosphere with an age of 10 million years and a top temperature of 293 K. A spherical perturbation of 250 K with a diameter of 80 km is added in the center of the bottom boundary of the model to start the plume ascent. Initially, there is no porosity present in the model. The temperature boundary conditions are prescribed according to the initial values at top and bottom, and insulating at the sides; the velocity boundary conditions are free slip everywhere except for the bottom boundary layer, where the hydrostatic pressure is applied, but material is allowed to flow in and out. This leads to inflow of hot material acting as a plume tail. The rheology is purely Newtonian, but both shear and compaction viscosity are temperature- and porosity-dependent in the form

$$\eta(\phi, T) = \eta_0 e^{\alpha(\phi-\phi_0)} e^{-\beta(T-T_0)/T_0}, \tag{4.32}$$

$$\xi(\phi, T) = \xi_0 \frac{\phi_0}{\phi} e^{-\beta(T-T_0)/T_0}, \tag{4.33}$$

with exponents of $\alpha = -5$ and $\beta = 10$, which are chosen lower compared to what experiments suggest to limit the viscosity contrast in the model to approximately 6 orders of magnitude. The melting parametrisation (Katz et al., 2003) is described in Appendix 4.A. We apply no freezing of melt here, as we are mainly interested in how the volume of generated melt evolves over time and the related differences between the compressible and incompressible formulation. However, latent heat of melting is incorporated, with an entropy change of $\Delta S = -300$ J/(kg K) upon melting.

In this setting, the porosity can exceed values of 25–35%, where the host rock ceases to be a connected matrix and starts to disaggregate into individual blocks and grains. It has been argued (Keller et al., 2013) that Darcy flow can still be a valid approximation for this type of flow, in this case describing the settling and interaction of a mush or single grains of solid in the melt phase. The permeability is then a measure for how much the relative flux of one phase is hindered by the other phase. We follow the approach of Keller et al. (2013) and use the parametrized permeability law

$$k_\phi = k_0 \phi^n (1-\phi)^m \qquad \text{with } n = 3 \text{ and } m = 2. \tag{4.34}$$

To test the influence of considering the individual compressibility of solid and fluid on the model evolution, we performed models with three different formulations of the density parametrisation (Figure 4.9a):

1. with constant melt and solid densities $\rho_f = 3000\,\mathrm{kg/m^3}$ and $\rho_s = 3400\,\mathrm{kg/m^3}$, only depending on temperature,

2. pressure- and temperature-dependent densities, with the solid density fit to PREM (Dziewonski and Anderson, 1981) and the melt density fit to data for komatiite melts (Agee and Walker, 1993) using a dependency in the form $\rho = \rho_0(1 - \alpha_{\mathrm{thermal}}(T - T_{\mathrm{adi}}))e^{\kappa p}$, but incompressible formulation of the mass and momentum conservation equation,

3. the same densities as in (2), but with the fully compressible system of equations.

A comprehensive list of model parameters can be found in Table 4.3, and except for the properties mentioned above the material model is the same as described in Section 4.4.2.

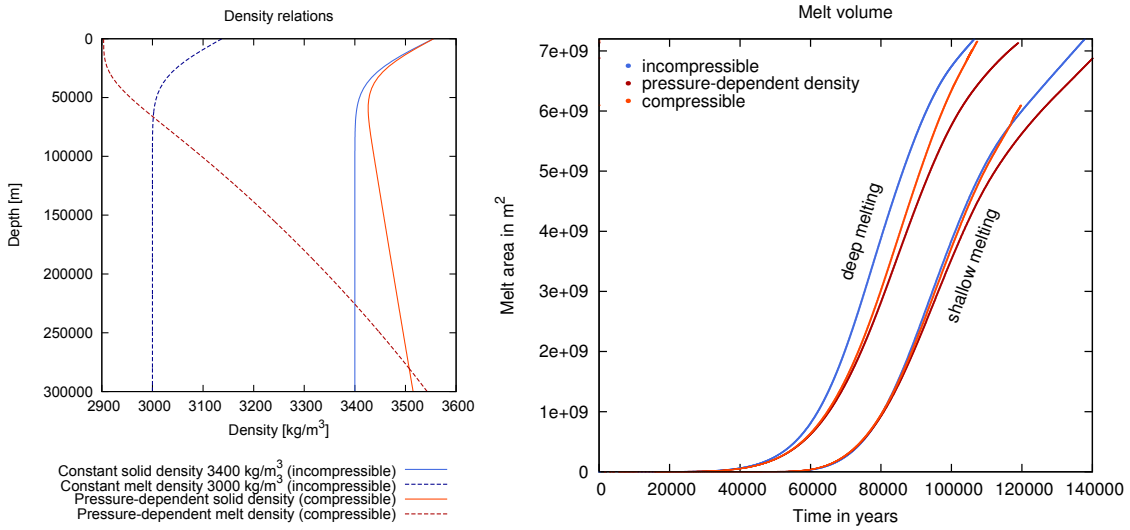

Figure 4.9: *Buoyancy and melt volume in a rising mantle plume.* ***(left)*** *Density profiles used for the different plume models: Solid lines denote solid density, dashed lines denote melt density. Colours illustrate the density formulation: Blue lines mark a density that only depends on temperature, but not on pressure, red lines mark both temperature- and pressure-dependent densities.* ***(right)*** *Development of melt volume over time in dependence of the employed density formulation. Blue lines mark a model where both solid and melt phase are individually incompressible, and the density does not depend on pressure (blue density profiles on the left, purely incompressible formulation); dark red lines mark a model where both solid and melt phase are individually incompressible, but the density depends on pressure (red density profiles on the left, this is analogue to the extended Boussinesq approximation for Stokes flow); and light red lines mark a model where both solid and melt phase are individually compressible and the density depends on pressure (red density profiles on the left, full compressible formulation). The two sets of lines mark different melting parametrisations, leading to melt production in different depth regions of the mantle.*

During the model evolution, the plume ascends from the bottom of the model due to its high buoyancy. At a pressure of approximately 5 GPa material starts to melt, lowering the viscosities and further reducing the density. While the plume rises, the melt first accumulates at its top until it reaches a depth of 50 km, where the melt starts to separate from the plume head, moving further up and spreading laterally at the base of the lithosphere (Figure 4.10). In agreement with previous studies of melt migration in mantle plumes with lower melt fractions (Schmeling, 2000), melt segregation velocities point almost vertically upwards, and within the plume head magnitudes of melt and solid velocities are comparable. Horizontal movement occurs when melt is advected with the solid plume material (for low melt fractions) and as it stagnates below the impermeable lithosphere in a melt-rich layer. The generated shear initiates small-scale downwellings of cold and dense lithosphere above into the low-viscosity plume material, leading to mixing in the plume head and thinning of the lithosphere. The full model evolution is shown in Supplementary Movie S2. We evaluate the volume of generated melt over the model evolution time and compare this quantity between the different setups (Figure 4.9b).

In the purely incompressible model, the density of the melt is very low, leading to a fast plume ascent and earlier melting and upwards migration of melt. In the models with pressure-dependent density, the buoyancy of the plume is smaller, and the plume rises more slowly. This explains the faster growth of melt volume for the purely incompressible model. However, there is also a volume difference between the compressible case and the incompressible, but pressure-dependent density case. As there is no difference in density parametrisations between these models, the plume buoyancy, melt generation rate and ascent velocity is identical. But as the compressible formulation considers the extension of the melt phase when it reaches lower pressures, a higher overall melt volume is reached in this model. The difference in melt volume between these two cases depends on the melt compressibility, but it is also influenced by where and how much melt is generated, i.e. the melting parametrisation. For melt generated at greater pressures, the change in density and thus the volume change is higher. For the example cases shown here it amounts to 5% in the case with shallow melting and 11.4% in the case with deep melting. As the models are only two-dimensional, these values technically represent melt areas, and not melt volumes, so that for a three-dimensional model an even stronger effect of compressibility (of $\Delta V \approx \Delta A^{3/2}$) is expected, leading to differences of up to 18%.

Figure 4.11 shows a model with identical setup as in the incompressible case, but in three dimensions, and illustrates how melt accumulates at the top of the rising plume head. It also demonstrates how a combination of static and adaptive mesh refinement can be used to resolve features of interest while saving computational resources: the mesh is refined statically in a cylinder around the plume and in the lithosphere, and in addition to that is refined adaptively where melt is present.

4.4.6 Influence of melt migration on a global convection model

After showcasing our implementation on a realistic example of melt migration in a rising mantle plume, we will demonstrate that with the aid of adaptive mesh refinement our software also allows it to combine models of global mantle convection and melt migration. We study how melt generation and segregation impact the dynamics of such a model by comparing a classic mantle convection model – where only the equilibrium melt fraction in dependence of temperature and pressure is computed – and a model with coupled magma/mantle dynamics, where melt is allowed to migrate. More precisely, we consider the distribution of melt, the flow field, and average velocities and temperatures.

As our focus is on the qualitative influence of melt migration on the model dynamics, we

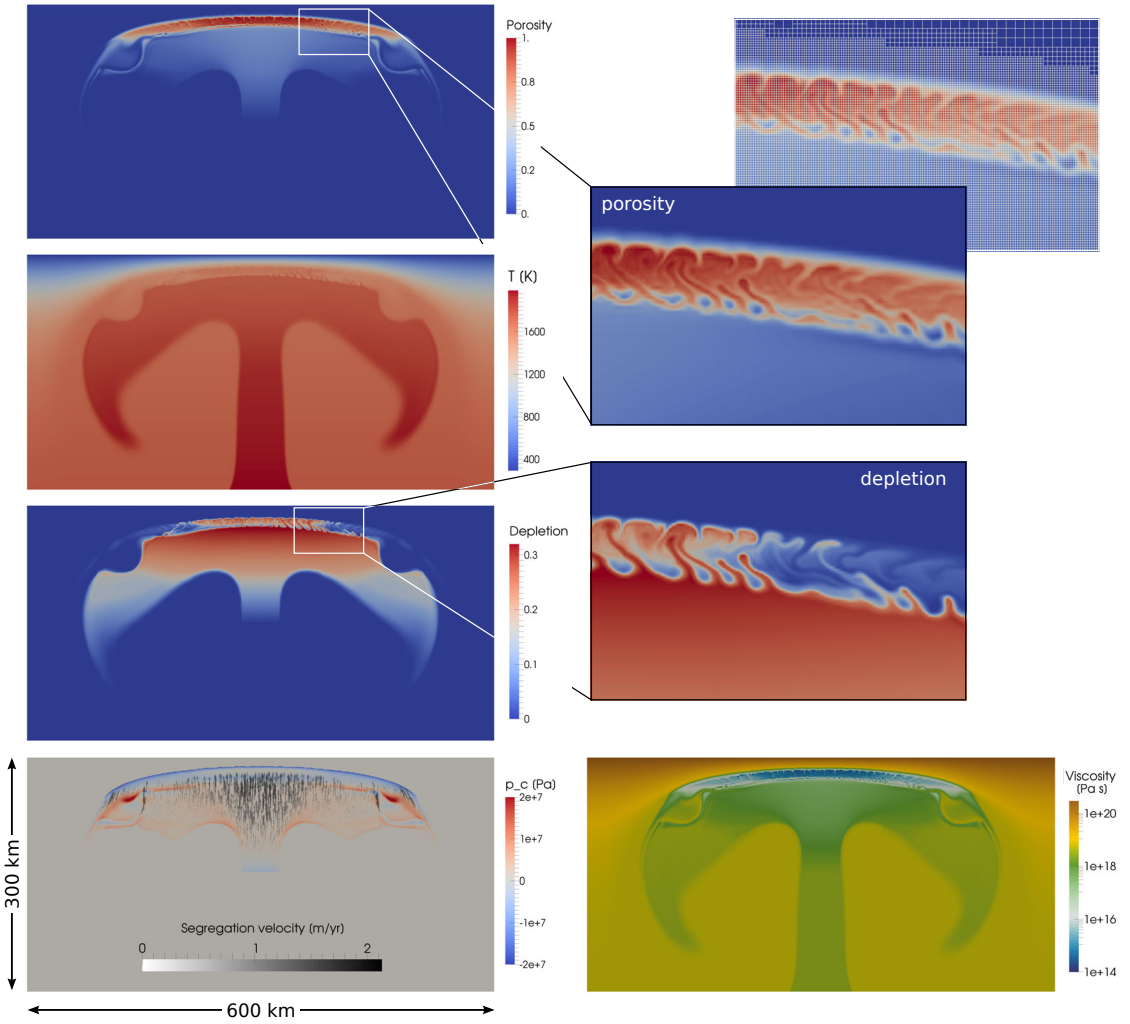

Figure 4.10: *Dynamics of melt migration in a rising mantle plume. Snapshots of melt fraction (also showing the finite element mesh), depletion, temperature, compaction pressure, segregation velocity (difference between melt and solid velocity) and viscosity in the plume after a model time of $t = 142000$ years as it spreads below the lithosphere (incompressible model). During the plume ascent, melt accumulates at the top of the plume head and starts to separate from the melting region when the plume approaches the base of the lithosphere and spreads laterally. Interaction with the cold lithosphere leads to small-scale convection and mixing inside of this lens of molten material. An animation of the plume ascent is provided in Supplementary Movie S2.*

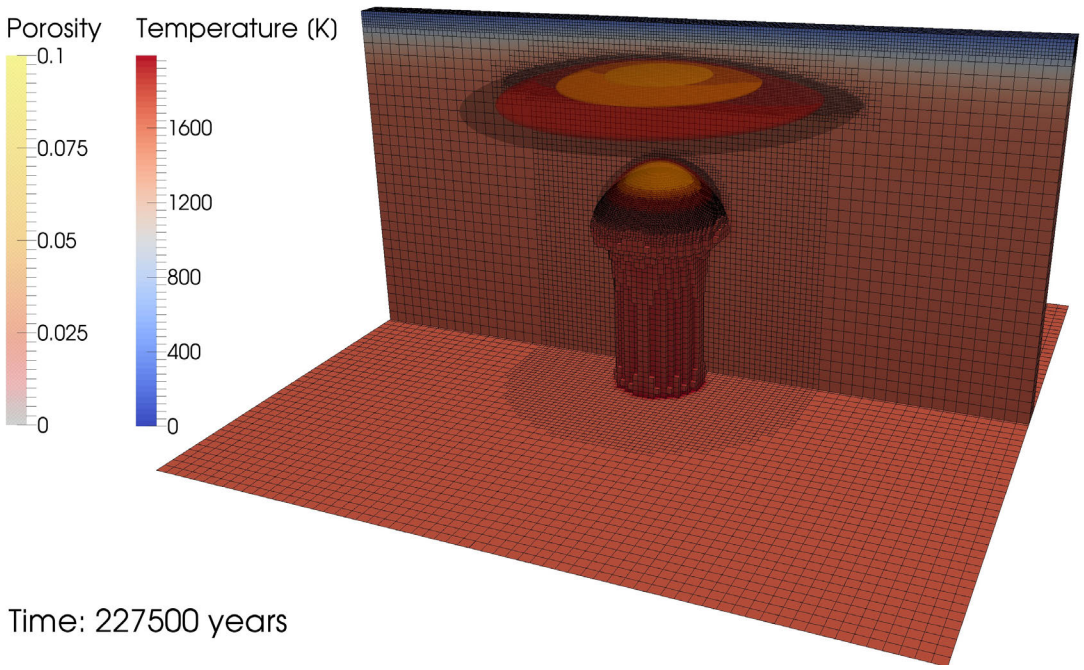

Figure 4.11: *Temperature, porosity and mesh in a three-dimensional model of melt migration in a rising mantle plume. Background colours represent temperature, contours show porosity. The mesh is refined towards the center of the plume, in the top boundary layer and adaptively in regions where melt is present.*

simplify the model setup to only include basic features important to study this dependence. We choose a Cartesian geometry with an aspect ratio of three and dimensions of 2900 × 8700 km. The model is heated from the bottom and cooled from the top, with no additional heat sources in the form of internal heating, latent heat or shear heating. We employ a simplified melting parametrisation with a linear dependence of the solidus temperature on pressure p and depletion C, and assume that the generated melt is proportional to the temperature in excess of the solidus:

$$\phi_{\text{equilibrium}} = \frac{T - T_{\text{sol}}}{T_{\text{liq}} - T_{\text{sol}}} \qquad \text{with } T_{\text{sol}} = T_{\text{sol},0} + \Delta T_p\, p + \Delta T_c\, C \tag{4.35}$$

$$T_{\text{liq}} = T_{\text{sol}} + 500 \text{ K} \tag{4.36}$$

$$T_{\text{sol},0} = 1300 \text{ K} \tag{4.37}$$

$$\Delta T_p = 6 \times 10^{-8} \text{ K/Pa} \tag{4.38}$$

$$\Delta T_c = 200 \text{ K} \tag{4.39}$$

The melting rate is computed as the difference between the equilibrium melt fraction and the melt present in the model. While these melting relations are strongly simplified, they capture the qualitative influence of temperature, pressure and depletion/enrichment on the melting rate and are an appropriate approximation for studying the general model behaviour with the present melt fractions of up to 20% and the dependence of melt generation and migration on the model dynamics. Whenever melt is generated in the model and migrates upwards, it leaves behind depleted material, and when the porosity present in the model exceeds the computed equilibrium melt fraction, melt freezes, creating enriched material. This change in material composition is modelled by a density change of the material proportional to enrichment/depletion, with depleted material being less dense and enriched material being denser than the surrounding mantle. In addition, porosity

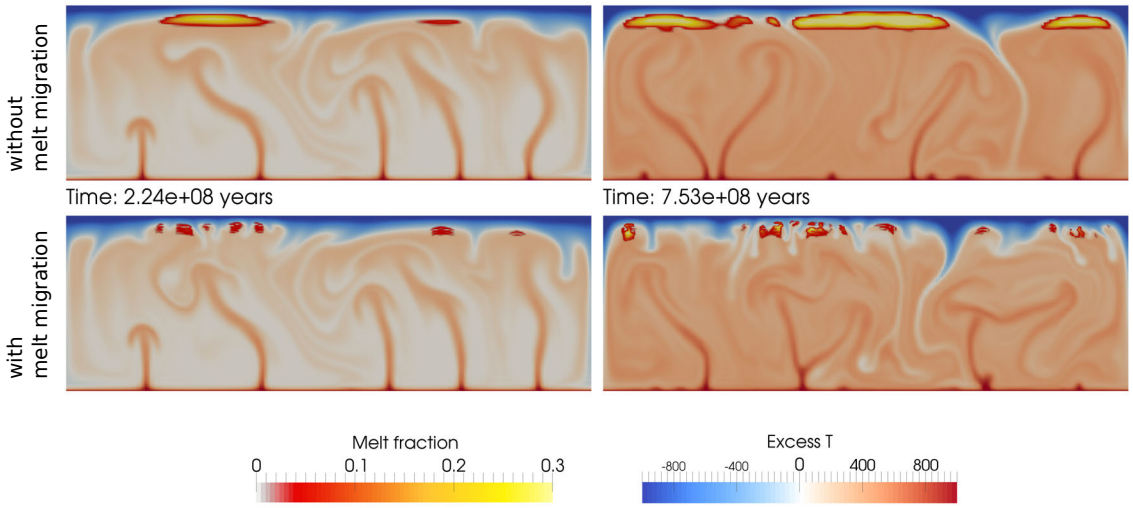

Figure 4.12: *Time snapshots of temperature and melt fraction in global models with melt migration. The upper row shows a model without melt migration, where the melt fraction is calculated as postprocessor for the present temperature and pressure conditions (i.e. batch melting), the lower row shows a model with melt migration (and fractional melting). Columns are different points in time. The model without melt migration features broad patches of melt, generated in regions of upwelling in the model. In contrast, the model with melt migration shows several smaller patches of melt with downwellings in between, where the lithosphere is eroded due to the destabilising effect of the high-density, crystallised material. Different average temperatures are due to the fact that the model initial conditions are not the steady state values, but due to the model geometry (i.e. box domain and 2D) the equilibrium conditions would not reflect realistic temperatures for the Earth.*

weakens the material as described in Section 4.4.5, except for the compaction viscosity, which follows an exponential dependence equivalent to the one for the shear viscosity. All model parameters can be found in Table 4.3.

In the classic mantle convection model (Figure 4.12, top), melt is generated by decompression melting where hot material reaches a shallow depth and partially molten areas remain relatively stationary as long as the general pattern of the flow field does not change. In the model with melt migration (Figure 4.12, bottom), the same mechanism of melt generation is active, initially leading to melting in the same regions where hot material is upwelling and approaching the surface. However, as the melt migrates upwards, it reaches regions with lower ambient mantle temperatures and starts to freeze, leaving behind depleted material that is not fertile enough to generate new melt. This means that the overall melt volume is much smaller (Figure 4.13, bottom left), as is expected for fractional melting in comparison to batch melting. Moreover, patches of enriched material created by freezing of melt influence the model dynamics: as it has a higher density than the surrounding mantle, cold and enriched material sinks down, initiating several small downwellings that do not occur in the model without melt migration. Figure 4.13 (top) illustrates the evolution of enrichment and depletion over time: As soon as melt is generated in the model, it migrates upwards from its source, where it freezes again, creating a layer of enriched material close to the top of the model, and leaving behind a layer of depleted material below, in 200 – 400 km depth. In principle, even though the model is extremely simplified, these layers correspond to the Earth's crust (or at least the part of the crust generated by plumes, as there are no divergent plate boundaries in the model where oceanic crust and lithosphere would be generated) and the asthenosphere. Of course, the melt does not migrate through the previously existing cold top layer in our

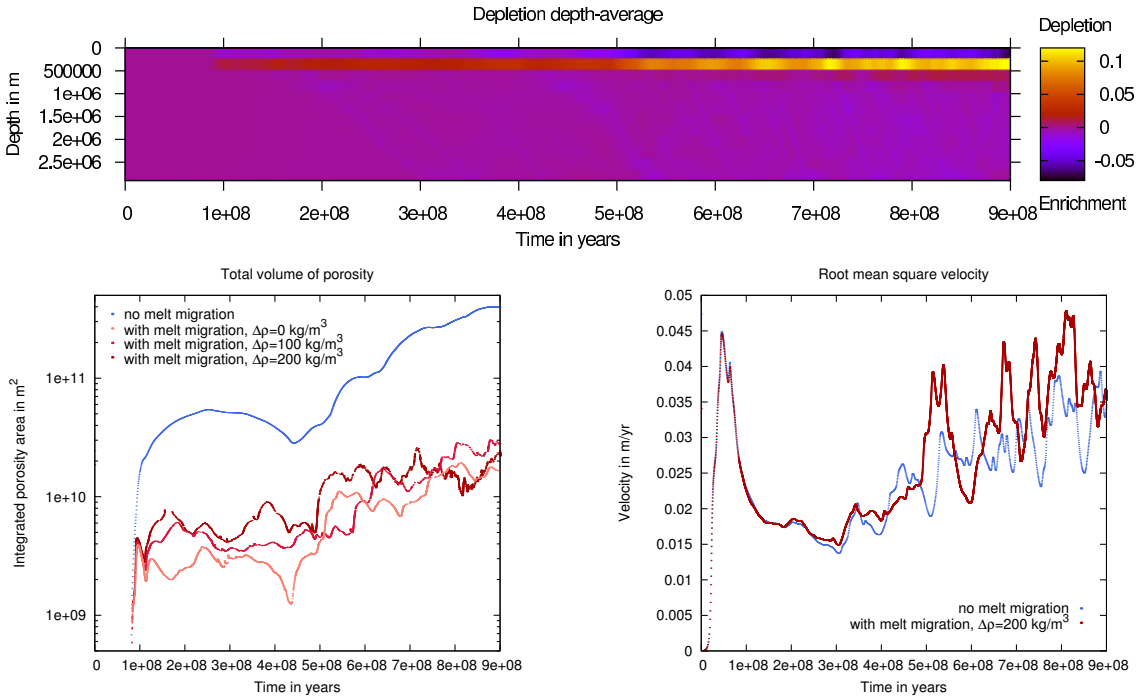

Figure 4.13: *Time evolution of global models with melt migration.* ***(top)*** *Depletion field, depth-averaged in 12 slices. Once melt starts to be generated, enriched material accumulates in the top layer, and depleted material in a layer below in 200 – 400 km depth. Part of the enriched material also flows downwards and is distributed over the whole model domain.* ***(bottom left)*** *Development of the melt volume for models with (red lines) and without (blue line) melt migration, and varying density contrasts between "enriched" and "depleted" material. For the model without melt migration, melt volume is calculated as equilibrium melt fraction for the present temperature and pressure conditions (i.e. batch melting).* ***(bottom right)*** *Development of the root mean square velocity for models with (red line) and without (blue line) melt migration. While the model evolution is similar in the beginning, it diverges once a significant amount of melt is generated (compare left side), and the model with melt migrations shows higher velocity peaks.*

models and hence can not reach the surface. However, the small-scale convection initiated by the downwellings of dense enriched, crystallised material allows for new, hot material to flow upwards, and melt intruding further upwards into the lithosphere. This is already a similar process as what is described by Sobolev et al. (2011) as thermo-magmatic erosion of the lithosphere by mantle plumes. The downwelling enriched material is subsequently distributed over the whole model domain (blue streaks towards the end of the time evolution in 4.13, top).The full model evolution is presented in Supplementary Movie S3.

This diverging model dynamics is also visible in the root mean square velocities (Figure 4.13, bottom right): During the first 250 million years both models behave almost identically, but afterwards different peaks develop in the two models. However, as the root mean square velocity is mainly influenced by upwellings instead of downwellings (due to the lower viscosities) both the average value and the frequency of peaks remain similar.

It is very likely that the model behaviour will change if a more complex melting and material behaviour is incorporated, but our model shows that already this very simple approximation of melting, together with melt migration, has a strong influence on the model dynamics, including average model velocities, predicted melt volumes and number and frequency of downwellings.

4.5 Conclusions and Outlook

In this study, we described how to implement two-phase flow in two and three dimensions in a finite element code with adaptive mesh refinement. The proposed formulation, which includes the compressibility of the individual solid and melt phase in addition to compaction, allows models to be extended consistently to greater depth in the Earth's mantle. The presented applications demonstrate the accuracy and efficiency of our software and its ability to capture the behaviour of melt in relevant application cases of magma/mantle dynamics on different scales, ranging from millimetres to thousands of kilometres. Simulations of mantle plumes and global convection show that including melt migration in a model significantly changes the convection pattern, and for deep melts the compressibility can have an effect of an order of 20% on the computed melt volume. The main advantages of the presented method are (1) the effectiveness of adaptive mesh refinement, allowing for higher resolution or larger model domains with the same computational resources, (2) the potential to study applications with three-dimensional geometries and (3) the capability to couple melt migration to processes deeper in the Earth's mantle and global mantle convection in a consistent formulation considering the compressibilities of solid and melt phase.

Despite all this, the methods described here are not sufficient to solve all conceivable models related to melt migration realistically: The focus of this study is on the coupling of magma dynamics to mantle dynamics on larger scales, and our current approach does not consider elastic and plastic deformation of the material. Hence, it does not allow for modelling of melt transport through fractures or dikes, one of the main modes of melt extraction on smaller scales such as in the lithosphere and crust (Keller et al., 2013). These deformation mechanisms introduce additional non-linearities and make the problem numerically challenging, demanding the use of more efficient non-linear solvers, ideally employing Newton's method, to be viable in three dimensions.

In addition, we here concentrate on the mechanical evolution of the two-phase system, simplifying its thermal and chemical evolution and using parametrisations for calculating melting and freezing rate and the influence of melt on material properties. This approximation considers the qualitative influence of compositional changes on solidus, liquidus, density, viscosity and other material properties. However, it does not allow an accurate computation of the melt and residuum composition in a multicomponent system or the associated chemical heterogeneities generated by the melting process – which would be required for a more realistic description of the rheology of partially molten regions and a more sophisticated comparison of the model to geochemical data. Employing thermodynamic data to calculate melting rates self-consistently and keeping track of the evolution of solid and melt composition should be a goal for future modelling studies.

Finally, we assume that melt and solid are always in thermodynamic equilibrium. However, this might not be a valid approximation for all applications of porous flow in the Earth's mantle and excludes modelling disequilibrium melting such as described in Rudge et al. (2011). Geochemical evidence suggests that the melts that formed mid-ocean ridge basalts were not in chemical equilibrium with the matrix they were migrating through; and modelling has shown that disequilibrium is important for the formation of reactive instabilities, leading to melt focusing and channelized flow below mid-ocean ridges (Spiegelman et al., 2001).

Nevertheless, we have shown that ASPECT can be applied to a number of relevant model setups for coupled magma/mantle dynamics and that it has the potential to become a versatile and useful tool for the magma migration community.

Acknowledgments

J. Dannberg would like to thank Rene Gassmoeller for helpful suggestions regarding the implementation and for carefully and critically reading the manuscript, and Tobias Keller for many insightful discussions on coupled magma/mantle dynamics.

Both authors were partially supported by the Computational Infrastructure for Geodynamics initiative (CIG), through the National Science Foundation under Award No. EAR-0949446 and The University of California – Davis. T. Heister was partially supported by National Science Foundation grant DMS1522191. J. Dannberg acknowledges the support of the Helmholtz graduate research school GeoSim.

Most of the computational resources were provided by the North-German Supercomputing Alliance (HLRN) as part of the project "Plume-Plate interaction in 3D mantle flow – Revealing the role of internal plume dynamics on global hot spot volcanism". Clemson University is acknowledged for generous allotment of compute time on Palmetto cluster.

4.A Parametrisation of the melting model

Modelling of melt generation requires a parametrisation for the melting rate in dependence of temperature, pressure and composition. We use the parametrisation from Katz et al. (2003) for melting of dry peridotite (Figure 4.14).

In addition, when material undergoes the phase transition from solid to fluid (or the other way round), latent heat is consumed (or released). The effects of latent heat are included in the energy conservation equation in form of the term $\rho_s T \Delta S \left(\frac{\partial F}{\partial t} + \mathbf{u}_s \cdot \nabla F\right)$. Here, ΔS is the change of entropy (positive for exothermic phase transitions) and F is the degree of depletion (the fraction of the source rock that has already been molten; without melt extraction from the source this is equal to the melt fraction). As the phase of the material, for a given composition, depends on the temperature and pressure, the latent heat term can be reformulated:

$$\begin{aligned}\frac{\partial F}{\partial t} + \mathbf{u}_s \cdot \nabla F &= \frac{DF}{Dt} \\ &= \frac{\partial F}{\partial T}\frac{DT}{Dt} + \frac{\partial F}{\partial p_s}\frac{Dp_s}{Dt} \\ &= \frac{\partial F}{\partial T}\left(\frac{\partial T}{\partial t} + \mathbf{u}_s \cdot \nabla T\right) + \frac{\partial F}{\partial p_s}\mathbf{u}_s \cdot \nabla p_s.\end{aligned}$$

The last transformation results from the assumption that the flow field is always in equilibrium and consequently $\partial p/\partial t = 0$. This means, we have to calculate the partial derivatives of our melt fraction parametrisation with respect to temperature and pressure.

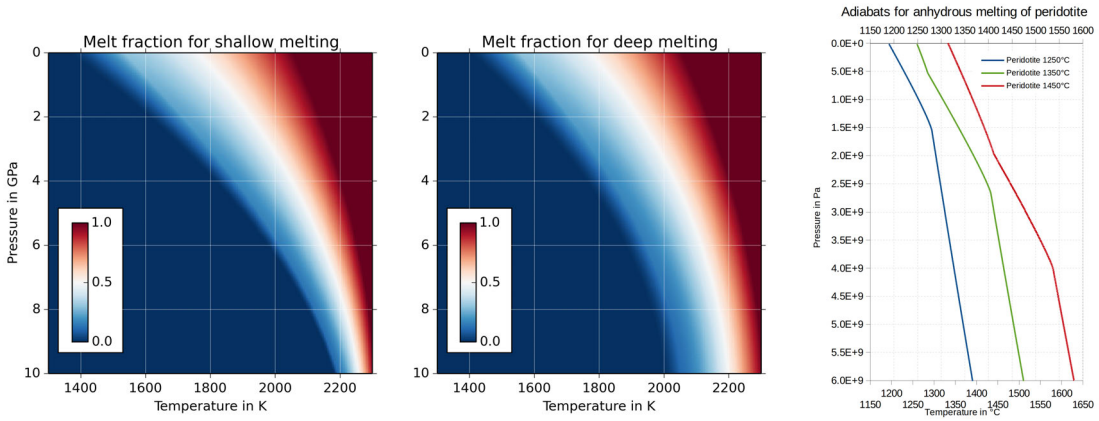

Figure 4.14: *Melt fraction in dependence of temperature and pressure after Katz et al. (2003, left) and modified for deep melting (middle), and temperature profile of adiabatically upwelling material when latent heat of melting is taken into account for batch melting of anhydrous peridotite. Parametrisations after Katz et al. (2003).*

4.A.1 Melting of peridotite prior to the exhaustion of clinopyroxene

For peridotite, there are two different functions prior to and after the exhaustion of clinopyroxene. Prior to the exhaustion of clinopyroxene

$$
\begin{aligned}
F(p,T) &= \left(\frac{T - T_{\mathrm{sol}}(p)}{T^{\mathrm{lh}}_{\mathrm{liq}}(p) - T_{\mathrm{sol}}(p)}\right)^{\beta} \\
\frac{\partial F(p,T)}{\partial T} &= \beta \left(\frac{T - T_{\mathrm{sol}}(p)}{T^{\mathrm{lh}}_{\mathrm{liq}}(p) - T_{\mathrm{sol}}(p)}\right)^{\beta-1} \frac{1}{T^{\mathrm{lh}}_{\mathrm{liq}}(p) - T_{\mathrm{sol}}(p)} \\
\frac{\partial F(p,T)}{\partial p} &= \beta \left(\frac{T - T_{\mathrm{sol}}(p)}{T^{\mathrm{lh}}_{\mathrm{liq}}(p) - T_{\mathrm{sol}}(p)}\right)^{\beta-1} \\
&\quad \left(\frac{\partial T^{\mathrm{lh}}_{\mathrm{liq}}(p)}{\partial p}(T_{\mathrm{sol}}(p) - T) + \frac{\partial T_{\mathrm{sol}}(p)}{\partial p}(T - T^{\mathrm{lh}}_{\mathrm{liq}}(p))\right) \frac{1}{(T^{\mathrm{lh}}_{\mathrm{liq}}(p) - T_{\mathrm{sol}}(p))^2}
\end{aligned}
$$

with the solidus $T_{\mathrm{sol}}(p) = A_1 + A_2 p + A_3 p^2$,
the lherzolite liquidus $T^{\mathrm{lh}}_{\mathrm{liq}}(p) = B_1 + B_2 p + B_3 p^2$
and the true liquidus $T_{\mathrm{liq}}(p) = C_1 + C_2 p + C_3 p^2$.

4.A.2 Melting of peridotite after the exhaustion of clinopyroxene

The exhaustion of clinopyroxene happens at the melt fraction

$$F_{\text{cpx-out}} = \frac{M_{\mathrm{cpx}}}{R_{\mathrm{cpx}}(p)} \quad \text{with} \quad R_{\mathrm{cpx}}(p) = r_0 + r_1 p$$

and marks a change in the productivity of the system. M_{cpx} is the mass fraction of clinopyroxene in the peridotitic host rock and R_{cpx} is the reaction coefficient for cpx in

Table 4.4: Parameters used for melting of anhydrous peridotite. Modified from Katz et al. (2003).

Parameter	Used for	Value	Value for deep melting	Unit
A_1	T_{sol}	1085.7	1120.7	K
A_2		$1.329 \cdot 10^{-7}$	$1.1 \cdot 10^{-7}$	K Pa^{-1}
A_3		$-5.1 \cdot 10^{-18}$	$-5 \cdot 10^{-18}$	K Pa^{-2}
B_1	$T_{\text{liq}}^{\text{lh}}$	1475.0		K
B_2		$8.0 \cdot 10^{-8}$		K Pa^{-1}
B_3		$-3.2 \cdot 10^{-18}$		K Pa^{-2}
C_1	T_{liq}	1780.0		K
C_2		$4.5 \cdot 10^{-8}$		K Pa^{-1}
C_3		$-2.0 \cdot 10^{-18}$		K Pa^{-2}
β	F	1.5		
M_{cpx}		0.15		mass fraction
r_0		0.5		mass fraction
r_1		$8 \cdot 10^{-11}$		mass fraction Pa^{-1}
ΔS	latent heat	-300		J kg^{-1} K^{-1}

the melting reaction. For $F > F_{\text{cpx-out}}$

$$
\begin{aligned}
F(p,T) &= F_{\text{cpx-out}} + (1 - F_{\text{cpx-out}}) \left(\frac{T - T_{\text{cpx-out}}(p)}{T_{\text{liq}}(p) - T_{\text{cpx-out}}(p)} \right)^{\beta} \\
\frac{\partial F(p,T)}{\partial T} &= \beta (1 - F_{\text{cpx-out}}) \left(\frac{T - T_{\text{cpx-out}}(p)}{T_{\text{liq}}(p) - T_{\text{cpx-out}}(p)} \right)^{\beta - 1} \frac{1}{T_{\text{liq}}(p) - T_{\text{cpx-out}}(p)} \\
\frac{\partial F(p,T)}{\partial p} &= \frac{\partial F_{\text{cpx-out}}}{\partial p} \left[1 - \left(\frac{T - T_{\text{cpx-out}}(p)}{T_{\text{liq}}(p) - T_{\text{cpx-out}}(p)} \right)^{\beta} \right] \\
&\quad + \beta (1 - F_{\text{cpx-out}}) \left(\frac{T - T_{\text{cpx-out}}(p)}{T_{\text{liq}}(p) - T_{\text{cpx-out}}(p)} \right)^{\beta - 1} \\
&\quad \frac{\frac{\partial F_{\text{cpx-out}}}{\partial p} (T_{\text{cpx-out}}(p) - T_{\text{liq}}(p)) + \left(\frac{\partial T_{\text{liq}}}{\partial p} - \frac{\partial T_{\text{cpx-out}}}{\partial p} \right) (T_{\text{cpx-out}}(p) - T)}{(T_{\text{liq}}(p) - T_{\text{cpx-out}}(p))^2}
\end{aligned}
$$

with $T_{\text{cpx-out}} = {F_{\text{cpx-out}}}^{\frac{1}{\beta}} \left[T_{\text{liq}}^{\text{lh}}(p) - T_{\text{sol}}(p) \right] + T_{\text{sol}}(p)$.

4.A.3 Parameters

The parameters used for the solidus and liquidus temperatures and the melt fraction are taken from Katz et al. (2003) for the case of anhydrous melting and are given in Table 4.4. For modelling melting under higher pressures, such as shown in Section 4.4.5 (deep melting), we modified the solidus temperature (reflecting a compositional change or change in volatile fraction), resulting in the deepest melts in the plume being generated in approximately 230 km depth.

4.A.4 Validation

We test our melting model by computing the numerical solution for the temperature profile of adiabatically upwelling material that undergoes melting and the associated latent heat

effects. Figure 4.14 (right) shows these results, which can be compared to equivalent data for anhydrous melting in Katz et al. (2003, figure 11b), who calculate a simplified version of the productivity function

$$\left.\frac{dF}{dP}\right|_S = \frac{-\frac{c_p}{T}\frac{\partial T}{\partial P}\big|_F + F\frac{\alpha_f}{\rho_f} + (1-F)\frac{\alpha_s}{\rho_s}}{\Delta S + \frac{c_p}{T}\frac{\partial T}{\partial F}\big|_P} \tag{4.40}$$

and then numerically integrate

$$\left.\frac{dT}{dP}\right|_S = \frac{T}{c_p}\left(F\frac{\alpha_f}{\rho_f} + (1-F)\frac{\alpha_s}{\rho_s} + \Delta S\left.\frac{dF}{dP}\right|_S\right) \tag{4.41}$$

to receive the P-T path of the adiabat.

4.B Supplementary Movies

The provided animations show the development of several of the presented models:

Movie S1. Animation of the development of magmatic shear bands in three dimensions in a partially molten host rock that is exposed to shearing. Setup, colours and scaling are the same as in Figure 4.4 (bottom). The animation can also be found at `https://www.youtube.com/watch?v=zOEqhaiBswU`.

Movie S2. Animation of the evolution of a rising mantle plume that undergoes melting. Setup, colours and scaling are the same as in Figure 4.10. The animation can also be found at `https://youtu.be/aWndYbMIjVQ`.

Movie S3. Animation of the evolution of a global mantle convection model that incorporates melting, illustrating the difference between only computing melt fractions (top) and allowing melt to migrate and influence the model behaviour (bottom). Setup, colours and scaling are the same as in Figure 4.13. The animation can also be found at `https://youtu.be/Kwyp4Jvx6MU`.

4.C Supplementary Data

All model input files, scripts and data files that are required to reproduce the presented results are available at `https://github.com/jdannberg/melt-transport-data`.

Bibliography

Agee, C. B. and D. Walker (1993). "Olivine flotation in mantle melt". *Earth and Planetary Science Letters* 114 (2–3): 315 –324.

Ballmer, M. D. et al. (2013). "Double layering of a thermochemical plume in the upper mantle beneath Hawaii". *Earth and Planetary Science Letters* 376: 155 –164.

Bangerth, W., T. Heister, et al. (2015). *ASPECT: Advanced Solver for Problems in Earth's ConvecTion*. `https://aspect.dealii.org/`.

Bangerth, W. et al. (2011). "Algorithms and Data Structures for Massively Parallel Generic Adaptive Finite Element Codes". *ACM Trans. Math. Softw.* 38 (2).

Bangerth, W. et al. (2015). "The dealii Library, Version 8.2". *Archive of Numerical Software* 3 (1).

Barcilon, V. and O. M. Lovera (1989). "Solitary waves in magma dynamics". *Journal of Fluid mechanics* 204: 121–133.

Barcilon, V. and F. M. Richter (1986). "Nonlinear waves in compacting media". *Journal of Fluid mechanics* 164: 429–448.

Cagnioncle, A.-M., E. M. Parmentier, and L. T. Elkins-Tanton (2007). "Effect of solid flow above a subducting slab on water distribution and melting at convergent plate boundaries". *Journal of Geophysical Research: Solid Earth* 112 (B9). B09402.

Dannberg, J. and T. Heister (2015). *Supporting computer code*. `https://github.com/jdannberg/aspect/tree/melt_reorder_fields`.

Dziewonski, A. M. and D. L. Anderson (1981). "Preliminary reference Earth model". *Physics of the Earth and Planetary Interiors* 25 (4): 297 –356.

Gerya, T. (2011). "Future directions in subduction modeling". *Journal of Geodynamics* 52 (5): 344 –378.

Holtzman, B. K. and D. L. Kohlstedt (2007). "Stress-driven Melt Segregation and Strain Partitioning in Partially Molten Rocks: Effects of Stress and Strain". *Journal of Petrology* 48 (12): 2379–2406.

Katz, R. F. (2006). "The dynamics of melt and shear localization in partially molten aggregates". *Nature* 442: 676–679.

Katz, R. F. (2008). "Magma Dynamics with the Enthalpy Method: Benchmark Solutions and Magmatic Focusing at Mid-ocean Ridges". *Journal of Petrology* 49 (12): 2099–2121.

Katz, R. F. (2010). "Porosity-driven convection and asymmetry beneath mid-ocean ridges". *Geochemistry, Geophysics, Geosystems* 11 (11): Q0AC07.

Katz, R. F., M. Spiegelman, and C. H. Langmuir (2003). "A new parameterization of hydrous mantle melting". *Geochemistry, Geophysics, Geosystems* 4 (9): 1073.

Keller, T., D. A. May, and B. J. P. Kaus (2013). "Numerical modelling of magma dynamics coupled to tectonic deformation of lithosphere and crust". *Geophysical Journal International* 195 (3): 1406–1442.

Kronbichler, M., T. Heister, and W. Bangerth (2012). "High accuracy mantle convection simulation through modern numerical methods". *Geophysical Journal International* 191 (1): 12–29.

McKenzie, D. (1984). "The generation and compaction of partially molten rock". *Journal of Petrology* 25 (3): 713–765.

Mittelstaedt, E., G. Ito, and J. van Hunen (2011). "Repeat ridge jumps associated with plume-ridge interaction, melt transport, and ridge migration". *Journal of Geophysical Research: Solid Earth (1978–2012)* 116 (B1).

Ohtani, E. and M. Maeda (2001). "Density of basaltic melt at high pressure and stability of the melt at the base of the lower mantle". *Earth and Planetary Science Letters* 193 (1–2): 69 –75.

Rhebergen, S. et al. (2014). "Analysis of Block Preconditioners for Models of Coupled Magma/Mantle Dynamics". *SIAM Journal on Scientific Computing* 36 (4): A1960–A1977.

Rhebergen, S. et al. (2015). "Three-Field Block Preconditioners for Models of Coupled Magma/Mantle Dynamics". *SIAM Journal on Scientific Computing* 37 (5): A2270–A2294.

Rudge, J. F., D. Bercovici, and M. Spiegelman (2011). "Disequilibrium melting of a two phase multicomponent mantle". *Geophysical Journal International* 184 (2): 699–718.

Ruedas, T. et al. (2004). "Temperature and melting of a ridge-centred plume with application to Iceland. Part I: Dynamics and crust production". *Geophysical Journal International* 158 (2): 729–743.

Sanloup, C. et al. (2013). "Structural change in molten basalt at deep mantle conditions". *Nature* 503: 104–107.

Schmeling, H. (2000). "Partial melting and melt segregation in a convecting mantle". *Physics and Chemistry of Partially Molten Rocks*. Springer: 141–178.

Schmeling, H. (2010). "Dynamic models of continental rifting with melt generation". *Tectonophysics* 480 (1–4): 33 –47.

Schmeling, H. and G. Marquart (2008). "Crustal accretion and dynamic feedback on mantle melting of a ridge centred plume: The Iceland case". *Tectonophysics* 447 (1-4): 31–52.

Scott, D. R. and D. J. Stevenson (1986). "Magma ascent by porous flow". *Journal of Geophysical Research B* 91 (B9): 9283–9296.

Simpson, G. and M. Spiegelman (2011). "Solitary wave benchmarks in magma dynamics". *Journal of Scientific Computing* 49 (3): 268–290.

Sobolev, S. V. et al. (2011). "Linking mantle plumes, large igneous provinces and environmental catastrophes". *Nature* 477: 312–316.

Spiegelman, M. (1996). "Geochemical consequences of melt transport in 2-D: The sensitivity of trace elements to mantle dynamics". *Earth and Planetary Science Letters* 139 (1): 115–132.

Spiegelman, M. (2003). "Linear analysis of melt band formation by simple shear". *Geochemistry, Geophysics, Geosystems* 4 (9): 8615.

Spiegelman, M., P. B. Kelemen, and E. Aharonov (2001). "Causes and consequences of flow organization during melt transport: The reaction infiltration instability in compactible media". *J. geophys. Res* 106 (B2): 2061–2077.

Stevenson, D. J. (1989). "Spontaneous small-scale melt segregation in partial melts undergoing deformation". *Geophysical Research Letters* 16 (9): 1067–1070.

Suzuki, A. and E. Ohtani (2003). "Density of peridotite melts at high pressure". English. *Physics and Chemistry of Minerals* 30 (8): 449–456.

Weatherley, S. M. and R. F. Katz (2012). "Melting and channelized magmatic flow in chemically heterogeneous, upwelling mantle". *Geochemistry, Geophysics, Geosystems* 13 (5): Q0AC18.

Wiggins, C. and M. Spiegelman (1995). "Magma migration and magmatic solitary waves in 3-D". *Geophysical Research Letters* 22 (10): 1289–1292.

Chapter 5

Discussion

5.1 Linking scales and coupling physics

This study contributes to the general understanding of mantle plumes as part of the Earth's mantle convection and in interaction with the lithosphere. Previous studies mainly focused on individual aspects of mantle plumes, or mantle convection in general. The present work links different scales, techniques and disciplines to obtain a more general view on the evolution, dynamics and ongoing processes in mantle plumes, and it discusses how this integrated picture differs from the classical mantle plume concept.

- *Length scales:* This work links the core–mantle boundary and the surface by studying the plume ascent though the whole mantle, including the influences of the thermal and compositional structure of both plume and ambient mantle and the associated density contrasts and mineral phase transitions. This connection between the global mantle scale and the plume scale is also analysed by investigating influences of global mantle flow on the plume development and its surface expressions. Moreover, the presented models relate processes in the plume to the much smaller length scales of melt migration and compaction.

- *Disciplines:* The present study incorporates insights from different disciplines to gain a better understanding of the processes occurring in mantle plumes. Geodynamic models, visualising and complying with the underlying physics, are combined with geochemical data regarding the plume composition and chemical heterogeneities, mineral physics data about mineral densities, compressibilities and phase transitions, geologic knowledge about the history of specific regions such as plate reconstructions and predicted plume positions, advanced numerical methods like adaptive mesh refinement and parallelization of the code developed by the mathematics community allowing for faster and more precise computations, and seismic tomography models as part of the global mantle flow computation and model constraint.

- *Physical processes:* Solid state creep in the mantle, as it is commonly assumed to take place in mantle plumes, is coupled to compaction and two-phase flow in a new formulation of magma/mantle dynamics.

- *Models and Observations:* Models can only represent what happens in the Earth when they are combined with observations. Here, observations are included both directly in form of model initial conditions (plume temperature, composition, lithospheric structure), boundary conditions (plate reconstruction, plume position, global flow model from seismic tomography), material properties (density structure, phase

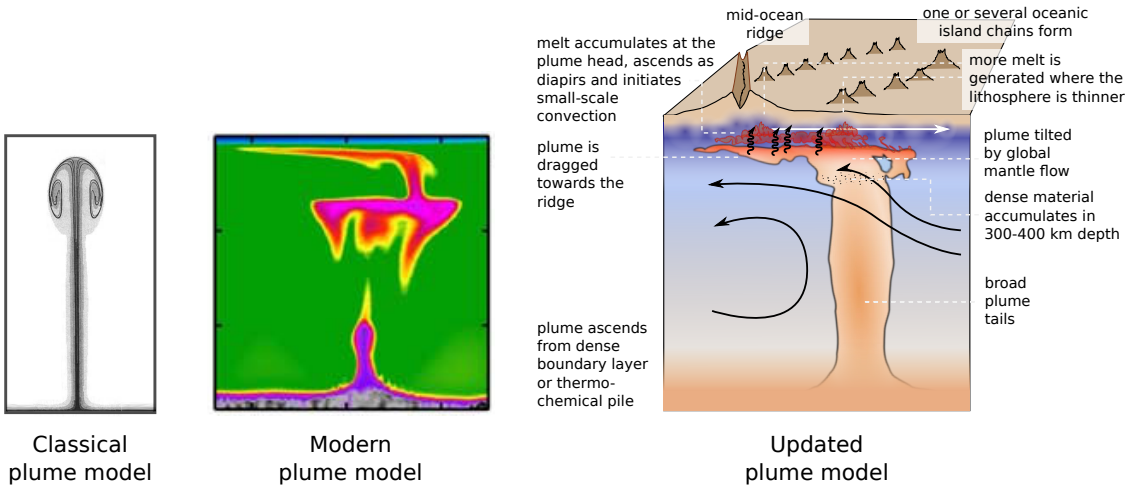

Figure 5.1: Update of the plume model. (left) Classical plume model of van Keken (1997), (middle) modern plume model of Farnetani and Samuel (2005), (right) updated plume model presented in this work.

transitions, melting parametrisation, rheology) and indirectly as part of the model interpretation when model results are compared to observations (such as generated surface uplift, seismic profiles, crustal thickness maps). A combination of both approaches is used to improve the assumptions made when converting observations to physical properties that are used in geodynamic models: Model input parameters inferred from observations are varied, and the associated model results are compared to other observations to reveal which scenarios are plausible. This allows to better constrain these model input parameters such as plume temperatures and fluxes, plate reconstructions or plume positions.

From this integration of different approaches a new, updated picture of mantle plumes emerges (Figure 5.1): Instead of the classical head–tail structure, plumes containing recycled oceanic crust are predicted to be broad features in the lower mantle with much less pronounced plume heads that thin in the upper mantle, where viscosities are lower. They can form a variety of shapes and regimes, including primary plumes directly advancing to the base of the lithosphere, stagnating plumes, secondary plumes rising from the core–mantle boundary or a pool of eclogitic material in the upper mantle and failing plumes. Which morphology develops and if a plume reaches the surface depends on the plume temperature, volume flux, composition and the ambient mantle temperature. In the upper mantle, plumes can be tilted and deflected by global mantle flow, and the shape, size and stability of the melting region is influenced by the distance from nearby plate boundaries, the speed of the overlying plate and the movement of the plume tail arriving from the lower mantle. In addition, the structure of the lithosphere influences where hot material is accumulated and melt is generated. This does not only include upwards flow to regions of thinner lithosphere, but also the presence of fracture zones and plate boundaries and the movement of plates in general, favouring plume flow towards and melt generation in rifted areas and mid-ocean ridges. In dependence of all these factors, the surface expressions of plumes can be broad ridges of thickened magmatic crust or one or multiple thinner lines of sea mount chains; and plumes do not necessarily generate kilometre-scale surface uplift when they approach the surface if their buoyancy is lowered by recycled oceanic crust. Once melt is generated within the plume, it influences its dynamics, lowering the viscosity and density, and while it rises the melt volume is

increased significantly due to decompression. Melt has the tendency to accumulate at the plume head, forming diapirs and initiating small-scale convection when the plume reaches the base of the lithosphere. Together with the introduced unstable, high-density material produced by freezing of melt, this provides an efficient mechanism to thin the lithosphere above plume heads.

In detail, the presented models advance our understanding of mantle plumes in the following areas:

Observations have shown that major mantle plumes contain up to 15–20% of recycled oceanic crust in a form of dense eclogite, which drastically decreases their buoyancy and makes it depth dependent. Although entrainment of dense material into plumes and its impact on surface manifestations has already been studied, it remained unclear if these thermochemical plumes can indeed rise through the whole mantle despite their low buoyancy while retaining realistic excess temperatures. This work shows that if their volume is sufficiently large and the lower mantle is subadiabatic, these low-buoyancy plumes (LBPs) can indeed rise through the whole mantle generating only minor surface uplift. They ascend more slowly, and their tails are bulky (>200 km radius) and remain in the upper mantle for 100 millions of years. In addition, considering a depth-dependent plume buoyancy constrained by mineral physics and geochemical data reveals different barriers for the ascent of LBPs compared with what was reported in previous studies: Buoyancy minima are at the core-mantle boundary and in 300 – 400 km depth, causing potential for stagnating plumes in these regions. In contrast, the buoyancy maximum in 660–750 km depth lets eclogite-bearing plumes cross the spinel-perovskite phase transition easily despite its negative Clapeyron slope. The fact that seismic tomographic observations suggest that many major plumes are broad features that can be well imaged implies that a number of plumes are thermochemical rather than purely thermal, and are described better by LBP models than by classical models.

Previous modelling studies have considered plume–ridge interaction as an isolated process and did not include external influences. This led to the derivation of general scaling relations, or it related physical processes to the plume surface expressions of a specific region. However, the influence of global mantle convection has not been considered in this context, these methods have only been applied to a few regions and the results can not always be generalized. At the example of the South Atlantic, the present work demonstrates that a convection model that takes into account plate motion, mantle flow, plume movement and decompression melting of peridotite resembles well the main features of both the current-day geometry of the hotspot track and the distribution of syn-rift magmatism. In addition, the comparison to seismic profiles allowed further constraining the physical properties of the Tristan mantle plume within the existing uncertainties. Broadening of the hotspot track and the separation into several volcanic chains can be explained by the interaction of a single plume with the nearby ridge. In addition to the melt generation at the surface arrival position of the plume tail, flow towards the ridge and regions of thinner lithosphere leads to additional melting regions that can also create age-progressive sea mount chains. In the analysed models, the global flow field has the potential to enhance material motion from below the off-ridge track towards the ridge, to influence local plume temperatures, to change the overall volume of plume-related melt by 40 % and to tilt the plume in the upper mantle. This can be the difference between generating one broad or several smaller sea mount chains, and it illustrates that models without plate motion and mantle flow may significantly misestimate plume properties. This method can be readily generalized and adopted to study plume-ridge interaction for other hotspots close to mid-ocean ridges.

Melting and melt migration in mantle plumes have so far only been studied by simplifying melt extraction or two-phase flow or for very low melt fractions, and in two dimensions. Moreover, individual compressibilities of fluid and solid have not been considered. This study derives a new formulation of two-phase flow, considering melt and host rock compressibility in addition to compaction, and demonstrates how to implement it in a mantle convection code. It illustrates how advanced numerical methods such as adaptive mesh refinement and massive parallelization of the code can overcome challenges associated with modelling coupled magma/mantle dynamics and allow for linking scales of global mantle convection and melt migration/compaction in two and three-dimensional models. These models show that decompression can change predicted melt volumes by up to 20%, and that melt migration has the potential to significantly change patterns of convection. This is achieved by mechanisms previously attributed to mantle plumes when interacting with the lithosphere: By reducing the viscosity they initiate small-scale convection at the base of the lithosphere; and they trigger downwellings when melt solidifies to high-density eclogitic material. The presented method can easily be applied to other problems of coupled magma/mantle dynamics that comprise larger scales, such as subduction zones, plume–ridge interaction or melting in the deep mantle.

This shows that mantle plumes are more complex than previously considered, and agreement with many observations can only be reached if these complexities are included in geodynamic models.

5.2 Summary

These results can be summarised as follows:

- Plumes with realistic excess temperatures can transport up to 15% of recycled oceanic crust from the core-mantle boundary to the base of the lithosphere.
- They can advance to the surface if their temperature and volume are sufficiently high, and if the lower mantle is subadiabatic or they rise from the top/the edges of a thermo-chemical pile.
- These low-buoyancy plumes can form three different regimes: primary plumes advancing directly from the CMB to the base of the lithosphere with high temperatures and eclogite contents, secondary plumes rising from the top of material stagnating at the CMB or in 300 – 400 km depth with lower temperatures and eclogite contents, and failing plumes.
- Even primary low-buoyancy plumes cause a surface uplift as low as 260 m, which is much smaller than predicted for purely thermal plumes.
- The broadening of the Tristan hotspot track in the South Atlantic and the apparent separation into the Tristan and Gough volcanic chains can be explained by the interaction of a single plume with the nearby mid-ocean ridge.
- A plume excess temperature of 150 K and a buoyancy flux of around 500 kg/s lead to a crustal production comparable to seismic observations for the Tristan hotspot track. Larger plumes overpredict the generated crustal thickness.
- The lithospheric structure influences melt generation in a plume, and using a variable lithosphere thickness derived from the present-day lithospheric structure in numer-

ical models can explain the size and extent of magmatism better than a constant lithosphere thickness (for example for the Etendeka LIP in the South Atlantic).

- Global mantle flow can influence local plume temperatures by up to 50 K, change the overall volume of plume-related melt by 40 % and tilt the plume up to 20°, making the difference between generating one broad or several smaller sea mount chains
- Adaptive mesh refinement reduces the computational effort for models of coupled magma/mantle dynamics, while retaining the same accuracy. How much resources can be saved depends on the amount of melt present in the model and its localisation. While a cost reduction of a factor of two to four was achieved in 2D theoretical models, it is expected to be much higher in applications, in particular in global models and three-dimensional setups.
- Massive parallelization of the code makes it possible to model coupled two-phase flow and mantle convection in three dimensions for relevant applications.
- The compressibility of melt can increase its volume by up to 20% from the source region to the surface.

5.3 Outlook

The present work has shown that plumes can transport a significant amount of dense recycled oceanic crust from the core–mantle boundary to the surface. However, it still remains unanswered if and how plumes can entrain such a large fraction of eclogitic material, and how its distribution within the plume would influence the plume buoyancy. Subducted slabs – pushing material from the hot thermal boundary layer towards the stable thermo-chemical piles, which have been proposed to reside in the lowermost mantle (Lay and Garnero, 2011, and references therein), and forcing the material to ascend – have the potential to crucially influence this process. Moreover, investigating these mechanisms could answer the question if entrained material would generate a chemical zonation inside of the plume, if this chemical gradient can be preserved until the plume reaches the lithosphere despite the density differences and if the zonation would be reflected in melt compositions. These melt compositions can then be compared to basalts from oceanic islands, which have been shown to posses different chemical trends that run parallel to each other, but originate from the same hotspot, indicating a chemical gradient within the plume (Weis et al., 2011; Farnetani et al., 2012). In addition, the 3D plume structure developing in interaction with the plate motion could be compared to recent seismic tomographic observations, which indicate elongated structures of low seismic velocities in the direction of absolute plate motion in a depth of 200 – 350 km (French et al., 2013). For this purpose, the presented plume models featuring a single plume and incorporating a realistic mantle density profile could be extended to three dimensions and combined with models of global mantle convection using the same method as presented here for plume–ridge interaction. The global model, including the dense piles and subducting slabs, could provide initial and boundary conditions for the smaller plume model, which would have sufficient resolution for studying entrainment and plume ascent.

Another direction for further research is the combination of models of plume–ridge interaction and melt migration. The presented models predict crustal thickness from where melt is generated, assuming either that all of the melt is extracted instantly, or that it is advected with the solid flow field. Both approximations are extremes of the behaviour expected in the Earth, and applying more realistic melt migration models could improve

our understanding of how melt behaves in plume–ridge systems. Potential mechanisms are the vertical segregation, horizontal movement towards the ridge in a low-permeability channel at the base of the lithosphere, advection with the solid flow away from the ridge, or freezing due to cold temperatures at the base of the lithosphere; and these models could provide insight as to under which conditions which mechanism is dominant. In addition, employing a visco-elasto-plastic rheology instead of purely Newtonian creep mechanisms could potentially better reflect where and how melt migrates through the lithosphere and reaches the surface, and could also account for the development of faults and fractures, which are especially important in the early stages of rifting, but can also play a role for the focusing of melt. Moreover, the developed method of studying plume–ridge interaction can readily be applied to other hotspots that have interacted with or are still close to mid-ocean ridges. Potential study areas include both regions that have not yet been investigated extensively, such as Réunion, and the revision of plume–ridge interaction models of previously studied areas where many observations are available, such as Iceland.

The presented code to model coupled magma/mantle dynamics has the potential to be applied in many areas. So far, mostly accuracy, functionality, effectiveness and versatility of the methods have been demonstrated, but already the examples chosen for this purpose can provide further insights into the behaviour of partially molten rock if studied in more detail. One example are magmatic shear bands: Previous studies have been in two dimensions, and it is unclear if and how the angle of the bands in relation to the applied shear differs in three-dimensional models. Moreover, models have not yet been able to find a mechanism to stabilise these bands (over the model runtime, porosity localises further and further) or to yield similar spacing between the bands compared to what is observed in experiments and in natural rocks. Furthermore, linear stability analysis (Rudge and Bercovici, 2015) suggests that two-phase damage may play a role in the formation of magmatic shear bands, a theory that still has not been applied in fully numerical models. Another promising study topic is magmatic thinning of the lithosphere, a mechanism that plays a crucial role for the surface manifestations of mantle plumes as it can significantly enhance melt production. Hence, it can also play an important role for continental breakup. Employing a more realistic thermal and chemical evolution in our models of two-phase flow in mantle plumes could improve our understanding under which conditions and to which extent this process can take place.

Bibliography

Farnetani, C. and H Samuel (2005). "Beyond the thermal plume paradigm". *Geophysical Research Letters* 32 (7).

Farnetani, C. G., A. W. Hofmann, and C. Class (2012). "How double volcanic chains sample geochemical anomalies from the lowermost mantle". *Earth and Planetary Science Letters* 359: 240–247.

French, S., V. Lekic, and B. Romanowicz (2013). "Waveform tomography reveals channeled flow at the base of the oceanic asthenosphere". *Science* 342 (6155): 227–230.

Lay, T. and E. J. Garnero (2011). "Deep mantle seismic modeling and imaging". *Annual Review of Earth and Planetary Sciences* 39: 91–123.

Rudge, J. F. and D. Bercovici (2015). "Melt-band instabilities with two-phase damage". *Geophysical Journal International* 201 (2): 640–651.

van Keken, P. (1997). "Evolution of starting mantle plumes: a comparison between numerical and laboratory models". *Earth and Planetary Science Letters* 148 (1): 1–11.

Weis, D. et al. (2011). "Role of the deep mantle in generating the compositional asymmetry of the Hawaiian mantle plume". *Nature Geoscience* 4 (12): 831–838.

Acknowledgements

This work would not have been possible without the help and support of many people. First, I would like to express my gratitude to my mentor Stephan Sobolev for sparking my interest in geodynamic modelling, for always giving feedback and answering my questions and for giving me the freedom to try out new things. He encouraged me to travel a lot and gave me the opportunity to broaden my horizon and exchange my findings with other researchers. I would also like to thank my supervisors Volker John and Michael Weber for their interest and support, in particular with obtaining computational resources for my study.

Special thanks go to René Gassmöller, for his great support both during the coding and the writing phase, for fixing a huge number of cluster problems and for always finding the bug in the code when I was at my wits' end. Huge thanks go to Timo Heister, for spending a lot of of time and effort on figuring out how to implement melt migration in ASPECT, for always being motivating and for fixing my merge conflicts again and again. Many thanks also to Wolfgang Bangerth, who introduced me to the ASPECT code and from whom I learned a lot about programming and scientific writing. I also want to thank my other co-authors, Bernhard Steinberger, Eva Bredow and Trond Torsvik, for the great cooperation and teamwork during the work on our Tristan paper.

My project is part of the Helmholtz graduate school GEOSIM, and I would like to express my thanks to all GEOSIM students and PIs, and especially our coordinator Karen Leever, who always created an atmosphere that made it easy to exchange experiences and learn from each other. In particular, I want to thank Camilla Cattania, Elvira Mulyukova and Natalia Zamora, for fun times and the many scientific and non-scientific discussions. Thanks also go to Jens Tympel, Sascha Brune, Sarah Schröder, Marius Walter and my other colleagues at the Geodynamic Modelling Section at GFZ for the pleasant working atmosphere and inspiring discussions. Special thanks go to our secretary Till Bruens, who contributes a lot to this friendly atmosphere and always makes sure that everyone feels welcome.

This thesis greatly profited from discussions and cooperation with many other researchers, including Tobias Keller, from whom I learned a lot about implementing two-phase flow; Nick Arndt, with whom I had many interesting discussions about the chemical properties of mantle plumes; and Jonathan Perry-Houts and Gene Humphreys, with whom I worked on melt migration in mantle plumes. I would also like to thank Bob Myhill, Zach Eilon and Raj Moulik for fun times working on grain-size dependent rheology.

The computational infrastructure for this thesis was provided by the GFZ and the HLRN (North-German-Supercomputing-Alliance), and the essential tools Citcom and ASPECT are provided and supported by the CIG (Computational Infrastructure for Geodynamics). In particular, I would like to thank Ian Rose, Jacky Austermann, Anne Glerum, Menno Fraters, Sarah Stamps, Ryan Grove and all the other members of the ASPECT community for their contributions to the code, for always being helpful and for

all the fun hackathons.

Finally, I would like to thank my parents, who always supported me and helped me in difficult times, and without whom I would not be the person I am now.